UNIVERSITY OF LONDON THESIS

Degree PHD Year 2006 Name of Author HORESH LIOR

Some Novel Approaches in Modelling and Image Reconstruction for Multi-Frequency Electrical Impedance Tomography of the Human Brain

Lior Horesh

Submitted for the degree of Doctor of Philosophy

Department of Medical Physics
University College London
2006

ProQuest LLC
789 East Eisenhower Parkway
P.O. Box 1346
Ann Arbor, MI 48106-1346

Abstract

Electrical Impedance Tomography (EIT) is a recently developed imaging technique. Small insensible currents are injected into the body using electrodes. Measured voltages are used for reconstruction of images of the internal dielectric properties of the body. This imaging technique is portable, safe, rapid, inexpensive and has the potential to provide a new method for imaging in remote or acute situations, where other large scanners, such as MRI, are either impractical or unavailable. It has been in use in clinical research for about two decades but has not yet been adopted into routine clinical practice. One potentially powerful clinical application lies in its use for imaging acute stroke, where it could be used to distinguish haemorrhage from infarction. Hitherto, image reconstruction has mainly been for the more tractable case of changes in impedance over time. For acute stroke, it is best operated in multiple frequency mode, where data is collected at multiple frequencies and images can be recovered with higher fidelity. Whereas the eventual idea appears to be good, there are several important issues which affect the likelihood of its success in producing clinically reliable images. These include limitations in accuracy of finite element modelling, image reconstruction, and accuracy of recorded voltage data due to noise and confounding factors. The purpose of this work was to address these issues in the hope that, at the end, a clinical study of EIT in acute stroke would have a much greater chance of success. In order to address the feasibility of this application, a comprehensive literature review regarding the dielectric properties of human head tissues in normal and pathological states was conducted in this thesis. Novel generic tools were developed in order to enable modelling and non-linear image reconstruction of large-scale problems, such as those arising from the head EIT problem.

Table of Contents

List of Tables

List of Figures

1 INTRODUCTION

1.1 Overview

Electrical Impedance Tomography (EIT) is a relatively new imaging method with which reconstructed images of a subject can be made with array of external electrodes. It is inexpensive, fast, small and portable and has the potential to provide images at the bedside, in the community or for continuous monitoring. Set against these is a relatively poor spatial resolution. It has been in use in clinical research for about two decades but has not yet been adopted into routine clinical practice.

So far, most EIT applications addressed the more tractable case of changes in impedance over time, which permitted effective elimination of stationary artefacts through time-difference imaging. For some applications, such as differentiation of ischaemic from haemorrhagic acute cerebral stroke, time-referenced data is not available, and therefore, employment of spectral information is essential. For this purpose, comprehensive knowledge regarding the dielectric properties of biological tissues in normal and pathological states is required. In this work, such a survey was conducted for the tissues which constitute the human head. These values can be used in order to reliably estimate the magnitude of the peripheral changes which result from these conditions. Accurate Finite Element modelling of complex geometry, such as the human head, and in particular in a multi-frequency setting, result in the requirement to process multiple large-scale problems. In this work, a generic framework for solving multiple large-scale models efficiently was developed. The human head contains thin layers of large impedance contrast, such as the Cerebrospinal Fluid (CSF); therefore, generic methods for image reconstruction, which can effectively deal with large-scale inverse problems, were also developed here. Lastly, in a feasibility study for the application of stroke differentiation, the knowledge and tools developed in this work were combined together to assess the likelihood of such application in the face of realistic confounding factors.

In this opening chapter, EIT is briefly reviewed, and then the scope and outline of this thesis are presented.

1.2 Background

1.2.1 Impedance characteristics of tissues

The body can be considered as a composite volume conductor which comprises tissues with differing electrical properties [5]. Electric conduction within biological tissues occurs through movement of mobile ions. Such conduction is related to the ionic content and ionic mobility of each particular tissue type. Functional activity, as well as pathological conditions, results in structural and histological changes in the tissue. These changes are accompanied by characteristic temporal and spectral electric behaviour. Knowledge regarding the spatial dielectric properties distribution can provide useful information regarding the functional and pathological condition of the tissues.

1.2.2 EIT principles

Electrical Impedance Tomography (EIT) is a recently developing medical imaging modality that provides information regarding the internal electrical properties inside a body based on non-invasive voltage measurements on its boundary. Data acquisition is performed through an array of electrodes which are attached to the boundary of the imaged object. Sequences of small insensible currents are injected into the object through these electrodes and the corresponding boundary electric potentials are measured over a predefined set of electrodes. The process is repeated for numerous different configurations of applied current (Figure 1-1). The internal admittivity distribution can be inferred using this boundary data.

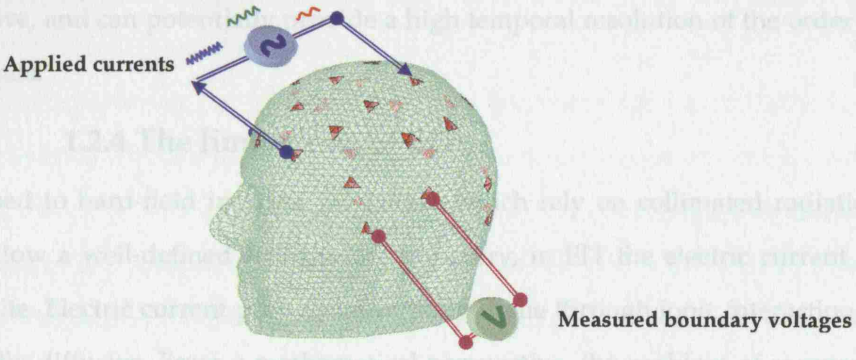

Figure 1-1. EIT data acquisition principle. Single or multi-frequency current waveform are injected through set of electrodes, while boundary voltages are recorded through a predefined set of electrodes

1.2.3 The role of EIT

EIT was first proposed as a medical imaging method already in 1978 by Webster [6], and in 1980 uniqueness was proven for the linearised inverse problem by Calderón [7]. The realisation and popularisation of the method can be attributed mainly to Barber and Brown [8].

The potential medical applications of EIT are vast, including detection and classification of tumours from breast tissue [9-11], detection of pulmonary emboli and edema [12;13], monitoring of pulmonary and cardiac functions [14-18], gastric imaging [19;20], detection and monitoring of cerebral ischaemia and haemorrhage [21-26], and localisation of epileptic foci [27;28].

In the 1930's, a similar technique was suggested for geophysics applications, namely Electrical Resistivity Tomography (ERT). This method is used to locate resistivity anomalies using electrodes on the surface of the earth or in bore holes. In the field of industrial process tomography, this method is used to monitor mixtures of conductive fluids in vessels or pipes [29] and for non-destructive testing and evaluation of materials and machine parts [30;31].

In the past two decades, there have been major advances in medical imaging, with the development of *hard-field* imaging methods, such as Magnetic Resonance Imaging (MRI), X-ray Computer Tomography (CT) and Positron Emission Tomography (PET). In spite of their immense benefits, these methods are all immobile, expensive, and image either anatomy or slow metabolic changes over time. Conversely, EIT is non-invasive, portable, inexpensive, and can potentially provide a high temporal resolution of the order of tens of milliseconds.

1.2.4 The limitations of EIT

As opposed to hard-field imaging modalities which rely on collimated radiation beams which follow a well-defined straight-line trajectory, in EIT the electric current paths are less definite. Electric current propagates in body tissue through ionic interaction, which is intrinsically diffusive. From a mathematical perspective, the problem of recovering inner admittivity distribution from boundary information is a nonlinear *inverse problem.*

Moreover, the problem is also severely ill-posed in the sense that even small errors in the measured data may cause arbitrarily large errors in the estimate of the internal admittivity. In the presence of measurement noise, the solution can become unstable. Due to these inherited limitations, the spatial resolution of EIT reconstructed images is generally relatively poor.

1.2.5 Modelling and image reconstruction

Image reconstruction comprises two separate stages: In the *forward solution,* boundary voltages are calculated using an analytical or numerical model of the internal properties and boundary conditions. Accurate forward models need to be capable of representing reliably the governing partial differential equations (PDE) associated with the problem over complex geometry with inhomogeneous impedance distribution and non-trivial boundary conditions [32-34]. The *inverse solution* procedure uses this information to infer the internal properties from the boundary measurements. Due to the ill-posedness of the problem, conventional image reconstruction methods, such as backprojection, cannot be used reliably. Most reconstruction algorithms for EIT rely on a perturbation approach, in which small variations of the recovered parameters from a known reference state are assumed. Due to the ill-posedness of the problem, a-priori knowledge and assumptions are used in order to regularise and constrain the solution space [35;36]. The general approach is to minimise an objective function, which include two main components: one represents the goodness of fit between the forward model and the given data, and the second include additional arguments which represent priors that are used to regularise, and consequently stabilise the solution [37].

Image reconstruction can be categorised into two main approaches: *difference imaging* and *static imaging*. In difference imaging two data sets are measured which correspond to two different target admittivity distributions. Based on the difference between these measurements, the difference in admittivity distributions can be estimated [27;38;39]. This approach is relatively robust, since most stationary noise and error sources are cancelled out. In static imaging, the image reconstruction process employs only a single data set of voltage measurements and the aim is to reconstruct the absolute admittivity distribution.

This approach involves highly accurate computation of the forward model in an arbitrary admittivity distribution (simulated reference) [40-42]. Such accurate models are typically of large-scale and therefore, introduce great computational difficulties for forward modelling and inverse problem solution.

Apart from introducing priors into the reconstruction procedure, image fidelity can be improved by the addition of independent information, and, in particular, by harnessing spectral information. This information can be used in order to constrain the inverse solution to physiologically plausible solutions. Moreover, this information is essential for improved forward modelling, which allows accurate predictions of the impact of functional and pathological conditions over the boundary voltage, and therefore assists in acquisition and hardware design. It is, therefore, crucial to get a firm understanding for the spectral tissue characteristics as well as the various mechanisms which characterise functional and pathophysiological behaviour. The addition of spectral information results in the requirement for solving multiple forward and inverse problems of larger scale. This requires development of appropriate forward and inverse problem frameworks which can efficiently treat large-scale problems.

1.3 Scope of Thesis

The overall purpose of this thesis was to develop generic methods which would enable improved modelling and image reconstruction of large-scale 3D EIT problems. In particular, the thesis focuses on the challenging problem of head EIT. The thesis has addressed these topics:

1. Physiology and modelling - A comprehensive critical review of the impedance spectrum of human head tissues in normal and pathological conditions was undertaken. This was utilised for a forward modelling study which aimed to set a specification for measurement accuracy for EIT in acute stroke with scalp electrodes
2. Forward problem - Novel generic tools have been developed for efficient solution of multiple large-scale forward models

3. Inverse problem - Novel generic methods for the solution of large-scale non-linear EIT inverse problems have been developed

This thesis is divided into seven chapters. In Chapter 2, a critical literature review of the local impedance properties of normal head tissue throughout the measurable EIT frequency range is given. The structural representation of the head compartments for modelling purposes was also reviewed. In Chapter 3, the spectral and temporal impedance-related changes during pathological conditions are reviewed. Pathophysiological mechanisms are discussed together with their expected influence over impedance. In Chapter 4, a quasi-static approximation for the EIT forward problem is introduced from the Finite Element Modelling (FEM) perspective. Two novel approaches for processing large-scale forward models efficiently are introduced: monopolar current sources and inverse-based multi-level preconditioning. First, a validation study was performed which set out to compare the accuracy of the developed forward solver with tank data. Second, the method of multi-level preconditioning was utilised for solving the forward problem, and the improvement in computational efficiency was assessed. The 5th chapter begins with a critical review of inverse problem methods with respect to their suitability for large-scale problems and the human head problem in particular. The most suitable non-linear methods were implemented, and a new novel non-linear Newton-Krylov method is presented. Lastly, a comparative study between the non-linear approaches is undertaken. The 6th chapter provides a qualitative estimation for the expected peripheral voltage change due to stroke, derived from an anatomically accurate finite element model. Physiological and acquisition errors were modelled and evaluated as well. The feasibility of performing classification by means of bioimpedance, absolute imaging and MFEIT is addressed. In Chapter 7, there is an overall discussion of the thesis with recommendations for future work.

An undergraduate level familiarity with physics, biology, and a familiarity with the principles of numerical analysis is required for comprehension of this thesis.

1.4 Authorship Statement

The bioimpedance review presented in Chapter 2 was performed with Andrea Romsauerova and Ori Gilad. The pathophysiological review in Chapter 3 was performed with Andrea Romsauerova and Lorenzo Fabrizi. Analysis of the feasibility study presented in Chapter 6 was performed with the assistance of Ori Gilad. The author undertook the substance of the work in these joint chapters, and all other work was entirely the author's own work.

1.5 Acknowledgements

This thesis was made possible by the assistance given to me by number of people. Firstly, I wish to thank my supervisors David Holder and Simon Arridge for their guidance throughout this work. In addition I would like to acknowledge Richard Bayford who supervised me the first year of my studies.

I am particularly grateful to Martin Schweiger and Bill Lionheart who introduced me to the intricacies of EIT reconstruction and modelling and to Matthias Bollhöfer and Eldad Haber for their endless patience in guiding me through the mysterious paths of numerical analysis.

Different parts of the research presented in the thesis would not have materialised without the contribution of the following people. Andrew Tizzard kindly provided realistic mesh models of the human head whenever required. Jason Godbold assisted with CT scanning of the latex tank model. Davide Poccecai gave endless help in solving all the computational problems which arose. Special thanks are given to Andrea Romsauerova for her advice in medical issues, to Alistair McEwan for his professional advice in instrumentation issues and tank data collection, to Louise Enfield for her expert advice in physiology and to Ori Gilad for his advice in data analysis.

I would also like to thank Adam Gibson, Ori Gilad and Inga Martinkute who were vital sources of strategic advice throughout and provided warm support. I would like specially to thank Raya Shindmes who reviewed this thesis and probably knows it as well as I do (or even better), and freed me from the mundane house maintenance tasks so that I could concentrate on this work.

I would like to use this opportunity to acknowledge all other UCL EIT group's members: Lorenzo Fabrizi, Juan Abascal, Marzia De-Lucia, Juan Frithchy and Gershon Ahadzi for their team work and many moments of joy.

This work was supported by UCL Graduate School (GSRS) and Universities UK (ORS scheme), to whom I am grateful. I would also like to acknowledge the Department of Medical Physics for their administrative support.

Finally, but by no means least, my thanks to my family and friends, and in particular to Yesheskel, Dora and Yair Horesh, Michel and Nadine Lubelski, Yaron Shammay, Tomer Ossi and Elad Sherman for their support during this work.

2 DIELECTRIC PROPERTIES OF TISSUES IN THE NORMAL ADULT HUMAN HEAD

2.1 Introduction

Bioimpedance measurements reflect the dielectric properties of the body tissues. It is possible to determine tissue type and integrity by its distinct spectroscopic signature. Reliable multi-frequency EIT modelling, effective reconstruction algorithms and appropriate instrumentation specifications require comprehensive knowledge regarding the dielectric properties of the tissues under examination, the participating mechanisms during pathological states, and knowledge regarding the expected physiological variability between one subject and another.

For forward modelling, this knowledge is essential in order to determine the propagation of electric fields throughout the medium in normal and abnormal states. For the inverse solution, this information can serve as a gold standard allowing differentiation between different tissues and their condition.

To date, dielectric properties of the human head have been investigated for a limited range of frequencies for the use of EIT [26;32;43]. However, exploiting a wide frequency range can offer better contrast between the different tissues and their conditions.

In this chapter, a literature review for normal impedance values has been conducted. The reviewed studies were incomplete, as there were relatively few for human tissue, measurements have not been made over the entire desired frequency bandwidth of 5Hz to 5MHz, and numerous technical considerations, such as acquisition method, and sample preparation procedures, differed from one study to another. In order to provide a reasonable set of working values for modelling purposes, extrapolations and physiologically plausible estimates were needed.

2.2 Purpose

The purpose of the work in this chapter is to review critically the frequency dependant dielectric properties of the tissues which constitute the head: grey and white matter, cerebrospinal fluid (CSF), blood, skull, scalp, skin and the eye. The anatomical boundaries needed for structural representation of the head tissues for Finite Element modelling are also reviewed. The final estimated and extrapolated values of impedance were subsequently used for simulation studies and image reconstruction purposes in this thesis.

2.3 Design

A short introduction concerning the physiology of each tissue type is provided, followed by a chronological literature review of the dielectric properties of each tissue. The entire measurable frequency range of an EIT system is reviewed, starting at 5Hz up to 5MHz. An emphasis was set on the frequency - dependant behaviour of the tissues, rather than their absolute admittivity at a certain frequency.

Extensive data have been published over the years regarding dielectric properties of the head tissues in their normal state. Various *In-vivo* and *in-vitro* measurements and analysis techniques have been used, which encompass different species, freshness levels, and temperatures. There are several useful compendium studies which were helpful in sourcing the available published data [5;44-49]. However, data included in this review have all been obtained directly from the original papers.

Where necessary, impedance values were translated into SI units, and have been presented both graphically and in table form to permit ready comparison.

2.4 Background

Electric current propagation within biological tissues occurs through ionic interactions. This flow is determined by the ionic content and ionic mobility of each particular tissue type. Different tissues vary in their cell structure and cell type composition. These differences result in characteristic dielectric properties and spectroscopic behaviour for each tissue type. However, these properties are also influenced by additional experimental and tissue related factors, such as the temperature and the directions in which the measurements were taken. Many studies attempted to define the dielectric properties of the head tissues; those studies involved tissue samples from various sources and conditions, and varied in their experimental setups. Reported results were represented in various units. In this section, a glossary of terminology is provided, and is followed by an introduction of dielectric relaxation mechanisms which provide a generalised description of the spectroscopic tissue behaviour. Finally, an overview of the various factors which influence recorded impedance properties is given.

2.4.1 Terminology

Interdisciplinary researchers, including physicists, electrochemists, biomedical engineers and electrophysiologists, gave rise to cross-fertilisation of ideas, but also

chose to use different jargon, which unfortunately included confusing misnomers. Before proceeding to the literature review, a description of the basic concepts and definitions of dielectric properties is provided.

The complex parallel admittance of a right prism shaped sample placed between two parallel electrodes of surface area A and separation distance d is defined as:

$$Y^* = G + i\omega C = \frac{A}{d}\sigma^* = \frac{A}{d}[\sigma + i\omega\varepsilon_0\varepsilon] \tag{2.1}$$

where $i = \sqrt{-1}$, $\omega = 2\pi f$ is the angular frequency, f is the given frequency in Hz, $Y^*, G, C, \sigma^*, \sigma$ *and* ε are frequency dependant and are defined in Table 2-1. The asterisk sign in this context denotes complex valued parameters.

The series equivalent complex impedance Z^* is defined as

$$Z^* = \frac{1}{Y^*} = R + iX = \frac{d}{A}z^* = \frac{d}{A}[\rho' + i\rho''] \tag{2.2}$$

where Z^*, R, X, z^*, ρ' and ρ'' are frequency dependent and are defined in Table 2-1. The prime and second signs denote the real and imaginary valued components respectively. The complex impedance can also have the following form

$$Z^* = \frac{1}{Y^*} = R + iX = \frac{G - i\omega C}{G^2 + (\omega C)^2} \tag{2.3}$$

And similarly the specific complex impedance z*

$$z^* = \frac{1}{\sigma^*} = \rho' + i\rho'' = \frac{\sigma - i\omega\varepsilon_0\varepsilon}{\sigma^2 + (\omega\varepsilon_0\varepsilon)^2} \tag{2.4}$$

The resistivity is defined as $\rho = 1/\sigma$ which is different to the real specific resistance ρ', which according to equation (2.4) is defined as

$$\rho' = \frac{\rho}{1 + (\omega\varepsilon_0\varepsilon\rho)^2} \tag{2.5}$$

The complex capacitance C^* can be defined as

$$C^* = \frac{Y^*}{i\omega} \tag{2.6}$$

which leads to the definition of the complex relative permittivity ε*

$$\varepsilon^* = \varepsilon' - i\varepsilon'' = \varepsilon' - i\sigma/\varepsilon_0\omega \tag{2.7}$$

where $\varepsilon' = \varepsilon_r = \varepsilon$. In the common case of an isotropic medium, the permittivity is scalar, but, in anisotropic media, this is not the case and ε is a rank-2 tensor. The admittivity, or complex conductivity, is the preferred quantity in this study. This quantity is composed of a real valued component (the conductivity) and an imaginary

component (known as susceptivity). The admittivity and complex permittivity are related by

$$\sigma^* = i\omega\varepsilon^*\varepsilon_0 \tag{2.8}$$

Table 2-1. Dielectric properties definitions. (S [Ω^{-1}] denotes Siemens units, and F are Farads)

Name	Symbol / definition	Units
Conductance ; Conductivity	G ; σ	S ; S/m
Capacitance ; Specific capacitance	C ; $c = \varepsilon_0\varepsilon_r$	F ; F/m
Admittance	$Y^* = G + i\omega C$	S
Complex conductivity / Admittivity	$\sigma^* \equiv \gamma = \sigma + i\omega\varepsilon_0\varepsilon_r$	S/m
Permittivity of vacuum	$\varepsilon_0 = 8.85 \cdot 10^{-12}$	F/m
Relative permittivity	$\varepsilon \equiv \varepsilon_r \equiv \varepsilon'$	-
Out of phase loss factor	$\varepsilon'' = \sigma / \varepsilon_0\omega$	-
Complex relative permittivity	$\varepsilon^* = \varepsilon' - i\varepsilon'' = -i\sigma^* / \varepsilon_0\omega$	-
Resistivity	$\rho = 1/\sigma$	Ωcm
Resistance ; Real specific resistance	R; $\rho' = \rho / \left[1 + (\omega\varepsilon_0\varepsilon\rho)^2\right]$	Ω ; Ωcm
Reactance ; Imaginary specific resistance	X ; $\rho'' = (\omega\varepsilon_0\varepsilon\rho^2) / \left[1 + (\omega\varepsilon_0\varepsilon\rho)^2\right]$	Ω ; Ωcm
Impedance; Specific impedance / Impedivity	$Z^* = R + iX$; $z^* = \rho' + i\rho''$	Ω ; Ωcm

2.4.2 Dielectric relaxation mechanisms

The impedance of live tissue comprises resistive elements, such as the intracellular and extracellular space and the membrane resistance, and reactive ones, such as the bi-lipid layer of the cell membrane. A dispersion refers to a steep conductivity increase and decrease of the relative permittivity over frequency, due to increased interaction of the applied current in these bands. The three main steps are termed the α, β and γ dispersions [50]. (Figure 2-1)

The low frequency α dispersion is associated with three factors: 1) A frequency-dependent conductance of the protein channels in the cell's membrane. 2) A frequency-dependent counter-ion environment near the charged cell surface. 3) An endoplasmic-reticulum effect in muscle tissue only.

The β dispersion is typically manifested at hundreds of kHz. It is mainly due to the polarisation of cellular plasma membranes, which act as barriers to the flow of ions between the intra and extra cellular media. The plasma membrane capacitance, the cell radius and the fluid conductivities determine the associated relaxation time. An additional contribution to this dispersion is due to polarisation of proteins and other organic macromolecules [51].

The γ dispersion is due to the polarisation of water molecules. Tissue water displays a broad dispersion spectrum, ranging between 100MHz and few GHz [51].

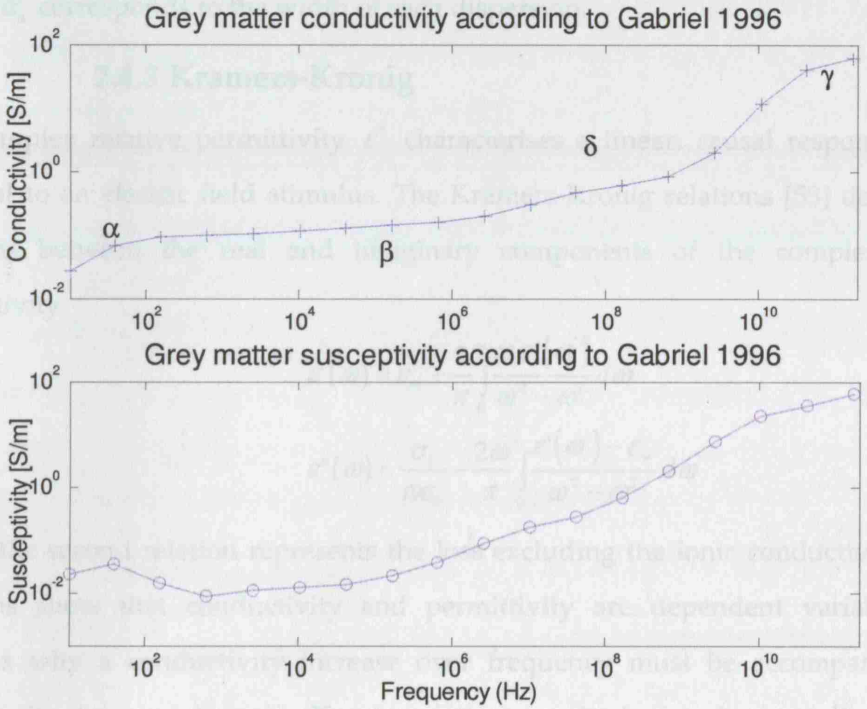

Figure 2-1. Admittivity of grey matter across frequency

Each of these relaxation regions is characterised by a single time constant, τ which to a first order approximation, can be expressed by the Debye expression [1] for the complex relative permittivity $\hat{\varepsilon}$ as a function of angular frequency ω

$$\hat{\varepsilon} = \varepsilon_{\infty} + \frac{\varepsilon_s - \varepsilon_{\infty}}{1 + i\omega\tau} \tag{2.9}$$

where ε_{∞} is the permittivity at frequencies $\omega\tau \gg 1$, and ε_s is the permittivity at field frequencies $\omega\tau \ll 1$. Hurt [52] modelled the dielectric spectrum of muscle to the summation of five Debye dispersions together with a static ionic conductivity term σ_i

[1] Debye relaxation is the dielectric relaxation response of an ideal, noninteracting population of dipoles to an alternating external electric field. This expression can be derived from density of states approximation in quantum mechanics

$$\hat{\varepsilon}(\omega) = \varepsilon_\infty + \sum_{n=1}^{5} \frac{\Delta\varepsilon_n}{1 + i\omega\tau_n} + \frac{\sigma_i}{i\omega\varepsilon_0} \tag{2.10}$$

where $\Delta\varepsilon_n = \varepsilon_s - \varepsilon_\infty$, and ε_0 is the permittivity of free space. The complexity of both the structure and the composition of biological material is such that each dispersion region may be broadened by multiple contributions to it. The broadening of the dispersion could be compensated empirically by introducing a distribution parameter. This approach is represented by the Cole–Cole multiple equation

$$\hat{\varepsilon}(\omega) = \varepsilon_\infty + \sum_{n=1}^{5} \frac{\Delta\varepsilon_n}{1 + (i\omega\tau_n)^{(1-\alpha_n)}} + \frac{\sigma_i}{i\omega\varepsilon_0} \tag{2.11}$$

where α_n corresponds to the width of each dispersion.

2.4.3 Kramers-Kronig

The complex relative permittivity ε^* characterises a linear, causal response of any material to an electric field stimulus. The Kramers-Kronig relations [53] describe the relations between the real and imaginary components of the complex relative permittivity

$$\begin{aligned} \varepsilon'(\omega) &= \varepsilon_\infty + \frac{2}{\pi}\int_0^\infty \frac{\omega'\varepsilon''(\omega')}{\omega'^2 - \omega^2} d\omega' \\ \varepsilon''(\omega) &= \frac{\sigma_i}{\omega\varepsilon_0} - \frac{2\omega}{\pi}\int_0^\infty \frac{\varepsilon'(\omega') - \varepsilon_\infty}{\omega'^2 - \omega^2} d\omega' \end{aligned} \tag{2.12}$$

where the second relation represents the loss excluding the ionic conductivity. These relations show that conductivity and permittivity are dependent variables. This explains why a conductivity increase over frequency must be accompanied by a permittivity decrease. Kramers-Kronig relations are limited to low amplitude fields, where a linear response applies. For biological materials, this condition is generally met.

2.4.4 Measurement techniques

Bioimpedance can be measured by four main techniques, known as: 2, 3, or 4-terminal measurement. Two-terminal measurements are the easiest and are typically used in the load impedance range of 100Ω to 10kΩ. In this method, the same two leads are used to drive currents into the medium and to acquire potential difference measurements. Three-terminal measurements are performed with two terminals and a guard. This technique is useful for high-impedance measurements when the effect of stray

capacitance can introduce errors as well as when guarded, in-circuit measurements are necessary. Four-terminal measurements are performed using two electrodes to drive current and two to record voltage. This method in principle eliminates series impedances and contact-resistance errors. The impedance of current injecting electrodes becomes immaterial as a constant current source injects a constant current irrespective of electrode impedance; the impedance of electrodes on the recording becomes negligible if the input impedance of the recording amplifiers is so high that negligible current is drawn across the electrodes [54].

When low impedances are measured, a two-terminal connection introduces errors caused by the addition of the series impedance of the connecting leads. As a result, most instruments now use the four-terminal method to perform low-impedance measurements. The measured impedance range and the required accuracy therefore determine the choice of suitable measurement method for a given application.

Most EIT systems apply sine wave, or a composite of sine waves from different frequencies. However, another approach is application of pulse wave form. Such pulse can effectively apply infinite frequency spectrum altogether. In this study, measurements taken in 4 terminal mode were favoured; higher fidelity was accounted for studies in which a calibration procedure is well described.

2.4.5 Anisotropy

Some of the head tissues possess considerable anisotropic admittivity property. This is most pronounced in tissues with a regular cylindrical composition, such as white matter and scalp muscle, and can significantly affect the forward model predictions. Tuch [55] suggested mapping a conductivity tensor using diffusion tensor MRI; he demonstrated a strong linear relationship between conductivity and the diffusion tensor eigenvalues. Wolter et al [56] have demonstrated recently the impact of anisotropy for EEG and MEG field calculations. However, hitherto, there has been no established method for the inclusion of anisotropic admittivity tensors into head models and the inverse solution of the anisotropic case for EIT requires substantial usage of priors to restore uniqueness [57].

2.4.6 Temperature effects

Typically, most bioimpedance measurements were performed at room temperature of 20°C or at body temperature, which for most large mammalian species is around 37°C. Up to the GHz region, there is a linear relation between tissue conductivity and temperature. This behaviour is similar to that of a simple electrolyte, i.e. the temperature coefficient $\frac{100}{\sigma}\frac{\Delta\sigma}{\Delta T}\left[\frac{1}{^{\circ}C}\right]$ is about $+2\frac{\%}{^{\circ}C}$. Less consistent but similar behaviour was derived for the permittivity temperature coefficient $\frac{100}{\varepsilon}\frac{\Delta\varepsilon}{\Delta T}\left[\frac{1}{^{\circ}C}\right]$, which was found to be around $+1\frac{\%}{^{\circ}C}$ [46]. For most practical applications, a majority of the information content is related to the spectroscopic curvature of tissues, and therefore in this respect, these coefficients are negligible. Nevertheless, measurements acquired at body temperature are required for modelling purposes, and are therefore favoured here. In order to compare results from different studies in a reliable manner, the temperature at which the impedance was measured is mentioned for each reviewed study.

2.4.7 The effect of age

The age of the subject from which a tissue sample was taken is another source of variation in the dielectric properties. The heads of infants and neonates are structurally different from those of adults. This affects mainly the skull, which is less calcified, but also the brain itself and the skin impedance [58]. Moreover, there are large structural variations of the brain tissues between young adults and older subjects [59]. Apart from the structural differences, over the years the head tissues, and in particular the brain, skull and skin, become less hydrated and of lower permittivity.

2.4.8 *In-vivo* vs. *in-vitro*

Many studies have been performed on excised tissues. This allows full control over the tissue measurement conditions, such as separation of tissue types and measured volume. However, the impedance is materially affected as cell death rapidly alters the extracellular space and intracellular organelles [46]. Differences of up to 17% in conductivity and up to 49% in permittivity at the frequency range of 10kHz and 10MHz have been observed [60]. The applied pressure of probes may also influence the recorded impedance values.

2.4.9 Inter-species and inner-specificity

Many relevant measurements have been made in other animal species, usually mammalian. The effect of this difference is unclear but, in general, it appears that most mammalian values are similar and that the variation in tissue properties within each species exceeds variations between species [47].

2.5 Normal Tissue Dielectric Properties

2.5.1 Skin

The skin comprises epidermis, dermis and subcutaneous fat. Skin impedance is determined mostly by two layers: an outer dry keratin layer of the epidermis (stratum corenum), which consists of dead epidermal cells, and the underlying deep tissue (dermis and subcutaneous tissue) which contain granular layers of live cells (Figure 2-2). The skin impedance is mainly determined by stratum corneum at low frequencies and by the viable skin at higher frequencies. For the purposes of EIT applications, the dry keratin layer is completely removed when the skin is abraded prior to the application of surface electrodes. Reduction of the skin impedance is important for EIT data acquisition, as it minimises common mode errors when using differential mode measurements [61-63]. For that reason, only the figures given for the granular layers are in our scope of interest.

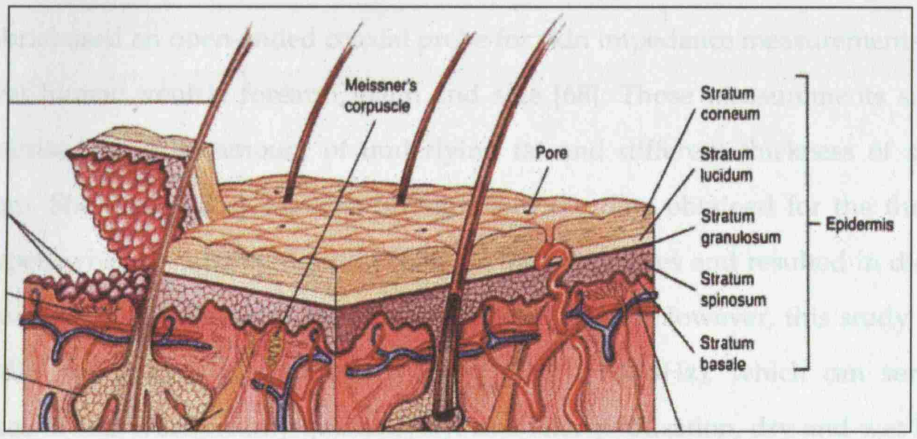

Figure 2-2. Skin and underlying subcutaneous tissue (adapted from Marieb 1991)

Yamamoto et al [64;65] used an AC bridge with two electrodes to measure the skin impedance of the human forearm at 2Hz to 1MHz. The polarisation impedance of the electrodes and the residual, or stray impedance of the lead wires, were measured separately for all frequencies and subtracted from the human measurements. The

measurements were repeated along a set of 15 stepwise removals of the stratum corneum (the 5th and bottom-most layer of the epidermis) by stripping cellulose tape pressed on the skin. No α and β dispersions were observed in the keratin layers. This was attributed to the deceased nature of the stratum corneum layers which contained no live cells and so negligible capacitance [66;67].

While the ventral forearm is essentially a convenient measurement site, skin impedance exhibits a considerable regional variability over the body, showing lower impedance in the regions where sweat ducts are abundant, such as the palms. For this study, measurements from the human head are most appropriate. Rosell et al [61] performed skin impedance measurements over 10 human subjects at 10 different sites including the head. A three terminal measurement technique was used with a coaxial probe; their measurements were at the frequency range of 1Hz to 1MHz and were taken over non-abraded skin and so may be expected to have higher impedance at low frequencies with respect to those acquired over abraded skin. The highest skin impedance was obtained for the leg, whereas the lowest was at the forehead. Unfortunately, their report did not include any quantitative information for the extent of this effect. This study raised another interesting point; immediately after gel application, an impedance increase of up to 20% was reported, a phenomenon that they attributed to the closure of the sweat ducts after application of the cool gel.

Gabriel used an open-ended coaxial probe for skin impedance measurements of dry and wet human ventral forearm, palm and sole [68]. Those measurements sites are characterised by little amount of underlying fat and different thickness of stratum corneum. She reported systematic differences of the data obtained for the three dry skin-types, whereas wetting the skin reduced the differences and resulted in dielectric responses similar to those for high-water-content tissues. However, this study was at the radio and microwave frequency range (1MHz-100GHz), which can serve the purposes of this work mainly qualitatively. In a later publication, dry and wet human ventral forearm skin measurements were taken through the wide frequency range of 10Hz to 20GHz [49].

Another study demonstrating the impact of stratum corneum hydration level over the reliability in which such coaxial probes can measure the true impedance of the

granular skin layer was performed by Raicu et al [69]. They measured dry and 0.9% NaCl saline moistened skin impedance through the frequency range of 100Hz to 100MHz. Special care was given to the effective depth of the measurement probe, which increases as the contact region (including the stratum corneum) becomes more conductive.

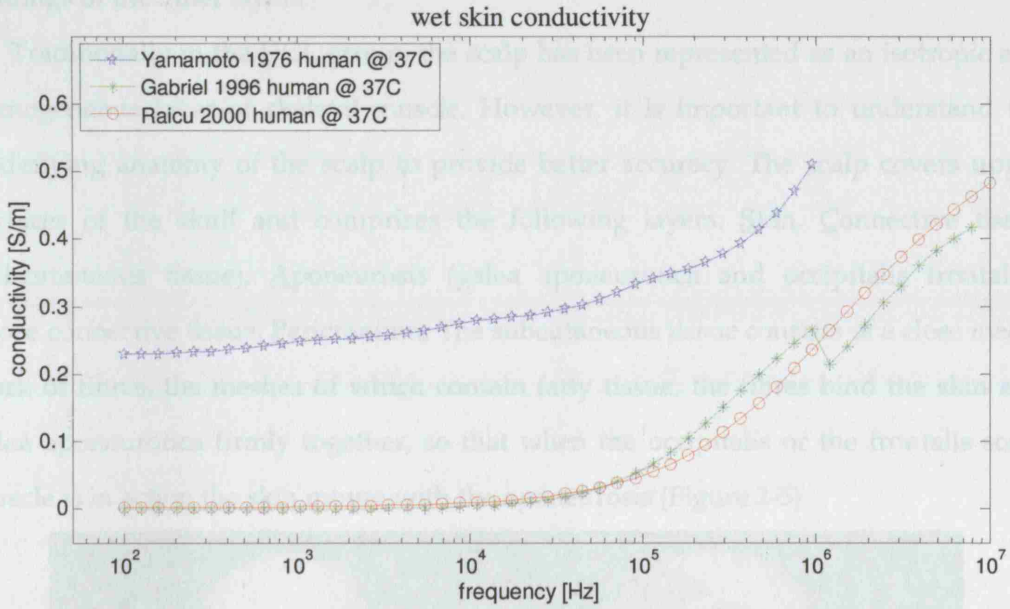

Figure 2-3. Wet skin conductivity over frequency

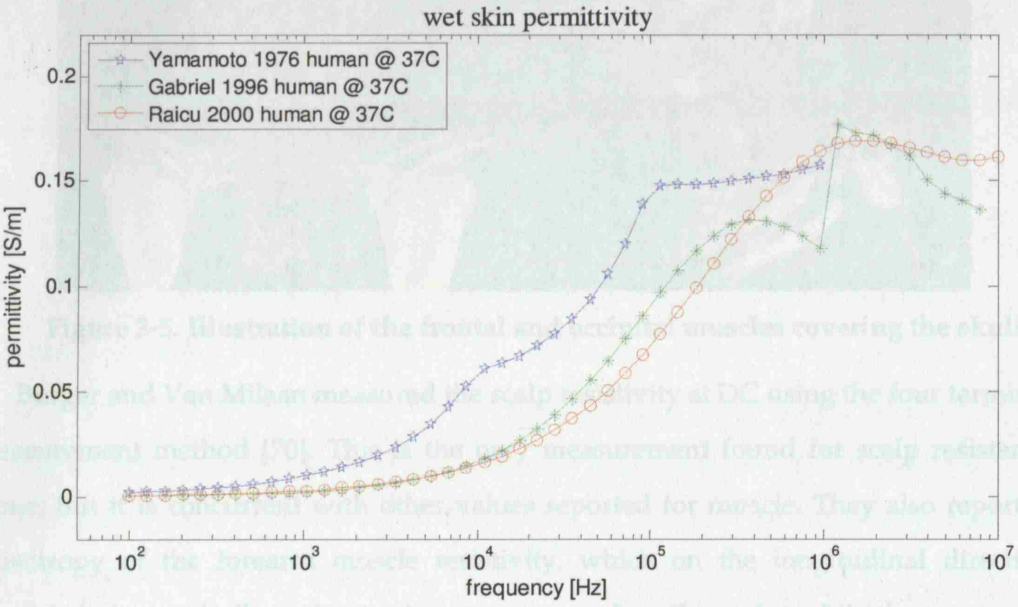

Figure 2-4. Wet skin permittivity over frequency

Discussion and conclusions for this tissue are presented in 2.6.2.

2.5.2 Scalp

As contra-intuitive as it might seem, the scalp impedance plays a major role in head EIT, as it engaged with currents of the highest density coming from the electrodes, and therefore it is the first stage in which distribution of current into the rest of the layers is determined. Any inaccuracies at this stage will substantially affect the impedance readings of the inner layers.

Traditionally in the UCL group, the scalp has been represented as an isotropic and homogeneous layer of skeletal muscle. However, it is important to understand the underlying anatomy of the scalp to provide better accuracy. The scalp covers upper surfaces of the skull and comprises the following layers: Skin, Connective tissue (subcutaneous tissue), Aponeurosis (galea aponeurotica and occipitalis frontalis), Loose connective tissue, Pericranium. The subcutaneous tissue consists of a close meshwork of fibres, the meshes of which contain fatty tissue; the fibres bind the skin and galea aponeurotica firmly together, so that when the occipitalis or the frontalis scalp muscle is in action the skin moves with the aponeurosis (Figure 2-5).

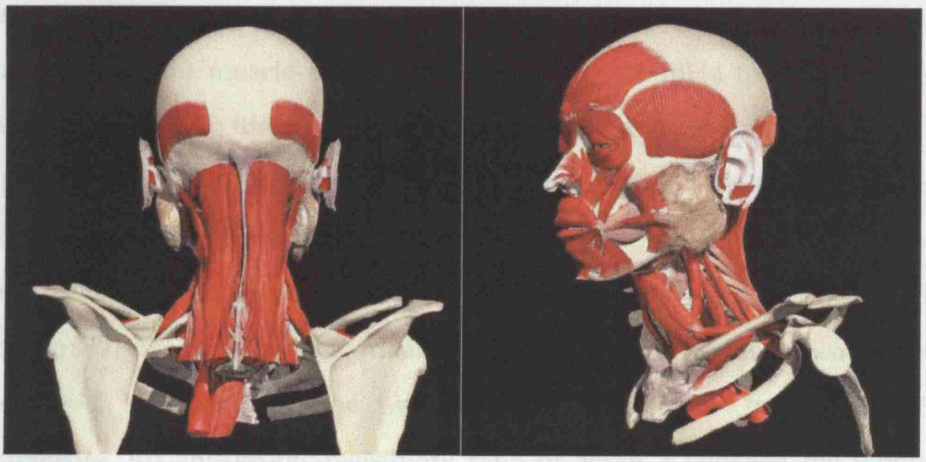

Figure 2-5. Illustration of the frontal and occipital muscles covering the skull

Burger and Van Milaan measured the scalp resistivity at DC using the four terminal measurement method [70]. This is the only measurement found for scalp resistance alone, but it is concurrent with other values reported for muscle. They also reported anisotropy of the forearm muscle resistivity, which on the longitudinal direction provided almost similar value to the one measured on the scalp, while the transverse measurement was more than twice as resistive.

Schwan used alternating currents for *in-situ* muscle impedance measurements of canine skeletal muscle [44;71]. His measurements were of a non-specified direction and were performed using a two terminal measurement. In a later study, electrodes covered in platinum black were used, in order to reduce electrode polarisation errors. Burger and Van Dongen repeated the human forearm measurement 17 years later in the frequency range of 20-5,000Hz [72]. They reported similar values on the longitudinal direction as before, but with transverse impedance, which was about 2.8 times larger than the longitudinal. Stoy et al performed two terminal impedance measurements over freshly killed rabbits and rats, and post-mortem dogs. Their measurements were in the frequency range of 100kHz and 100MHz [73]. For rat tissue, the β dispersion centre frequency was estimated at 197.5kHz with a rapid dispersion slope manifested by dispersion width (alpha parameter) of 0.078. This study did not distinguish between the longitudinal and transverse directions; however, their measurements appear to agree with other measurements made in the transverse direction. Epstein et al took two terminal measurements of canine muscle in the frequency range of 100Hz to 1MHz [74]. The year after, Gielen et al acquired *In-vivo* measurements of rat muscle at the frequency range of 10Hz to 100kHz [75]. Both studies were examining the anisotropic character of the muscle tissue. They concluded an impedance ratio of 5-7 times between the longitudinal and the transverse direction. Bodakian et al were comparing the dielectric properties of freshly excised chicken and beef muscle tissue with defrosted samples at the frequency range of 5Hz - 1MHz [76]. A two terminal needle array electrodes were used in most of their measurements; a choice, which undermined the reliability of their low frequency (<500Hz) measurements. An anisotropic resisitivity ratio of about 2 between the longitudinal and the transverse directions observed for the freshly excised tissues between 100Hz and 100kHz. Gabriel et al made two terminal measurements of ovine muscle in the frequency range of 10Hz and 20GHz. These measurements were also modelled as a sum of four Debye dispersions [47-49]. Hart et al [77] took two terminal resistivity measurements of the bullfrog muscle in the frequency range of 1kHz to 1MHz. In addition to the analytical anisotropic models [78] they also calculated the exact contribution of each direction, based on a finite difference model they have generated.

With their method, they confirmed that the longitudinal conductivity is higher than of the transverse direction. However, the difference in conductivity between these directions appeared smaller than in previous publications, especially for the lower frequencies that were considered in their study.

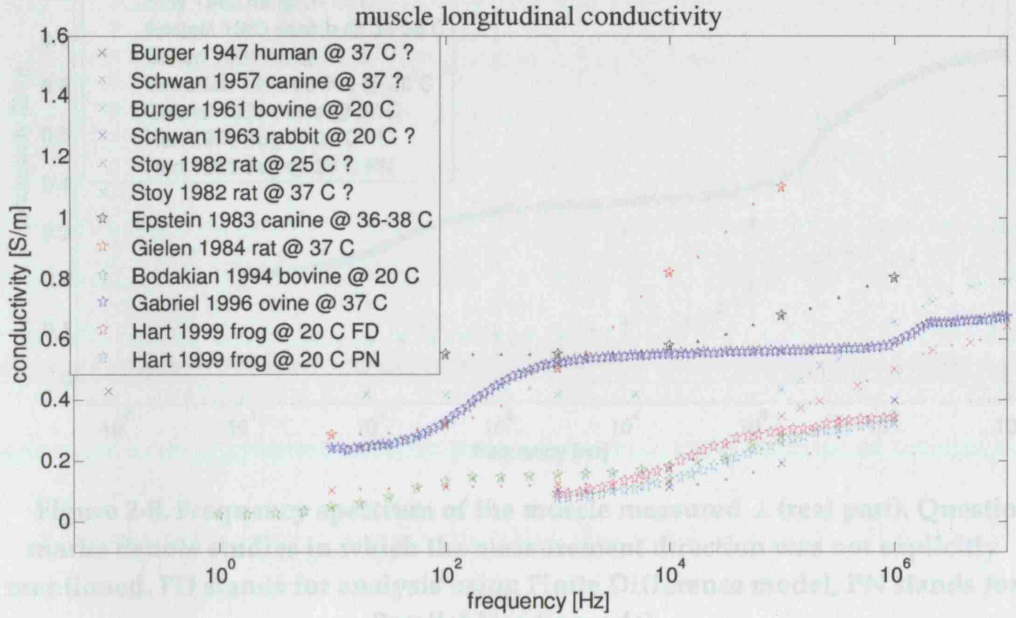

Figure 2-6. Frequency spectrum of the muscle measured || (real part). Question marks denote studies in which the measurement direction was not explicitly mentioned. FD stands for analysis using Finite Difference model, PN stands for Parallel Needle model

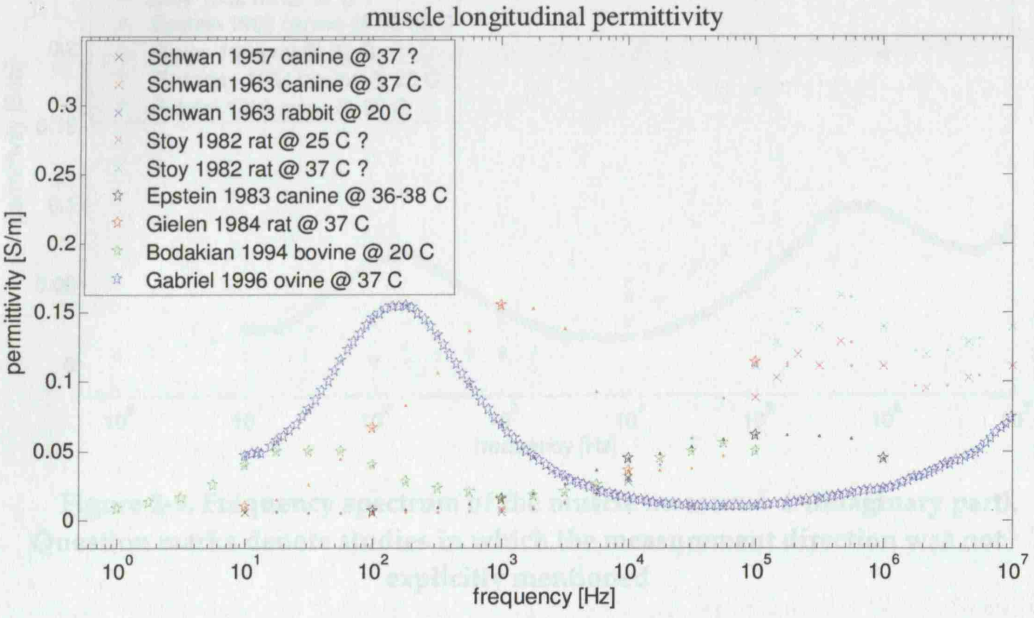

Figure 2-7. Frequency spectrum of the muscle measured || (imaginary part). Question marks denote studies in which the measurement direction was not

explicitly mentioned. FD stands for analysis using Finite Difference model, PN stands for Parallel Needle model

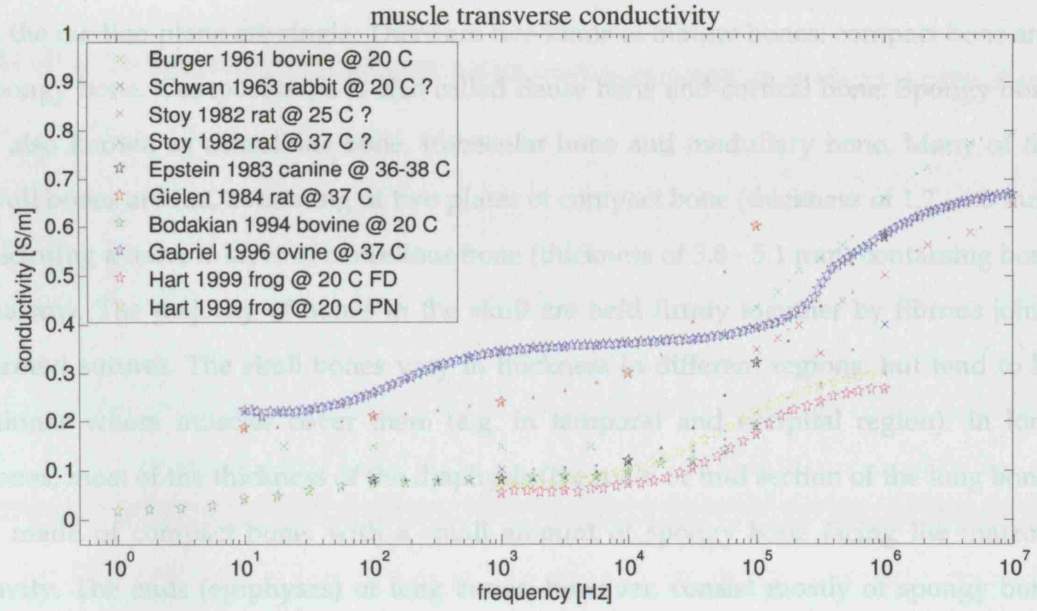

Figure 2-8. Frequency spectrum of the muscle measured ⊥ (real part). Question marks denote studies in which the measurement direction was not explicitly mentioned. FD stands for analysis using Finite Difference model, PN stands for Parallel Needle model

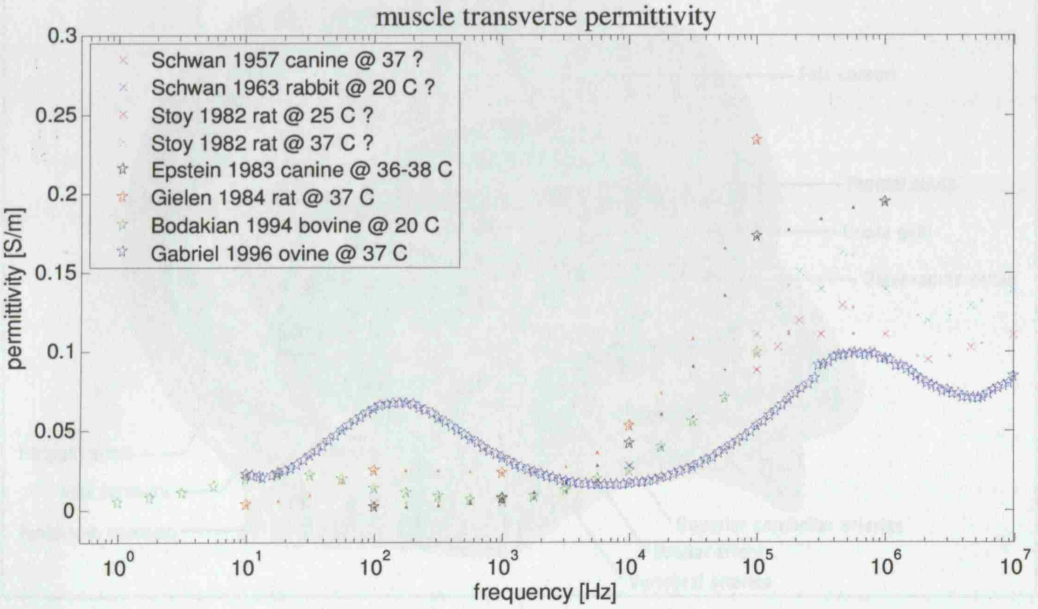

Figure 2-9. Frequency spectrum of the muscle measured ⊥ (imaginary part). Question marks denote studies in which the measurement direction was not explicitly mentioned

2.5.3 Skull

The skull is a collection of 28 separate bones, of which most are paired, although some in the median plane are single. There are two kinds of mature bones: compact bone and spongy bone. Compact bone is also called dense bone and cortical bone. Spongy bone is also known as cancellous bone, trabecular bone and medullary bone. Many of the skull bones are flat, consisting of two plates of compact bone (thickness of 1.7 - 4.3 mm) enclosing a narrow layer of cancellous bone (thickness of 3.8 - 5.1 mm) containing bone marrow. The majority of bones in the skull are held firmly together by fibrous joints termed sutures. The skull bones vary in thickness in different regions, but tend to be thinner where muscles cover them (e.g. in temporal and occipital region). In long bones, most of the thickness of the diaphysis (the main or mid section of the long bone) is made of compact bone, with a small amount of spongy bone facing the marrow cavity. The ends (epiphyses) of long bones, however, consist mostly of spongy bone covered with a shell of compact bone.

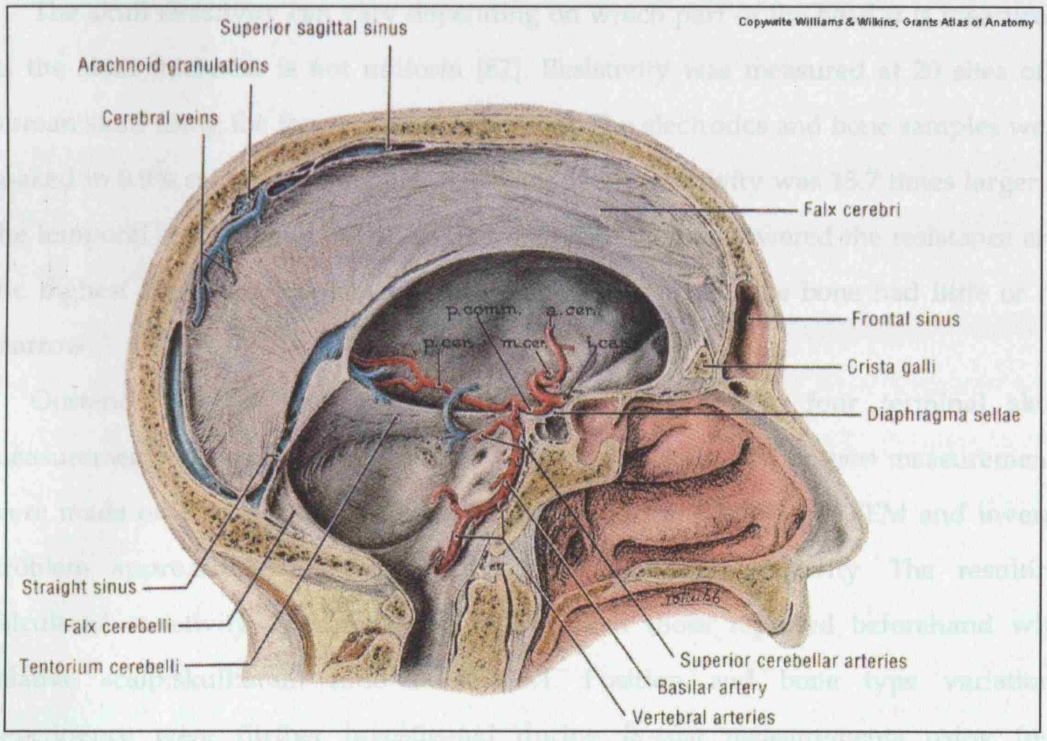

Figure 2-10. Mid-sagittal projection of the skull. [79]

The skull is indeed a bone of contention [32]. Data published regarding skull impedance covers a wide range of values, and while the impedance is not affected by brain pathology or functional activity, the resistivity of the skull affects measurements

made and images created if the ratio of brain:skull:scalp is incorrect in the models used.

Since the trabecular bone is an inhomogeneous composite material, containing a porous bony matrix filled with fluid, and is structurally and mechanically anisotropic, its electrical characteristics are complex. The high-frequency limit of relative permittivity depends on the water content of the tissue, and the collagen fibres are the main source of dielectric dispersion in a long bone.

Rush and Driscoll [80] measured impedances for half a skull immersed in saline. They assumed that dry skull is effectively an insulator, and that the effective conductivity of the skull is directly proportional to the conductivity of the fluid with which it is permeated. They found that the conductivity ratio of the permeating fluid to the immersed skull was 80. Subsequently, they used a conductivity ratio of 1:1/80:1 for brain, skull and scalp in a concentric spheres model to study EEG electrode sensitivity [81].

The skull resistivity can vary depending on which part of the head it is measured, as the skull thickness is not uniform [82]. Resistivity was measured at 20 sites of a human skull using the four terminal technique. The electrodes and bone samples were soaked in 0.9% saline 24 hours before testing. Skull resistivity was 15.7 times larger at the temporal regions than at the back of the head. Sutures lowered the resistance and the highest resistance values were found in regions where the bone had little or no marrow.

Oostendorp et al performed both *In-vivo* and *in-vitro* four terminal skull measurements at the frequency range of 100Hz to 10kHz [83]. *In-vivo* measurements were made on two subjects, both transversely and sagittally using FEM and inverse problem approach to measure the effective isotropic resistivity. The resulting calculated resistivity appeared much lower than those reported beforehand with relative scalp:skull:brain ratio of 1:1/15:1. Position and bone type variations dependence were further investigated during *In-vivo* measurements using four terminal technique at 10-90Hz on skull flaps excised from 4 patients during surgery (with a 15 - 65 minute delay between excision and measurement) [84]. Holes were

drilled in the samples to allow the resistivity to be measured at the different layers in the bone sample. (Table 2-2)

Table 2-2: Resistivity of different layers of skull [84]

Layer	Range ρ [Ωcm]	Mean ρ [Ωcm]	Mean decrease in ρ over 10-90Hz [%]
Top compact layer	13900-18400	16200	1.8
Spongiform layer	2400-6200	4700	5.4
Lower compact layer	9800-35300	20500	8.6
Bulk	10700-11800	10500	4.6

A year later, frequency dependence of the conductivity of different layers and the bulk were measured and modelled at the same frequency range [85]. The samples were cut from calvarial, temporal, temporal-parietal and inferior occipital regions of the skull. Goncalves et al estimated the effective isotropic skull conductivity by an EIT-based method using spherical shells for analytical solutions [86;87]. In that study, 64 measurement electrodes and 7-10 pairs were used to inject sinusoidal current of 60Hz. Data acquisition was in 4-terminal mode. They also used a combined analysis of EEG/MEG inverse problem of Somatosensory Evoked Fields / Somatosensory Evoked Potential (SEF/SEP) and calculated the brain and skull resistivity [88]. Extension of their EIT analysis method to include realistic head model using Boundary Element Method (BEM) provided lower skull resistivity values with similar resistivity values for the brain.

Further conductivity measurements were made in five temporal bone samples temporarily removed during epilepsy surgery [89]. A series of measurements were made with an array of 16 electrodes, using two electrodes to inject the current, two electrodes as reference and ground, and the other electrodes to measure the potential distribution in an extended 4-terminal measurement. Measurements were also made on a piece of post mortem skull. The conductivity measured was about 10 times higher than any previously published data (see Appendix A for a summary of the data presented in this section). This difference could be due to the fact that the measurements were made a very short time after excision, while other samples have been dried and then re-soaked. The high conductivity could also be due to a thin layer of saline on the surface of the skull.

Since there is no published data regarding the spectroscopy of the skull throughout a wide frequency range, long bone which consist of lamellar and trabecular (or cancellous) bone are considered. Such bone has a similar composition to skull.

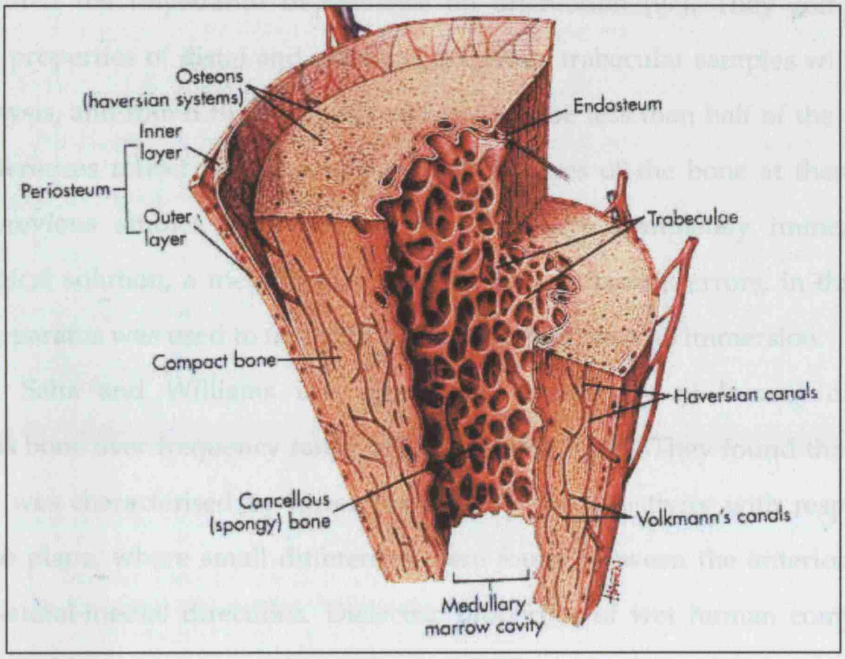

Figure 2-11. Long bone microstructure [90]

Chakkalakal et al investigated the impedance of bovine cortical bone immersed in saline with DC current [91;92]. They reported resistivity values in the radial direction, which were two orders of magnitude smaller than reported before at 98% relative humidity conditions [93]. They have suggested that the larger pores in the bone were not filled with fluid. Kosterich et al compared the dielectric properties of freshly excised and formalin fixed femoral rat bone over the wide frequency range of 10Hz to 100MHz [94]. They noted that for frequencies lower than 100kHz, conductivity was almost constant, whereas at higher frequencies there was a rapid increase.

Reddy et al investigated the dielectric properties of bovine cortical bone in three orthogonal planes in the frequency range of 1kHz - 1MHz [95]. They employed a differential two terminal method in which a known reference was measured at each frequency to account for stray capacitance effect. They reported the largest frequency dependence to be in the radial direction. Dielectric properties of bone marrow and cortical bone were measured in frequency range of 1kHz to 1GHz and 1kHz to 30MHz respectively, using two electrodes method at a temperature of 25°C for bone marrow or

37°C for bone tissue [96]. A small dispersion was noticed in the permittivity data from the marrow with a centre frequency of 1MHz; this probably corresponded to β dispersion of the blood included in the sample. De Mercato and Garcia-Sanchez demonstrated the impedance dependence on orientation [97]. They compared the dielectric properties of distal and proximal epiphysis trabecular samples with those of the diaphysis, and found the epiphysis resistivity to be less than half of the diaphysis; these differences reflect the microstructural differences of the bone at these regions. Unlike previous studies in which the samples were completely immersed in a physiological solution, a method that give rise to polarisation errors, in this study a special apparatus was used to maintain bone saturation with no immersion.

Later, Saha and Williams investigated the anisotropy of human distal tibia cancellous bone over frequency range of 120Hz-10MHz [98]. They found that the axial direction was characterised by lower permittivity and resistivity with respect to the transverse plane, where small differences were found between the anterior-posterior and the lateral-medial directions. Dielectric properties of wet human compact bone from distal tibia were measured by Saha and Williams in three orthogonal directions (axial, transverse, circumferential) using two terminal mode at 120Hz to 10MHz for axial direction and 10kHz, 100kHz and 1MHz for the normal directions [99]. The measurements were taken at 27°C and 100% relative humidity. The resistivity of the bone samples for the axial direction exhibited frequency dependent behaviour; the resistivity of the sample decreased by 23% in the frequency range of 120Hz to 10MHz. De Mercato and Garcia-Sanchez [100] measured dielectric properties of bovine femur in three directions (radial, axial, circumferential), using the two terminal technique at temperature of 23°C at three frequencies of 100Hz, 10kHz and 1MHz. They found a linear relation between the conductivity and the relative permittivity in each direction. Both conductivity and permittivity were larger in the axial direction than in the other two normal directions. This reflects the conductivity's dependence on the bone's anisotropic structure as fluid content in the axial Haversian systems is larger than in radial or tangentially connective channels. Gabriel et al [49] measured the impedance of cancellous human bone which contained red bone marrow at 23°C in the frequency range of 100kHz - 20GHz, ovine cortical bone at 37°C at 1MHz - 20GHz and bovine

marrow at 37°C between 10Hz - 20GHz. These were taken with two terminal measurements. Sierpowska et al demonstrated the dependency of volumetric trabecular bone mineral density and its relative permittivity [101]. The dielectric and mechanical properties of femoral bovine trabecular bone samples from various regions were measured. The bones were frozen and defrosted prior to the measurement procedure. Measured frequencies were between 50Hz and 5MHz. Later they [102] measured the impedance of cadaver human trabecular knee bone at the same frequency range. Tibia and femoral trabecular bones were defrosted to room temperature (22°C) after they were kept frozen for 12 months. While there were no significant differences between the tibia and the femoral bone throughout the entire frequency range, human trabecular bone was found to be twice as conductive as bovine.

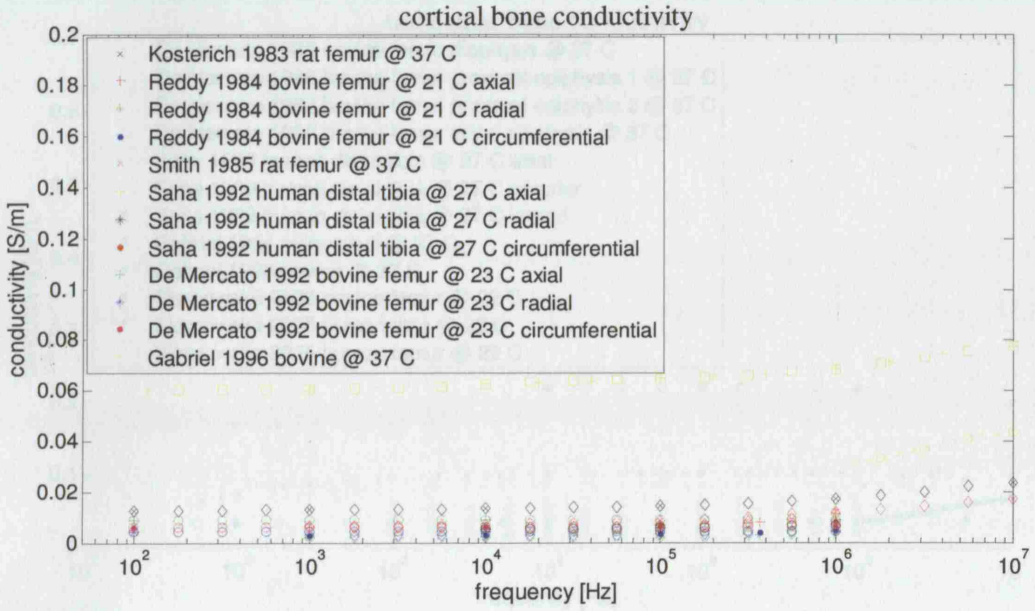

Figure 2-12. Cortical bone conductivity

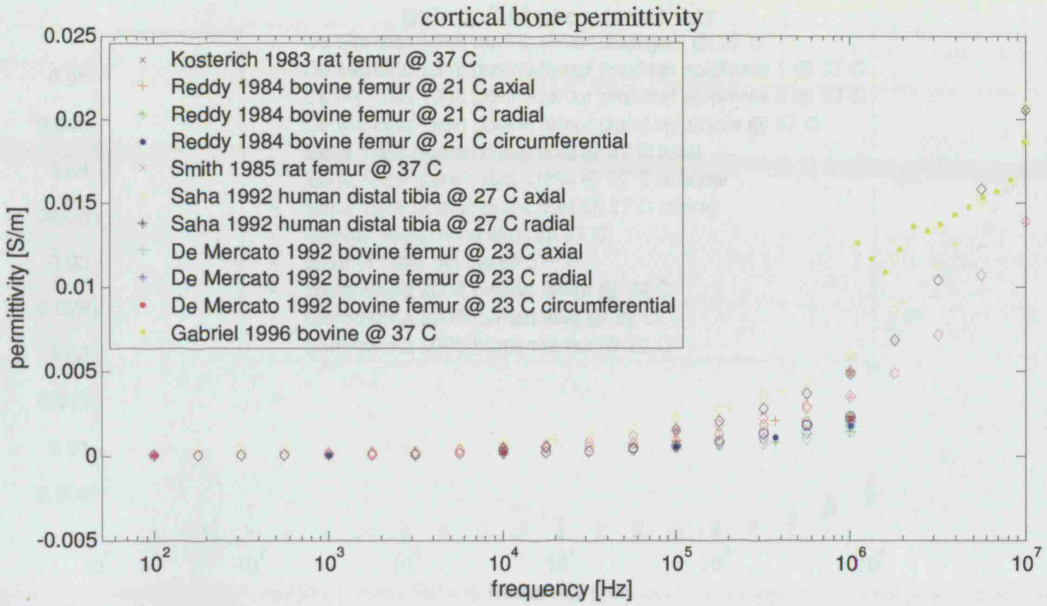

Figure 2-13. Cortical bone permittivity

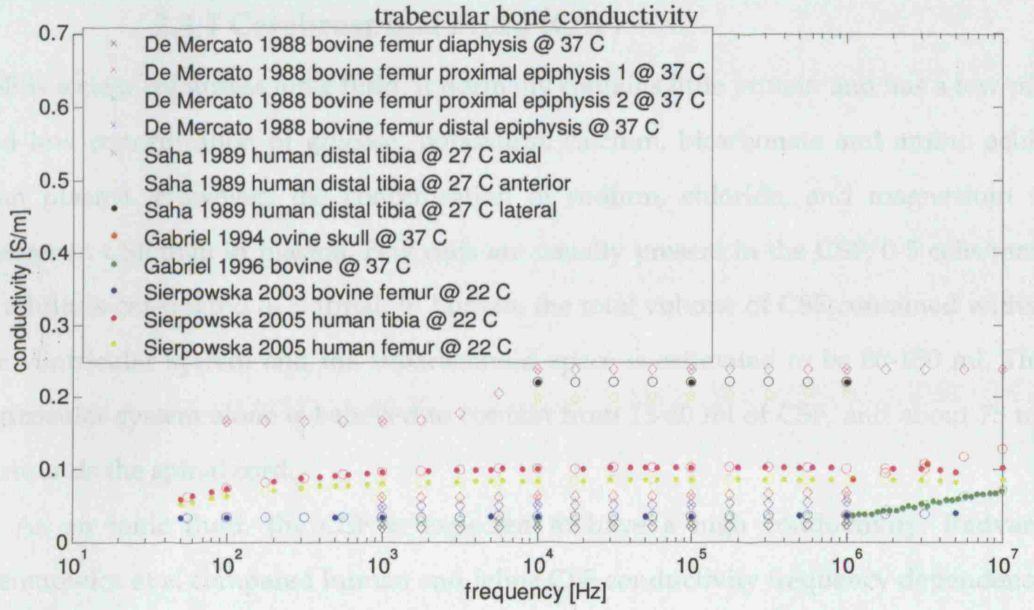

Figure 2-14. Trabecular bone conductivity

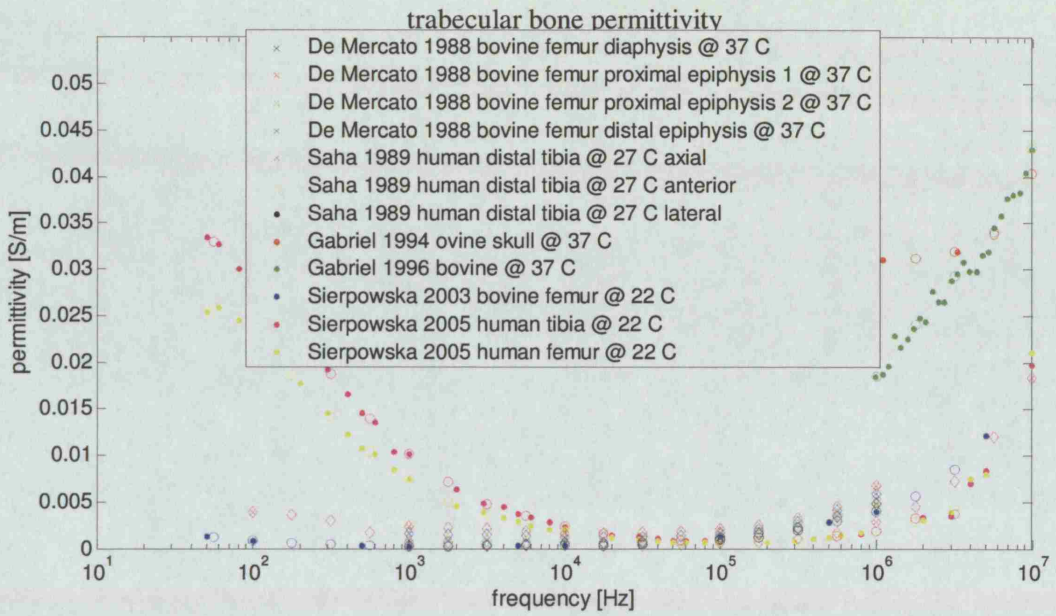

Figure 2-15. Trabecular bone permittivity

2.5.4 Cerebrospinal Fluid (CSF)

CSF is a clear colourless ionic fluid. It normally contains little protein and has a low pH and low concentration of glucose, potassium, calcium, bicarbonate and amino acids than plasma. However, the concentration of sodium, chloride, and magnesium is greater in CSF than in plasma. Few cells are usually present in the CSF; 0-5 cells/mm^3 in adults is considered as normal. In human, the total volume of CSF contained within the ventricular system and the subarachnoid space is estimated to be 80-150 ml. The ventricular system alone is believed to contain from 15-40 ml of CSF, and about 75 ml surrounds the spinal cord.

As an ionic fluid, the CSF is expected to have a high conductivity. Radvan-Ziemnowicz et al compared human and feline CSF conductivity frequency dependence at 1kHz - 30kHz [103]. They reported conductivity temperature dependency to be $+1.9\frac{\%}{^oC}$. Baumann et al measured the properties of CSF using the four terminal technique in a Perspex measuring cell at 10Hz - 10kHz, they comparedthe measured values at room temperature with those obtained at body temperature [104]. The samples were frozen and then deforested. As expected, no evidence for reactive component were found ($\varepsilon = 0$). Latikka et al measured the CSF resistivity *In-vivo* in patients with brain tumours during surgery with a monopolar needle at a single frequency of 50kHz [105].

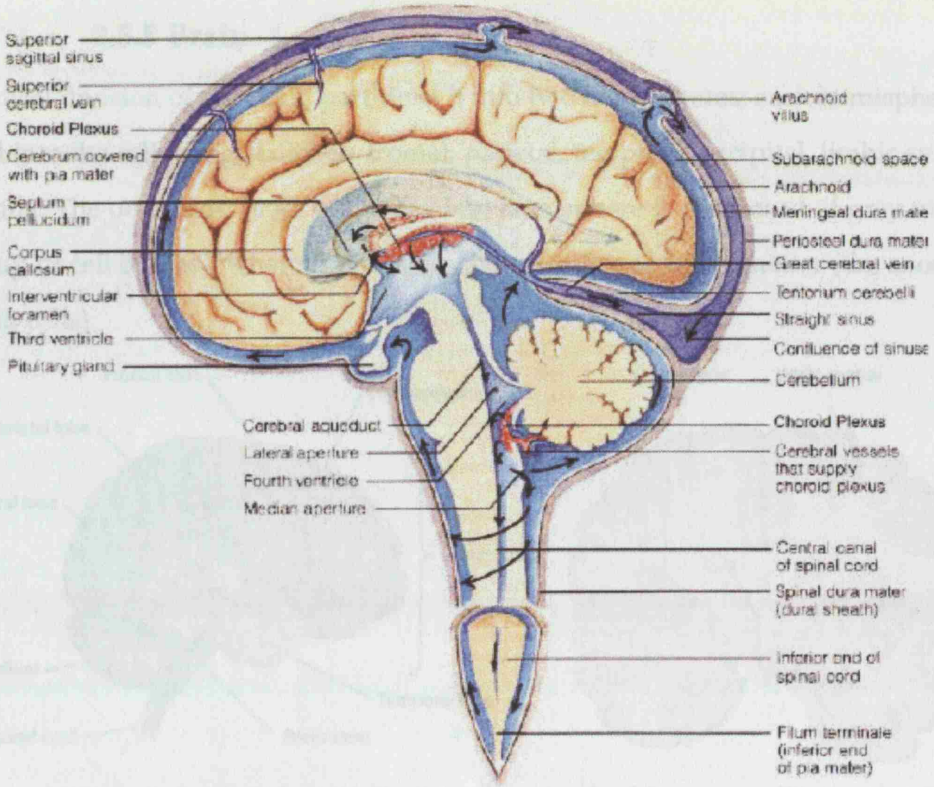

Figure 2-16. CSF (marked in blue) adapted from Marieb 1991

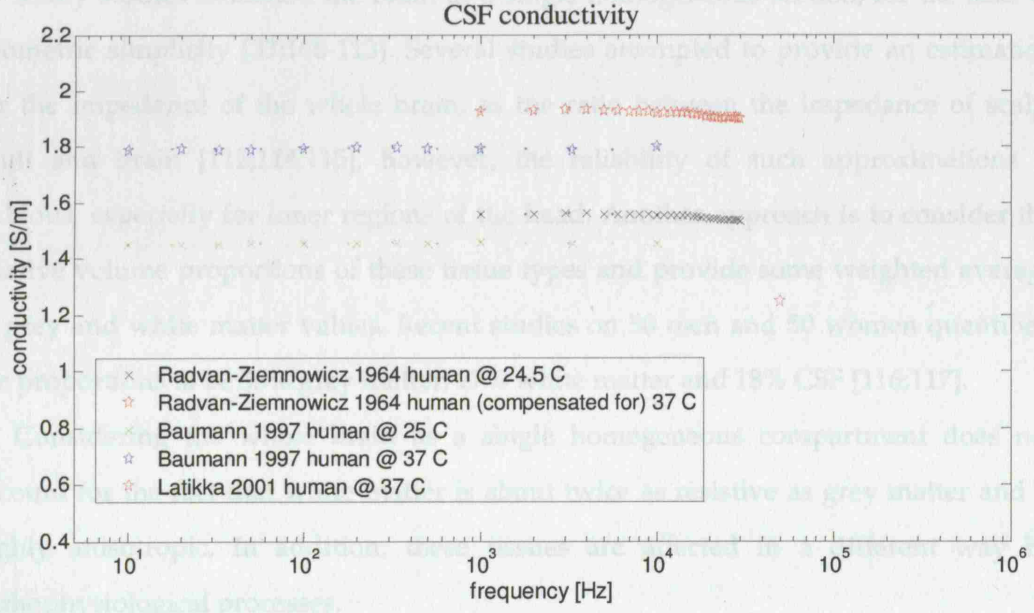

Figure 2-17. CSF conductivity

2.5.5 Brain

Anatomical division of the brain partitions it into two hemispheres; each hemisphere is divided into the following six lobes: frontal, parietal, temporal, occipital, limbic system and insula. The outermost layer of the cerebral hemisphere is composed of grey matter (made up of cell bodies), whereas the inner layer consists of white matter (the axons of the brain cells).

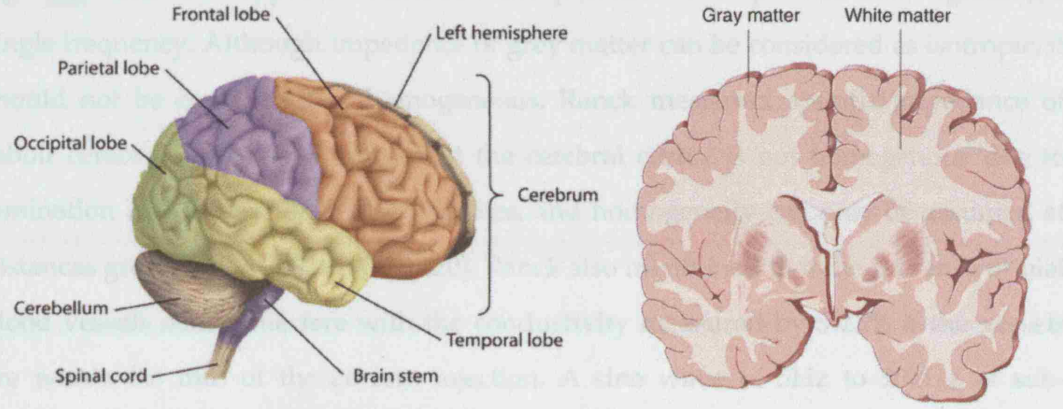

Figure 2-18. Left: brain lobes [106]; Right: grey and white matter illustration [107]

Many studies modelled the brain as a single homogeneous section, for the sake of geometric simplicity [33;108-113]. Several studies attempted to provide an estimation for the impedance of the whole brain, as the ratio between the impedance of scalp, skull and brain [112;114;115], however, the reliability of such approximations is dubious, especially for inner regions of the head. Another approach is to consider the relative volume proportions of these tissue types and provide some weighted average of grey and white matter values. Recent studies on 50 men and 50 women quantified the proportions to be 55% grey matter, 27% white matter and 18% CSF [116;117].

Considering the whole brain as a single homogeneous compartment does not account for the fact that white matter is about twice as resistive as grey matter and is highly anisotropic. In addition, these tissues are affected in a different way by pathophysiological processes.

2.5.6 Grey matter

Grey matter mainly consists of nerve cells soma and their supporting glial cells. Its structure is predominantly isotropic with nerves running in diverse directions.

Freygang and Landau used current pulses of 0.3-0.7ms duration on cat grey matter using four terminal measurement method [118]. Assuming a single pulse is delivered without periodicity, the spectrum of such a pulse included a strong DC component and a continuous frequency packet in the form of sinc(f), where the first lobe which encompassed 67% of the energy has a null at $\frac{1}{PW}$. Therefore, this impedance measurement was a superposition of DC measurement and the entire band below $\frac{1}{PW} \approx \frac{1}{0.5ms}$ = 2kHz, as opposed to sine wave acquisition which provide data regarding a single frequency. Although impedance of grey matter can be considered as isotropic, it should not be considered as homogeneous. Ranck measured specific impedance of rabbit cerebral cortex, and noted that the cerebral cortex is not homogenous due to lamination and the presence of cell bodies, and homogeneity can only be assumed at distances greater than 200 μm [119;120]. Ranck also mentioned that the presence of pial blood vessels could interfere with the conductivity measured by 5-25% if the vessels are within 0.5 mm of the current injection. A sine wave of 5Hz to 50kHz of sub-stimulating amplitude (2.8-11 μA) was injected into the cortex, and two electrodes were used to measure the impedance. The electrodes were placed 300 μm apart due to the suspected local inhomogenity. Shunting effect of the blood vessels was taken into account on this study by compensation of 10% correction for blood conductivity. Measurements on rat during REM sleep were performed 3 years later using a similar method at frequencies between 1.5Hz and 3kHz [121]. He reported max reactivity of 7° at 50-100Hz which can be related to the α dispersion of grey matter.

Van Harreveld et al studied the impedance of rabbit cortex using a tissue slab containing both white and grey matter [122]. The impedance was measured using two terminal measurements. One electrode was placed on the cortical surface and one on the lateral ventricle underneath. A sinusoidal current of 1kHz was used. Li et al performed four terminal measurements with needle electrodes of cat grey and white matter at the low frequency of 0.1-1Hz [117]. Whilst the fact that white matter impedance is in agreement with other work, the values are almost twice that of other papers. The increased values maybe due to the fact that current at very low rate was used (0.1 to 1Hz), which effectively measured the resistivity for DC.

In their review, Geddes and Baker [5] reported resistivity values averaged over low-frequency of 5Hz to 5kHz. To calculate the average, they used values obtained from the papers by Crile, Freygang, Ranck and Van Harreveld, [118;119;122;123]. These values should be considered with caution as they were averaged over frequencies, species and measurement techniques. In addition, they also report the ratio of transverse to longitudinal resistivity of this fibrous tissue ranging between 5.7 and 9.4 obtained from the various papers they reviewed.

Robillard and Poussart studied grey and white matter impedance dependency with depth over frequency range of 20Hz to 2kHz using four terminal measurements [124]. As impedance can differentiate between tissue types, they demonstrated that depth electrodes localisation could be assessed using impedance measurements. Stoy et al measured the dielectric properties of canine grey and white matter *in-vitro* at frequency range of 100kHz - 100MHz at room and body temperature [73]. Surowiec et al measured the dielectric properties of post-mortem bovine grey matter at similar frequencies at room temperature [125]. Gabriel et al measured both ovine and human brain impedance using the two terminal method [49]. Ovine was measured over a wide frequency range from 10Hz to 20GHz, whereas post-mortem human brain was measured between 300kHz and 20GHz. Latikka et al recorded the impedance of white and grey matter *in-situ* using a needle electrode in human subjects undergoing brain surgery for deep brain tumours [105]. A monopolar blunt needle was placed in the path of surgery. Measurements were acquired in white and grey matter as the needle was moved towards the centre of the brain. Measurements were performed at frequency of 50kHz and a current of 2 μA. Greater variation was seen in the grey matter, both inter and intra-individually, possibly due to different physiological structures in different areas of grey matter. It may also be due to the fact the measurements were made during surgery on patients with brain tumours, which may have spread to surrounding tissue affecting the results.

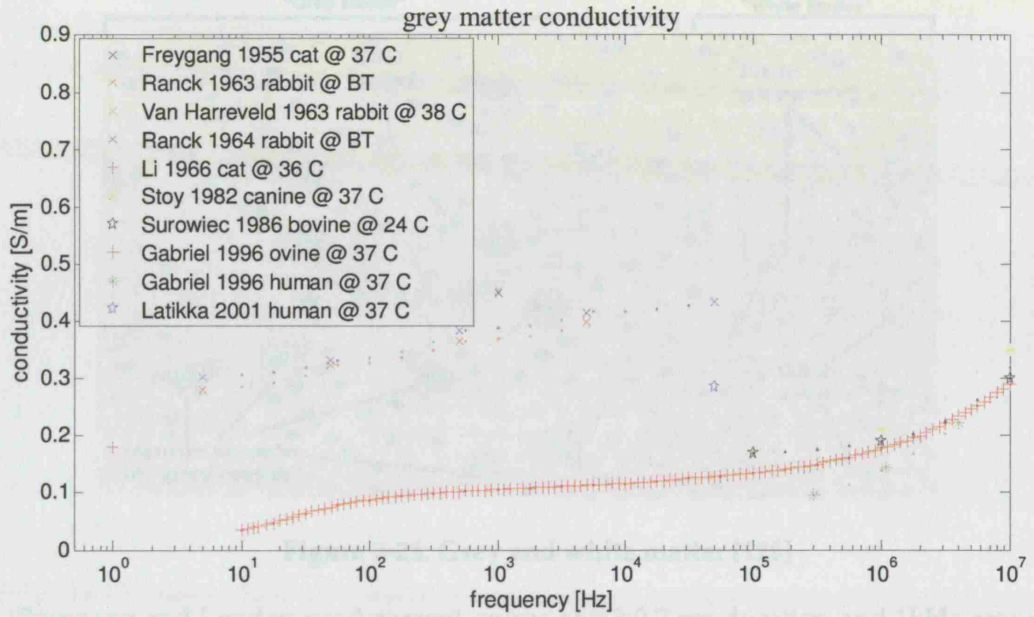

Figure 2-19. Grey matter conductivity

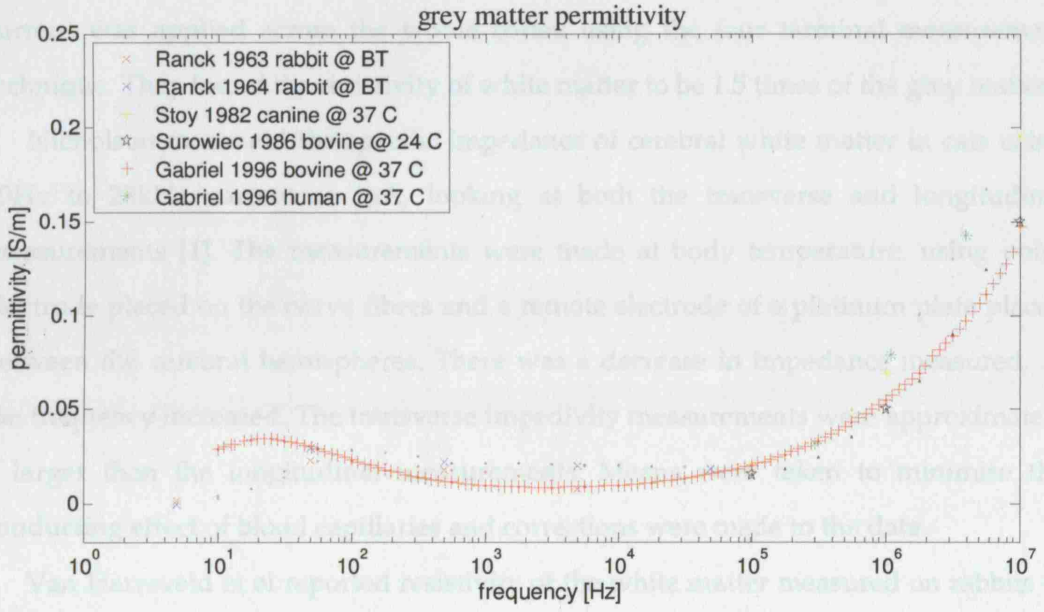

Figure 2-20. Grey matter permittivity

2.5.7 White matter

White matter constitutes nerve fibres, which are highly anisotropic. Impedance measurements therefore depend on the orientation of the measuring electrodes in the nerve fibre bundles.

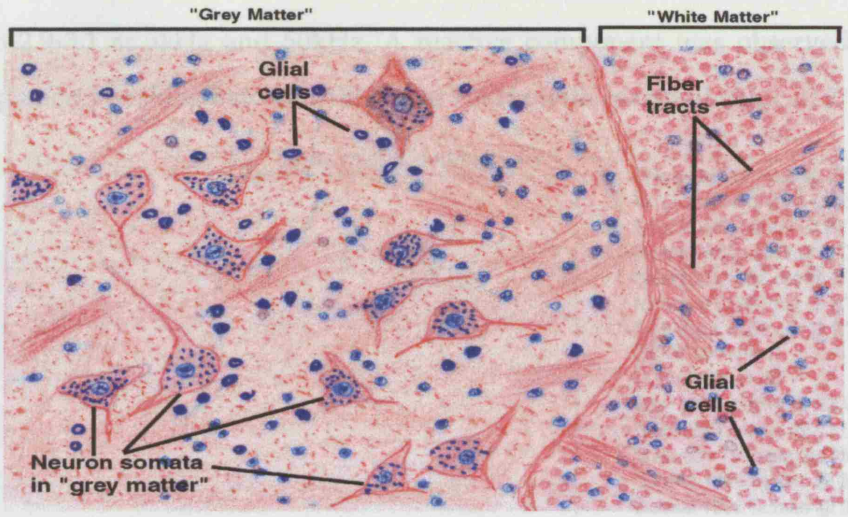

Figure 2-21. Grey and white matter [126]

Freygang and Landau used current pulses of 0.3-0.7 ms duration and 1kHz rate on cat white matter in a similar method as described in 2.5.6 [118]. In this study, the current was applied across the whole cortex using the four terminal measurement technique. They found the resistivity of white matter to be 1.5 times of the grey matter.

Nicholson measured the specific impedance of cerebral white matter in cats using 20Hz to 20kHz current at 1μA, looking at both the transverse and longitudinal measurements [1]. The measurements were made at body temperature, using point electrode placed on the nerve fibres and a remote electrode of a platinum plate placed between the cerebral hemispheres. There was a decrease in impedance measured, as the frequency increased. The transverse impedivity measurements were approximately 9 larger than the longitudinal measurements. Means were taken to minimise the conducting effect of blood capillaries and corrections were made to the data.

Van Harreveld et al reported resistivity of the white matter measured on rabbits to be 4.6 ± 0.2 times that of grey matter [122]. The study of Ranck and Bement on the cat dorsal column indicated the ratio between transverse and longitudinal resistivity of 8.8 or 5.7 respectively [2]. Sinusoidal current of 5-10μA at 5-10Hz was passed through 40μm diameter platinum wire placed near the midline on the surface of the dorsal columns. The voltage was measured with an additional pair of glass microelectrodes. In the same paper, Ranck characterised the frequency dependence of the dorsal column at frequencies of 5Hz to 50kHz using the same method he used to measure the grey matter of rabbit [119]. The ratio between transverse and longitudinal resistivity was 5.6

at 5Hz to 2.9-3.1 at 5kHz and 50kHz. A reactive component was observed between these frequencies peaking between 5kHz and 50kHz with maximal value of 7°.

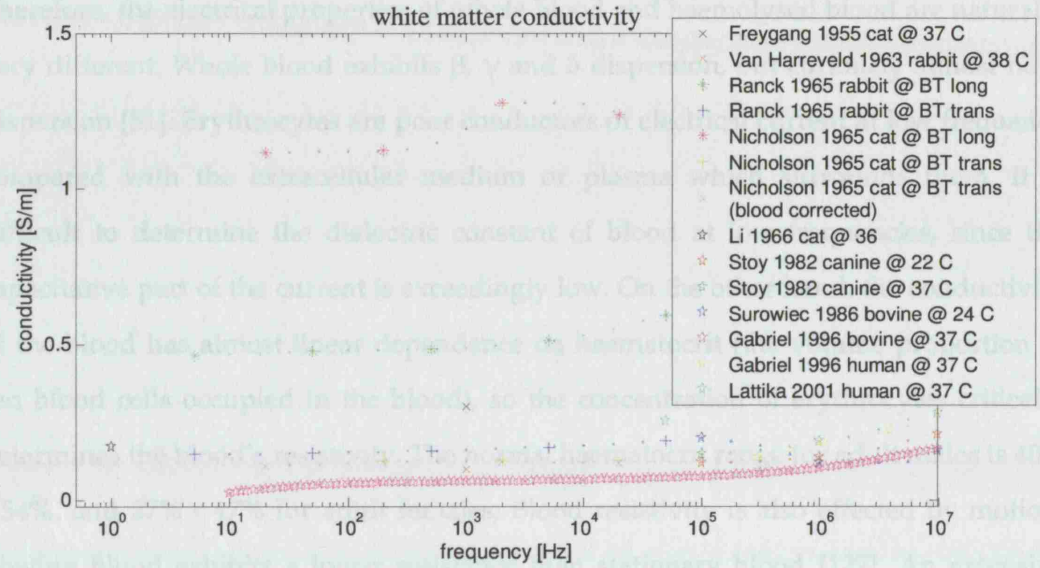

Figure 2-22. White matter conductivity

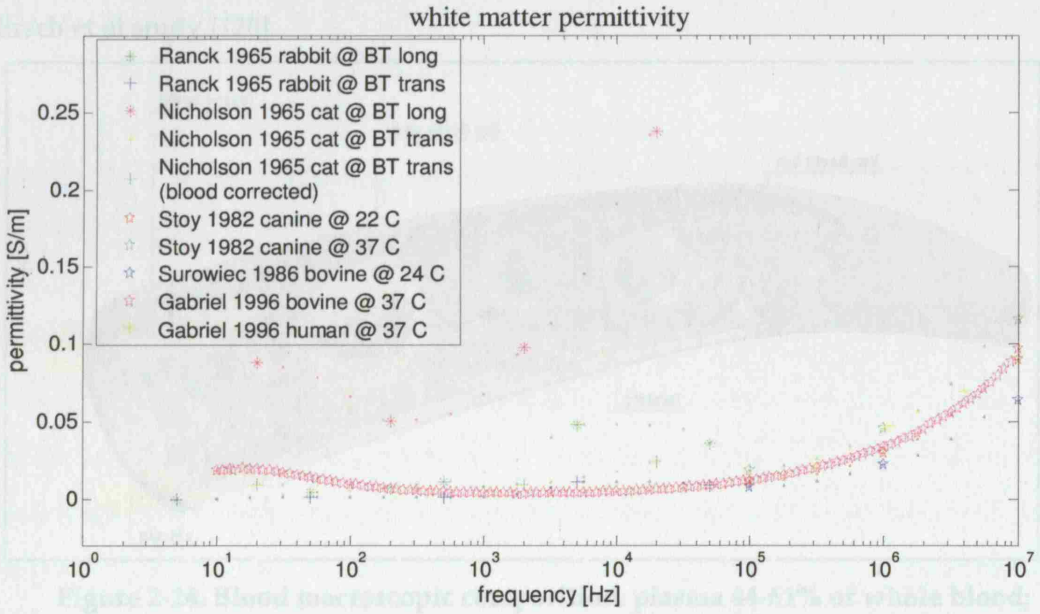

Figure 2-23. White matter permittivity

2.5.8 Blood

Blood is a circulating tissue composed of fluid plasma and cells. The plasma forms the liquid part containing electrolytes and large organic electrically polarised molecules. Apart from the plasma, the blood consists of several kinds of corpuscles: about 96% of them are red blood cells (also known as *erythrocytes*), 3% are white blood cells

(*leukocytes*) and the reminders are platelets (*thrombocytes*). In haemolysed blood, erythrocytes are disrupted and their intracellular material is discharged into the liquid. Therefore, the electrical properties of whole blood and haemolysed blood are naturally very different. Whole blood exhibits β, γ and δ dispersion, but curiously almost no α dispersion [51]. Erythrocytes are poor conductors of electrical current at low frequency compared with the extracellular medium or plasma which surrounds them. It is difficult to determine the dielectric constant of blood at low frequencies, since the capacitative part of the current is exceedingly low. On the other hand, the conductivity of the blood has almost linear dependence on haematocrit (the volume proportion of red blood cells occupied in the blood), so the concentration of erythrocytes critically determines the blood's resistivity. The normal haematocrit range for adult males is 40% - 54%, and 37% - 47% for adult females. Blood resistivity is also effected by motion, flowing blood exhibits a lower resistance than stationary blood [127]. An extensive table that summarises most of the factors that influences impedance can be found in Hirsch et al study [128].

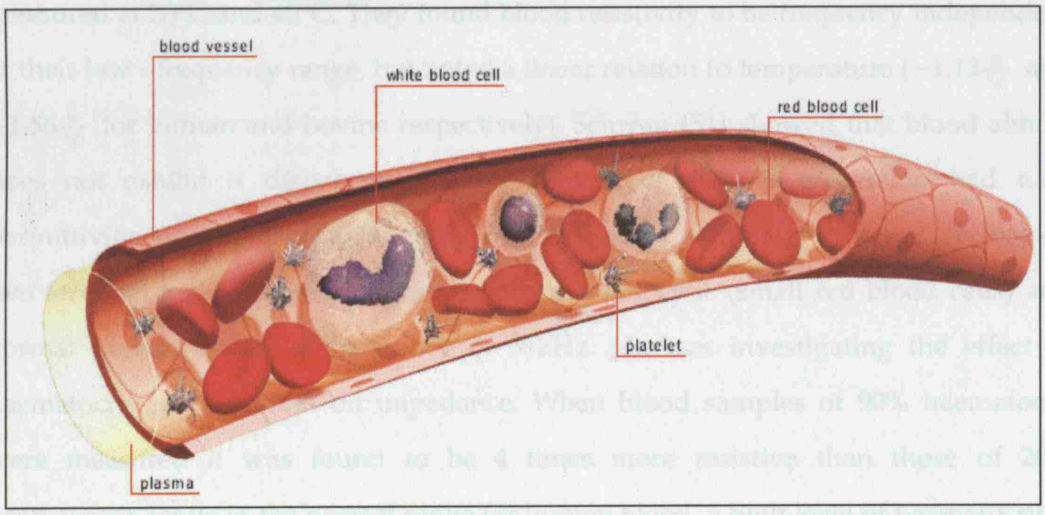

Figure 2-24. Blood macroscopic composition: plasma 44-61% of whole blood; buffy coat containing leukocytes and platelets about 2% of whole blood; erythrocytes about 37-54% of whole blood (adapted from QA international 2004)

Hober [129-131] was first to measure red blood cells impedance at low and very high frequencies, and noted that after the cells had been haemolysed and their membrane destroyed, the resistivity became frequency independent.

Burger and Van Milaan [70] performed four terminal measurements of human blood at DC frequency. They were using 0.01 - 0.001% heparin (a non electrolyte solution) to avoid coagulation, stressing that the low concentration used should not produce a significant influence on the measured impedance. Rosenthal and Tobias conducted impedance measurements of normal human blood at 1kHz and at 37°C using two terminals and an impedance bridge [132]. This study was investigating the effect of haematocrit level on impedance. Hirsch et al were investigating the relationship between blood resistivity and its erythrocyte concentration [128]. Their two terminal experiment setup included design of a horizontal cylinder measurement cell to avoid sedimentation effects. They derived a relation between red cell count and its conductivity. Schwan [71] compendium study quote whole blood measurements taken from rabbit at body temperature over the frequency range of 1kHz - 10MHz. Burger and Van Dongen [72] took four terminal measurements of human and bovine blood and bovine plasma over the frequency range of 20Hz - 5kHz using a horizontal tube as a measurement cell. Heparin was added to all samples and they were measured at 20°C and 40°C. They found blood resistivity to be frequency independent at their low - frequency range, but noted a linear relation to temperature ($-1.13\frac{\%}{^\circ C}$ and $-1.56\frac{\%}{^\circ C}$ for human and bovine respectively). Schwan [51] showed that blood almost does not exhibit α dispersion; for haematocrit of 40%, β dispersion had total permittivity increment of 2000, and centre frequency of 3MHz. Pfutzner performed two terminal measurements of sheep, porcine, microcytic (small red blood cells) and normal human blood, at frequency of 50kHz. He was investigating the effect of haematocrit concentration on impedance. When blood samples of 90% haematocrit were measured it was found to be 4 times more resistive than those of 20% haematocrit, while in the normal range for human blood, a high level of haematocrit is twice as resistive as a low level of haematocrit[133].

The relationship between the electrical impedance parameters and haematocrit of normal human blood was determined at 37°C in the haematocrit range of 20 - 40% for four types of anti-coagulants: acid citrate (ACD), ethylene diamine tetra - acetic acid (EDTA), sodium heparin (SH) and sodium citrate (SC) [134]. Zhao et al reported the largest resistivity when SH was used to anti-coagulate the samples, while those with

SC had the lowest values. In another publication Zhao et al [135] performed four terminal measurements of human blood flow at body temperature. The 4 electrodes were in the middle of the blood column to reduce the effect of sedimentation of blood cells. The cylinder measurement cell design allowed laminar blood flow. Gabriel et al conducted two terminal measurements over ovine blood at temperature of 37°C in the frequency range of 1MHz - 20GHz [47-49]. Casas reported mean ratio of R_0/R_∞ 1.9 ± 0.4, with centre frequency of 2020 ± 420kHz, with α of 0.16 ± 0.03, measured in porcine blood samples [136]. Jaspard et al studied the influence of haematocrit on the dielectric properties of animal blood in the frequency range of 1MHz to 1GHz and temperature of 37°C [137]. They found that an increase in haematocrit level induced an increase in the number of cell membranes with a decrease in the volume of plasma. Similarly, when haematocrit increased a drop of conductivity and an increase of relative permittivity were observed.

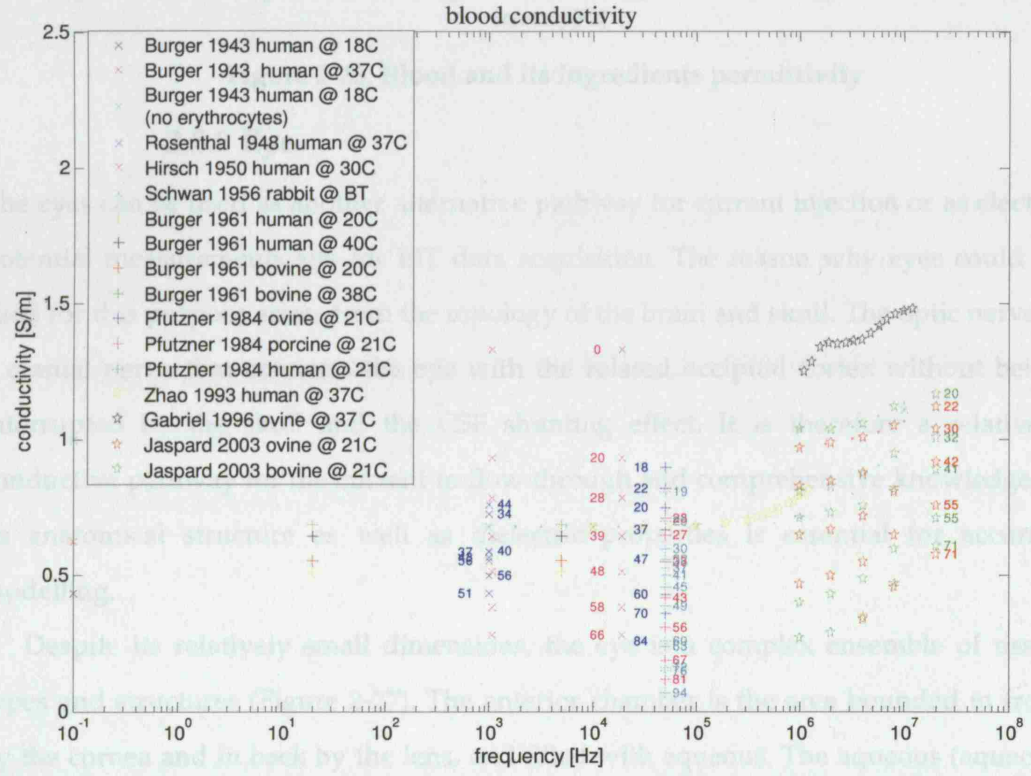

Figure 2-25. Blood and its ingredients conductivity

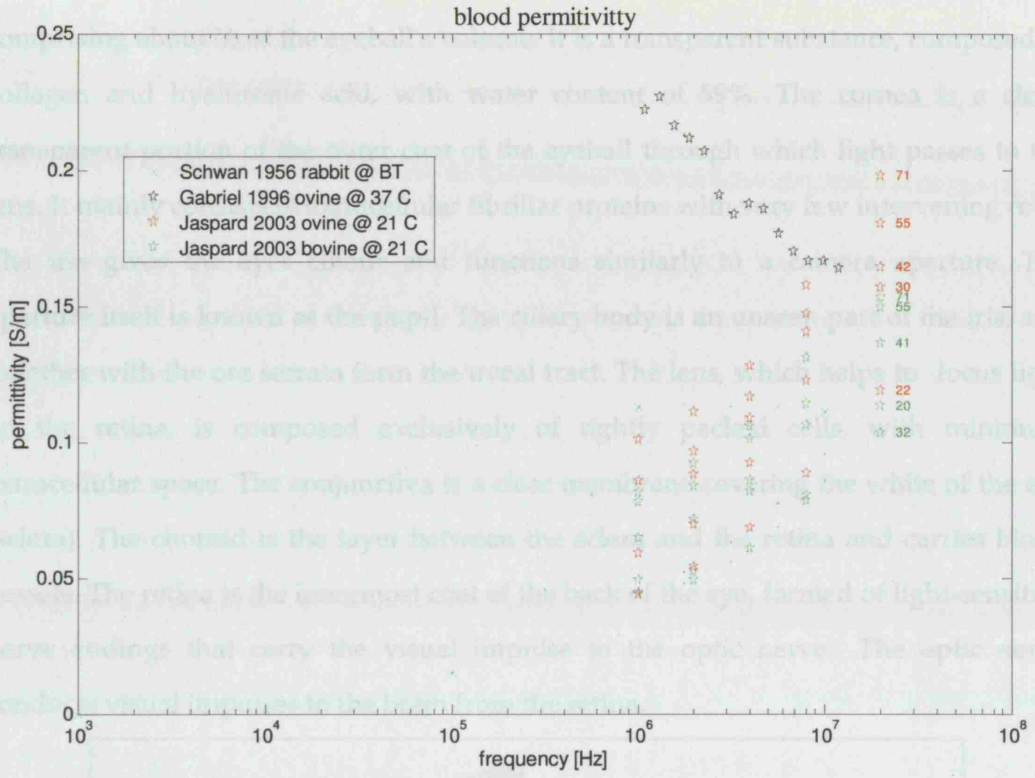

Figure 2-26. Blood and its ingredients permittivity

2.5.9 Eye

The eyes can be used as another alternative pathway for current injection or as electric potential measurements site for EIT data acquisition. The reason why eyes could be used for this purpose arises from the topology of the brain and skull. The optic nerve is a cranial nerve that connects the eye with the related occipital cortex without being interrupted by the skull and the CSF shunting effect. It is therefore a relatively conductive pathway for the current to flow through and comprehensive knowledge of its anatomical structure as well as dielectric properties is essential for accurate modelling.

Despite its relatively small dimensions, the eye is a complex ensemble of tissue types and structures (Figure 2-27). The anterior chamber is the area bounded in front by the cornea and in back by the lens, and filled with aqueous. The aqueous (aqueous humour) is a clear, watery solution in the anterior and posterior chambers. Its electrolytic composition is similar to that of blood plasma. The canal of Schlemm provides drainage for the aqueous fluid to leave the eye. The rest of the eye is filled with vitreous humour, a transparent, colourless mass of soft, gelatinous material

comprising about 2/3 of the eyeball's volume. It is a transparent substance, composed of collagen and hyaluronic acid, with water content of 99%. The cornea is a clear, transparent portion of the outer coat of the eyeball through which light passes to the lens. It mainly consists of extracellular fibrillar proteins with very few intervening cells. The iris gives the eyes colour and functions similarly to a camera aperture. The aperture itself is known as the pupil. The ciliary body is an unseen part of the iris, and together with the ora serrata form the uveal tract. The lens, which helps to focus light on the retina, is composed exclusively of tightly packed cells, with minimum extracellular space. The conjunctiva is a clear membrane covering the white of the eye (sclera). The choroid is the layer between the sclera and the retina and carries blood vessels. The retina is the innermost coat of the back of the eye, formed of light-sensitive nerve endings that carry the visual impulse to the optic nerve. The optic nerve conducts visual impulses to the brain from the retina.

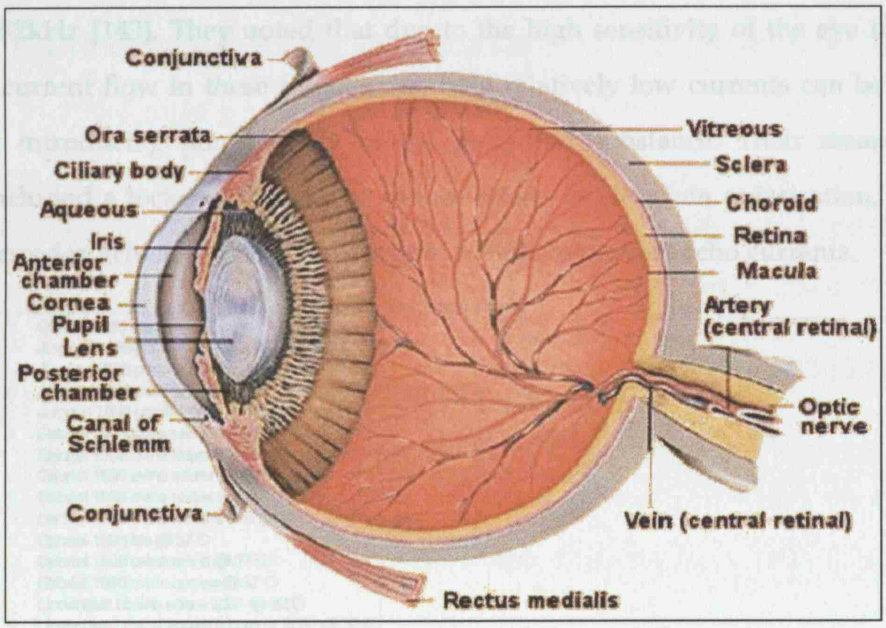

Figure 2-27. The anatomy of the eye [138]

Watanabe et al performed *in-situ* two terminal measurements of white rabbit cornea impedance [139]. Their measurements were at the frequency range of 10kHz - 1MHz. They noted two sub-dispersions, a low frequency (f_c = 70kHz) associated with the endothelial layer, and the second at higher frequencies (f_c = 2MHz) related to the cornea epithelial layer. Gandhi quoted a value of 0.11 S/m for the eye and the lens as a unified unit, for 60Hz [140]. However, as the eye consists of several membrane

structures, this value is expected to rise significantly at higher frequencies. Jurgens performed *in-vitro* four terminal measurements of porcine eyes at room temperature, 24-48 hours after excision [141]. Measurements conducted at the frequency range of 10kHz-1MHz. As expected, the aqueous and vitreous humours and the cornea displayed a flat frequency response, with no relaxation, as their cell content is negligible. The cortical and nuclear compartments of the lens, on the other hand, displayed relaxations. Gabriel et al measured the cornea, lens (cortex and nucleous) and the retina of ovine eyes at temperature of 37°C and frequency range of 10Hz-20GHz [47-49]. Kohli et al used a computer assisted AC impedance system to measure the DC voltage current characteristics and AC impedance of a goat lens [142]. The impedance of the eye lens against frequency showed an α dispersion at 0.1Hz. Lindenblatt carried out *in-vitro* measurements of the complex conductivity of bovine eye cornea, lens, sclera, vitreous humour and aqueous humour, at the frequency range of 10Hz-2kHz [143]. They noted that due to the high sensitivity of the eye tissues to electric current flow in these frequencies, only relatively low currents can be applied without introducing non-linearity of the measured substance. Their measurement setup included a lock-in amplifier to reduce effects of electrode polarisation, and flat ring electrodes, which did not penetrate the sample to prevent echo currents.

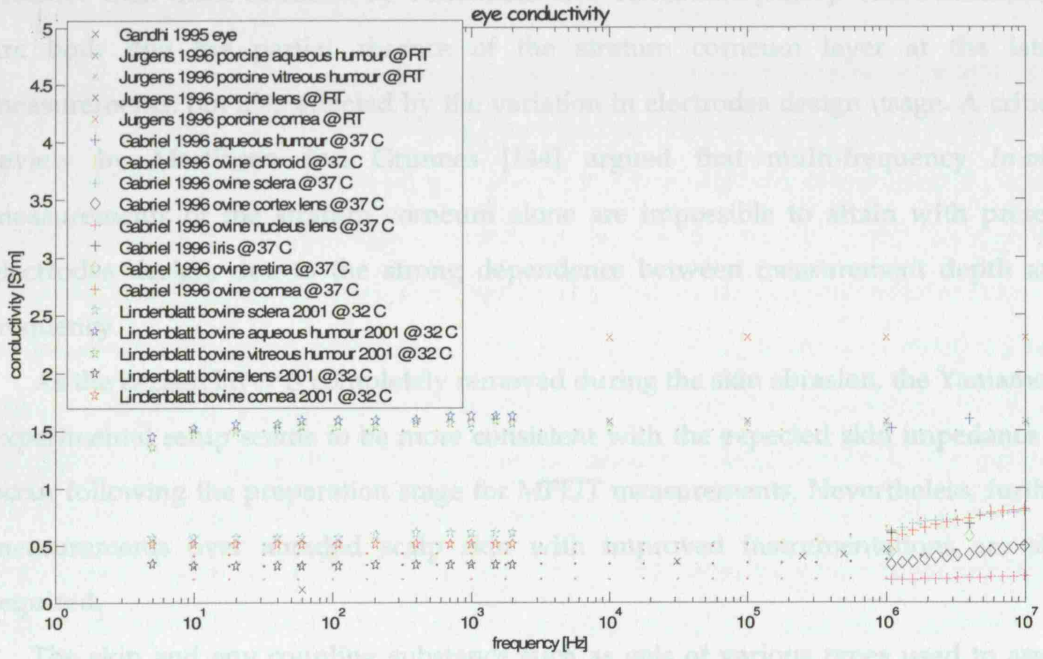

Figure 2-28. Eye tissues conductivity

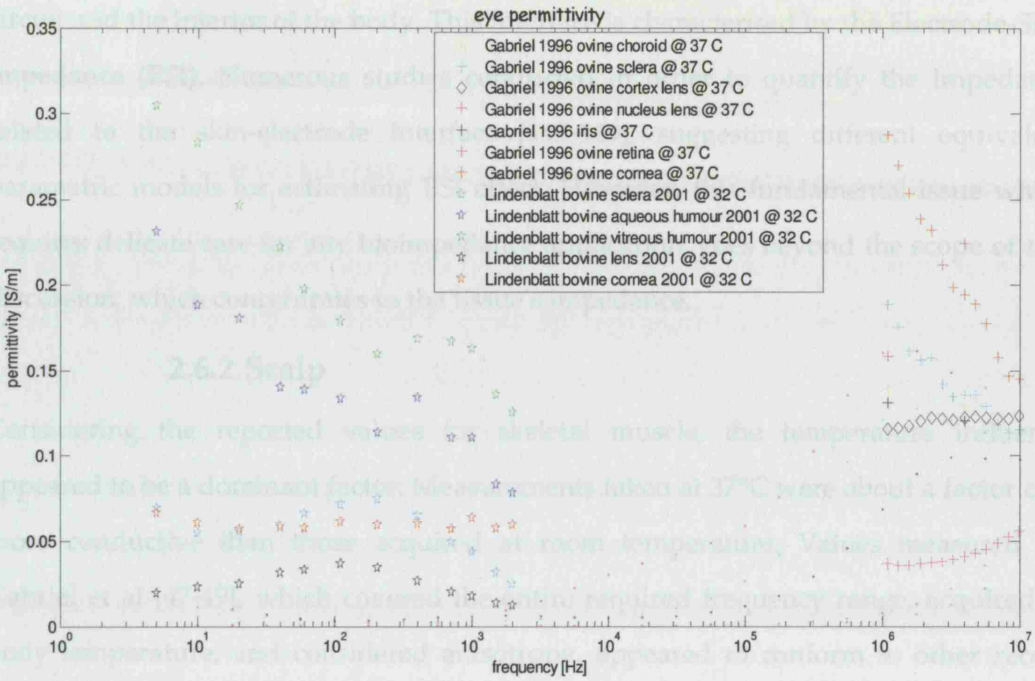

Figure 2-29. Eye tissues permittivity

2.6 Discussion and Conclusions

2.6.1 Skin

Measurements for wet skin acquired by Gabriel et al [49] and Raicu et al [69] were in good agreement over the entire frequency range. These values were considerably more resistive than those obtained by Yamamoto and Yamamoto [64;65]. These differences are both due the partial absence of the stratum corneum layer at the latter measurements, but also affected by the variation in electrodes design usage. A critical review by Martinsen and Grimnes [144] argued that multi-frequency *In-vivo* measurements of the stratum corneum alone are impossible to attain with present electrodes design, due to the strong dependence between measurement depth and frequency.

As the keratin layer is completely removed during the skin abrasion, the Yamamoto experimental setup seems to be more consistent with the expected skin impedance to occur following the preparation stage for MFEIT measurements. Nevertheless, further measurements over abraded scalp skin with improved instrumentations are still required.

The skin and any coupling substance such as gels of various types used to assist electrode contact, together form an interface between the external measurements

circuit and the interior of the body. This interface is characterised by the Electrode-Skin Impedance (ESI). Numerous studies conducted in order to quantify the impedance related to the skin-electrode interface [145-149], suggesting different equivalent parametric models for estimating ESI effect. However, this fundamental issue which requires delicate care for any bioimpedance application, goes beyond the scope of this discussion, which concentrates in the tissue's impedance.

2.6.2 Scalp

Considering the reported values for skeletal muscle, the temperature influence appeared to be a dominant factor. Measurements taken at 37°C were about a factor of 2 more conductive than those acquired at room temperature. Values measured by Gabriel et al [47-49], which covered the entire required frequency range, acquired at body temperature, and considered anisotropy, appeared to conform to other recent results with respect to the characteristic behaviour of the tissue over frequency. For these reasons, these values were chosen to represent skeletal muscle admittivity most reliably for modelling purposes. Nevertheless, four terminal measurements incorporating numerical modelling over this frequency range is yet desired.

The scalp is indeed composed mostly of muscle, but there are distinctive regions which are composed of other tissues which were not been considered in this review. Further measurements of the scalp impedance at various positions are still desirable.

Ultimately, an anisotropic forward model should account for the large extent of muscle anisotropy. For the time being, no established method was developed to map the scalp muscles' directionality. Given a simplistic isotropic model, crude assumptions and compromises needed to be considered in order to provide representative values. This task is especially difficult as the portion of transverse and longitudinal current flow is subject to the orientation of the tissue with respect to the injecting electrode positions. A crude assumption would be to consider $^2/_3$ of the current to flow transversely and $^1/_3$ longitudinally, which represent the relative likelihood of current in random orientation to flow in each direction. However, the high resistivity of the skull would draw the current to flow in parallel to the skull, rather than over the normal direction. On the other hand, for in-depth measurements, which are favoured for MFEIT of the head, injection is more likely to be in

diametrically opposed direction, which means that the current would have a large component that would flow in the normal direction, which would then encounter mostly the transverse component of the scalp impedance.

2.6.3 Skull

Dielectric properties of the skull are influenced by several factors: bone composition (skull layers-structure), non-uniform geometry, anisotropy and age (water content is reduced and bone marrow is changing from red to yellow with age, which increases resistivity). In addition, the reliability of the impedance measurements is also affected by the freshness of the samples, exposure to air and freezing effects.

Low-frequency skull impedance manifested a wide range of values, which for direct measurements varied by a factor of 8.4, and in location by a factor of almost 16. The main conclusion is that reliable representation of the skull impedance should consider its layered nature [84;85;117] and its geometric variability [89]. Any attempt to provide a simplified representation as a single homogeneous and isotropic tissue is likely to provide indefinite results.

All available studies measuring dielectric properties of the skull were conducted either at low frequencies to allow accurate EEG modelling, or at high frequencies above 1MHz. For the intermediate frequencies, the frequency response of long bones, which have similar composition to skull, can be considered.

Moreover, the cortical part of the skull appears to have a notable degree of anisotropy. In such case, the circumferential direction of long bone can be considered as equivalent to the tangential direction of the skull cortical layers. Similarly, the radial direction of long bone can represent the radial component of the skull top and lower cortical layers.

Only Gabriel et al [49] and Kosterich et al [94] made impedance measurements of cortical bone at body temperature. The values they obtained were notably higher than those measured at room temperature. Yet neither study, had considered the bone anisotropic properties. From measurements acquired by Reddy et al [95], De Mercato and Garcia-Sanchez [100] and Saha and Williams [99], it is clear that the axial direction is consistently more conductive than the radial and the circumferential directions. These results agree with the histological composition of long bone. However, there is a large discrepancy as to the extent. This dispute is of small relevance for this discussion

as only the radial and circumferential directions need to be considered to represent the skull. Another apparent difference is related to the samples' species. Measurements from human cortical bone were more conductive than bovine cortical bone (a factor of 2.9 - 7.2 in the radial direction).

In this respect measurements reported by Saha and Williams which were made on human bone are favoured. Unfortunately, the absence of permittivity measurements in that study in the circumferential directions dismisses this data for EIT purposes. Due to the limited frequency range of the other two alternative anisotropic studies, Kosterich et al's [94] isotropic measurements, which were performed over a wide frequency range at body temperature, remained most relevant. It is reasonable to assume that rat cortical bone is more conductive than of human; however, no qualitative figures are available to substantiate this presumption.

Bovine trabecular bone is known to be denser and less porous than the human trabecular bone [150]. Comparison of measurements reported by Sierpowska et al on bovine [101] and human [102], using similar method and temperature, showed a conductivity ratio of 1.8 - 2.4. Another source of variability for this type of bone is related to the site from where the sample was taken. The latter study showed that tibia appears to be more conductive than femur by about 18% - 20%. Moreover, even measurement from the same bone sample taken from different regions varied by a factor of about 3 [97].

A possible choice for modelling purposes would be to correct values acquired for trabecular bovine femur samples by Sierpowska et al [101] by the ratio of conductivity acquired between human and bovine samples in their later study [102]. In addition a correction is required to adjust the measurement temperature from 22°C to 37°C.

The live skull impedance values measured by Hoekema et al [89] and Akhtari et al [84;151] fall within the range of weighted conductivities of the chosen values for cortical and trabecular bone.

Generation of a three-layered finite element skull mesh is a challenging task, which requires precise knowledge regarding the inner structure of the skull. In cases where the skull is modelled with a single layer a compromise need to be considered. A crude approximation can be a homogeneous distribution of weighted average of ½ cortical

bone and ½ a trabecular bone, which roughly represents the average volume distribution of the two bone types.

Nevertheless, both choices for cortical and cancellous bone are far from being ideal for representing the skull impedance reliably. Direct *In-vivo* measurements of a live skull over a wide frequency range at different skull sites, accounting for anisotropy are yet required.

2.6.4 CSF

Due to small concentrations of cells this fluid displays negligible frequency dependence. The high ionic concentration translates into high conductivity of the CSF with respect to any other tissue constituted in the head. As the CSF surrounds the whole brain and occupies the ventricles within the brain, this conductivity contrast gives rise to a substantial shunting effect of currents injected through the head. Therefore, despite the difficulty in modelling such a thin layer, it is important to account for this compartment effect as well as account for the presence of ventricles.

There is a good agreement between the temperature dependent values provided by Radvan-Ziemnowicz [103] and Baumann [104]. The latter measurements covered the widest frequency range and reported a mild frequency response, which appear more reasonable. However, Baumann used defrosted samples; a process which might damage the cell membranes. This could partly explain the higher resistivity values obtain by Latikka et al for *In-vivo* measurements [105]. On the other hand, as samples used by Latikka et al were obtained from brain tumour patients, those samples might have been infiltrated by malignant cells [152], resulting in resistivity increase.

For modelling purposes Baumann values can be considered, however, non-defrosted CSF impedance measurements at body temperature and over a wider frequency range are required.

2.6.5 Grey matter

Most of the variation between white and grey matter, apart from the anisotropy of white matter, is due to the water content of the different tissue types [96]. Calculations by Foster indicated that grey matter consist of 82% water while white matter consist of 72% water [153]. Nightingale examined the water content of the three brain regions of mouse dissected out and desiccated. For the cerebellum the water content was

0.765g/1g of tissue, 0.737g/1g of tissue for the cerebrum and 0.723g/1g of tissue for the brain stem [154].

The most profound discrepancy arose between *In-vivo* versus *in-vitro* measurements. *In-vivo* reported values [117-121;155] were 3-8 times more conductive than values obtained *in-vitro* [49;73;125]. This variance could possibly be attributed to a poor compensation for the resistive contribution of the electrodes contact impedance over the two terminal studies. *In-vitro* measurements conducted by Gabriel et al [49] indicated that human grey matter is up to 52% more resistive than ovine grey matter at frequency range of 300kHz and above. This claim substantiated by Latikka et al's *In-vivo* human measurements [105] as compared with Ranck's rabbit measurements (53%).

There is a good agreement regarding the permittivity values among all authors. The α dispersion appears to occur around the 30 - 100Hz region.

Although measurements obtained by Gabriel et al spanned over a wide frequency range, they were performed up to 2 hours after the ovine death, which questions their validity for low frequencies. For modelling purposes, measurements acquired by Latikka et al can be regarded as a gold standard for the frequency of 50kHz [105]. Thus, with respect to the considerations above, Ranck [155] measurements adjusted to Latikka et al values at 50kHz could serve as a valid estimate for grey matter admittivity values for the frequency range of 5Hz - 50kHz. For higher frequencies, results acquired by Gabriel et al attuned accordingly could be used. Similar *In-vivo* human measurements as performed by Latikka et al over the entire frequency range are required.

2.6.6 White matter

Several studies demonstrated the influence of white matter anisotropy property for EEG and MEG modelling [56;156;157]. However, no studies had been published for the influence on the EIT problem.

Again, *In-vivo* measurements were considerably more conductive than *in-vitro* values. As opposed to the grey matter tendency, bovine white matter was found to be up to 63% more conductive than human [49].

Only the studies of Nicholson and Ranck [1;2] accounted for the anisotropic nature of white matter. Their measurements showed the conductivity in the longitudinal direction to be about 10 or 3 times larger than that in the transverse respectively. Ranck's measurements were performed over cat spinal cord dorsal columns. This site is characterised by well-defined nerve fibres directionality. Nevertheless, the anisotropic ratio he found was lower than the one reported by Nicholson or by Geddes and Baker [5] compendium review.

Stoy's measurements of canine at room and body temperature showed conductivity difference of 25%-37% above 100kHz [73]. Such ratio is expected for this temperature difference.

Due to the large anisotropic variability, raw results reported by Latikka et al [105] could not be considered as a gold standard in this case. For isotropic approximation, nerve fibres can be assumed to be randomly oriented. In such case, contributions of $^1/_3$ and $^2/_3$ over the longitudinal and the transverse direction respectively, together with compensation of about 10-20% for the inter-species difference brings Ranck and Bement [2] results with a very good agreement with those of Latikka et al [105]. For higher frequencies, *in-vitro* values obtained by Gabriel et al [49] can be considered. These values need to be translated according to the mean difference from the spectrum obtained from Ranck and Bement recording, for the overlapping frequency range. Such choice could serve as a crude estimation for isotropic modelling of the white matter. Still, reliable *In-vivo* values accounting for anisotropy over a wider frequency range are required.

2.6.7 Blood

Three main factors have the largest influence upon blood impedance. The haematocrit level had the most profound effect, altering blood conductivity by a factor of up to 11.6 between 19% to 94% haematocrit. For a normal range of haemtocrit these differences reduce to about 54% for male and 36% for female blood at 50kHz [133]. Temperature provided a difference of about 40% between 18°C and 37°C [70;72]. Another significant factor was the samples source (species), which introduced a difference of about 6% between human and bovine, 21% between human and ovine. These differences reflect the different metabolic demands related to these species and genders.

There were no continuous measurements throughout the entire reviewed frequency range. There seems to be an agreement among the authors that up to about 100kHz blood exhibits no, or minimal frequency response. From then on a pronounced impedance change, which corresponds to the β dispersion occurs, with a centre frequency between 2-3MHz [51;135-137].

For modelling purposes at the low frequency range Zhao's measurements, which accounted for haematocrit level, temperature and sample species appear to be most trustworthy. These values should be extrapolated down to lower frequencies with relatively minor deviation from the true values. For frequencies above 1MHz, Jaspard et al [137] values for bovine blood which accounted for haematocrit and temperature can be considered.

Nevertheless, further measurement with flowing blood at body temperature, with controlled haematocrit level on wide frequency range are still required.

2.6.8 Eye

Only the cornea, lens, retina sclera, vitreous and aqueous humours compartments were considered, as the smaller compartments were normally too small to be measured independently or had very small influence over the total conductivity of the eye. The volume ratios were estimated from the image given in [158] to be 4% for cornea 3% lens, 9% retina, 14% sclera, 5% and 65% aqueous and vitreous humour respectively.

There is an agreement among the authors that the cornea, vitreous and aqueous humours display no relaxation up to 10MHz. The high density of cellular membranes and low extra-cellular water content of 5%, can explain the relaxation manifested by the lens. The conductivity values given by Jurgens et al [141] for the cornea were considerably larger then those reported by Gabriel et al [49] and Lindenblatt et al [159]. Considering the cornea's composition Jurgens findings are surprising.

Due to the lack of available measurements through the entire desired frequency range, in this exceptional case, extrapolated values derived by Gabriel et al [48] were considered. Comparison of these values with Lindenblatt et al [159] for the low frequency range of 10Hz and 20kHz showed a good agreement for all eye tissues except the vitreous humour permittivity. This value was measured by the latter at

higher frequencies than our scope of interest, and its extrapolation poorly matched the expected values.

Eye admittivity can be approximated for modelling purposes to have the volumetric average of its compartments, along with the extrapolated values reported by Gabriel et al. The vitreous humour should be considered to have similar frequency dependency behaviour to saline.

The vitreous humour which comprises the largest relative volume has the foremost role in determining the eye impedance. However, the presence of blood vessels across the vitreous humour may result in higher conductivity; an effect which was not accounted in the measurements. There is still a requirement for human eye measurements at body temperature, over the entire frequency range of interest.

Current density safety limits is another essential issue which requires a special attention while considering the eye as a possible current injection site. These limits are derived by the sensation threshold, stimulation of the retina's cones and rods, and by stimulation of the brain neurons. Attwell used the retina as a model for the field's effect over the central nerve system (CNS) [160]. The retina has practically evolved all the possible mechanisms of the brain: neurons in the outer retina process information as graded voltage changes similarly to dendrites of central neurons, amacrine and ganglion cells in the inner retina generate calcium and sodium action potentials, together with all the intra-extra cellular biochemical signalling pathways. The retina's role is the amplification of small signals under the presence of biochemical noise (even up to a single photon); hence its sensitivity can serve as a guideline for current magnitude while injecting current through the eyes. A reasonable estimate for an external field to produce retinal phosphenes (visual sensations arising from mechanical or electrical stimulation of the eyeball) is about $10\frac{mA}{m^2}$ for frequencies lower than 100Hz. Although one could argue, that for some applications, phosphenes can be allowed to occur as long as no damage is produced to the retina. However, as current is expected to flow through the cell's membrane as well as through the limited amount of ECF (about 2% for the retina) for frequencies above 100Hz, we must assess the limitation for higher frequencies as well. Dalziel measured the perception threshold of current delivered through the hand via copper wire at frequencies 50Hz-100kHz [161]. The

results are summarised at Table 2-3. While the current values are not relevant for EIT application, the overall trend is expected to be similar. Therefore, for the higher frequencies higher currents can be injected without stimulating the nerves [162].

Table 2-3. Effect of the frequency of applied current on the perception threshold. These values refer to the perceptions of current passed through the hand

Frequency	Current level for 0.5 percentile perception [mA]	Current level for 50 percentile perception [mA]	Current level for 95 percentile perception [mA]
50	0.4	1.1	1.8
100	0.5	1.1	1.8
1000	1.1	2	3
10000	8	15	20
100000	100	150	200

2.7 Summary Graphs

The figures below represent an isotropic approximation for the admittivity values of the human head tissues in body temperature (Figure 2-30 and Figure 2-31). These graphs were constructed according to the recommendations and guidelines suggested in this study. Yet these values should be used with caution due to the large extent of adjustments and corrections, which were required in order to obtain this data.

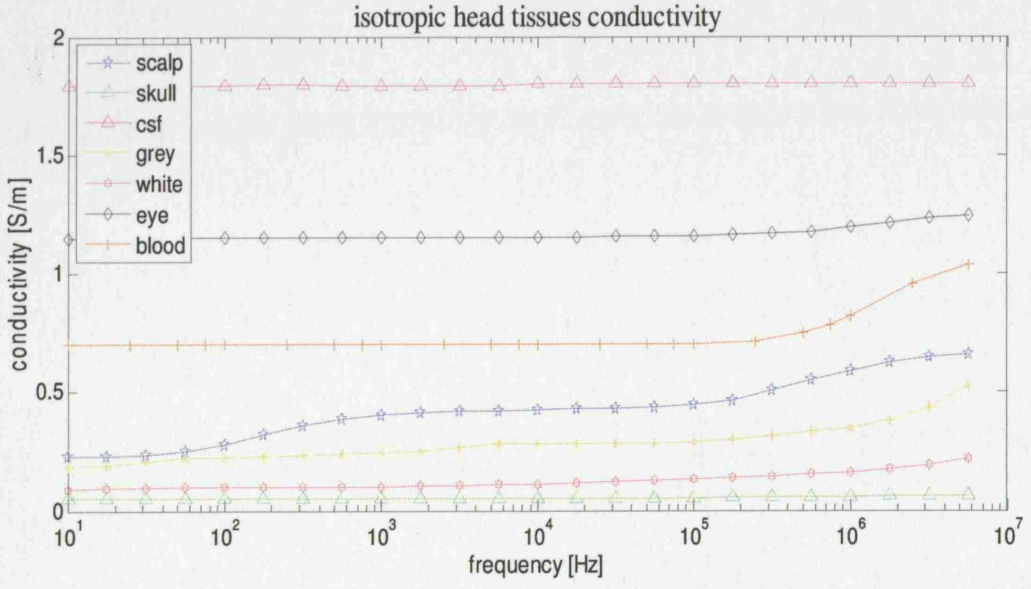

Figure 2-30. Conductivity of the head tissues

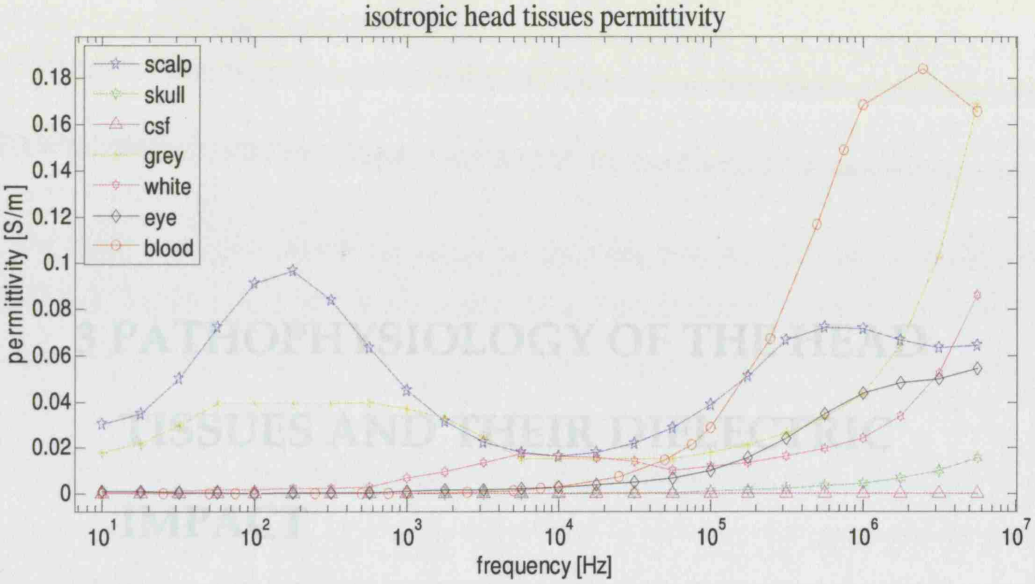

Figure 2-31. Permittivity of the head tissues

3 PATHOPHYSIOLOGY OF THE HEAD TISSUES AND THEIR DIELECTRIC IMPACT

3.1 Introduction

In Chapter 2, a literature review of the admittivity values for tissues which constitute in the normal head was presented. During pathological states, various pathophysiological mechanisms can be observed on the microscopic and macroscopic level. These changes alter the biochemical composition and structure of the cells and their environment, and therefore result in a characteristic electrical spectroscopic behaviour. As a result of these changes, differentiation between various tissues' conditions by means of bioimpedance measurements may be possible.

Comprehensive knowledge regarding these mechanisms and their impact on dielectric properties of the head tissue is crucial for development of multi-frequency EIT techniques. For modelling purposes, this key information enables reliable estimation of the expected multi frequency peripheral boundary voltage changes subject to the local changes introduced by certain pathologies. These model-based predictions can assist in studying the feasibility of MFEIT applications, such as distinguishing between ischaemic and haemorrhagic stroke [163;164] and the localising of epileptic foci during long-term epilepsy monitoring [28]. Such studies also provide essential input for hardware and acquisition design. Another beneficiary of this knowledge would be the image reconstruction process. Images of higher fidelity can be achieved by adjustment of the reconstruction algorithms to enhance changes of particular spectral signature and reject others as artefacts.

3.2 Purpose

This chapter introduces the pathophysiological mechanisms occurring in the human brain in acute stroke, epilepsy and tumours. The purpose of this work was to review the literature on published impedance values of these conditions. These values are used later on for modelling of stroke in this thesis.

3.3 Design

A description of the impedance-related participating mechanisms is provided, followed by a chronological review of the available publications. The considerations for favouring one study over another are brought in the discussion section.

3.4 Background

3.4.1 Stroke

Stroke can be broadly divided in those resulting from infarction of the brain (*Ischaemic stroke*) and those resulting from *intracerebral* and *subarachnoid* haemorrhage (*Haemorrhagic stroke*) [165]. Approximately 86% of strokes result from infarction, and the remaining 14% are due to haemorrhage according to the Lausanne Stroke Registry (LSR) [166]. (Figure 3-1)

The LSR reports that about 55% of strokes are caused by cerebral vessel thrombosis. This stroke, which occurs due to formation of a blood clot within cerebral arteries damaged by arteriosclerosis, falls into two subcategories: large-vessel thrombosis and small-vessel thrombosis. Large-vessel thrombosis accounts for approximately 43% of strokes. 20% involve small-vessel disease, which causes a type of thrombotic stroke known as *lacunar* stroke. Approximately 15% of strokes are caused by cerebral embolism, a type of ischaemic stroke that occurs when circulation to a portion of the brain is blocked by an embolus originating elsewhere in the circulation, most frequently from the heart or from the cervical portion of the carotid artery. Part or all of the embolus is carried through the bloodstream until it lodges within an artery too small to allow passage, preventing the blood behind it from passing as well.

Haemorrhagic stroke may be due to an intracerebral haemorrhage or subarachnoid haemorrhage. An intracerebral haemorrhage occurs when an affected artery within the brain ruptures, flooding the surrounding brain tissue with blood. The major risk factor for intracerebral haemorrhage is hypertension. Most signs and symptoms associated with intracerebral haemorrhage are caused by the compression of brain structures and blood vessels. Subarachnoid haemorrhage (bleeding into subarachnoid space) usually follows the rupture of an aneurysm or an arteriovenous malformation (AVM).

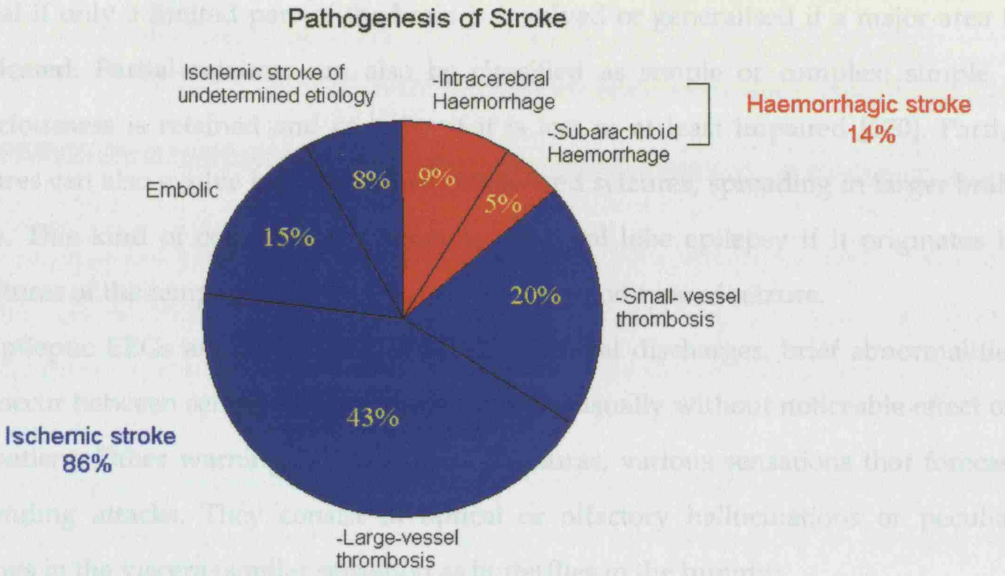

Figure 3-1. Pathogenesis of stroke according to the LSR

Recent developments in stroke treatment allow triage of clot busting therapy for ischaemic stroke. The treatment, which is performed through the administration of tissue Plasminogen Activator (t-PA) drug, requires definite elimination of haemorrhagic stroke case within 3 hours from the stroke onset, as the treatment is hazardous for patients who suffer haemorrhagic stroke [167]. Differentiation between the two stroke types has been addressed as a possible MFEIT application [163;164], and is revisited in Chapter 6.

3.4.2 Epilepsy

Epilepsy is the most common neurological disorder after stroke, with about 60 million individuals affected worldwide. According to the National Society for Epilepsy (NSE) [168] 1 in every 200 adults in the UK has epilepsy and 1 in every 100 children.

Epileptic seizures are identified as episodic, uncontrolled, excessive, synchronous discharges of groups of central neurons, that can be generated from excessive synaptic excitation, decreased inhibition, or increased activity of both excitatory and inhibitory synapses [169]. This condition characterises a particular type of discharge, known as *clonic*, in opposition to the tonic discharge, where neurons are firing incoherently and randomly.

Seizures can be classified according to their symptoms and the portion of the brain involved in the discharge. A general distinction divides them into convulsive if there is twitching or cramping of muscles or nonconvulsive in their absence. Seizures can be

partial if only a limited part of the brain is involved or generalised if a major area is implicated. Partial seizures can also be classified as simple or complex: simple if consciousness is retained and complex if it is lost or at least impaired [170]. Partial seizures can also evolve into secondary generalised seizures, spreading in larger brain areas. This kind of condition is known as temporal lobe epilepsy if it originates in structures of the temporal lobe and is the most common type of seizure.

Epileptic EEGs are also characterised by interictal discharges, brief abnormalities that occur between seizures (*ictus* or *ictal* activity), usually without noticeable effect on the patient. Other warning symptoms are the auras, various sensations that forecast impending attacks. They consist in optical or olfactory hallucinations or peculiar feelings in the viscera (similar sensation as butterflies in the tummy).

Structural imaging of the brain provides means to distinguish epilepsies into symptomatic and essential. Symptomatic epilepsy is the manifestation of an identifiable brain lesion or disease, while essential epilepsy does not have a clear origin.

Although epilepsy can be controlled by an appropriate drug treatment in up to 75% of the patients, some continue to have seizures despite these treatments. A small percentage of the remainder may be eligible for neurosurgery (approximately 3%), during which the part of the brain that is considered to be the cause of the seizures is removed with a surgical operation [171]. The localisation of epileptic foci has been addressed as a possible application of MFEIT [172;173].

3.4.3 CNS Neoplasms (Brain tumours)

Primary Central Nerve System (CNS) neoplasms represent 2% of all cancers and are the 6th most common group of tumours in adults and the 2nd most common form of cancer in children, accounting for 20% of cancers in children under the age of 15 years [174].

The classification of CNS neoplasms is based on the World Health Organisation (WHO) classification of central nervous system tumours. The neuroepithelial group of tumours accounts for approximately 60% of all primary brain tumours. The majority of these are astrocytic tumours. The most common primary brain tumours are glioma and they begin in the glial cells. There are many types of gliomas, of differing histology.

Astrocytomas arise from star-shaped astrocytes. In adults, astrocytomas most often arise in the cerebrum. In children, they occur in the brain stem, the cerebrum, and the cerebellum. Brain stem glioma occurs in the lowest part of the brain. A brain stem gliomas most often are diagnosed in young children and middle-aged adults. Oligodendroglioma arises from cells that form the fatty substance that covers and protects nerves. These tumours usually occur in the cerebrum. They grow slowly and usually do not spread into surrounding brain tissue. They are most common in middle-aged adults.

Some types of brain tumours do not begin in glial cells. A meduloblastoma usually arises in the cerebellum. It is the most common brain tumour in children. Meningioma arises from the meninges (the membranes surrounding the brain and spinal cord) and is most commonly found in children and young adults. They are usually slow growing. Schwannomas arise from Schwann's cells that line the nerve that controls balance and hearing in the inner ear. The tumour is also called an acoustic neuroma. It occurs most often in adults. Craniopharyngeoma grows at the base of the brain, near the pituitary gland. This type of tumour most often occurs in children.

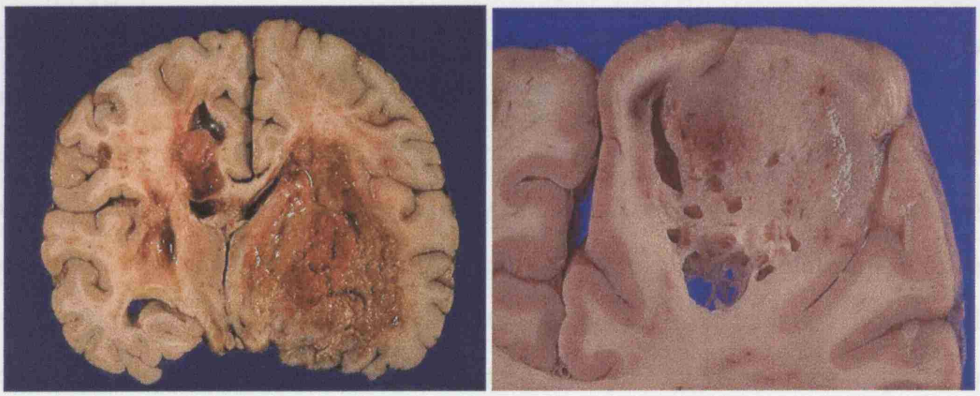

Figure 3-2. Left: Severe glioma-glioblastoma multiforme (GBM). These neoplasms are quite vascular with prominent areas of necrosis and haemorrhage [175]; Right: Macroscopic example of glioma arising in the cerebral hemisphere [175]

Brain tumours have a number of originating aetiologies and may arise following head injury, viral or bacterial infection, metabolic and other systematic diseases, and are associated with exposure to toxins and radiation as well as genetic abnormalities [176]. Some are due to tumours that metastasised to the brain from other parts of the body in which they were developed. Others are believed to have originated in embryonic cells left in the brain during development [177]. In some cases, tumours are

a consequence of embryological timing and migration errors - if germ cell layers differentiate too rapidly or the cells migrate to the wrong location, they exert neoplastic influences within their unnatural environment. These are a primary cause of congenital tumours.

Vargova et al have compared diffusion parameters of the extracellular space of the brain tumours and control [178]. Their measurement showed that the extra cellular space (ECS) volume was increased in all studied glial tumours and meduloblastomas except for oligodendrogliomas. There was a positive correlation between the size of the ECS volume and proliferative activity of the tumour.

3.5 Pathophysiological Tissue Properties

3.5.1 Ischaemic stroke

Two main pathological states violate the cell's homoeostatic condition: hypoxia and ischaemia. While hypoxia is merely a state of reduction in the availability of oxygen, affecting oxidative phosphorylation and ATP production, ischaemia is caused by a reduction in blood flow, which results in addition in the accumulation of catabolites.

On the cellular level, the ischaemic cell attempts to overcome the lack of oxygen by switching from aerobic to anaerobic metabolism [2]. Anaerobic metabolism leads to the accumulation of osmotically active products, such as lactic acid, which causes a reduction in intracellular pH value, and this result in increased intracellular osmotic pressure. At the next stage, the availability of ATP is severely reduced; subsequently the energy dependent sodium-potassium pump in the plasma membrane reduces or even ceases its transport activity. The Active transport mechanism failure, leads to alteration in the intracellular ionic contents. Subsequently membrane depolarisation occurs, as the intracellular sodium concentration increases and potassium concentration decreases. Then chloride ions and a large amount of calcium flow into the cell. The influx of calcium leads to the release of a number of neurotransmitters, which in turn activate N-methyl-D-aspartate (NMDA) and other excitatory receptors on other neurons. These neurons then become depolarised, causing further calcium influx, further glutamate release, and, therefore, a local amplification of the initial

[2] i.e. from production of ATP by oxygen (aerobic) to use of glycogen and creatine phosphate instead (anaerobic)

ischaemic insult. The joint effect of failure of the active transport, opening of the voltage-dependant ionic channels and anaerobic metabolism, results in substantially high concentration of ions and catabolites. This state induces an influx of water aiming to balance the osmotic pressure on both sides of the cell's membrane. Consequentially the cell swells, causing oedema. This phenomenon occurs primarily among the grey matter glial cells.

The extra-cellular space of grey matter is about 10-20%; therefore even a small change in its volume complement results in a considerable impedance increase. Due to the cell membrane permeability at high frequencies, this effect is most profound at low frequencies. Different cell types react differently to a state of hypoxia/ischaemia. Brain cells are especially vulnerable to the lack of oxygen, as the transmission of electric impulses and biosynthetic reactions within the neurons requires a continuous intracellular energy supply. This energy is mainly produced by glucose breakdown during aerobic glycolysis. When brain cells resort to anaerobic glycolysis, the availability of intracellular glucose is dramatically reduced and therefore neurons are more susceptible to hypoxia than most other cell types.

Within seconds to minutes of the loss of perfusion to a portion of the brain, an ischaemic cascade is unleashed, which if left unchecked, causes a central area of irreversible infarction surrounded by a penumbra of potentially reversible ischaemic tissue. A hypothesis for the expected changes over longer periods of 10 hours to few days can be considered as similar to the one following tissue excision. After all metabolisms had almost ceased, the β dispersion is expected to decline noticeably and eventually to disappear completely. Accordingly, a resistivity decrease accompanied with a decrease in permittivity at low frequency is expected [46].

Van Harreveld measured cerebral impedance of rabbit brain using a two terminal method, during circulatory arrest [179]. The measurements were performed at a fixed frequency of 1kHz. Five minutes after circulatory arrest, there was a sudden large drop in conductivity, assigned to the development of a cortical negativity (*asphyxial* potential). After the rapid drop, the conductivity continued to decrease at a decreasing rate. After 4-5 hours the conductivity became only 20-30% of the original value. The reactance change was significantly smaller than that of the resistance in amplitude,

though similar in terms of percentage change. This significant conductivity change is a result of the contribution of several mechanisms: 1) Cooling of the brain to room temperature (about 20% decrease), 2) Draining of fluid from the cortical surface and lateral sinus and possibly intercellular fluid (additional drop of 15-20%), 3) Emptying of blood vessels (10% decrease). Van Harreveld postulated that the rapid conductivity drop was due to a transport of ions from the intercellular compartment into the cells and fibres. Unfortunately, these results cannot be interpreted to specific impedance, as the geometry of conductance is not clear and the measurements reflect changes at a single frequency only.

Surowiec measured the dielectric properties of bovine brain, liver, kidney and spleen after excision, at frequencies from 20kHz to 100MHz [180]. Organs had been removed and kept refrigerated, and periodically, a sample was removed and examined. Their report regarding grey and white matter was only qualitative, indicating significant changes in permittivity for grey matter, and similar, but much less profound changes for white matter.

Holder measured *In-vivo, in-situ* cerebral impedance changes in rats during ischaemia [22]. Ischaemia was invoked by diathermy of the vertebral arteries and reversible occlusion of the common carotid arteries. Cortical and scalp electrode arrays were positioned in the frontal occipital plane. Four terminal measurements were performed using the Sheffield EIT system at 51kHz. Cortical measurement showed an impedance increase of 50-200%, whilst the scalp measurements resulted in 10% of that increase (i.e. 5-20%). In another publication, Holder repeated the experiment using a single channel system at 50kHz, of higher accuracy than the Sheffield system used previously [181]. He reported a cortical impedance change of 15-60%, whilst the change over the scalp was 10-20% of this increase.

Gabriel et al took measurements of 24-48 hours post-mortem human grey and white matter tissues at the high frequency range of 1MHz-20GHz, and ovine up to two hours after excision at the frequency range of 10Hz-20GHz [47-49]. The values measured for grey and white matter can serve as ischaemic tissues, though care should be taken as other possible bio-chemical processes may have occurred while the tissue was not alive.

Lingwood et al measured cerebral ischaemia in neonatal piglets using 4 scalp electrodes [182]. Impedance has been measured at 4-1012kHz with a four terminal method. They used Cole-Cole analysis in order to derive the resistance at DC (R_0) which is most closely related to extracellular fluid volume [183]. Following cerebral hypoxia, cerebral impedance increased by 8.5% in mild ischaemia and returned to baseline after resuscitation. Upon induction of severe hypoxia cerebral impedance increased by 23.5% and remained elevated.

Wu et al performed *In-vivo* measurements of rabbit brain tissue impedance under both normal and ischaemic conditions by using two terminal measurements in the frequency range of 0.1Hz to 1MHz [184]. The results of *In-vivo* measurement showed that the impedance increase ratio was up to 75% at frequencies lower than 10Hz. In the frequency range from 1kHz to 1MHz, the ratio showed a constant value of 15%. In another publication, Wu et al conducted *in-vitro* four terminal measurements at the same frequency range in rabbits [185]. The impedance frequency response curves showed a significant difference ($P < 0.001$) when ischaemia occurred. The magnitude of the real part and imaginary part increased remarkably. The imaginary part of the frequency response increased monotonically. They concluded that the whole brain impedance cannot be represented by a traditional 3-component model.

Seoane et al measured neonate porcine brain impedance *In-vivo* in the frequency range of 20kHz-750kHz prior to, during and following hypoxia [186]. 1-4 days old piglets were anaesthetised and ventilated to maintain normal blood oxygenation. Severe hypoxia was instituted for 45 minutes by reducing the oxygen level. Four terminal measurements were made with electrodes positioned over the dura located at P_3 P_4 C_3 and C_4. After 45 minutes of hypoxia resistance increased by 63% at 50kHz. Following subject resuscitation, resistance reached its maximum increase of 71%, and then later dropped down gradually to a level of about 18% above the original resistance 2 hours later. Later they performed a similar study with fetal sheep, comparing only the frequencies 30kHz and 200kHz [187]. Mean changes were 35% and 30% respectively, from which they concluded that lower frequencies are more susceptible over time to ischaemia onset, allowing identification of the phenomena within 50 seconds earlier and reaching 10% over baseline level about 75 seconds earlier

than higher frequencies. The next study included two separate sessions: one for measurement of the trajectory of resistance change, and the second for measurement of the complex impedance spectroscopy following ischaemia [188]. 7 adult and 2 neonatal pigs were used as subjects respectively, over the frequencies ranges of 50kHz-200kHz and 20kHz-750kHz correspondingly. Again, a similar setup and protocol as [186] has been performed. Resistance at 50kHz increased between 23% and 119%, and following normal oxygenation there was a short period of additional resistance increase reaching 25%-121%. Similar behaviour with smaller changes manifested at 200kHz. Following ischaemia, the Cole-Cole plot radius increased and the centre was shifted to higher resistance values. While maximal resistive increase of about 34% was reported around 20kHz, maximal reactive increase of 58.5% occurred at 300kHz. (See Appendix B for a summary table of the data presented in this section)

3.5.2 Haemorrhagic stroke

Haemorrhagic stroke is caused by a rupture of a blood vessel in the brain. Subarachnoid haemorrhage (SAH) accounts for 65% of haemorrhagic strokes, whereas intracerebral haemorrhage accounts for 35% of haemorrhagic strokes (Figure 3-3). This occurrence could be either spontaneous or traumatic. A rupture of a cerebral aneurysm or Arterio-Venous Malformation (AVM) causes the more common spontaneous SAH.

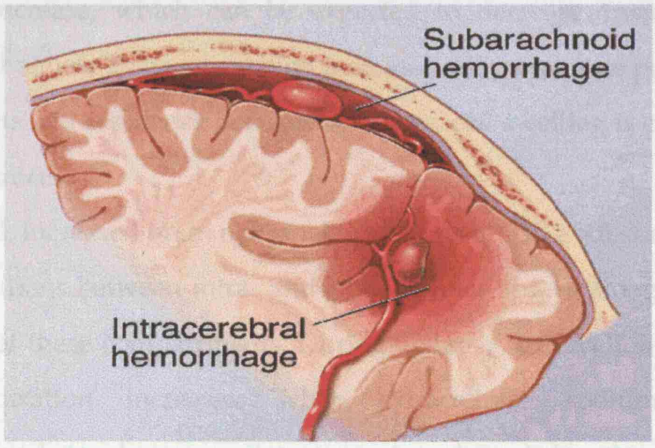

Figure 3-3. Subarachnoid and intracerebral haemorrhage [189]

Two pathophysiological mechanisms occur during haemorrhagic stroke: a ruptured vessel causes a focal or diffused blood volume expansion, which results in a small local impedance decrease, due to the high conductivity of the blood.

The second mechanism to appear is a rapid ischaemia of the surrounding brain region due to a loss of cerebral blood flow (CBF) autoregulation so that reduction in cerebral perfusion pressure (CPP) or increased intracranial pressure (ICP) causes global or regional brain ischaemia. This fall in CPP may be due to elevated intracranial pressure or reduced mean arterial pressure (MAP). The physical properties of a haemorrhage result in increased local tissue pressure around the lesion. This result in squeezing of the microcirculation and focal ischaemia. After the initial haemorrhage, erythrocytes are trapped in the subarachnoid cisterns or vessels and slowly haemolyse and release by-products to circulate within the subarachnoid space. These by-products are spasminogens, which increase the influx of calcium into the vascular smooth muscle, altering myocyte function and causing prolonged contraction and vasospasm [190-195]. In fact, cerebral vessels constriction induced by vasospasm is estimated to occur in 70 to 90% of patients with SAH. Therefore, a haemorrhage would appear as an inner bleed, surrounded by ischaemic tissue.

3.5.3 Epilepsy

A seizure is manifested as a prolonged repetitive neuronal activation. Consequently, three key mechanisms occur: 1) Cell swelling due to the ionic equilibrium breakdown, which results in an impedance increase. 2) Tissue activation causes vasodilatation and blood volume increase, which can be expected to decrease tissue impedance. 3) Opening of ion channels during excitation increases cell membrane permeability to ion flux, which results in a resistance decrease. Of these, cell swelling is expected to be the most profound process.

In more detail, increased brain neuronal activity results in a substantial alteration of the ionic distributions between intra- and extra-cellular spaces along with changes of the dimensions of these compartments. During epilepsy, extracellular potassium and chloride concentration increases, while extracellular sodium and calcium concentrations tend to decrease. Potassium is released by the neurons in the extracellular space during activation; therefore extracellular potassium concentration is high where neuronal activity is increased. Potassium is partially removed from the extracellular space by the glial cells through potassium-chloride uptake and spatial

glial buffering [3]. Both mechanisms are associated with water fluxes from the extracellular space into the cells, causing an osmotic swelling of the cells and shrinkage of the extracellular space in areas of enhanced neuronal activity.

During the action potential, extracellular sodium decreases by about 10% due to the sodium influx. Although this influx is mitigated by active ATPase pumps, it creates an ionic unbalance across neuronal membranes that cause water to move into neurons, which then swell, shrinking again the extracellular space. Consequently, where the neuronal activity is maximal the size of the extracellular space decreases by about 30%. Moreover, this ionic pick-up traps ions inside the highly resistive cell membrane, which therefore prevent them from freely participating in the extracellular current flow.

During the 1960's, impedance changes related to induced epileptic activity have been locally measured in various animal experiments with cortical and implanted electrodes. Van Harreveld and Schadé [196] measured cortical impedance changes with an AC bridge at 1kHz using two terminals (silver electrodes resting on the cortex) on rabbits and cats with encephale isolé [4]. The magnitude of the changes depended on the way the convulsion was induced (with Metrazol or with electrical stimulation) and whether it was developing into spreading depression (SD) [5] or not. The conductivity drop during convulsions was usually no more than 5%, while decreases of 10% were measured if convulsions were triggering SD.

In the same year, Adey et al [197] induced hippocampal seizures with electrical stimulation in cats and measured local resistance changes with a coaxial electrode (two terminals) and a Wheatstone bridge. They found small, irregular, rapid resistance perturbations during the seizures without consistent baseline shifts at first and with a small baseline drift on repeating the experiment after 10 days. Following seizure termination slow frequency rhythmic waves appeared. The first change was a

[3] A process by which glial cells dissipate local potassium gradients by transferring potassium ions from areas of high to low concentration

[4] An animal with its caudal medulla transacted and its respiration maintained artificially; it remains alert, has sleep-wake cycles, normal papillary reactions, and a normal EEG.

[5] This state is characterised by rapid and nearly complete depolarisation of a large population of brain cells with massive redistribution of ions between intracellular and extracellular compartments, that evolves as a regenerative process, and propagates slowly as a wave in brain tissue

resistance increase and a small baseline drift in the same direction was often present. In successive seizures, a slow progressive resistance increase of 2.5-33% was encountered.

Porter et al reported preliminary observations on 3 human patients with temporal lobe epilepsy using implanted manufactured coaxial electrodes (two terminals) in the hippocampus and hippocampal gyrus [198]. A Wheatstone bridge with provision for balancing parallel capacitance and resistance at 1kHz was used to measure in-phase and quadrature components. No changes were present during spontaneous and electrically induced seizures, while resistance drops between 2-14% and capacitance increases of almost 1% were recorded in Metrazol induced seizures.

Shalit measured cat cortical impedance variations with two terminals and a Wheatstone bridge at 10kHz, in assessing the influence of Metrazol on cerebral blood flow [199]. Despite the increase in blood flow during convulsions, impedance increases were found in 85% of the cases, decreases in 9% and a combination of the two phenomena in the remaining 6%. The magnitude of the changes was highly variable: from few ohms to several hundreds ohms.

Elazar et al induced spontaneous seizures with a tungstic acid in cats [200]. They measured separately local resistive and capacitive components at 1kHz with a coaxial stainless steel electrode (two terminals). The resistance changes started within 10 seconds after the beginning of the electrical seizures and were reaching peaks of 10-12% for long attacks (>150 sec), while the capacitance was changing in the opposite direction. The region of maximal variation did not always correspond with the region of the lesion, but was strictly correlated with the maximal EEG activity. During interictal periods baseline fluctuations between 1-3% were observed.

Rao measured local cortical impedance changes associated with electrically-induced focal and generalised seizures using four terminal measurements in rabbits at 47kHz [173]. During focal activity an increase of 9.5±1.4% was found near the stimulation site together with an increase of 1.7±0.5% a few mm away. During generalised activity, instead, an increase of 14.3±0.5% followed by a second increase of 15.6±1.5% was detected in the vicinity of the stimulation site together with an increase of 11.9±2.0% a few mm away after 2 minutes delay.

Fox et al measured resistivity increases of 22±3% in the pyramidal cell layer of rats transverse hippocampal slices bathed in a 'low-Ca^{2+}' artificial CSF (ACSF), which induces spontaneous seizures and prohibits synaptic connections [201]. A three-terminal system with high spatial resolution was used with DC pulsed current. No significant differences in resistivity were observed between normal ACSF and 'low-Ca^{2+}' ACSF.(See Appendix B for a summary table of the data presented in this section)

3.5.4 Tumours

No studies have been conducted to directly measure electrical properties of the brain tumour tissue. On the other hand, there have been many studies looking at the dielectric properties of other cancer tissue in general.

In a study of dielectric properties of breast carcinoma and surrounding tissues by Surowiec et al, excised infiltrating breast carcinoma was measured at frequencies from 20kHz to 100MHz at 37°C [202]. Three main categories of cancer tissue were considered: the central part of the tumour, the tumour surrounding tissue, and the peripheral tissue away from the tumour. The conductivity of tumour tissue was about 20-25 times larger than of normal tissue. The relative permittivity of the tumour tissue was up to 15 times higher than of the normal tissue. However, the frequency behaviour was very similar to that of the normal tissue up to the GHz band. Breast carcinoma involves a proliferation of cells that more closely resemble the glandular and ductal tissues, which have higher conductivity and permittivity than normal breast tissue.

Morimoto et al measured the impedance of various tumours over a frequency range of 0 to 200kHz by a three-electrode method [203]. The electrical impedance was measured *In-vivo* in patients with either breast or pulmonary disease. On the basis of those impedance measurements and the equivalent circuits, they calculated the extracellular resistance R_e, intracellular fluid resistance R_i, and cell membrane capacitance C_m in tissues. They found that R_e and R_i were significantly higher in breast cancers than in benign tumours and normal breast tissues and that C_m was significantly lower in breast cancers than in other tissues. These results contradict other reports, and are further discussed in the discussion section 3.6.4. Conversely, R_e and R_i were significantly higher, and C_m was significantly lower, in normal lung tissues than in pulmonary masses and in malignant tumours than in organised pneumonias.

Osypka et al has used a four terminal method to measure impedance of the *in-situ* sarcoma of the rat in frequency range of 0.1Hz to 10MHz [204]. Tumour tissue exhibited characteristic frequency of 250kHz at 35°C and 500kHz during hyperthermia of 42.5°C. Unfortunately in this study, measurements for normal tissue were not reported.

Blad and Baldetorp measured the dielectric properties of normal and tumour (squamous cell carcinoma) mouse thigh muscle *ex-vivo*. They used a four terminal mode at frequencies 1.5kHz to 700kHz at different temperatures [205]. The measurement cell was calibrated on known impedances of different concentrations of saline solution. Normal tissue showed higher resistivity at low frequencies. The imaginary impedance component exhibited a minimum at about 20kHz representing the centre frequency of the tissue, whilst the centre frequency for the tumour tissue was found at 100kHz.

Jossinet has measured the admittivity of samples of three groups of normal tissue (mammary gland, connective tissue and dipose tissue) and three groups of pathological tissue (mastopathy, fibroadenoma, carcinoma) at frequencies from 488Hz to 1MHz [206]. The conductivity of the normal connective and adipose tissues were significantly smaller than any other groups. Significant differences in conductivity were found at low frequencies (<32kHz) in carcinoma vs. fibroadenoma and carcinoma vs. normal mammary gland. The phase angle of the group of carcinomas has differed from all the other groups at frequencies 125kHz to 1MHz. The normal mammary gland group differed from all the other groups by the phase angle at frequencies below 16kHz, but large variability of the phase angles in this group resulted in large error, therefore these values cannot be explained by the tissue response at low frequency.

Haemmerich et al has measured *In-vivo* the conductivity of liver tumours in rats by four terminal mode at frequencies 10Hz to 1MHz [207]. The histology of all the excised tumours was assessed after the conductivity measurement. As a tumour grows, the connecting liver tissue becomes compressed, which results in higher density of liver tissue. They found that tumour tissue had a higher conductivity than normal tissue. This increase was more pronounced at low frequencies (a factor of 2.1 at 10Hz vs. 1.1 in 1MHz). There was a significant correlation between each of the Cole-Cole parameters

and percentage necrosis. (See Appendix B for a summary table of the data presented in this section)

3.6 Discussions and Conclusions

3.6.1 Ischaemic stroke

All studies reported a rapid and substantial impedance increase following the initiation of the ischaemic event. The variations in the magnitude of changes can mainly be attributed to the variability in the ischaemia severity. This claim can be substantiated by the difference in impedance changes obtained by Lingwood et al for mild and severe ischaemia (8.5% vs. 23.5%). Only two studies, by Wu et al [184;185], included measurements in frequency below 1kHz. These studies demonstrated that impedance changes of up to 75% are expected to appear at the low frequency range of 50Hz, whereas for frequencies above 1kHz a constant change across frequency of about 15% is anticipated. At low frequencies, current flows mainly within the extracellular fluid which is about 10-20% fraction of the total volume in grey matter. As a result, even a small variation related to cell swelling results in a significant impedance change. At higher frequencies, the permeability of the cell membrane allows ionic current to pass thorough the cell. Therefore, the overall impact of cell swelling over impedance is less profound. As changes in cell membrane mobility can be associated with the tissue dispersions, it is sensible to inspect the changes in impedance in the α and β dispersion regions, which lie in the measurable frequency range of EIT. The α dispersion of grey matter is around 50-150Hz, whereas the β dispersion occurs around 10kHz [119;120]. If tissue excision is considered to cause a comparatively similar process to ischaemia, the α dispersion is affected immediately, while β dispersion is expected to decline noticeably only after all metabolism has ceased, a process which occurs only after few days [46]. These reported changes were concurrent with the values reported by Lingwood et al [182] at the intersecting frequency band. It is therefore recommended to represent ischaemic brain tissue using changes reported by Wu et al [184] fitted over the normal brain behaviour.

3.6.2 Haemorrhagic stroke

No studies were found to directly quantify the effect of haemorrhagic stroke over the dielectric properties of the head. The physiology suggests that the inner part of the

lesion will have a mixed impedance value of the original brain tissue and blood according to their volume proportions. The extent of blood saturation is dependent on the severity of the stroke. For severe cases, the whole extracellular fluid will be displaced by blood, which can account for 10-20% volume in grey matter. In the severest scenario, the original tissue could be deformed out by the blood and therefore the affected region will contain blood only. While the inner part of the region will be saturated with blood to some extent, the surrounding layer will be comprised of ischaemic matter. Further studies are required in order to quantify the dielectric changes expected in this pathology.

3.6.3 Epilepsy

Considering the limited published information across frequency, apart from Porter et al report [198] showing an impedance decrease, there seems to be an agreement between the authors measuring at 1kHz that a local impedance increase of about 10% is expected during seizure.

Nevertheless, none of the authors provided any spectroscopic information, which could assist in deciding about favoured frequencies to represent the largest change. Assuming that the cardinal factor is indeed cell swelling, similar considerations as applied for ischaemia can be considered here. This claim can be supported by the larger changes reported by Fox et al [201] for low frequency. An alternative approximation to reveal the frequency dependant behaviour of brain tissue is to consider epileptic tissue to have similar, but weaker behaviour of tissue undergoing spreading depression. For this related condition, Ranck's [155] study for the low frequency band of 5Hz to 50KHz can be used together with Yoon et al [208] study for the higher frequencies of 100kHz and above. The reported changes in these studies need to be treated with care, and scaled down to comply with the more moderate changes expected during epilepsy.

3.6.4 Tumours

There has been no scientific paper published so far regarding the dielectric properties of brain tumours. Therefore, this literature review has been focused on the dielectric properties of cancer tissue in general. It has been previously published [66;176], that tumour cells demonstrate greater permittivity and conductivity than normal tissue.

This can be attributed to two reasons: 1) Cancer cells tend to have higher sodium concentration and larger water content than normal cells. 2) Membranes of cancer cells have different electrochemical properties.

Hypercellularity of brain neoplasms may seem to suggest a reduced intercellular space in tumour tissue. Yet, despite this prediction a varying degree of extracellular space enlargement has been observed across a range of different brain tumours [178;209]. There also has been a strong correlation between an extracellular space volume and malignancy of the tumours.

It is possible that the migratory capacity of the tumours will also be dependent on the ability of the tumour to create space for migrating cells. Authors [202;204;206;207] have found an increase of the conductivity of the measured tumour tissue in comparison with the normal tissue with its characteristic frequencies varying between 100kHz and 1MHz. The increase in conductivity at high frequencies however, was not as pronounced as at low frequencies. One author [203] has reported a conductivity decrease in the tumour tissue at lower frequencies. There is not clear mechanism which can explain these results, and therefore further studies are required to assess their validity.

Tumour tissue is much more inhomogeneous than normal tissue, the cells vary in size and shape and the arrangement of the cells is less uniform. When cells die by the mechanism of necrosis, eventual rupture of the cell membrane occurs and therefore the impedance difference between extra- and intracellular space decreases. Therefore, it is possible that necrosis and vascularisation of the tumours, which are the signs of high-grade tumours, will cause an increase that is even more pronounced in conductivity than the conductivity change of lower grade tumours.

4 THE FORWARD PROBLEM

4.1 Introduction

The ability to model a physical problem reliably is often desirable in applied and engineering sciences. Modelling can assist in experimental design; it can provide supplementary information in cases where measurement is impractical or only possible invasively. In many cases, modelling can spare the large resource costs needed for physical experiments, and whenever experiments are indeed performed, modelling can provide crucial guidance for the expected signals and noise contribution for validation purposes. From the imaging perspective, the solution for the inverse problem relies on the accuracy and reliability of the forward model; modelling errors should therefore be smaller than measurement error to allow reliable imaging. In the imaging world, such a model is termed a *forward model*, or *forward problem*, as opposed to its inverse which is often less well determined.

There are several ways by which the EIT forward problem is defined; generally speaking, it can be regarded as finding boundary voltage distribution of an object, for known geometry, admittivity distribution and injected currents [6].

The forward problem formulation comprises three main stages: the physical, mathematical, and numerical models. The physical model stage comprises selection of the appropriate physical theory and related governing equations (e.g. electromagnetics), along with a set of assumptions related to the physical nature of the problem (e.g. quasi-static, and three dimensional geometry). The next stage is a mathematical representation of the physical model; at this stage, the independent variables, differential/integral equations and specific boundary conditions are defined. Numerous mathematical models for the EIT forward problem have been developed over the years; the most accurate model, up to date, is the so-called Complete Electrode Model [210;211] which will be introduced further in this chapter. The third stage is a numerical model of the problem. This can be performed either analytically or numerically. An analytical solution should ultimately provide the most accurate solution; however, this approach is only applicable for a limited number of models. These include mainly simple geometries, such as concentric spheres [32;39;109;110], spheroids and cylinders [212]. At the early days of EIT, this approach was in common

[6] For some applications, such as sensitivity calculations, derivation of the internal fields is also desirable

use, as its computational efficiency played a major role with respect to its computationally intensive numerical counterparts. Nowadays, there are still some applications, mostly related to process tomography, for which this approach is still employed. Nevertheless, as most medical applications require imaging of complex geometries, numerical methods, which offer great versatility and generality, are commonly favoured.

Recent advances in acquisition involve harnessing spectral information into the reconstruction process [24;213;214]. However, this requires handling the calculations of more models or alternatively, larger problems. While the former can be addressed relatively easily using distributed computing [215;216], the latter still poses a major difficulty. Recent advances on the modelling front include the use of realistic MRI/CT-based volume meshes [33;217;218]. This minimises geometric errors, which, up to recently, were among the cardinal error contributors. Nevertheless, reliable and precise geometry representation of physiological organs introduces a limitation, as the models become increasingly large, which results in significant computational demands. Other improvements in modelling involve better approximation of the governing equations, such as accounting for the complete Maxwell equations set [219], or using high order element basis functions [34]. This results in a rapid rise in the problem size. Lastly, recent advances on the algorithmic front involve the development of effective non-linear inverse solvers [40;220-222]. Such iterative frameworks compensate well for the non-linearity of these problems, but, on the other hand, require repeated calculation of the forward model for each of the non-linear iteration steps. In addition, within each step, numerous evaluations of the forward model are required for the process of globalisation, such as line-search or trust regions methods [163;223].

The underlying goal of the work presented in this chapter was to provide an improved generally applicable method for EIT forward modelling for use in medical applications which require large-scale models.

4.2 Purpose

The purpose of this work was to develop methods for processing large-scale forward models efficiently. Two novel approaches to achieve this goal are presented: 1) The employment of multi-level inverse-based preconditioning [224], in order to accelerate

the solution of the complex-valued linear system of equations derived from Finite Element discretisation of the forward problem. 2) Use of virtual *monopolar current sources*, which minimises the number of forward models that are required to be solved for modelling and for construction of the sensitivity matrix.

In addition, the chapter includes two separate studies, the first aims to assess the benefit of multi-level preconditioning, while the other aims to compare the results of the forward modeller developed here, based on EIDORS 3D code suite [225], with empirical experimental measurements.

4.3 Design

In this chapter, a Finite Element (FE) formulation of the three dimensional EIT forward problem is presented, followed by a comprehensive review of different numerical tools for its processing. The necessity for preconditioning large-scale complex valued linear system matrices is introduced, for which the utilisation of two novel multi-level approaches are proposed. The first method performs a complex-to-real splitting of the linear matrix and construction of an implicit Algebraic Multi-Grid (AMG) preconditioner, and the second employs an inverse-based multi-level incomplete LU preconditioning. Later, the principles of the novel monopolar current sources method are presented.

In this chapter, two studies are presented: the first one is an empirical validation study for a Matlab forward modeller, developed chiefly for the head EIT problem. In the setup of this study, modelling results were compared with measurements from a saline filled head shaped tank which contained a human skull. The second study is a numerical study, aimed to assess the benefits of employing a multi-level inverse-based preconditioner along with effective numerical solver for large-scale models. In this study, the performance of conventional preconditioning methods was compared with multi-level techniques over problems of growing scale.

The forward modeller developed here has been adopted as the principal modelling tool in the UCL research group [25;28;113;162-164;215;216;226;227;227-233]. The application of the multi-level preconditioner and numerical solver has also been extended for the use of Optical Tomography. These were presented along with the monopolar current excitation approach in the special issue for computational aspects of

soft-field modelling in the Journal of Information and Sciences [234] and in the World Congress on Medical Physics and Biomedical Engineering in Seoul 2006 [235].

4.4 Background

4.4.1 Forward problem formulation

4.4.1.1 Problem definition

Let Ω be the domain under consideration, with surface Γ; the forward problem can informally be defined as: given current injection sources and sinks $\{q\}$ on Γ, and admittivity distribution γ over Ω, find the boundary electric potential V_Γ on Γ.

4.4.1.2 Governing equations

The governing equations which represent the EIT problem are derived from stationary Maxwell's equations. Maxwell's time domain equations for inhomogeneous media, without magnetic sources, are defined as

$$\nabla \times E = -\frac{\partial B}{\partial t} \tag{4.1}$$

$$\nabla \times H = J + \frac{\partial D}{\partial t} \tag{4.2}$$

$$\nabla \cdot D = \rho \tag{4.3}$$

$$\nabla \cdot B = 0 \tag{4.4}$$

The continuity conservation law is given by

$$\nabla \cdot J = -\frac{\partial \rho}{\partial t}. \tag{4.5}$$

where H is the magnetic field, B magnetic induction, E electric field, D electric displacement, J current density and ρ charge density. In fact, only three out of the five equations above (4.1)-(4.5) are independent; either the first three (4.1)-(4.3), or the first two (4.1),(4.2) and the fifth (4.5), the remaining two, can be derived out of the three others. For time-harmonic injected currents of angular frequency ω, the electric and magnetic field take the form

$$E_\omega(t) = \Re e\left(\hat{E}e^{i\omega t}\right) \tag{4.6}$$

$$H_\omega(t) = \Re e\left(\hat{H}e^{i\omega t}\right). \tag{4.7}$$

The following relations hold for isotropic linear medium

$$D = \varepsilon E \tag{4.8}$$

$$B = \mu H\,. \tag{4.9}$$

Since biological tissues are mostly nonmagnetic, only the free space permeability is thought $\mu = \mu_0 = 1.25663 \cdot 10^{-6} \frac{N}{A^2}$. The magnetic flux density becomes

$$B = \mu_0 H . \tag{4.10}$$

The EIT acquisition technique is based on injection of currents. The total amount of current density is given by $J = J_{conduction} + J_{source}$, where $J_{conduction} = \sigma E$ denotes the ohmic current and J_{source} stands for the current sources. Incorporating relations (4.8)-(4.10) together with (4.6)-(4.7) into (4.1)-(4.2) provides

$$\nabla \times E = -i\omega\mu_0 H \tag{4.11}$$

$$\nabla \times H - \gamma E = J_{source} \tag{4.12}$$

where $\gamma \equiv \sigma + i\omega\varepsilon$ is the admittivity. The electric field can be derived out from a scalar and vector potentials, which in the time domain have the form

$$E = -\nabla u - \frac{\partial A}{\partial t} \tag{4.13}$$

and in the frequency domain

$$E = -\nabla u - i\omega A \tag{4.14}$$

where A is a magnetic vector potential, and u is the electric scalar potential.

4.4.1.3 The quasi - static approximation

For low frequencies, a quasi - static approximation holds. Under this assumption, a simplification of Maxwell equations can be considered. The quasi-static approximation employs the following assumptions: 1) At low frequencies $\mu = \mu_0$ for biological tissues. 2) The effect of magnetic induction, which generates induced electric field can be neglected, i.e. the second term in (4.13) and (4.14) is negligible. In order to know when this assumption is valid, the following condition has to be fulfilled [3;4]

$$\mu\sigma\omega L_c^2 \left(1 + \frac{\omega\varepsilon}{\sigma}\right) \ll 1 \tag{4.15}$$

where L_c is the characteristic distance over which E varies significantly.

In the quasi-static approximation, the modified Maxwell equations of linear isotropic medium becomes

$$E = -\nabla u \tag{4.16}$$

$$\nabla \times H = \gamma E + J_{source} . \tag{4.17}$$

By applying divergence over (4.17) and substitution of (4.16),

$$\nabla \cdot (\gamma \nabla u) = \nabla \cdot J_{source} . \tag{4.18}$$

If there is no current source inside the medium and on the boundary, then (4.18) becomes the generalised Laplace equation

$$\nabla \cdot (\gamma \nabla u) = 0 \tag{4.19}$$

4.4.1.4 The complete formulation

As described in Chapters 2 and 3, the impedance of biological tissues may change remarkably at frequencies, which may not be encompassed within the quasi-static approximation domain. Hence, it is crucial to know where the quasi-static conditions break down, and different governing equations rule. Biophysical modelling of mammalian tissue in the range 1kHz-10MHz has indicated that displacement currents are significant above 1MHz. The induced magnetic field rises slightly in the 100KHz-1MHz region, and becomes rapid around the 1MHz region [236;237].

Let us follow the non-quasi-static formulation. The magnetic flux B is defined as

$$B = \nabla \times A. \tag{4.20}$$

Maxwell equation (4.1), can be written in the frequency domain in the following form

$$\nabla \times E = -i\omega B \tag{4.21}$$

Substitution of (4.20) into (4.21), provides

$$\nabla \times E = -i\omega \nabla \times A \tag{4.22}$$

which can be also written in the following form

$$\nabla \times (E + i\omega A) = 0. \tag{4.23}$$

By using the general vector relation $\nabla \times \nabla u \equiv 0$, the electric field can be represented as

$$E = -i\omega A - \nabla u \tag{4.24}$$

Applying divergence over (4.24) provides

$$\nabla \cdot E = \nabla \cdot (-i\omega A - \nabla u) = -i\omega (\nabla \cdot A) - \nabla \cdot (\nabla u) \tag{4.25}$$

Employing Lorentz's gauge

$$\nabla \cdot A = -\mu \gamma u = -\mu (\sigma + i\omega \varepsilon) u \tag{4.26}$$

Equation (4.25) becomes

$$\nabla \cdot E = i\omega \sigma \mu u - \omega^2 \varepsilon \mu u - \nabla^2 u \tag{4.27}$$

Substituting (4.8) into (4.3) provides

$$\nabla \cdot E = \frac{\rho}{\varepsilon} \tag{4.28}$$

Combining (4.27) with (4.28) provides

$$\nabla^2 u + k^2 u = -\frac{\rho}{\varepsilon} \tag{4.29}$$

where $k^2 \equiv -i\omega\mu(\sigma + i\omega\varepsilon) = -i\omega\mu\gamma$ is the wave number for the resulting Helmholtz wave equation. Equation (4.29) is the scalar governing equation for EIT. For low frequencies and no current sources, this relation indeed reduces back into the modified Laplace equation derived at 4.4.1.3.

4.4.1.5 Electrode models

A general solution for the domain interior is presented above; however, boundary conditions should be introduced for the problem. Let $\Omega \in \mathbb{R}^3$, with C^2- continuous boundary Γ, for which n_L electrodes are attached. It is assumed that there are no interior sources of charges, and quasi-static fields. Under these conditions, time-harmonic Maxwell's equations reduce to the generalised Laplace equation (as shown in 4.4.1.2), which provides the following relation for the electric potential

$$\nabla \cdot (\gamma(\mathbf{r};\omega)\nabla u) = 0 \tag{4.30}$$

where u is the scalar electric potential, and $\gamma(\mathbf{r};\omega) = \sigma(\mathbf{r};\omega) + i\omega\varepsilon(\mathbf{r};\omega)$ is the electric admittivity coefficients tensor, and ω is the angular frequency of the applied current. This equation holds for the potential inside the domain of interest. In practice, currents are applied through electrodes located on the surface Γ of the body, which impose boundary conditions for the problem. Let us denote the inward pointing normal component of the surface current density by J, and introduce the following Neumann boundary condition

$$\gamma \frac{\partial u}{\partial v} = J \text{ on } \Gamma \tag{4.31}$$

where v is normal to the boundary Γ.

Formerly, terms (4.30) and (4.31), together with a current conservation condition $\int_{\partial\Omega} J = 0$ and ground (or reference voltage) condition $\int_{\partial\Omega} u = 0$, formed the *Continuum Model*. Unfortunately, this simple model is not practical for real application, as the current density J is unknown. Still, the total amount of current injected through discrete set of electrodes attached to the body is well known. The underlying idea behind the *Gap Model* was to approximate the unknown current density to be constant for each of the electrodes. Nevertheless, this model turned to be inadequate as well. A more accurate model requires allowance for the discreteness of the electrodes, and the need to consider them as an additional conductive material.

The integral of the current density over each electrode is equal to the total current driven to that electrode

$$\int_{e_l} \gamma \frac{\partial u}{\partial v} dS = I_l \quad \text{on } \Gamma_l \quad l = 1,2,...,n_L \tag{4.32}$$

where I_l is the current driven into the l^{th} electrode through the surface e_l, and $\Gamma_1 \subset \Gamma$ denotes the boundary area underneath the electrode. In a complementary way, there are no normal current density components throughout the rest of the boundary surface, i.e. the gaps

$$\gamma \frac{\partial u}{\partial v} = 0 \qquad \text{on } \Gamma_2 \tag{4.33}$$

where $\Gamma_2 = \Gamma \setminus \Gamma_1$ the gaps boundary.

The high conductance property of the electrodes can conventionally be interpreted as uniform constant potentials V_l on each electrode, which are effectively the measured boundary voltages

$$u = V_l \qquad \text{on } e_l \qquad l = 1,2,...,n_L \tag{4.34}$$

This model is known as the *Shunt Model*. Although this model confers an improvement from the Continuum Model, there were discrepancies between the model's predictions and experimental results. The missing link was to account for the electrochemical effect, which is formed at the contact layer between the electrode and the body. This effect can be modelled by a thin highly resistive layer over the electrode contact area, which characterised by effective contact impedance z_l. In practice, electrodes have a finite area and displays complex impedance in series with that of the body alone. Thus, relation (4.34) becomes

$$u + z_l \gamma \frac{\partial u}{\partial v} = V_l \qquad \text{on } e_l \qquad l = 1,2,...,n_L . \tag{4.35}$$

In addition to the above relation, a current conservation term is added

$$\sum_{l=1}^{L} I_l = 0 . \tag{4.36}$$

For the sake of uniqueness, a reference condition over the potential is added by grounding

$$\sum_{l=1}^{L} V_l = 0 \tag{4.37}$$

This set of conditions forms the *Complete Electrode Model* which, up to date, is the most accurate model for EIT [34;210]. This model provides a unique solution up to an additive constant introduced by (4.37). It is capable of predicting measured potentials at better precision then 0.1% error with respect to the measurement system [211]. An in depth theoretical study of the model can be found in [238].

4.4.2 Numerical approaches

Once the physical properties of the problem have been formulated mathematically, knowledge regarding the geometry and the specific known parameters are required in order to define a model uniquely. Over the years, numerous numerical methods were developed to meet this need. The common feature for these approaches is the requirement for discretisation of the original problem, reformulation of the governing equation over a discrete problem and eventually solution of the resulting system of equations. Among these methods, probably the simplest is the *Finite Difference* (FD) approach, for which the domain is divided into equidistant vertices. Some properties, such as the admittivity, are considered to be constant for each discrete unit (voxel or vertex) and the potentials can be calculated using a system of linear equations which approximate the partial differential derivative relations between them. A more sophisticated related approach is the popular *Finite Elements Method* (FEM), where the domain is divided into elements of various sizes and orientations. This approach offers more accurate modelling of interfaces between sub-domains, and better control over the discretisation density at various regions. However, the meshing process, in which the connectivity of the elements is defined, has been a labour intensive procedure up to date, which often requires the services of a specialist [33]. An alternative approach in which only boundary of the domain mesh is required is the *Boundary Element Method* (BEM). This approach is based on the integral form of the problem, and employs Green's functions as kernel. Thus, no approximation over the domain is required, as only an approximation over the boundary is applied. Consequently, BEM offers higher accuracy and in some cases a computational advantage over FEM. On the other hand, its formulation is complex for general curved surfaces and it is limited to homogeneous and continuous internal regions [239;240]. A way to benefit from both methods is to employ BEM for homogeneous isotropic layers, and FEM for the remainder, while coupling both methods. This recent approach, known as hybrid BEM-FEM, is gaining increasing interest recently [241;242], but yet has not been developed for the EIT problem. Another group of recent approaches are meshless or mesh-free, methods. These methods require only a cloud of vertices to be defined over the domain, whereas no connectivity information is required. These have not yet been developed for the EIT problem.

4.4.3 Finite Element Modelling (FEM) formulation

In Finite Element Modelling, the potential is free to vary as a polynomial function from vertex to vertex within an element. For each of the elements in a mesh an interpolation function (or basis function) is suggested and a summated series of those are used to approximate the solution over the entire model. These functions can have any degree, but it is most common to use only linear or quadratic functions. For the quadratic case, extra nodes are added at the midpoints of each element edge. Increasing the number of linear elements improves the linear solution accuracy but, in practice, a quadratic solution is likely to be more accurate than a linear solution for the same number of elements, especially in regions of high field variation [34].

The discrete problem is commonly approached in two ways: Rayleigh-Ritz or Galerkin method. In the former, a variational expression is minimised with respect to its variables, which provides a differential matrix whose entries depends on the chosen interpolation functions. The latter is a weighted residual method, from which a similar system is derived [243].

In order to solve (4.30) together with the boundary conditions (4.32), (4.33) and (4.35), the domain is partitioned into k tetrahedral elements with total amount of n_v vertices. The admittivity coefficients are approximated by a piecewise constant function over the mesh. The nodal potential can then be written as

$$u_h = \sum_{i=1}^{n_v} u_i \phi_i \tag{4.38}$$

where u_i stands for the discrete sample of u at the ith node, and ϕ_i is the standard nodal basis for a set of piecewise linear functions. Derivation of the Galerkin weak form [243] of the solution is performed by multiplication of (4.30) by a sufficiently smooth arbitrary test function w, and integration over the domain Ω

$$\int_\Omega w\nabla\cdot(\gamma\nabla u_h)d\mathbf{r} = 0 \qquad \text{in } \Omega. \tag{4.39}$$

Relation (4.39) can be rewritten as

$$\int_\Omega w\nabla\cdot(\gamma\nabla u_h)d\mathbf{r} = \int_\Omega \nabla\cdot(\gamma\nabla u_h\cdot w)d\mathbf{r} - \int_\Omega \gamma\nabla u_h\cdot\nabla w d\mathbf{r}. \tag{4.40}$$

By the divergence theorem, this relation becomes

$$\int_\Omega \gamma\nabla u_h\cdot\nabla w d\mathbf{r} = \int_{\Gamma_1} \gamma\nabla u_h\cdot\hat{n}\cdot w dS + \int_{\Gamma_2} \gamma\nabla u_h\cdot\hat{n}\cdot w dS. \tag{4.41}$$

Where Γ_1 and Γ_2 are the boundary area beneath the electrodes and elsewhere respectively. Imposition of (4.33) and (4.35) over u_h yields

$$\int_{\Omega} \gamma \nabla u_h \cdot \nabla w d\mathbf{r} = \sum_{l=1}^{L} \int_{e_l} \frac{1}{z_l}(V_l - u_h) w dS . \tag{4.42}$$

Substitution of u_h from (4.38) into (4.42) provides

$$\sum_{i=1}^{n} \left\{ \left(\int_{\Omega} \gamma \nabla \phi_i \cdot \nabla w d\mathbf{r} + \sum_{l=1}^{L} \int_{e_l} \frac{1}{z_l} \phi_i w dS \right) \right\} u_i - \sum_{l=1}^{L} \left(\int_{e_l} \frac{1}{z_l} w dS \right) V_l = 0 . \tag{4.43}$$

Therefore, setting the test function to be $w = \phi_j$ for $j = 1 \ldots n_V$ yields n_V algebraic equations. Imposition of the remaining boundary condition (4.32) over u_h together with the application of (4.35) provides additional n_L algebraic equations

$$\frac{1}{z_l} V_l |e_l| - \sum_{i=1}^{n_V} \left(\int_{e_l} \frac{1}{z_l} \phi_i dS \right) u_i = I_l \qquad l = 1 \ldots n_L \tag{4.44}$$

where $|e_l|$ denotes the area of the l^{th} electrode. This relation implies that the current I_l injected through the l^{th} electrode, is partially dissipated by the power loss across the electrode contact impedance, while the rest is designated to generation of potential across the medium. Let us introduce the following notation

$$\begin{aligned}
A_M(i,j) &= \int_{\Omega} \gamma \nabla \phi_i \cdot \nabla \phi_j d\mathbf{r} \qquad i,j = 1 \ldots n_V ; A_M \in \mathbb{C}^{n_V \times n_V} \\
A_Z(i,j) &= \sum_{l=1}^{n_L} \int_{e_l} \frac{1}{z_l} \phi_i \phi_j dS \qquad i,j = 1 \ldots n_V ; A_Z \in \mathbb{C}^{n_V \times n_V} \\
A_V(i,l) &= -\int_{e_l} \frac{1}{z_l} \phi_i dS \qquad i = 1 \ldots n_V, l = 1 \ldots n_L ; A_V \in \mathbb{C}^{n_V \times n_L} \\
A_D(s,l) &= \begin{cases} \frac{1}{z_l}|e_l| & s = l \\ 0 & s \neq l \end{cases} \qquad s,l = 1 \ldots n_L ; A_D \in \mathbb{C}^{n_L \times n_L}
\end{aligned} \tag{4.45}$$

Therefore, the assembled complete system would be of the form

$$\begin{pmatrix} A_M + A_Z & A_V \\ A_V^T & A_D \end{pmatrix} \begin{pmatrix} \mathbf{u} \\ \mathbf{v} \end{pmatrix} = \begin{pmatrix} \mathbf{0} \\ \mathbf{I} \end{pmatrix} \tag{4.46}$$

where $\mathbf{u}(i) = u_i$, $\mathbf{v}(l) = V_l$ and $\mathbf{I}(l) = I_l$ for $i = 1 : n_V$ and $l = 1 \ldots n_L$. The right hand side (RHS) is typically composed of zeros apart from pairs of positive entries and their negations, representing the source and sink electrodes. This is due to the fact that current is not able to enter or leave the medium in any other site than through the injecting and receiving electrodes. For further use, the system will be denoted as

$$Ax = b$$

$$A := \begin{pmatrix} A_M + A_Z & A_V \\ A_V^T & A_D \end{pmatrix}, \quad x := \begin{pmatrix} \mathbf{u} \\ \mathbf{v} \end{pmatrix}, \quad b := \begin{pmatrix} \mathbf{0} \\ \mathbf{I} \end{pmatrix} \tag{4.47}$$

4.4.4 Computation of the forward solution

The linear system of equations obtained in (4.47) is well-posed, as opposed to the system which typically arise from the inverse problem. Moreover, the rank of this system is full, and therefore has a unique least square solution; it is sparse and therefore relatively compact in storage, and lastly the system is symmetric, thus can be decomposed into small factors.

Such systems can be solved directly or iteratively. Direct methods explicitly compute an inverse of the coefficient matrix A, which is then multiplied by the RHS sources term b to produce the desired solution. The main advantage of this approach is that once A^{-1} is derived, solutions for multiple RHS sources terms can be rapidly obtained with the modest computational cost of matrix vector multiplication. Nevertheless, this procedure is excessively demanding computationally, even for systems derived from moderate size 3D problems, and anyway, moderate solution accuracy levels normally suffice. The precision of this procedure is bounded by floating-point round-off limits; which can be quantified by the relative solution residual error expression

$$\frac{\left\|A^{-1}b - x\right\|_2}{\left\|b\right\|_2} \leq \varepsilon \tag{4.48}$$

In Matlab, for instance, a relative residual accuracy of the order of 10^{-16} is obtained by default for PC architecture [244]. Controlled measurements using a high specification EIT system would optimistically provide 60 - 80dB SNR. Hence, calculation of the inverse with accuracy beyond 10^{-5} is somewhat redundant. An additional drawback is the storage requirement for the inverted system, which is typically less sparse than the system itself. Iterative solvers approximate the solution gradually with no explicit formulation of the inverted system. These methods offer control over the desired accuracy level, and therefore avoid redundant over-refinement of the solution. The convergence rate of these methods is strongly dependant on the spectrum of the system matrix; the more clustered the eigenvalues of A, the more rapid and stable the convergence would be. A characteristic measure of the spectral properties of a real-valued system matrix is the condition number, which defines the ratio between the largest and smallest eigenvalues

$$\kappa = \frac{\lambda_{max}}{\lambda_{min}} \tag{4.49}$$

The smallest eigenvalue λ_{min} is closely related to the properties of the physical system that is being modelled, and the elements sizes in its discretisation. The lower and upper bounds of this eigenvalue are proportional to the volumes of the smallest and largest elements respectively. Fortunately, this entity is only weakly related to the shape of the elements. In contrast, the largest eigenvalue λ_{max} can become arbitrarily large by a single badly-shaped element [7] [245]. The complex geometry of realistic physiological models, and in particular head models, imposes strict constraints over the regularity of the model discretisation. Furthermore, such models comprise of large regions of inhomogeneities, which can be assigned with a wide diverse of local properties. Consequently, a typical coefficient system is prone to be ill-conditioned.

4.4.5 Linear iterative solvers

The solution for the linear system of equations $A\mathbf{x} = \mathbf{b}$ derived from FEM discretisation (4.47), can be formulated in terms of least squares minimisation of the norm of the residual of the system

$$\arg\min_{\mathbf{x}} \|A\mathbf{x} - \mathbf{b}\|_2^2 \tag{4.50}$$

There is a wide range of methods for minimising this term iteratively. Two important groups are stationary and non-stationary techniques. Stationary methods, also known as fixed-point methods, update the solution by the following iterate step

$$\mathbf{x}_t = B\mathbf{x}_{t-1} + \mathbf{c} \tag{4.51}$$

where both B and $\mathbf{c}$ are independent of the iteration count t. Despite their simplicity, the effectiveness of this group of solvers is rather limited. Nevertheless, stationary techniques, which include methods such as Jacobi, Gauss-Seidel and Successive Over-Relaxation (SOR), can effectively precondition non-stationary methods. Conversely, non-stationary methods use information that arises at each iteration. This group of techniques is more recent, their algorithms and convergence analysis is more complex, but they are more effective [246]. Among those, Krylov subspace family of solvers are among the most effective and efficient for large and sparse systems of coefficients.

[7] Different importance is given to each of the mesh quality measures, with respect to the purpose (condition, interpolation or discretisation). In the conditioning context, the small angles measure is the primary indicator.

The underlying principle is construction of sequence of A-orthogonal (conjugate) search directions $\mathbf{p}_t$ using either the *Lanczos* or *Arnoldi* method. Where two vectors $\mathbf{v}_i$, $\mathbf{v}_j$ $(i \neq j)$ defined as A-orthogonal if

$$\mathbf{v}_i^T A \mathbf{v}_j = 0 \qquad i \neq j. \tag{4.52}$$

These search directions span a Krylov subspace, using the coefficient matrix A and a vector $\mathbf{v}$

$$\mathrm{K}_t(A, \mathbf{v}) \equiv span\{v, Av, ..., A^{t-1}v\} \tag{4.53}$$

Starting with an initial guess $\mathbf{x}_0$, a Krylov method will produce iteratively an approximate solution $\mathbf{x}_t$ using the Krylov subspace A-orthogonal search directions. This selection for search direction is what distinguishes Krylov subspace methods from the local gradients approach commonly used for *Steepest Descent* and Newton-type methods. In some respects, efficiency is granted since progression is performed at any direction only once. This concept can intuitively be interpreted by demanding A-orthogonality of the remaining error $\mathbf{e}_{t+1} = \mathbf{x}_{t+1} - \mathbf{x}$ for the t+1th iteration and the current search direction $\mathbf{p}_t$

$$\mathbf{e}_{t+1}^T A \mathbf{p}_t = 0 \tag{4.54}$$

The initial error $\mathbf{e}_0$ can then be expressed as a sum of A-orthogonal components (corresponds to the A-orthogonal search directions); thus, at each iteration one of the error components is eliminated until the desired solution is reached (or its predefined vicinity).

Krylov subspace methods are characterised by two main properties, which makes them especially effective for large-scale problems. The first virtue is their highly economical memory requirement. Most of these methods employ Lanczos method for orthogonalisation, which for symmetric matrices can generate subsequent search directions, using only a three-term vector reoccurrence. Methods based on the Arnoldi method features a modified version of the Gram-Schmidt process, which is tailored for Krylov subspace. This approach requires the storage of the entire search directions sequence, or at least, a moderate part of it. The second virtue, is the fact that A, and sometimes also its conjugate transpose A^*, are only accessed in the form of matrix-vector product. The importance of this property is that an explicit formulation of A is not compulsory, as long as some mechanism which provides the product, exists.

In the following, the Conjugate Directions method is introduced, which set the grounds for the popular linear Conjugate Gradients solver. Later, a review of some of the most suitable solvers for the indefinite linear system is provided.

4.4.5.1 Conjugate Directions

Solving a linear system of equations $A\mathbf{x}=\mathbf{b}$, where $A\in\mathbb{R}^{n\times n}$ is Symmetric Positive Definite (SPD) [8], is equivalent to minimisation of a quadratic form function

$$\mathbf{f}(\mathbf{x})=\frac{1}{2}\mathbf{x}^T A\mathbf{x}-\mathbf{b}^T\mathbf{x}+\mathbf{c} \tag{4.55}$$

since at the minimum the derivation obeys

$$\frac{\partial\mathbf{f}(\mathbf{x})}{\partial\mathbf{x}}=\nabla\mathbf{f}(\mathbf{x})=A\mathbf{x}-\mathbf{b}=0 \quad\Leftrightarrow\quad A\mathbf{x}=\mathbf{b}. \tag{4.56}$$

For linear systems, the gradient of the minimised function is equal to the residual error $\mathbf{r}(\mathbf{x})$

$$\mathbf{r}(\mathbf{x})=A\mathbf{x}-\mathbf{b}=\nabla\mathbf{f}(\mathbf{x}). \tag{4.57}$$

The general iterative step is given by

$$\mathbf{x}_{t+1}=\mathbf{x}_t+\alpha_t\mathbf{p}_t. \tag{4.58}$$

Substitution of (4.58) into (4.55) provides the minimised function at the (t+1)th iteration

$$\mathbf{f}(\mathbf{x}_{t+1})=\frac{1}{2}(\mathbf{x}_t+\alpha_t\mathbf{p}_t)^T A(\mathbf{x}_t+\alpha_t\mathbf{p}_t)-\mathbf{b}^T(\mathbf{x}_t+\alpha_t\mathbf{p}_t)+\mathbf{c}. \tag{4.59}$$

The one-dimensional step size α_t minimiser of this quadratic function along $\mathbf{x}_t+\alpha_t\mathbf{p}_t$ can be found by differentiation with respect to α_t

$$\frac{\partial\mathbf{f}(\mathbf{x}_{t+1})}{\partial\alpha_t}=(A\mathbf{x}_t-\mathbf{b})^T\mathbf{p}_t+\alpha_t\mathbf{p}_t^T A\mathbf{p}_t=\mathbf{r}_t^T\mathbf{p}_t+\alpha_t\mathbf{p}_t^T A\mathbf{p}_t=0 \tag{4.60}$$

where $\mathbf{r}_t=A\mathbf{x}_t-\mathbf{b}$ as defined in (4.57). Therefore, we obtain

$$\alpha_t=-\frac{\mathbf{r}_t^T\mathbf{p}_t}{\mathbf{p}_t^T A\mathbf{p}_t}. \tag{4.61}$$

A set of A-conjugate vectors are linearly independent, hence, had one conjugate direction $\{\mathbf{p}_0,\mathbf{p}_1,...,\mathbf{p}_n\}$ been picked as a search direction at each iteration, $\mathbf{f}$ would be minimised within, at most n steps [247]. This important property can be proved by expressing the error term as a linear combination of the search directions

$$\mathbf{e}_0=\mathbf{x}_0-\mathbf{x}=\sum_{i=0}^{n-1}\delta_i\mathbf{p}_i \tag{4.62}$$

where δ_i values can be determined by pre-multiplication of (4.62) by $\mathbf{p}_t^T A$

---

[8] A matrix $A\in\mathbb{C}^{n\times n}$ is called positive definite if for any non-zero complex valued vector $x\in\mathbb{C}^n$ if $\Re e(x^* Ax)>0$, where x^* stands for the conjugate transpose of x.

$$\mathbf{p}_t^T A\mathbf{e}_0 = \sum_i^{n-1} \delta_i \mathbf{p}_t^T A\mathbf{p}_i = \delta_t \mathbf{p}_t^T A\mathbf{p}_t \tag{4.63}$$

which leads to

$$\delta_t = \frac{\mathbf{p}_t^T A\mathbf{e}_0}{\mathbf{p}_t^T A\mathbf{p}_t} = \frac{\mathbf{p}_t^T A\left(\mathbf{e}_0 + \overbrace{\sum_{i=0}^{t-1} \alpha_i \mathbf{p}_i}^{0 \text{ by A-orthogonality}}\right)}{\mathbf{p}_t^T A\mathbf{p}_t} = \frac{\mathbf{p}_t^T A\mathbf{e}_t}{\mathbf{p}_t^T A\mathbf{p}_t}. \tag{4.64}$$

Since $A\mathbf{e}_t = \mathbf{r}_t$, it follows that

$$\delta_t = \frac{\mathbf{p}_t^T \mathbf{r}_t}{\mathbf{p}_t^T A\mathbf{p}_t} = -\alpha_t. \tag{1.65}$$

From here, it is apparent that the process of constructing the solution $\mathbf{x}$, component by component, is equivalent to the process of cutting down the error term component by component

$$\mathbf{e}_t = \mathbf{e}_0 + \sum_{i=0}^{t-1} \alpha_i \mathbf{p}_i = \sum_{i=0}^{n-1} \delta_i \mathbf{p}_i - \sum_{i=0}^{t-1} \delta_i \mathbf{p}_i = \sum_{i=t}^{n-1} \delta_i \mathbf{p}_i. \tag{4.66}$$

After n iterations, all the components are cut down, and $\mathbf{e}_n = 0$. The main flaw of this method is that construction of any new search direction via conjugate Gram-Schmidt process, requires retaining all previous search directions (as is the case for Arnoldi methods). Furthermore, this approach requires $O(n^3)$ operations for generation of the full set.

4.4.5.2 Conjugated Gradients (CG)

The underlying idea of Conjugated Gradients is very similar to Conjugate Directions method, only that now, the search directions are constructed by conjunction of the residuals. The use of residual is, in some sense, inspired from the Steepest Descent method, and motivated by the fact that the residual is orthogonal to the previous search direction. Therefore, the first search direction is chosen to be the steepest descent direction $-\nabla \mathbf{f}(\mathbf{x}_t) = -\mathbf{r}_t$, while the followings are a linear combination of the steepest descent direction and the previous search direction $\mathbf{p}_{t-1}$ [248]

$$\mathbf{p}_t = -\mathbf{r}_t + \beta_t \mathbf{p}_{t-1} \tag{4.67}$$

where β is determined by the A-orthogonality requirement by application of transpose over (4.67) and right multiplication by $A\mathbf{p}_{t-1}$

$$\mathbf{p}_t^T A\mathbf{p}_{t-1} = \left(-\mathbf{r}_t^T + \beta_t \mathbf{p}_{t-1}^T\right) A\mathbf{p}_{t-1} = 0 \tag{4.68}$$

$$\beta_t = \frac{\mathbf{r}_t^T A\mathbf{p}_{t-1}}{\mathbf{p}_{t-1}^T A\mathbf{p}_{t-1}}. \tag{4.69}$$

The general formulation can be written in an economic way using relation (4.67) and the fact that the residual is orthogonal to all the previous search directions

$$\mathbf{r}_t^T\mathbf{p}_t = -\mathbf{r}_t^T\mathbf{r}_t + \beta_t \underbrace{\mathbf{r}_t^T\mathbf{p}_{t-1}}_{0} = -\mathbf{r}_t^T\mathbf{r}_t \tag{4.70}$$

Now the step parameter (4.61) can be written as

$$\alpha_t = \frac{\mathbf{r}_t^T\mathbf{r}_t}{\mathbf{p}_t^T A\mathbf{p}_t} \tag{4.71}$$

The residuals can be formulated in a recursive way by plugging (4.71) into (4.58)

$$\mathbf{r}_{t+1} = \mathbf{r}_t + \alpha_t A\mathbf{p}_t \tag{4.72}$$

From here, it can be easily shown that the residual $\mathbf{r}_t$ is actually orthogonal to all previous residuals as well, and therefore, β_t can be reformulated as

$$\beta_t = \frac{\mathbf{r}_t^T A\mathbf{p}_{t-1}}{\mathbf{p}_{t-1}^T A\mathbf{p}_{t-1}} = \frac{\mathbf{r}_t^T(\mathbf{r}_t - \mathbf{r}_{t-1})}{\mathbf{p}_{t-1}^T(\mathbf{r}_t - \mathbf{r}_{t-1})} = \frac{\mathbf{r}_t^T\mathbf{r}_t - \overbrace{\mathbf{r}_t^T\mathbf{r}_{t-1}}^{0}}{\underbrace{\mathbf{p}_{t-1}^T\mathbf{r}_t}_{0} - \mathbf{p}_{t-1}^T\mathbf{r}_{t-1}} = \frac{\mathbf{r}_t^T\mathbf{r}_t}{\mathbf{r}_{t-1}^T\mathbf{r}_{t-1} - \underbrace{\beta_{t-1}\mathbf{p}_{t-2}^T\mathbf{r}_{t-1}}_{0}} = \frac{\mathbf{r}_t^T\mathbf{r}_t}{\mathbf{r}_{t-1}^T\mathbf{r}_{t-1}} \tag{4.73}$$

The general framework of the Conjugated Gradients method for normal equations can be finally introduced [249]

$$\textbf{while } \|\mathbf{r}_t\| > \varepsilon \begin{cases} \alpha_t = \dfrac{\mathbf{r}_t^T\mathbf{r}_t}{\mathbf{p}_t^T A\mathbf{p}_t} \\ \mathbf{x}_{t+1} = \mathbf{x}_t + \alpha_t\mathbf{p}_t \\ \mathbf{r}_{t+1} = A\mathbf{x}_{t+1} - \mathbf{b} \\ \beta_{t+1} = \dfrac{\mathbf{r}_{t+1}^T\mathbf{r}_{t+1}}{\mathbf{r}_t^T\mathbf{r}_t} \\ \mathbf{p}_{t+1} = -\mathbf{r}_{t+1} + \beta_{t+1}\mathbf{p}_t \\ t = t+1 \end{cases} \tag{4.74}$$

Algorithm 4-1. Linear Conjugated Gradients

Since the construction of any new search direction does not require explicit elimination of conjugated components from previous search directions, the typical runtime complexity per iteration of this algorithm is reduced from $O(n^2)$ to $O(nnz(A))$, where $nnz(A)$ stands for the number of non-zero entries in the coefficient matrix, which is typically $O(n)$. This solver holds the optimal approximation property, that $\mathbf{x}_t$ has minimal error $\mathbf{e}_t = \mathbf{x} - \mathbf{x}_t$ measured with respect to the norm $\|\mathbf{e}_t\|_A^2 = \mathbf{e}_t^T A\mathbf{e}_t$, over all possible choices of $\mathbf{x}_t$ of the associated Krylov subspace. The convergence is determined by the spectrum of the eigenvalues, with the following relation for the relative error

$$\frac{\|\mathbf{e}_t\|_A}{\|\mathbf{e}_0\|_A} \leq \min_{q_t} \max_{i=1}^{n} |q_t(\lambda_i)| \tag{4.75}$$

where q_t is any polynomial of degree t satisfying $q_t(0)=1$ and $\{\lambda_i\}_{i=1}^n$ stands for the set of eigenvalues of $A \in \mathbb{R}^{n\times n}$. The number of required iterations for reducation of the error norm by a factor of ε is given by

$$t \leq \left\lceil \frac{\sqrt{\kappa}}{2} \ln\left(\frac{1}{\varepsilon}\right) \right\rceil \tag{4.76}$$

where κ is the condition number. From (4.75) and (4.76) it is evident that the runtime complexity is of $O(\sqrt{\kappa}n)$, which means that the relative error can be sufficiently reduced by few iterations only if the eigenvalues of A are clustered. Unfortunately, systems derived from discretisation of the EIT problem do not possess this property.

4.4.5.3 General Minimal Residual (GMRes)

The *Generalised Minimal Residual* method (GMRes) [250] is an extension of the *Minimal Residual* method (MinRes), which is only applicable to symmetric systems, to unsymmetric systems.

At iteration t an approximation $\mathbf{x}_t$ of the Krylov subspace is generated by the vector $\mathbf{c}$

$$K_t(A,\mathbf{c}) = span\{\mathbf{c}, A\mathbf{c}, ..., A^{t-1}\mathbf{c}\} \tag{4.77}$$

where typically $\mathbf{c}=\mathbf{b}$ is taken. This method solves the least square problem

$$\min_{\mathbf{z}\in K_t(A,\mathbf{b})} \|\mathbf{b} - A\mathbf{z}\| \tag{4.78}$$

by constructing an orthonormal basis $\mathbf{V}_t = \{\mathbf{v}_1, \mathbf{v}_2, ..., \mathbf{v}_t\}$ for $K_t(A,\mathbf{c})$ using Arnoldi's method. Starting with $\mathbf{v}_1 = \frac{\mathbf{b}}{\|\mathbf{b}\|}$, the basis for $K_{t+1}(A,\mathbf{b})$ is constructed recursively

$$\mathbf{v}_{t+1} = \frac{\hat{\mathbf{v}}_{t+1}}{\|\hat{\mathbf{v}}_{t+1}\|} \tag{4.79}$$

where

$$\mathbf{v}_{t+1} = A\mathbf{v}_t - \sum_{i=1}^{t} (\mathbf{v}_i^* A \mathbf{v}_t)\mathbf{v}_i \tag{4.80}$$

which then lead to the following decomposition

$$A\mathbf{V}_t = \mathbf{V}_{t+1}\mathbf{L}_t \tag{4.81}$$

where $\mathbf{L}_t \in \mathbb{C}^{(t+1)\times t}$ is an upper Hessenberg matrix. $\mathbf{z}$ can be represented now as $\mathbf{z} = \mathbf{V}_t\mathbf{w}$ for some $\mathbf{w}$, and therefore

$$\begin{aligned} A\mathbf{z} &= \mathbf{V}_{t+1}\mathbf{L}_t\mathbf{w} \\ \mathbf{b} &= \|\mathbf{b}\|\mathbf{V}_{t+1}\mathbf{e}_1 \end{aligned} \tag{4.82}$$

where $\mathbf{e}_1$ denotes here the first column of the identity matrix. The least square problem (4.78) is now reduced to

$$\begin{aligned} &\min_{\mathbf{w}_t} \left\| (\|\mathbf{b}\|)\mathbf{e}_1 - \mathbf{L}_t \mathbf{w}_t \right\| \\ &\mathbf{x}_t = \mathbf{V}_t \mathbf{w}_t \end{aligned} \tag{4.83}$$

It can be seen that in order to generate the next basis vector, A is accessed at (4.80) only in the form of $A\mathbf{v}_t$. The major drawback of GMRes method is that the amount of work and storage required per iteration rises linearly with the iteration count. Unless one is fortunate enough to obtain extremely fast convergence, the computational cost rapidly become prohibitive. The customary way to overcome this limitation is by restarting the iteration. After a chosen number of iterations $t_{restart}$, the accumulated data is cleared and the intermediate results are used as the initial data for the next $t_{restart}$ iterations. This procedure is repeated until convergence is achieved. The difficulty is in choosing an appropriate value for $t_{restart}$. If $t_{restart}$ is too small, GMRes($t_{restart}$) may be slow to converge, or fail to converge entirely. A value of $t_{restart}$ that is larger than necessary involves excessive work and storage. Unfortunately, there are no definite rules governing the choice of $t_{restart}$. The complete pseudo-code can be found in [246].

4.4.5.4 Bi-Conjugated Gradients (BiCG, CGS, BiCGStab)

Bi-Conjugated Gradients is a Lanczos based alternatives to GMRes for non-symmetric systems. The basic principle is replacement of the orthogonal sequence of residuals with two mutually orthogonal (namely *bi-orthogonal*) sequences, which on the one hand requires only short recurrences, at the price of no longer providing minimisation. The residuals update now becomes

$$\begin{aligned} \mathbf{r}_t &= \mathbf{r}_{t-1} - \alpha_t A\mathbf{p}_t \\ \tilde{\mathbf{r}}_t &= \tilde{\mathbf{r}}_{t-1} - \alpha_t A\tilde{\mathbf{p}}_t \end{aligned} \tag{4.84}$$

with the following search directions

$$\begin{aligned} \mathbf{p}_t &= \mathbf{r}_{t-1} + \beta_t A\mathbf{p}_{t-1} \\ \tilde{\mathbf{p}}_t &= \tilde{\mathbf{r}}_{t-1} + \beta_t A\tilde{\mathbf{p}}_{t-1} \end{aligned} \tag{4.85}$$

where

$$\begin{aligned} \alpha_t &= \frac{\tilde{\mathbf{r}}_{t-1}^T \mathbf{r}_{t-1}}{\tilde{\mathbf{p}}_t^T A\mathbf{p}_t} \\ \beta_t &= \frac{\tilde{\mathbf{r}}_t^T \mathbf{r}_t}{\tilde{\mathbf{r}}_{t-1}^T \mathbf{r}_{t-1}} \end{aligned} \tag{4.86}$$

which ensures the bi-orthogonality relations

$$\tilde{\mathbf{r}}_i \mathbf{r}_j = \tilde{\mathbf{p}}_i^T A \mathbf{p}_j = 0 \qquad i \neq j . \tag{4.87}$$

In this method the residual vector at iterate t, can be regarded as a product of $\mathbf{r}_0$ and a t^{th} degree polynomial P_t in A, which satisfies

$$\begin{aligned} \mathbf{r}_t &= P_t(A)\mathbf{r}_0 \\ \tilde{\mathbf{r}}_t &= P_t(A)\tilde{\mathbf{r}}_0 \end{aligned} \tag{4.88}$$

This suggests that application of such a polynomial contracts the residual. The method of *Conjugated Gradients Square* (CGS) applies such contraction operator twice, rather than once at a time. However, there are no guarantees that such operation, which indeed reduces the initial residual, should work over an already reduced vector. The *Stabilised BiConjugated Gradients* (BiCGStab) method was developed in order to avoid irregular convergence pattern often manifested by CGS. The general idea is to compute a sequence $t \rightarrow Q_t(A)P_t(A)\mathbf{r}_0$ instead of the CGS sequence $t \rightarrow P_t^2(A)\mathbf{r}_0$, where Q_t is a t^{th} degree polynomial describing the steepest descent update. This method can also be interpreted as the product of BiCG and repeated application of GMRes(1). In this way, a residual vector is minimised at least locally, which leads to considerably smoother convergence. However, if the local GMRes(1) step stagnates, the method will breakdown. This breakdown comes in addition to the common breakdowns this family of solvers prone to have.

4.4.5.5 Quasi Minimal Residual (QMR, Symmetric QMR)

The *Quasi Minimal Residual* (QMR) method was presented by Freund and Nactigal, to solve indefinite nonsymmetric system matrices [251]. The general motivation was to overcome the breakdowns BiCG and its variants (CGS and BiCGStab) are susceptible to undergo [9], using short occurrences.

The main idea is to solve a reduced tridiagonal system in the least square sense, similar to the approach of GMRes. Since the constructed basis for the Krylov subspace is bi-orthogonal, rather than the orthogonal basis produced by GMRes, the solution is viewed as quasi-minimal residual. Freund and Nactigal presented general error bounds, which showed that QMR is expected to converge as fast as GMRes. Comparison of the relations of the residuals of BiCG and QMR, shows that whenever

[9] In exact arithmetic both CGS and BiCGStab breaks down whenever BiCG breaks down [251]

BiCG defines a search direction, which reduces the residual error substantially, QMR delivers similar results, however, when BiCG reaches a stagnant step or even diverge, QMR keep on converging. QMR implementation often facilitates a look-ahead strategy to avoid the breakdown threats inherited from the Lanczos procedure. Thus, the convergence behaviour is typically much smoother and robust than that obtained for BiCG, as well as for its variants CGS and BiCGStab. SQMR is an adaptation of the general nonsymmetric QMR method to exploit the symmetry of the matrix A.

Since EIT system matrices are symmetric, facilitation of the Symmetric (Simplified) QMR is possible. Although the runtime and storage requirements per iteration of SQMR are similar to those of SYMMLQ and MinRes it converges considerably faster [252]. A summary of the computational requirements for each of the solvers is brought in Table 4-1.

Table 4-1. Summary of operation and storage requirement for iteration t [246]

Method	Inner product	SAXPY [10]	Matrix-Vector product	Preconditioner applications	Storage requirements
CG	2	3	1	1	Matrix + 6n
GMRes	t+1	t+1	1	1	Matrix + (t+5)n
BiCG	2	5	1 + 1 transpose	1 + 1 transpose	Matrix + 10n
CGS	2	6	2	2	Matrix + 11n
BiCGStab	4	6	2	2	Matrix + 10n
QMR	2	8 + up to 4	1 + 1 transpose	1 + 1 transpose	Matrix + up to 16n

4.4.6 Preconditioning of sparse linear systems

4.4.6.1 Fixed level preconditioning

The error convergence rate and numerical stability of Krylov subspace iterative methods depends strongly on the spectral properties of the coefficient matrix. Matrices obtained from discretisation of the EIT problem are typically poorly conditioned. This situation tends to worsen with increase of the problem scale. A remedy for the ill-conditioning and broad eigenvalue spread of the coefficient matrix is by preconditioning. Preconditioning is a process in which the linear system is transformed

[10] SAXPY - (Scalar Alpha X Plus Y) is the basic operation of scalar multiplication and vector addition $\alpha x + y$, where α is a scalar and x, y are vectors

into an equivalent system (in the sense that it has the same solution), which has more favourable spectral properties, i.e. its eigenvalues are better clustered. A preconditioner M is a matrix that effect such transformation

$$M^{-1}A\mathbf{x} = M^{-1}\mathbf{b} \tag{4.89}$$

where

$$cond\left(M^{-1}A\right) \ll cond\left(A\right) \tag{4.90}$$

A good preconditioner possesses the following properties: for any vector $\mathbf{v}$, $M^{-1}\mathbf{v}$ can be obtained easily, and $M^{-1}A$ is close to an identity matrix. Various preconditioning schemes were developed in the past two decades. These were applicable for different matrix structures. For the real-valued admittivity case of the EIT problem (ERT), the coefficient system matrix $A \in \mathbb{R}^{(n_V+n_L)\times(n_V+n_L)}$ is symmetric positive definite (SPD). As such, it has a defined square root. *Cholesky factorisation* decomposes A by an upper triangular matrix U such that

$$A = U^*U \tag{1.91}$$

and

$$\left(U^*\right)^{-1} = \left(U^{-1}\right)^*. \tag{1.92}$$

Considering a preconditioner $M = M_1M_2 = U^*U$, only an inverse of U is required to be calculated. Complete factorisations may yield optimal convergence rates for iterative methods, and can be used effectively for direct methods as well; however, the computational cost for factorisation of large-scale problem is entirely unacceptable. Preconditioners based on incomplete-factorisation are constructed by executing a sparse factorisation algorithm, while dropping some of the fill elements. Elements can be dropped according to numerical criteria, or structural criteria. Since some of the fill elements are dropped, the resulting factorisation is sparser and takes less time to compute than the complete factorisation. The control over the completeness of these factors is done through selection of a drop tolerance parameter η. The trade-off between the computational effort required for factorisation and the effectiveness of the preconditioner, is manifested by the solution runtime. *Incomplete Cholesky* factorisation is highly effective while being used as a preconditioner for the Krylov-subspace method of *Preconditioned Conjugated Gradients* (PCG).

For the complex valued admittivity case, the coefficients system matrix is still symmetric, but, no longer positive definite. Thus, the presence of negative eigenvalues

prevents calculation of the square root factors. For such cases, *LU decomposition* can be used. In this process, the system matrix $A \in \mathbb{C}^{(n_V+n_L)\times(n_V+n_L)}$ is decomposed into a product of a lower triangular matrix L and an upper triangular matrix U

$$A = LU \,. \tag{1.93}$$

This decomposition, in its incomplete form, is widely used as a preconditioner for non-symmetric and complex valued (indefinite) matrices. As L and U have different inverse, two separate triangular matrix inversions are required. This highly versatile factorisation is the traditional choice for preconditioning most of the Krylov subspace methods.

A common drawback for incomplete factorisation schemes is that a-priori knowledge (which is not necessarily available) regarding the permitted level of fill-in is required. Selection of fill-in level needs to account for the overall runtime for construction of the preconditioner with respect to the solution runtime for multiple RHS. As a result, this decision is often taken empirically.

4.4.6.2 Multi-level preconditioning

While fixed - level preconditioners could be extraordinarily effective for stabilising and accelerating the EIT forward problem solution process, the computational cost for their construction, even in their incomplete form, grows rapidly with the problem size. Over the years, several attempts have been made to meet this computational challenge by the scalable approach of Geometric Multi-Grid [253;254]. This approach requires the construction of hierarchical domain meshes of decreasing resolution. While this is achievable for simple geometries, the complexity of real-life physiological models makes this task complicated at best, if possible at all. Head shape models for instance, include very thin layers, such as the Cerebrospinal Fluid (CSF), which cannot be coarsened geometrically without introducing significant errors. Moreover, mesh generation is a tedious process, which cannot be automated, and requires the services of a specialist.

An alternative approach that overcomes this obstacle is the Algebraic Multi-Grid (AMG) [255] method. This approach does not require any information regarding the FE mesh geometry, and act directly on large-scale linear system matrices. The motivation is rooted in the limitation of stationary relaxation schemes (smoothers), such as Jacobi

or Gauss-Seidel, to reduce the low-frequency components of the error. These schemes effectively damp the high frequency components of the error, while leaving the low-frequencies almost unaffected. In order to address this shortcoming, AMG suggests the construction of a hierarchy of system matrices $A_0 \subset A_1 \subset ... \subset A_{l_{max}}$, along with a set of prolongations $P_{l,l-1}$ and restriction $R_{l-1,l}$ operators that map between them. The algorithm works in a recursive manner, starting by applying relaxation smoothers S_l over the system, followed by application of restriction over the residual error. The next step is a recursive call, where the restricted residual serve as RHS for the restricted system. The next step is a recursive call, where the restricted residual serve as RHS for the restricted system. This procedure is followed down to the lowest-coarsest level, where a correction for the solution (error) is solved directly. From then and on, this correction is interpolated using the prolongation operators and added to the solution at each level, usually with the application of another post-relaxation stage. The general principle is that over the coarser grids, frequencies that were considered as low beforehand, are now, relatively high, and therefore effectively smoothed as well.

The application of the classical AMG algorithm is limited to a special type of system matrices called *M-matrices*. A matrix $A \in \mathbb{R}^{n \times n}$ is defined as M-matrix if

$$\begin{aligned} A_{ii} &> 0 \quad i = 1..n \\ A_{ij} &\leq 0 \quad i, j = 1..n \quad i \neq j \end{aligned} \tag{4.94}$$

and for some positive diagonal matrix D, AD is strictly diagonally dominant

$$\left|(AD)_{ii}\right| \geq \sum_{j=1, j \neq i}^{n} \left|(AD)_{ij}\right| \tag{4.95}$$

While used as a solver over classical elliptic PDE problems with M-matrix structure, the computational demand is optimal, i.e. scales like $O(n)$. However, it is most effective as a preconditioner for an iterative solver, rather than for providing a complete solution.

4.4.6.3 The classical Algebraic Multi-Grid (AMG) preconditioner

The inner part $A_M + A_Z$ of a real-valued system constructed according to (4.47), corresponds to the Gap-shunt model. Such matrix maintains the standard elliptic PDE structure and features and therefore can be regarded as an M-Matrix. However, the augmented parts A_V, A_V^T and A_D violate the M-matrix property of this system [256]. Soleimani et al [256] suggested the utilisation of a commercial [257] classical AMG as a

preconditioner for the ERT problem (real valued EIT). They postulated that the augmented section of the ERT system invalidates only slightly the M-matrix definition, and therefore permit the use of a classical blackbox algebraic multi-grid preconditioner for the real valued problem. This approach indeed demonstrated a significant speedup in the forward solution stage. Nevertheless, in practise, the proximity property to M-matrix is not granted. At the low and high frequency ends, contact impedance values are extreme, which in turn scales accordingly the augmented section, introducing severe violation of the M-matrix structure. Attempts to employ this preconditioner in a non-linear inverse framework introduced frequent breakdowns whenever conductivity values approached zero. Lastly, since this preconditioner can handle only real valued admittivity problems, it is not applicable for medical problems, where permittivity cannot be ignored. For real symmetric positive definite problems such as ERT, a symmetric smoother is required, which is not a property of classical smoothers in their standard form. For the complex valued case, unsymmetrical techniques are required which are proposed in the next sections.

4.4.6.4 The modified unsymmetrical classical AMG preconditioner

An elegant way to provide a multi-level preconditioner using the classical AMG formulation for complex valued matrices is by a complex-to-real splitting and construction of an implicit AMG preconditioner. The first step is conversion of the symmetric complex matrix into real valued non-symmetric system

$$A\mathbf{x} = (C + iB)\mathbf{x} = \mathbf{b} \Rightarrow \begin{pmatrix} C & B \\ -B & C \end{pmatrix} \begin{pmatrix} \mathbf{x}_{\Im m} \\ \mathbf{x}_{\Re e} \end{pmatrix} = \begin{pmatrix} \mathbf{b}_{\Im m} \\ \mathbf{b}_{\Re e} \end{pmatrix} \tag{4.96}$$

where $C, B \in \mathbb{R}^{n \times n}$, $\mathbf{b} \in \mathbb{C}^{n \times 1}$ and C is approximately an M-matrix. Such system could be solved using Krylov-subspace solvers, which are suitable for non-symmetric matrices, such as stabilised BiCG, GMRES or QMR. Let us consider first the following preconditioner

$$M = \begin{pmatrix} C & B \\ 0 & C \end{pmatrix} \tag{4.97}$$

At each nonsymmetric solver's iteration the system $M\mathbf{y} = \mathbf{z}$ is needed to be solved. This can be done by rewriting the system as

$$\begin{pmatrix} C & B \\ 0 & C \end{pmatrix} \begin{pmatrix} \mathbf{y}_{\Im m} \\ \mathbf{y}_{\Re e} \end{pmatrix} = \begin{pmatrix} \mathbf{z}_{\Im m} \\ \mathbf{z}_{\Re e} \end{pmatrix} \tag{4.98}$$

At this stage, the following procedures could be performed in order to solve the system

$$\text{solve } C\mathbf{y}_{\Re e} = \mathbf{z}_{\Re e} \tag{4.99}$$

$$\text{solve } C\mathbf{y}_{\Im m} = \mathbf{z}_{\Im m} - B\mathbf{y}_{\Re e} \tag{4.100}$$

These internal solution procedures can be performed by any method, such as the Conjugated Gradients. However, unlike $C+iB$, C is approximately an M-matrix, therefore, classical AMG can be employed here. While using an iterative method in (4.99) and (4.100), the required accuracy tolerance question need to be addressed. Classical multi-grid is a stationary method; therefore, application of a single AMG V-cycle rather than an accurate solution suffices [258]. In such case, the preconditioner becomes

$$\hat{M} = \begin{pmatrix} \hat{C} & B \\ 0 & \hat{C} \end{pmatrix} \tag{4.101}$$

where $\hat{C}$ is defined by the V-cycle, and therefore not formed explicitly. Although this approach can be used for a wide range of applications, it is still prone to solution convergence breakdown, whenever, the approximation of the system matrix to an M-matrix is violated. In addition, the complex-to-real-split process doubles the storage requirements of the system matrix, which for large-scale systems can be limiting.

4.4.6.5 Inverse based multi-level ILU

Bollhöfer and Saad [224] recently introduced the innovative approach of inverse-based multi-level preconditioning. Unlike other multi-level preconditioning approaches, this approach is capable of handling complex valued sparse matrices of general structure, as well as efficiently handling Hermitian and symmetric structures. The algorithm comprises three core stages. At the first stage, rescaling and static partial reordering is applied to define a well-suited leading block B. The coefficient system entries are being permuted to reduce the level of fill-in in the factorisation

$$A \to \tilde{A} = P^T A Q = \begin{pmatrix} B & F \\ E & C \end{pmatrix} \tag{4.102}$$

where P and Q are permutation matrices, B is the leading matrix block and C, E and F are the remaining block matrices. The next stage is a partial incomplete LU factorisation with diagonal pivoting, where the growth of the inverse triangular factors of $P^T A Q$ is controlled. In order to understand this stage better, let us consider the following approximate factorisation for a process which terminates after ι steps

$$\tilde{A}=\begin{pmatrix} B & F \\ E & C \end{pmatrix}=\underbrace{\begin{pmatrix} \widetilde{L_B} & 0 \\ \widetilde{L_E} & I \end{pmatrix}}_{\widetilde{\mathcal{L}_l}}\underbrace{\begin{pmatrix} \widetilde{D_B} & 0 \\ 0 & \widetilde{S_C} \end{pmatrix}}_{\widetilde{\mathcal{D}_l}}\underbrace{\begin{pmatrix} \widetilde{U_B} & \widetilde{U_F} \\ 0 & I \end{pmatrix}}_{\widetilde{\mathcal{U}_l}}+\mathcal{E}_l=\widetilde{\mathcal{L}_l}\widetilde{\mathcal{D}_l}\widetilde{\mathcal{U}_l}+\mathcal{E}_l \qquad (4.103)$$

where $\widetilde{L_B}$ and $\widetilde{U_B^T}$ are unit lower triangular matrices, the leading $\iota\times\iota$ part of $\widetilde{D_B}$ is diagonal and $\widetilde{S_c}$ is an approximation for the Schur complement $S_c=C-EB^{-1}F$.

The error $\mathcal{E}_k$ accommodates for the entries that are being dropped during the incomplete factorisation

$$\mathcal{E}_l=\tilde{A}-\widetilde{\mathcal{L}_l}\widetilde{\mathcal{D}_l}\widetilde{\mathcal{U}_l}. \qquad (4.104)$$

For most threshold-oriented incomplete factorisation approaches, the error norm is set to satisfy

$$\|\mathcal{E}_l\|=O(\eta) \qquad (4.105)$$

where η is the drop tolerance threshold. This error norm may provide a fair bound for the similarity of the factors to the original system; however, for preconditioning purposes the application of $\widetilde{\mathcal{L}_l}^{-1}$ and $\widetilde{\mathcal{U}_l}^{-1}$ over A in the form $\widetilde{\mathcal{L}_l}^{-1}A\widetilde{\mathcal{U}_l}^{-1}$ is more relevant. This leads to the definition of the inverse error, which essentially represents the actual concern of effective preconditioning

$$\mathcal{F}_l\equiv\widetilde{\mathcal{L}_l}^{-1}\mathcal{E}_l\widetilde{\mathcal{U}_l}^{-1}. \qquad (4.106)$$

This term emphasizes the importance of controlling the inverse triangular factors norms $\|\mathcal{L}^{-1}\|$ and $\|\mathcal{U}^{-1}\|$ [259;260]. These factors amplify the error related to the size of the entries which are being dropped during the incomplete LU decomposition [260]. Consequently, at this stage the reordered system P^TAQ is factored so that the growths of its inverse triangular factors are being controlled $\|\mathcal{L}^{-1}\|,\|\mathcal{U}^{-1}\|\le\kappa$ by a factor or skip strategy. At each step, rows or columns that exceed the prescribed bound are pushed to the end (Figure 4-1).

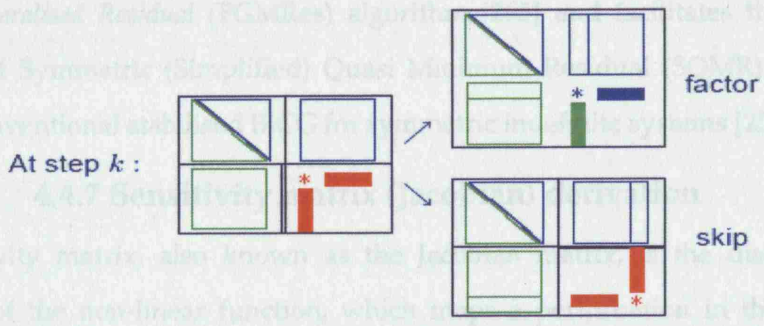

Figure 4-1. An illustration of the factor and skip strategy at level k, rows or columns which exceeds the prescribed bounds are omitted from the incomplete factorisation and moved towards the lower and righter part of the system matrix

The last step is incorporation of the scheme above in a multilevel manner, so that the sub-matrix which was skipped from the factorisation in the current level, will be treated on the next level (Figure 4-2). Therefore, a multi-level strategy is applied recursively to the approximate Schur complement S_c of the system at each level

$$A \xrightarrow{1} P^T A Q \xrightarrow{2} \hat{P}^T A \hat{Q} \xrightarrow{3} \begin{pmatrix} LDU & F \\ E & S \end{pmatrix}$$

$$S \xrightarrow{1} P_S^T S Q_S \xrightarrow{2} \hat{P}_S^T A \hat{Q}_S \xrightarrow{3} \begin{pmatrix} L_S D_S U_S & F_S \\ E_S & T \end{pmatrix} \tag{4.107}$$

$$\vdots$$

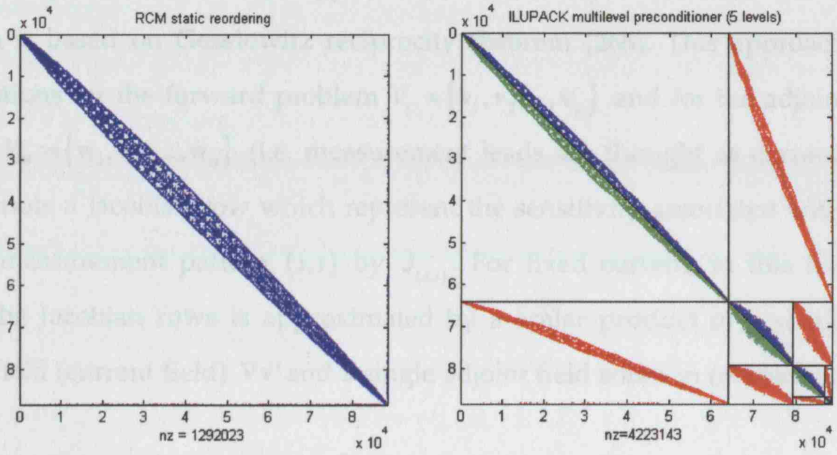

Figure 4-2. Large-scale EIT system matrix of 90k × 90k entries. Left: single level Reverse Cuthill McKee (RCM) ordering; Right: the obtained inverse-based multi-level preconditioner

An implementation of this framework is available in the ILUPACK package [261]. Extended functionality, and in particular broader variety of reordering schemes can be obtained by linking this package with the parallel sparse direct linear solver Pardiso [262-264]. The package also includes a selection of Krylov solvers, including the recent *Flexible Generalised Residual* (FGMRes) algorithm [265] and facilitates the use of the more robust Symmetric (Simplified) Quasi Minimum Residual (SQMR) [252], rather than the conventional stabilised BiCG for symmetric indefinite systems [251].

4.4.7 Sensitivity matrix (Jacobian) derivation

The sensitivity matrix, also known as the Jacobian matrix, is the discrete Fréchet derivative of the non-linear function, which maps a perturbation in the solution to variation in the boundary data

$$\nabla F(\gamma): \Delta\gamma|_{\Omega} \mapsto \Delta V|_{\partial\Omega} \tag{4.108}$$

In particular, for the EIT problem, given a set of boundary measurement combinations $V_\Gamma \in \mathbb{C}^m$ and admittivity map $\gamma \in \mathbb{C}^k$, the Jacobian $J \in \mathbb{C}^{m\times k}$ represents the variation in the ith boundary voltages measurement combination with respect to an admittivity perturbation in the jth element

$$J_{ij} = \frac{\partial V_{\Gamma i}}{\partial \gamma_j} \tag{4.109}$$

Naively, the Jacobian can be derived by introducing an admittivity perturbation $\delta\gamma$ at each element and calculating its effect over the boundary voltages δV_Γ; however, for realistic 3D problems such an approach is excessively inefficient. The alternative approach is based on Geselowitz reciprocity theorem [266]. This approach requires only solutions for the forward problem $V_C = \{\mathbf{v}_1, \mathbf{v}_2, ..., \mathbf{v}_p\}$ and for the adjoint forward problem $V_M = \{\mathbf{w}_1, \mathbf{w}_2, ..., \mathbf{w}_q\}$ (i.e. measurement leads are thought as current sources). Let us denote a Jacobian row which represent the sensitivity associated with a certain injection-measurement pattern (s,t) by $J_{(s,t)}$. For fixed current, in this formulation, each of the Jacobian rows is approximated by a scalar product of a single forward solution field (current field) $\nabla\mathbf{v}^s$ and a single adjoint field solution (measurement field) $\nabla\mathbf{w}^t$

$$J_{(s,t)} = -\int_\Omega \nabla\mathbf{v}^s \cdot \nabla\mathbf{w}^t d\mathbf{r} \qquad s = 1..p, t = 1..q \tag{4.110}$$

For real valued boundary voltages and purely real and positive admittivity, the Jacobian operator is positive, linear, compact and self-adjoint operator. As such, its inverse J^{-1} is discontinuous and therefore unstable with respect to variation in measured data. For complex valued boundary potentials and admittivity, another complication arises due to the coupling between real and imaginary components of the admittivity perturbation and the boundary voltage variation. For this case, assuming $\sigma \gg \omega\varepsilon$ at each element, the Jacobian $J \in \mathbb{R}^{2m\times 2k}$ can be decomposed as

$$J = \begin{bmatrix} J_{\Re e\Re e} & J_{\Re e\Im m} \\ J_{\Im m\Re e} & J_{\Im m\Im m} \end{bmatrix} = \begin{bmatrix} \dfrac{\partial V_{\Gamma\Re e}}{\partial \gamma_{\Re e}} & \dfrac{\partial V_{\Gamma\Re e}}{\partial \gamma_{\Im m}} \\ \dfrac{\partial V_{\Gamma\Im m}}{\partial \gamma_{\Re e}} & \dfrac{\partial V\Gamma_{\Im m}}{\partial \gamma_{\Im m}} \end{bmatrix}. \tag{4.111}$$

For practical applications, a complex valued Jacobian can be constructed using relation (4.110), with complex valued fields, while ensuring that the conjugated complex of the field $\nabla\mathbf{v}^s$ is employed. Using this formulation, images of both the conductivity and the permittivity can be obtained.

For most EIT applications, the number of elements in the discretisation is significantly larger than the amount of independent measurement data. Consequently, the Jacobian matrix is large and highly underdetermined. For such cases, it is advisable to consider some spatial restriction transformation: either element to nodal base transformation or a regular-grid transformation [267]. These approaches interpolate the sensitivity J^e at each element either over the finite-element vertices $R_n^e : J^e \mapsto J_n$, or over a regular grid $R_g^e : J^e \mapsto J_g$. Such operations can reduce the Jacobian size substantially and allow for more efficient Jacobian inversion at the inverse solution stage, on the expense of introducing large errors over the boundaries for multi-tissue models [268]. These weighted interpolation operators along with their prolongations are especially useful for large-scale problems.

4.4.8 Forward modelling developments in UCL group

A thorough review of available FEM packages was carried out by Gibson [269] with the aim of choosing one for use in EIT. These were mostly sophisticated, inflexible pieces of software and their adaptation for solving multiple boundary conditions sets for each of the excitation patterns was cumbersome. EEG source modelling software, like ASA [111] and Curry [270] were disregarded at that time, as they were based on BEM of the head. The suitability of I-DEAS [271], was investigated by Liston [110], who found its memory demand excessive, even for solving the problem for a subset of boundary conditions. Gibson used the TOAST [272] software developed at the Optical Tomography group in UCL, which solves for photon density throughout an object when light is injected at one optode on the surface. The scattering of light is comparable to resistivity but there is no analogue in EIT to the concept of absorption. Photon density and the diffusion coefficient were substituted for the electric potential and conductivity, and the absorption coefficient set to zero in order to adjust the diffusion equation to the generalised Laplace equation. The refractive index was set to one in order to prevent refraction and reflection at internal tissue boundaries. Current injection was through point electrodes using Robin boundary conditions.

Later, the UCL group received a version of TOAST written in Matlab for 2D and 3D problems, which incorporated appropriate boundary conditions for the case of EIT. This solver, namely *MaTOAST*, produced more realistic voltage profiles than those

reported earlier with TOAST [21;110]. However, MaTOAST code had several drawbacks: firstly, in terms of functionality, it was designed to work for the real part of the admittivity only, did not allow incorporation of anisotropic priors, employed arbitrary units and was limited to nodal base representation. In addition, this code included only a simple linear inverse solver. In terms of performance, it was slow and memory inefficient, and had not been validated for 3D problems. The author undertook improvements to this code on arrival in the group but later elected to pursue a different approach.

Fortunately, at that time a publicly available Matlab code library called EIDORS 3D had been released by Polydorides and Lionheart [225]. This code suite provided a framework for element based EIT forward modelling and Jacobian composition, based on the Complete Electrode Model. This enabled incorporation of anisotropic priors easily, was suitable for complex admittivity, and was well documented. Unfortunately, it has not been designed for large-scale models. The author took advantage of functions related to FEM system matrix composition, but then elected to develop new routines for the requirements of work in the UCL group for EIT of brain function.

Consequently, the author developed the *SuperSolver* Matlab toolbox, which was element based, but allowed nodal base formulation as well. This provided full complex admittivity support, inherently supported anisotropic priors, and was composed with special care for computational efficiency and scalability. The toolbox includes both forward and inverse solvers. It is fully documented, includes several demos, and works with physically meaningful units. The solver has been validated in tank and human measurements so far, in addition to the validation presented below in 4.6.1 [24;25;28;113;162;230;273].

4.5 Monopolar Current Excitations

The right hand side of system matrices derived from Optical Tomography contain a distribution of sources only, with no sinks. However, EIT has so far been modelled by a composition of sources and sinks, as derived from the stringent current conservation physical limitation. Nevertheless, mathematically, this limitation is not compulsory. Let $A \in \mathbb{C}^{n \times n}$ be the system matrix and $X = \{\mathbf{x}^1, ..., \mathbf{x}^v\} \in \mathbb{C}^{n \times v}$ a set of solutions

corresponding to the set of RHS column vectors $B=\{\mathbf{b}^1,...,\mathbf{b}^v\}\in\mathbb{R}^{n\times v}$, which together forms the following set of linear systems

$$AX=B \tag{4.112}$$

where a typical RHS term satisfies

$$\begin{aligned}\sum_i b_i^j &= 0 \quad i=1..n\\ \sum_i |b_i^j| &\neq 0 \quad j=1..v\end{aligned}. \tag{4.113}$$

In the most general case, each column vector $\mathbf{b}^j$ includes a composition of few positive entries and their negations. Modern acquisition systems would allow multiple excitation patterns, involving the usage of each source numerous times with different sinks. For such cases, the number of unique excitation patterns exceeds the number of unique sources and sinks. Let us denote by $Q=\{\mathbf{q}^1,...,\mathbf{q}^s\}\in\mathbb{R}^{n\times s}, s\le v$ the subset of unit basis vectors that spans the column space of B, and by $P=\{\boldsymbol{\alpha}^1,...,\boldsymbol{\alpha}^v\}\in\mathbb{R}^{s\times v}$ the corresponding coordinate matrix transformation

$$B=QP. \tag{4.114}$$

Thus, the linear systems can now be rewritten as

$$AX=QP. \tag{4.115}$$

Assuming A is invertible, and since matrix multiplication is associative, one has

$$X=A^{-1}(QP)=\underbrace{\left(A^{-1}Q\right)}_{\tilde{X}}P \tag{4.116}$$

where $\tilde{X}$ are the solutions for the monpolar sources given by

$$\tilde{\mathbf{x}}^i\equiv A^{-1}\mathbf{q}^i. \tag{4.117}$$

Since A is a linear operator, each solution vector $\mathbf{x}^j$, which corresponds to a RHS $\mathbf{b}^j$ term, can be also decomposed into linear combination of $\tilde{\mathbf{x}}^i$; each of which is the solution for a monopolar source $\mathbf{q}^i$. Hence, only a solution of the system for each of the RHS elementary basis vectors $\mathbf{q}^i$ is required in order to construct any solution as a simple linear combination.

With the growing cost of computation for each solution $\mathbf{x}^i$, and the relatively low computational cost of vector summation whenever $s<v$, there will be a clear benefit of almost a factor of v/s in speedup by utilisation of this approach. The number of forward solutions for a given coefficient system is bounded by this method to be the number of unique independent sources (for EIT this would be the number of electrodes). Considering simulation studies for an instance, where a complete dipolar excitation pattern is employed, this approach reduce the computational cost from

$n_L(n_L-1)/2$ to n_L, i.e. it requires about twice of the square root of the original number of systems to be solved. In some respects, this approach provides the most compact form of representing the total amount of independent information that resides in the system.

The same principle can be used also within the inverse solution framework. The basic component required for constructing a search direction within that framework is the sensitivity matrix. As derivatives are distributive, the latter can be composed using combinations of monopolar potential distribution solutions. This can be performed either in the conventional adjoint composition manner, or alternatively, using the adjoint-fields framework [274;275]. Rewriting the Jacobian term given in (4.110) using monopolar current potential solutions provides

$$\begin{aligned} J_{(s,t)} &= -\int_{\Omega}\nabla \mathbf{v}^s \cdot \nabla \mathbf{w}^t d\mathbf{r} = -\int_{\Omega}\nabla\left(\sum_{i\le v}\alpha_i^s \tilde{\mathbf{v}}_i\right)\cdot\nabla\left(\sum_{j\le v}\alpha_j^t \tilde{\mathbf{v}}_j\right)d\mathbf{r} = \\ &= -\int_{\Omega}\sum_{i\le v}\nabla\left(\alpha_i^s \tilde{\mathbf{v}}_i\right)\cdot\sum_{j\le v}\nabla\left(\alpha_j^t \tilde{\mathbf{v}}_j\right)d\mathbf{r} = -\sum_{i\le v}\sum_{j\le v}\alpha_i^s\alpha_j^t \underbrace{\int_{\Omega}\nabla\tilde{\mathbf{v}}_i\cdot\nabla\tilde{\mathbf{v}}_j d\mathbf{r}}_{\tilde{J}_{(i,j)}} \end{aligned} \tag{4.118}$$

where $\tilde{\mathbf{v}}_i$ and $\tilde{\mathbf{v}}_j$ stands for monopolar potential distributions and α^s, α^t represents the transformation coefficients which relate the monopolar solution to the forward solutions of the s^{th} current field and the t^{th} measurement field. Hence, the Jacobian derivation can be accomplished using the monopolar source potential solution and application of derivation over them.

4.6 Methods

4.6.1 Forward solver validation

In this study, boundary voltages measurements from a realistic head shaped tank containing a human skull, in reference and perturbed states, were compared with data calculated from accurate Finite Element modelling.

4.6.1.1 Acquisition setup and pre-processing

Measurements were taken from a head shape latex tank with a skull filled with 0.2% saline (0.43 S/m), with electrodes positioned according to the extended 10-20 scheme. Acquisition was performed using the UCH Mark 2.5 system [24], over 30 frequencies ranging in logarithmic scale from 2kHz - 1.6MHz. The applied currents were arranged in 3 waveforms composed of 10 frequencies. The setup included two states: the

reference state, as described above, and a perturbed state, where a conductivity decrease of 11.3% was introduced by placing a cylindrical sponge of 2.6cm diameter and 2.6 cm height (volume 13.8cm^3) centred 9cm above the foramen magnum. A Vitafoam green sponge of grade 40S, with density of $4\frac{g}{100ml}$ was used. It was held by thin wood sticks, which were present also in the reference measurement. The skull was immersed in the saline for a day, to allow air out (Figure 4-3). 258 electrode combinations were used. A ground electrode was positioned in the forehead between electrodes number 1 and 2 (Figure 4-4). Contact impedance was simulated by RC circuits, which were attached to each of the electrodes. These circuits were with 430Ω resistors in parallel with 22nF capacitor, both in series with 200Ω resistor. The injected current was of 276μA. A median of 20 sampled frames was taken, and 42 channels that deviated by more than 3 standard deviations over frequency or were noisy over time were eliminated.

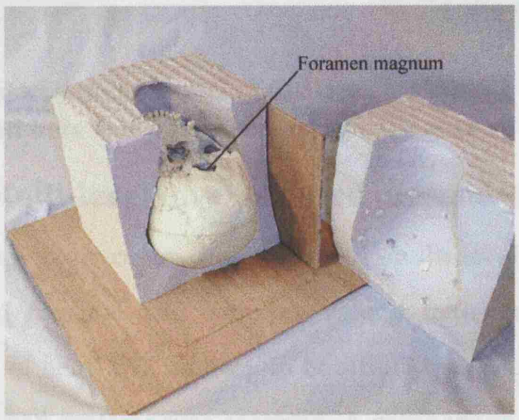

Figure 4-3. The experimental latex tank and the skull, which were used for the validation experiment

4.6.1.2 Modelling

An accurate 3 shell mesh model of 24,772 elements was generated [33] from a high resolution CT scan of the head-shaped latex tank and human skull which was acquired at the UCH CT unit (Figure 4-4). The skull conductivity was directly estimated, as this was deemed preferable to use of an estimate from the literature. This was achieved with a compartment-wise non-linear Damped Gauss-Newton recovery of the skull conductivity [25]. In this procedure, only the modelled skull conductivity value was free to change, while the remainder, which corresponded to the already assessed saline conductivity, maintained fixed. The scalp and brain region were assigned with saline

conductivity of 0.43 $^{S}/_{m}$ and the skull was assigned with the resulting optimised value of 0.0189 $^{S}/_{m}$. The injection-measurement protocol included 21 independent current injection patterns. The simulated contact impedances and current levels used were passed into *SuperSolver*, which was used to generate forward solutions. Later, a forward solution of the perturbed model was generated with conductivity value of 0.3814 $^{S}/_{m}$ assigned to the sponge region. The modelled sponge had a volume of 14.4 cm^3.

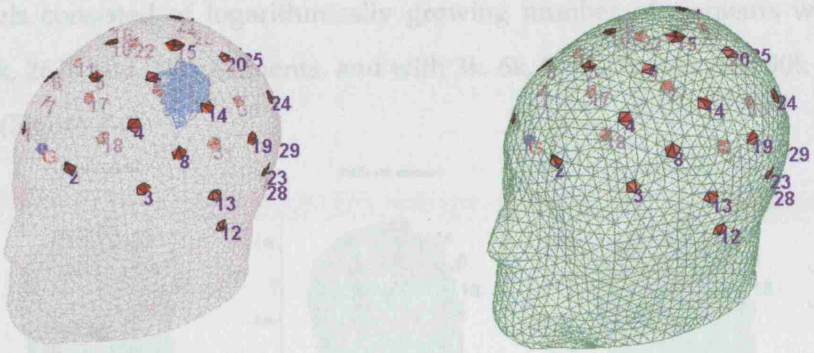

Figure 4-4. Finite Element model of the latex tank head. The volume mesh presented here was generated using a CT scan of the tank

4.6.2 Multi-level inverse-based preconditioning

The benefits of employment of an inverse-based multi-level ILU preconditioning scheme were assessed for real and complex valued matrices derived from Finite Element discretisation of head EIT models. In addition, the employment of the SQMR solver for complex valued systems was assessed. A comparison with the conventional incomplete preconditioners and solvers (PCG, stabilised Bi-CG and GMRes) with respect to the problem scale was performed.

4.6.2.1 Generation of test system matrices

Six MRI-based realistic adult head shape volume meshes of four layers each (scalp, skull, CSF and brain) were generated [33]. (Figure 4-5)

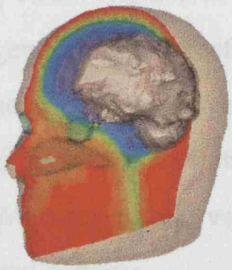

Figure 4-5. Multi - shell Finite Elements head model

The models consisted of logarithmically growing number of elements with 12k, 31k, 53k, 136k, 262k and 503k elements, and with 3k, 6k, 10k, 25k, 48k and 90k vertices respectively. (Figure 4-6)

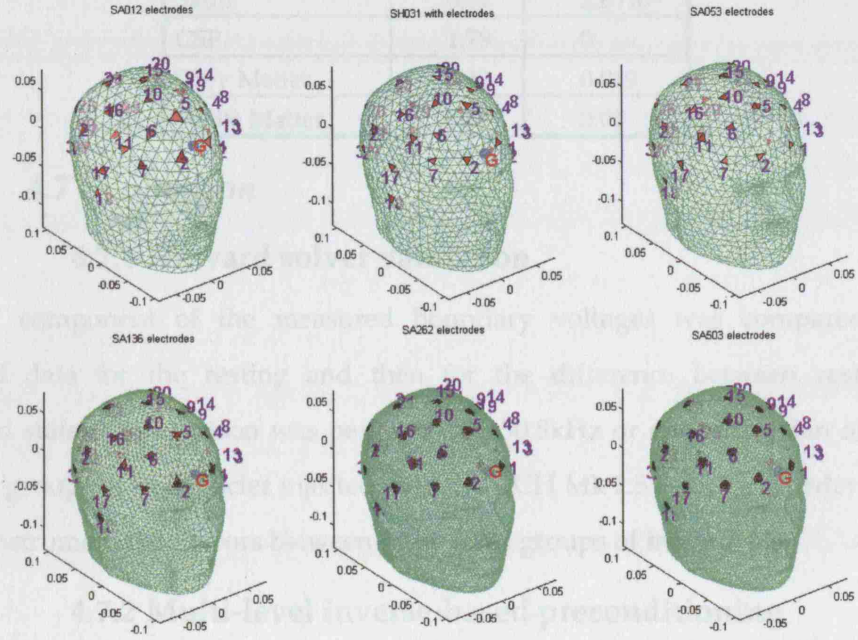

Figure 4-6. Finite element meshes of growing density. The models consisted 12k, 31k, 53k, 136k, 262k and 503k elements, and 3k, 6k, 10k, 25k 48k and 90k vertices respectively. Red makings represent the electrodes injection sites, and the G marks represent the grounding electrode

Admittivity values of normal human head tissues at the frequency of 75Hz were assigned to the model based on the values concluded in Chapter 2 [276]. 31 electrodes were positioned over the scalp according to the extended EEG 10-20 positioning, and a complete non-reciprocal dipolar current injection protocol with current level of 100μA was injected. Contact impedance of 1kΩ was set for all electrodes. These parameters were passed into *SuperSolver* [163] to generate symmetric complex valued system

classical AMG preconditioner. 4) SQMR (ILUPack) with multi-level inverse-based preconditioner. The latter was compared with an in-house Matlab implementation of the SQMR solver to eliminate platform and code architecture efficiency dependence.

For all solvers, the maximum number of iterations was set to 500, and desired relative residual error $\|Ax_k - b\|_2 / \|b\|_2 \leq \varepsilon$ levels of 10^{-6}, 10^{-9}, and 10^{-12} were attempted. The ILUPack stopping criterion for PCG is $\|x - x_k\|_A < \varepsilon \|x\|_A$, while for all other solvers it is the backward error criteria $\|Ax_k - b\| < \varepsilon(\|A\|\|x_k\| + \|b\|)$. These criteria were adjusted to comply with Matlab's relative residual error criterion mentioned above to allow a fair comparison. The actual relative residual error obtained from each solution procedure, along with the runtime and total number of iteration was monitored. Bounds for the inverse triangular factors from the incomplete LU decomposition were set by the 'condest' parameter to 10. All incomplete factorisation based preconditioners were formed with drop tolerances η of 10^{-2} and 10^{-3}. This choice was taken after initial experimentation in order to provide minimal complete runtime for a coefficient matrix with about 20-30 RHS commonly used for the type of imaging problems considered here. Storage requirement was recorded by the relative non-zeros (nnz) population in the preconditioner versus the original matrix, i.e. $nnz(preconditioner)/nnz(A)$. The comparison was performed with a dual Xeon 2.8 GHz, 2GB RAM workstation on a single processor mode with Debian Linux and Matlab 7.1 [244].

4.8 Results

4.8.1 Forward solver validation

Application of the non-linear Damped Gauss-Newton algorithm over the shelled compartments, permitting only the skull impedance to vary, converged to a residual error norm of $8 \cdot 10^{-5}$ within 2 steps and provided averaged skull conductivity of 0.0189 S/m. A plot of the modelled and measured boundary voltage in reference state is shown in Figure 4-7.

With the obtained skull conductivity value, the slope of the measured boundary voltage versus the modelled ones was 0.8874 with offset of 0.0005 and correlation coefficient of 0.892 (Figure 4-8 and Figure 4-9). A slope of 1 was achieved for skull conductivity of 0.023225 S/m with offset of 0.0004 and correlation coefficient 0.894.

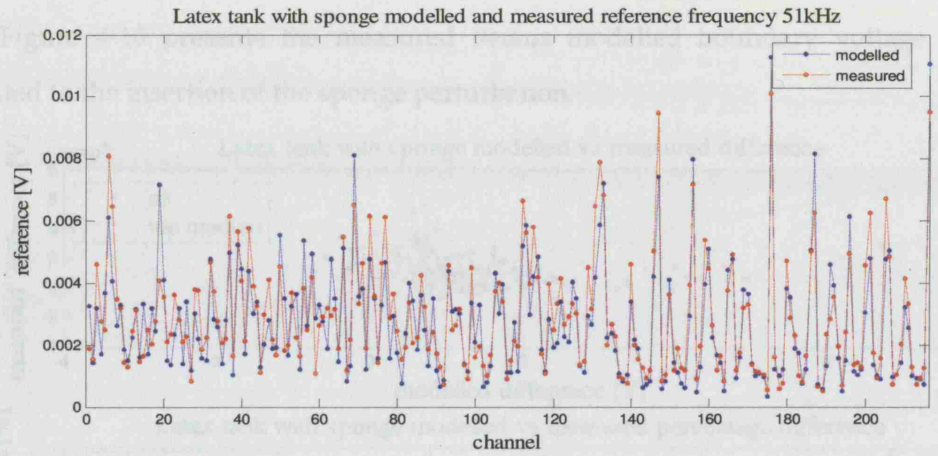

Figure 4-7. Modelled (blue) and measured (red) boundary voltages of the reference state at frequency 50.8kHz

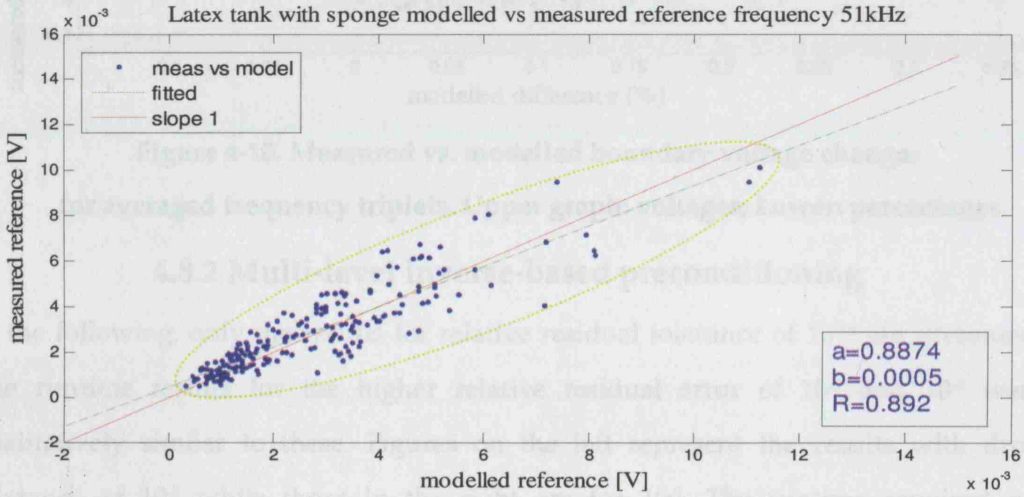

Figure 4-8. Measured vs. modelled boundary voltages for the reference state at frequency 50.8kHz

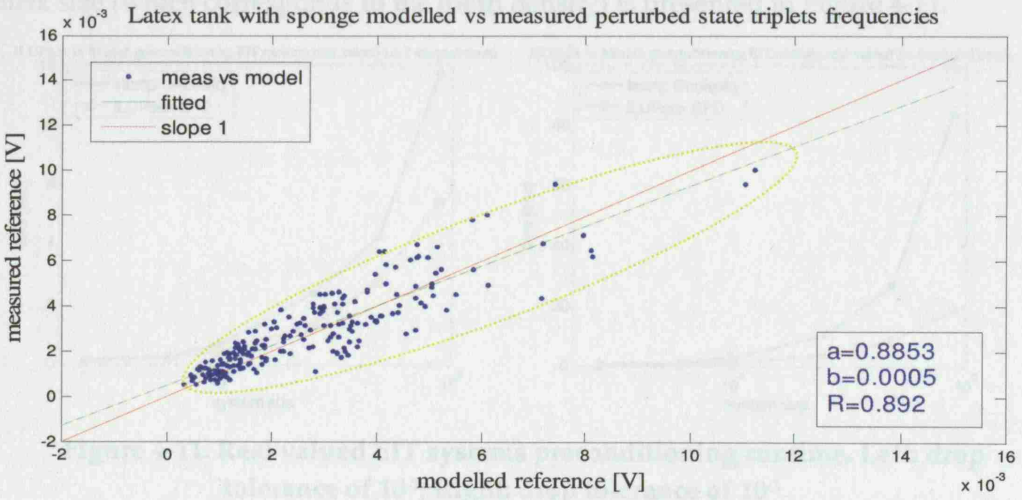

Figure 4-9. Measured vs. modelled boundary voltages for perturbed state for averaged frequencies triplets

Figure 4-10 presents the measured versus modelled boundary voltage change related to the insertion of the sponge perturbation.

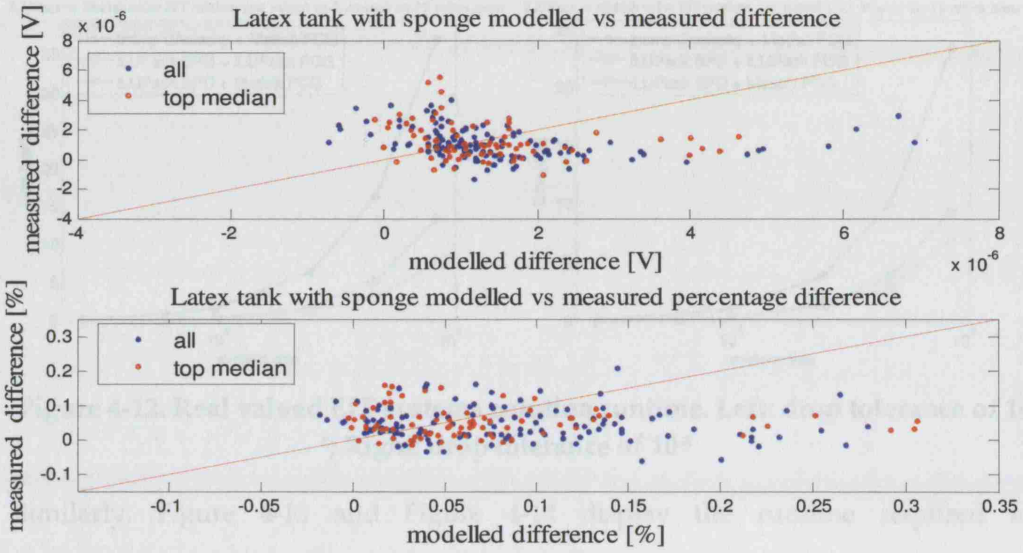

Figure 4-10. Measured vs. modelled boundary voltage changes for averaged frequency triplets. Upper graph: voltages; Lower: percentages

4.8.2 Multi-level inverse-based preconditioning

In the following, only the results for relative residual tolerance of 10^{-12} are presented. The runtime results for the higher relative residual error of 10^{-6} and 10^{-9} were qualitatively similar to these. Figures on the left represent the results with drop tolerance of 10^{-2} while those in the right are for 10^{-3}. The runtime required for construction of preconditioners for real valued matrices with respect to the system matrix size (which corresponds to the mesh density) is presented in Figure 4-11.

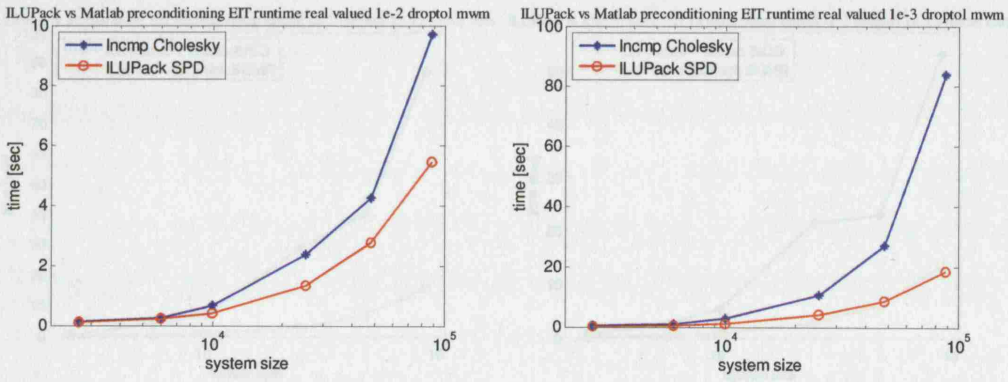

Figure 4-11. Real valued EIT systems preconditioning runtime. Left: drop tolerance of 10^{-2}; Right: drop tolerance of 10^{-3}

The runtime requirement for solving these systems with conventional preconditioning and with multi-level preconditioning is presented in Figure 4-12.

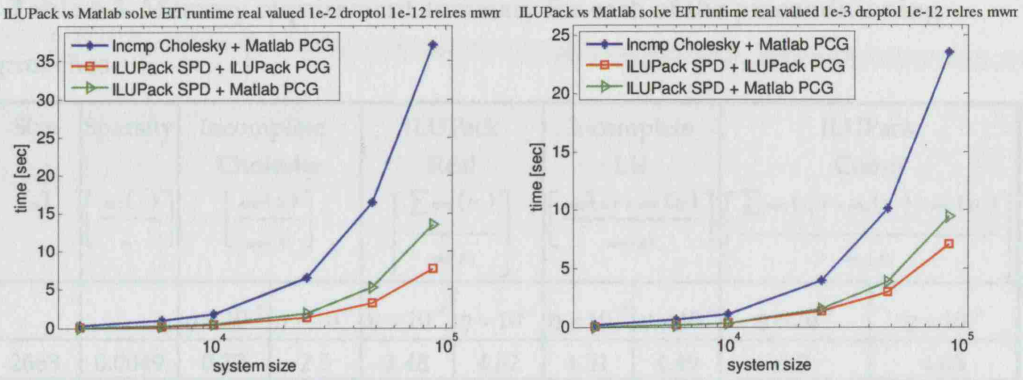

Figure 4-12. Real valued EIT systems solution runtime. Left: drop tolerance of 10^{-2}; Right: drop tolerance of 10^{-3}

Similarly, Figure 4-13 and Figure 4-14 display the runtime required for preconditioner construction and solution of complex valued problems.

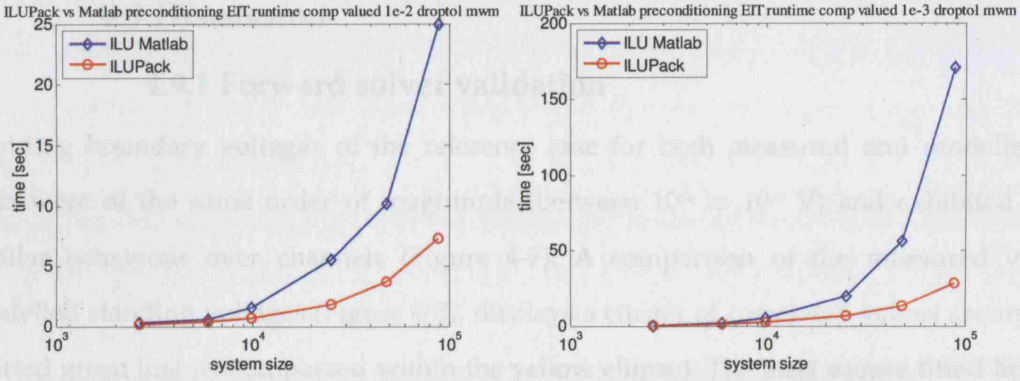

Figure 4-13. Complex valued EIT systems preconditioning runtime. Left: drop tolerance of 10^{-2}; Right: drop tolerance of 10^{-3}

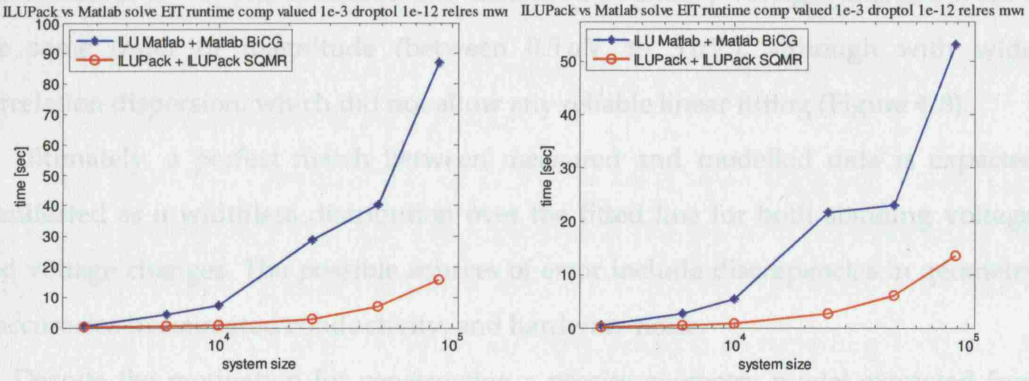

Figure 4-14. Complex valued EIT systems solution runtime. Left: drop tolerance of 10^{-2}; Right: drop tolerance of 10^{-3}

Table 4-3 represents the memory requirement for storage of each of the preconditioners.

Table 4-3. Memory requirement summary for each of the preconditioning approaches

Size [n]	Sparsity $\left[\frac{nnz(A)}{n^2}\right]$	Incomplete Cholesky $\left[\frac{nnz(U)}{nnz(A)}\right]$		ILUPack Real $\left[\frac{\sum nnz(U_i)}{nnz(A)}\right]$		Incomplete LU $\left[\frac{nnz(L)+nnz(U)}{nnz(A)}\right]$		ILUPack Comp $\left[\frac{\sum nnz(L_i)+nnz(U_i)-nnz(D_i)}{nnz(A)}\right]$	
		$\eta=10^{-2}$	$\eta=10^{-3}$	$\eta=10^{-2}$	$\eta=10^{-3}$	$\eta=10^{-2}$	$\eta=10^{-3}$	$\eta=10^{-2}$	$\eta=10^{-3}$
2668	0.0049	0.77	2.5	2.48	4.82	1.51	4.49	1.7	4.03
5970	0.0023	0.69	1.97	2.36	4.45	1.34	3.80	1.69	3.69
9955	0.0014	0.68	1.98	2.43	4.49	1.35	3.81	1.75	3.77
25200	0.0006	0.8	2.24	2.69	5.6	1.58	4.37	1.73	3.84
48425	0.0003	0.7	2.06	2.64	5.44	1.4	4.05	1.74	3.92
88523	0.0002	0.7	2.16	2.84	5.87	1.42	4.26	1.85	4.26

4.9 Discussion

4.9.1 Forward solver validation

Standing boundary voltages of the reference case for both measured and modelled data were of the same order of magnitude (between 10^{-4} to 10^{-3} V) and exhibited a similar behaviour over channels (Figure 4-7). A comparison of the measured vs. modelled standing voltages (Figure 4-8), displays a cluster of correlated values around a fitted green line (encompassed within the yellow ellipse). The least square fitted line (a = 0.8874, b = 0.0005, R = 0.892) deviates slightly from a perfect slope of a = 1 and correlation of R = 1. The modelled and measured boundary voltages changes were of the same order of magnitude (between $0.5\mu V$ to $3\mu V$), although with wider correlation dispersion, which did not allow any reliable linear fitting (Figure 4-8).

Ultimately, a perfect match between measured and modelled data is expected, manifested as a widthless distribution over the fitted line for both standing voltages and voltage changes. The possible sources of error include discrepancies in geometry, inaccuracies in estimated conductivity, and hardware noise.

Despite the motivation for constructing a precise geometry model extracted from the tank CT scan, discrepancies could rise due to several reasons: 1) Variability of the skull thickness - this skull has a small broken area near the nose region, which was

beyond the accuracy of the CT scan-based meshing. In addition the skull was modelled here as an isotropic and homogeneous layer, while an anisotropic three layered representation would have been more appropriate. 2) The skull orientation - the skull orientation inside the tank was not entirely fixed. Further assessment of this claim was substantiated later, as slight shifts and rotation of the skull gave rise to boundary voltage changes of the order of 10%. 3) Coarseness of the volume mesh - this factor affects especially the electrodes contact regions, as well as the modelled perturbation shape and location.

Gilad et al [230] managed to fit highly correlated linear curves of standing voltages (R = 0.98) and changes (R = 0.86), which resulted from a sponge perturbation in a spherical tank using the same modeller. Their tank did not include a skull, and was measured with acquisition system of higher SNR. This supportive evidence may suggest that some of the discrepancies are indeed due to the modelled skull geometry. Reassuring results were also acquired in human subjects, with data collected at 20 experimental blocks which was recorded from 7 subjects. The average slope was 1.1 ± 0.4 (R = 0.95). Whilst R was high there was a bias in the slope suggesting the conductivities in the model were not properly tuned. This result means that the model itself is accurate (as R was high) but is sensitive to the conductivity choice. Therefore, for realistic range in conductivity predictions this factor can be addressed to provide appropriate.

There is no overall agreement regarding the skull conductivity as discussed in Chapter 2, hence, selection of any other conductivity value for this region could provide different results. For an instance, setting the skull conductivity to be 0.023225 $^{S}/_{m}$, provides a perfect slope of a = 1. This value, like the value of 0.0189 $^{S}/_{m}$, lie within the range of values reported in the literature.

Law reported local variability of up to 15.7 times in skull resistivity between one region and another [82]. The skull was modelled in this study to have homogeneous conductivity. Therefore, even modelling the skull with variable conductivity should provide results that are more accurate. Another possible confounding factor is the inaccuracy in estimating the perturbation conductivity, since air bubbles can increase the measured boundary changes. However, had this effect been significant a steeper

slope would be achieved for the perturbed standing voltages, which was not the case at this study.

Hardware noise may also have contributed to this discrepancy; the acquisition system has been reported to have errors over load within channel of 0.9%, variation over frequency of ±1.5% and variation over electrode combinations of ±2% [228]. Contact impedance circuits included resistors with 1% error, and 20% capacitance error. One measure taken to assess this claim was averaging triplets of frequencies (Figure 4-9). The resulting slope and values dispersion were very similar to those achieved by considering only a single frequency. This result may suggest the following: either the effect of averaging is competing with the variance over frequencies, which then produced in similar results, or that the variability within each frequency over the channels is systematic and consistent, and therefore, frequency averaging does not provide any benefit there.

The differences between the measured and modelled standing voltages due to the inaccuracies mentioned above were of the order of 10%. Thus, one could not expect to match accurately the changes, which are smaller by more than two orders of magnitude than the standing voltages.

4.9.2 Multi-level Inverse-based preconditioning

4.9.2.1 Real valued problems

Factorisation

For the smaller models, the multi-level inverse-based factorisation runtime was comparable to the one achieved using incomplete Cholesky factorisation. However, as expected, benefits were apparent for the larger models, as, for the three larger models the former was about twice faster, and a larger speedup factor of up to 4.5 was achieved for the lower drop tolerance. This behaviour is expected, due to the overhead required for construction of a multi-level hierarchy, which for smaller models negates its benefit. Even so, the increasing speedup factor with the problem scale indicates the superiority of the multi-level approach in runtime complexity (Figure 4-11).

Solution runtime

PCG with inverse-based preconditioner was faster than PCG with incomplete Cholesky preconditioner by an increasing ratio of up to 4.8 and 3.3 for the higher and

lower drop tolerances respectively. A runtime comparison between Matlab's PCG implementation and the ILUPack's PCG implementation showed that the latter was faster by a factor of up to 1.8 and 1.3 for the higher and lower drop tolerances respectively. This step was performed to quantify the effect of implementation and software architecture over runtime, and therefore, assesses the effective efficiency of the algorithm in neutral conditions. A comparison of the inverse-based preconditioner versus the incomplete Cholesky using Matlab's PCG for both provided an effective speedup of about 2.7 and 2.5. (Figure 4-12)

Memory requirement

The memory requirement for the multi-level inverse-based preconditioner compared that required for construction of preconditioner based on incomplete Cholesky factorisation grew increasingly with the problem scale by a factor of 1.9 to 2.7 for the lower drop tolerance, and between 3.2 and 4 for the higher one. This comparison was based on the ratio of the relative non-zeros entries populations between the two preconditioners.

4.9.2.2 Complex valued problems

Factorisation

The construction of the multi-level inverse-based preconditioner was faster than that of the conventional incomplete LU factorisation with speedup factors of up to 3.4 and 6 for the higher and lower drop tolerances respectively. The speedup factor grew rapidly with the problem size, which demonstrates the ability of the multi-level preconditioner to handle problems of growing scales. (Figure 4-13)

Solution runtime

The fastest convergence was obtained with the SQMR solver with multi-level inverse-based preconditioning and Maximum Weight Matching. Its speed advantage over the stabilised BiCG with conventional incomplete LU based preconditioning increased with problem size. It provided a convergence runtime speedup of up to 12 and 7.6 for the higher and lower drop tolerance accordingly (Figure 4-14). GMRes preconditioned with incomplete LU failed to converge for the 2nd, 5th and 6th larger systems. Stabilised BiCG with complex-to-real splitting with implicit classical AMG preconditioner failed to converge for the 4th and 6th systems. A possible cause is the violation of the M-matrix

structure in the Complete Electrode Model. This claim was further substantiated by the fact that the same approach worked successfully for complex-valued Diffuse Optical Tomography systems which complied with the M-matrix definition requirements [234].

A direct runtime comparison with results obtained using the splitting transformation (4.4.6.4) of the classical AMG is difficult. At first glance, the runtime seems excessively larger than that obtained using the conventional or inverse-based alternatives. However, this approach requires only multi-level SPD system setup, which for these systems was up to 2 and 9 times faster than complex-valued multi-level preconditioning and incomplete LU factorisation respectively. Whenever this approach indeed converged, its overall runtime for a single RHS is still better than that of the conventional use of incomplete LU preconditioning. However, for multiple RHS, which is the common practice for most imaging problems, there will be a crossing point where the use of a conventional incomplete LU preconditioner will be more efficient.

An interesting point is the smoother convergence runtime with respect to the problem scale, offered by the inverse-based factorisation. This property can be attributed to the strict control over the factor growth with respect to the inverse error.

A runtime comparison between GMRes and SQMR solvers with Matlab implementation versus ILUPack implementation showed that the latter was faster by a factor of up to 1.5. This step was performed to quantify the effect of implementation and software architecture over runtime, and therefore, assessed that the effective speedup owed to inverse-based preconditioning in neutral conditions was about 8 and 5 for the higher and lower drop tolerance accordingly.

Memory requirement

For the higher drop tolerance, the inverse-based preconditioner memory requirement was lower than for incomplete LU preconditioner for all problem scales by up to 12%. However, for the lower drop tolerance, the former required more storage by up to 30% (Table 4-3). These results are somewhat surprising, as, typically, the memory requirements of multi-level techniques are expected to be consistently greater than those of a single level. Nevertheless, these results show that it is possible to construct a

multi-level preconditioner which is less populated than a single level one, as long as the entries which are affecting the inverse error are bounded properly.

4.10 Conclusions

4.10.1 Forward solver validation

The standing voltage of the measured and modelled voltages agreed within reasonable experimental error. The measured differences were of the same order of magnitude but the correlation between channels was weak.

On the modelling front, improved skull modelling along with finer mesh representation is desirable for future studies. The acquisition process should be able to provide reliable contact impedance estimation, which can then substitute precisely into the model. Instrumentation with a higher precision and smaller inter-channel and inter-frequency variability would also be desirable.

4.10.2 Multi-level Inverse-based preconditioning

A generic approach for reduction of the computational demand for processing large-scale forward problems was introduced by the facilitation of the novel inverse-based multi-level preconditioning approach. This approach was compared with several conventional strategies for preconditioning the large-scale sparse system matrices arising from forward modelling of medical applications.

Regarding the solvers compared in this study for complex valued systems, the SQMR solver provided smoother, faster and more stable convergence than the conventional stabilised BiCG or GMRes. Of the preconditioners studied, the inverse-based multi-level ILU preconditioner provided superior runtime both in terms of construction and solution convergence. Two factors affect this behaviour: the degree of ill-conditioning of the problem and the problem scale. The control over the prescribed bound for the norm of the inverse triangular factors can be derived from an estimate for the ill-conditioning of the system. Whenever the system is more ill-conditioned, this scheme provides greater speedup. Whilst for small-scale problems the benefits of this approach are not significant, at large-scales this preconditioning framework requires substantially lower runtimes than the leading conventional approaches.

A subject for future work would be evaluation of the inverse-based multi-level preconditioner performance in parallel architecture mode. This preconditioning

scheme can be utilised for other soft field methods, such as Magnetic Induction Tomography MIT, which would allow processing of problems of growing scale and complexity throughout the field.

5 LARGE SCALE INVERSE PROBLEMS

5.1 Introduction

One of the most challenging topics in EIT lies in solving the inverse admittivity problem. While the forward problem is well determined and rather straight forward to be treated, the inverse problem is both non-linear with respect to admittivity distribution and *ill-posed*. For a given mapping $J:\gamma \rightarrow V_\Gamma$, the system $J\gamma = V_\Gamma$ has been defined by Hadamard [279;280] to be well-posed provided: a) Existence - a solution γ exist. b) Uniqueness - the solution is unique. c) Stability - the solution has a continuous dependency in the observed data. i.e. an arbitrarily small perturbation of the data would represent a small perturbation in the solution. This implies that J^{-1} should be continuous. According to Hadamard's interpretation, problems which fail to comply with any of these criteria, cannot represent a real physical problem, and thus, are posed incorrectly, namely ill-posed. Whilst the first two criteria can be settled by considerate imposition of constraints, the third condition is the most problematic. One means of quantifying the severity of this implication is the condition number (ratio between the highest singular value and the lowest singular value) of the Jacobian matrix. This measure quantifies the spread of the Jacobian's singular values [281;282], which in practice, reflect the extent of the solution's instability with respect to small changes in the observation. Most EIT applications tend to have many more unknowns than observations, which also result in rank-deficiency of the Jacobian matrix.

Nowadays, a broad range of methods for solving ill-posed problems are available; most of them restore stability and uniqueness by imposition of a-priori information and filtration of high spatial frequency components through regularisation. By these means, the solution search space is constrained.

Up to now, EIT reconstruction methods (i.e. solving the inverse problem) were mainly unconstrained optimisation based, where a-priori information was incorporated by various regularisation techniques. This approach can be divided into two major streams: the first of which is stochastic in nature, hence based on probabilistic-statistical reasoning [283;284], the second is a deterministic approach, which can again be subdivided to linearised [27;38;285;286] and non-linear inversion methods [221;254;286-288].

In mathematical terminology, linearity of mapping accounts for two core aspects: 1) Output scales linearly with the input - the lack of scaling invariance in EIT exhibited by saturation of the forward solution. The spatial distribution of the ionic current flow is altered subject to an impedance perturbation. Therefore, a different number of ions flow through the perturbation, and consequently the response is not linear. For high admittivity contrast, linear reconstruction typically underestimates the true perturbation contrast. 2) Principle of superposition - complex perturbations, even with low admittivity contrast, can not be recovered fully with all the original admittivity distribution features by means of linear reconstruction.

5.1.1 Problem definition and formulation

The EIT inverse problem aims to recover the admittivity distribution γ_Ω inside the domain Ω from a given set of boundary voltages V_Γ and injected currents I_Γ at the boundary Γ. As the problem is severely ill-posed, in the framework of this thesis the solution γ is formulated in the context of a least-square minimum of a regularised functional $\mathbf{f}(\gamma)$

$$\gamma = \arg\min_{\gamma} \left\{ \overbrace{\left\| \xi \left(V_\Gamma - F_\Gamma(\gamma) \right) \right\|^2 + \tau \psi(\gamma, \eta)}^{\mathbf{f}(\gamma)} \right\} \tag{5.1}$$

where $F_\Gamma : \mathbb{C}^k \to \mathbb{C}^m$ is the forward model operator, which maps admittivity distribution γ into the data space, V_Γ stands for the given measured boundary voltages, $\xi \in \mathbb{R}^{m \times m}$ weighs the residual error term in the nominator $r(\gamma) = V_\Gamma - F_\Gamma(\gamma)$ according to the associated reliability of each of the measurements channels, τ is the regularisation hyper-parameter and $\psi(\gamma, \eta) : \mathbb{C}^k \to \mathbb{R}$ is a regularisation prior.

5.1.2 Motivation

In clinical applications, such as acute cerebral stroke or breast mammography large impedance contrasts between different tissues types occur, as well as complex and large impedance changes over frequency. These changes go well beyond the linear inverse approximation of this non-linear problem, and therefore require a non-linear reconstruction framework. For an approximately homogeneous medium, such as the breast, a compromise can be made as for the internal discretisation of the problem in the inverse solution stage, and therefore allow the use of dual/multi - grid

representation [254]. However, the head, which consists of thin and complex geometric structures of high impedance contrast, does not allow facilitation of such an approach without introducing severe degradation of the solution [268]. This stringent constraint regarding discretisation results in a requirement to solve large-scale non-linear inverse problems. This task is exceptionally computationally demanding and requires development of special methods to handle this challenge.

5.2 Purpose and Design

In this chapter, an overview of deterministic non-linear reconstruction methods is provided, together with the relevant topics of regularisation and globalisation (A summary of the linear inversion methods is presented in Appendix C). For coherence, these methods are presented from perspective of the EIT inverse conductivity problem, with special emphasis on scalability. Further, a novel non-linear inversion approach for large-scale problems is presented. This innovative approach, termed *Newton-Krylov inversion* combines the Krylov-subspace efficiency in production of an implicit Hessian inverse together with the effectiveness of Newton-type search direction. Furthermore, in this work suitable transformation strategies for the data and parameter space, which precondition the normal equations derived at each Newton step, are proposed. Newton-Krylov inversion was implemented in two non-linear schemes: Damped Gauss-Newton and Levenberg-Marquardt. The computational efficiency of these methods was assessed by comparison with four other non-linear inversion methods. This was accomplished for the problem of imaging of stroke in the adult human head, using two head models of increasing mesh-density. Comparisons of the minimised function value and solution error with respect to runtime, iteration count and memory consumption were performed.

This study was presented at the Applied Inverse Problems conference held in the Royal Agricultural College, UK 2005, and in the World Congress on Medical Physics and Biomedical Engineering in Seoul 2006.

5.3 Background

5.3.1 Non-linear inversion methods

5.3.1.1 Steepest Descent

The *Steepest-Descent* method is probably the most straightforward method in optimisation. For a multi-variant function $\mathbf{f}(\gamma_t):\mathbb{R}^n \to \mathbb{R}$, the gradient direction $\nabla\mathbf{f}(\gamma_t)$ is the direction in which the minimised function $\mathbf{f}(\gamma_t)$ increases most rapidly; therefore, advancing in the opposite direction is intuitively a promising direction for function minimisation. Since the gradient represents only local properties of the minimised function, this procedure is performed iteratively with some step size between one iteration and another. The solution update can be expressed as follows

$$\gamma_{t+1} = \gamma_t - \alpha_t \nabla\mathbf{f}(\gamma_t) \tag{5.2}$$

where α_t is the step size which can either be predefined by some constant or alternatively obtained by a 1D search (line search)

$$\alpha_t = \arg\min \quad \mathbf{f}(\gamma_t - \alpha_t \nabla\mathbf{f}(\gamma_t)). \tag{5.3}$$

A detailed discussion regarding line search strategies is given in section 5.3.2. This approach only requires the calculation of the gradient at each iteration. Yet, since only first order derivative information is used, this method frequently converges exceptionally slow. Conversely, steepest descent is very easy to implement and relatively robust.

5.3.1.2 Newton-type methods

Originally, Newton-type methods were developed for one dimensional solution of the roots of non-linear functions $f(x), f:\mathbb{R}\to\mathbb{R}$. Nowadays, these methods are among the most popular multi-variant minimisation techniques.

For a fair approximation of the function at the initial guess x_0, one could find a closer approximation x_1, by taking the point where the tangent to the function at x_0 crosses the x axis. The tangent is taken usually as a linearisation of the function at x_0. This process is repeated up to the desired accuracy level. In such case, the solution update can be expressed as follows

$$\begin{gathered} f'(x_t)(x_{t+1} - x_t) + f(x_t) = f(x_{t+1}) \approx 0 \\ \Downarrow \\ x_{t+1} = x_t - (f'(x_t))^{-1} f(x_t) \end{gathered} \tag{5.4}$$

Since the aim is function minimisation rather than root finding, roots of the derivative of the original function need to be taken, rather than roots of the function itself. Let us consider a multi-variant function of approximately a quadratic form $\mathbf{f}:\mathbb{R}^n \to \mathbb{R}$

$$\mathbf{f}(\mathbf{x}) \approx \mathbf{x}^T A\mathbf{x} + b^T\mathbf{x} + c \quad A \in \mathbb{R}^{n\times n}, b \in \mathbb{R}^n, \mathbf{x} = \{x_1, x_2, ..., x_n\} \in \mathbb{R}^n. \tag{5.5}$$

If the first and second derivatives are available, the Taylor expansion can be formed up to the second derivative term

$$\mathbf{f}(\mathbf{x}_t + \mathbf{p}_t) \approx \mathbf{f}(\mathbf{x}_t) + \nabla\mathbf{f}(\mathbf{x}_t)^T \mathbf{p}_t + \frac{1}{2}\mathbf{p}_t^T D^2(\mathbf{x}_t)\mathbf{p}_t \tag{5.6}$$

where

$$\nabla\mathbf{f}(\mathbf{x}_t)^T = \left[\frac{\partial\mathbf{f}(\mathbf{x}_t)}{\partial q_1}, \frac{\partial\mathbf{f}(\mathbf{x}_t)}{\partial q_2}, ..., \frac{\partial\mathbf{f}(\mathbf{x}_t)}{\partial q_n}\right] \tag{5.7}$$

$$D^2\mathbf{f}(\mathbf{x}_t)_{ij} = \left(\nabla\left(\nabla\mathbf{f}(\mathbf{x}_t)\right)^T\right)_{ij} = \left[\frac{\partial^2\mathbf{f}(\mathbf{x}_t)}{\partial q_i \partial q_j}\right] \tag{5.8}$$

$$\frac{\partial^2\mathbf{f}(\mathbf{x}_t)}{\partial q_i \partial q_j} = \frac{\partial^2\mathbf{f}(\mathbf{x}_t)}{\partial q_j \partial q_i} \tag{5.9}$$

and q_i are the coordinates of $\mathbf{x}$ variables. In order to find $\mathbf{p}_t$ that minimises the function, the expansion term is derived with respect to $\mathbf{p}_t$ and equalised to zero

$$\begin{aligned} &\nabla_{\mathbf{p}_t}\mathbf{f}(\mathbf{x}_t + \mathbf{p}_t) = \nabla\mathbf{f}(\mathbf{x}_t) + \frac{1}{2}\left(D^2\mathbf{f}(\mathbf{x}_t)^T + D^2\mathbf{f}(\mathbf{x}_t)\right)\mathbf{p}_t = \\ &= \nabla\mathbf{f}(\mathbf{x}_t) + D^2\mathbf{f}(\mathbf{x}_t)\mathbf{p}_t = 0 \\ &\qquad\qquad \Downarrow \\ &\nabla\mathbf{f}(\mathbf{x}_t) = -D^2\mathbf{f}(\mathbf{x}_t)\mathbf{p}_t \end{aligned} \tag{5.10}$$

which leads to the desired search direction $\mathbf{p}_t$

$$\mathbf{p}_t = -\left(D^2\mathbf{f}(\mathbf{x}_t)\right)^{-1}\nabla\mathbf{f}(\mathbf{x}_t). \tag{5.11}$$

$\mathbf{p}_t$ is commonly known as Newton direction. In general, Newton methods are formulated as follows

$$\mathbf{x}_{t+1} = \mathbf{x}_t - \alpha_t\mathbf{p}_t = \mathbf{x}_t - \alpha_t\left(D^2\mathbf{f}(\mathbf{x}_t)\right)^{-1}\nabla\mathbf{f}(\mathbf{x}_t). \tag{5.12}$$

Whenever the second derivative (the Hessian) is positive definite, i.e. for any $\mathbf{x}$, $\mathbf{x}^T D^2\mathbf{f}(\mathbf{x})\mathbf{x} > 0$, a unique minimum of (5.6) can be reached within a single step for any initial guess. In cases where the Hessian is positive definite and Lipschitz continuous in the approximation neighbourhood [11], Newton type methods offers quadratic convergence of the minimised function, as long as the initial guess is sufficiently close

[11] i.e. there exist a constant $B \geq 0$ for which $\left|D^2\mathbf{f}(\mathbf{x}_{\_}) - D^2\mathbf{f}(\mathbf{x}_{\_} + h)\right| \leq B|h|$

to the minimum. For Hessians that are not positive definite, the quadratic approximation does not hold. The curvature information encompassed in the Hessian, determine the effectiveness of Newton type methods.

The main advantages of Newton-type methods is their simplicity and prompt convergence. On the other hand, they all require smoothness of the first and the second derivative of the minimised function, which makes them intrinsically less general. The derivation and inversion of the Hessian is computationally demanding; therefore, its use in its conventional form is limited to small problems.

5.3.1.3 Newton-Raphson

The objective functional defined in (5.1) can be rewritten as follows

$$\mathbf{f}(\gamma) = \underbrace{\left\|\mathbf{r}_\xi\right\|^2}_{\mathbf{f}_1} + \underbrace{\tau\psi(\gamma,\eta)}_{\mathbf{f}_2} \tag{5.13}$$

where the weighted residual error term is given by

$$\mathbf{r}_\xi := \xi\left(V_\Gamma - F_\Gamma(\gamma)\right). \tag{5.14}$$

The gradient of this functional would then be

$$\mathbf{g}_1(\gamma) = \nabla\mathbf{f}_1(\gamma) = \frac{1}{2}\nabla\left(\mathbf{r}_\xi(\gamma)^T\mathbf{r}_\xi(\gamma)\right) = \frac{1}{2}\left(\nabla\left(\mathbf{r}_\xi(\gamma)^T\right)\mathbf{r}_\xi(\gamma) + \nabla\left(\mathbf{r}_\xi(\gamma)\right)\mathbf{r}_\xi(\gamma)^T\right)$$

$$= \nabla\left(\mathbf{r}_\xi(\gamma)^T\right)\mathbf{r}_\xi(\gamma) = \left[\frac{\partial\mathbf{r}_\xi(\gamma)_i}{\partial\gamma_j}\right]_{\substack{i=1..m\\ j=1..k}}\mathbf{r}_\xi(\gamma) = \left(J(\gamma)\right)^T\mathbf{r}_\xi(\gamma) \tag{5.15}$$

$$\mathbf{g}_2(\gamma) = \tau\nabla\psi(\gamma) \tag{5.16}$$

$$\mathbf{g}(\gamma) = \mathbf{g}_1(\gamma) + \mathbf{g}_2(\gamma) = \left(J(\gamma)\right)^T\mathbf{r}_\xi(\gamma) + \tau\nabla\psi(\gamma) \tag{5.17}$$

where $J(\gamma)\in\mathbb{R}^{m\times n}$ is the Jacobian matrix for $\mathbf{r}_\xi$. Similarly an expression for the Hessian can be derived

$$H_1(\gamma) = D^2\mathbf{f}_1(\gamma) = \nabla\left(\nabla\mathbf{f}_1(\gamma)\right)^T = \nabla\left(\left(J(\gamma)\right)^T\mathbf{r}_\xi(\gamma)\right)^T =$$

$$= \nabla\left(\mathbf{r}_\xi(\gamma)^T\left(J(\gamma)\right)\right) = \nabla\left(\mathbf{r}_\xi(\gamma)^T\right)\left(J(\gamma)\right) + \mathbf{r}_\xi(\gamma)^T\nabla\left(J(\gamma)\right) = \tag{5.18}$$

$$= \left(J(\gamma)\right)^T\left(J(\gamma)\right) + \sum_{i=1}^{m}\mathbf{r}_\xi(\gamma)_i D^2\mathbf{r}_\xi(\gamma)_i$$

$$H_2(\gamma) = \tau D^2\psi(\gamma) \tag{5.19}$$

$$H(\gamma) = H_1(\gamma) + H_2(\gamma) = \left(J(\gamma)\right)^T\left(J(\gamma)\right) + \sum_{i=1}^{m}\mathbf{r}_\xi(\gamma)_i D^2\mathbf{r}_\xi(\gamma)_i + \tau D^2\psi(\gamma) \tag{5.20}$$

By substituting the expressions for the Hessian (5.20) and gradient (5.17) into Newton method's general expression (5.12), Newton-Raphson relation is obtained

$$\gamma_{t+1} = \gamma_t - \alpha_t \left(\left(J(\gamma_t)\right)^T \left(J(\gamma_t)\right) + \sum_{i=1}^{m} \mathbf{r}_\xi(\gamma_t)_i \, D^2 \mathbf{r}_\xi(\gamma_t)_i + \tau D^2 \psi(\gamma_t) \right)^{-1} \left[\left(J(\gamma_t)\right)^T \mathbf{r}_\xi(\gamma_t) \tau \nabla \psi(\gamma_t) \right] \tag{5.21}$$

5.3.1.4 Damped Gauss-Newton

Hessian derivation is both time and memory consuming; to avoid this pitfall; one can employ an approximation for the Hessian instead. One of the simplest and intuitive ways is to assume that the weighted residual error term $\mathbf{r}_\xi(\gamma)$ is very small, and therefore, neglect the second term in the RHS of the Hessian (5.18)

$$\sum_{i=1}^{m} \mathbf{r}_\xi(\gamma)_i \, D^2 \mathbf{r}_\xi(\gamma)_i \approx 0 \tag{5.22}$$

and obtain

$$D^2 \mathbf{f}(\gamma) \approx \left(J(\gamma)\right)^T \left(J(\gamma)\right) + \tau D^2 \psi(\gamma) \tag{5.23}$$

which by substitution into Newton method's update term (5.12) provides the Damped Gauss-Newton method

$$\gamma_{t+1} = \gamma_t + \alpha_t \left(\left(J(\gamma)\right)^T \left(J(\gamma)\right) + \tau D^2 \psi(\gamma) \right)^{-1} \left[\left(J(\gamma)\right)^T \mathbf{r}_\xi(\gamma) + \tau \nabla \psi(\gamma) \right]. \tag{5.24}$$

The non-damped version, takes a full Gauss-Newton step, rather than performing a line search procedure. This variant spares significant computational effort at the price of loss of robustness: the solution would then be limited to admittivity guesses sited in the close vicinity of the desired solution. This drawback may be limiting, as physiological variability occasionally precludes a sufficiently accurate initial admittivity guess. Furthermore, clinical data is contaminated with physiological and measurement noise, which effectively increases the weighted residual error, and consequently, undermines the justification for neglecting its high orders. Apart from these considerations, an inversion of the immense dense Hessian's approximation matrix (number of elements by number of elements) is still required. For realistic 3D problems, this procedure is computationally expensive.

5.3.1.5 Levenberg-Marquardt

For most EIT models, the Jacobian is ill-conditioned; hence, its singular values decay rapidly [289]. Since the condition number of $J(\gamma)^T J(\gamma)$ is the square of that of $J(\gamma)$, the Hessian's system is highly ill-conditioned. Therefore, in the process of construction

of new search directions, small observations errors would be manifested as large errors in the parameter space. The Gauss-Newton method is especially sensitive in this sense.

An elegant way to overcome this difficulty is by replacing the line search strategy, with a *trust region* strategy. In this way, a convenient approximation for the Hessian is employed by replacement of the problem with a modified one, which still provides a good approximation for the real solution, and yet is more stable and less sensitive. The trust region approach accepts a quadratic model minimum only in case the model reflects adequately the behaviour of the original function. The rationale of this approach is somewhat complementary to the line search approach; only that here, a finite region of diameter Δ around the current solution γ_t is defined, for which the quadratic model assumed to represent adequately the minimised function. Thus, effectively, step size and search direction are correlated variables, which are obtained simultaneously. In case the step is unacceptable, the region size is reduced, and a new step parameter is produced.

The quadratic model for trust region minimisation is similar to the one defined in (5.6)

$$\mathbf{f}(\mathbf{x}_t+\mathbf{p}_t)\simeq\mathbf{f}(\mathbf{x}_t)+\nabla\mathbf{f}(\mathbf{x}_t)^T\mathbf{p}_t+\frac{1}{2}\mathbf{p}_t^T H(\mathbf{x}_t)\mathbf{p}_t \tag{5.25}$$

where H is some approximation of the Hessian. The required step $\mathbf{p}_t=\mathbf{x}_{t+1}-\mathbf{x}_t$ is then obtained by solving the following sub-problem

$$\min_{\mathbf{p}\in\mathbb{R}^k}\{\mathbf{f}(\mathbf{x}_t+\mathbf{p}_t)\} \tag{5.26}$$

where the search direction $\|\mathbf{p}_t\|\le\Delta$, and Δ is a scalar. In case there is a scalar $\lambda\ge 0$ for which the following conditions are satisfied

$$\begin{aligned}&(H+\lambda I)\mathbf{p}^*+\nabla\mathbf{f}(\mathbf{x}_t)^T=0\\&\lambda\left(\Delta-\|\mathbf{p}^*\|\right)=0\\&\mathbf{x}^T(H+\lambda I)\mathbf{x}\ge 0\qquad\forall\mathbf{x}\in\mathbb{R}^k\end{aligned} \tag{5.27}$$

$\mathbf{p}^*$ is the trust region global minimum [290]. The non-linear least squares problem can then be formulated as follows

$$\min_{\mathbf{p}\in\mathbb{R}^k}\left\{\frac{1}{2}\left\|\tilde{J}\mathbf{p}-\tilde{\mathbf{r}}_\xi\right\|^2+\tau\psi(\mathbf{p})\right\} \tag{5.28}$$

where

$$\tilde{J}=\begin{bmatrix}J(\gamma_0)\\\sqrt{\lambda}I\end{bmatrix} \tag{5.29}$$

$$\tilde{\mathbf{r}}_w = -\begin{bmatrix} \mathbf{r}_w(\gamma_0) \\ 0 \end{bmatrix}. \tag{5.30}$$

Extraction of (5.28) yields

$$\frac{1}{2}\left\|\tilde{J}\mathbf{p} - \tilde{\mathbf{r}}_w\right\|^2 + \tau\psi(\mathbf{p}) = \frac{1}{2}\mathbf{p}^T\tilde{J}^T\tilde{J}\mathbf{p} - \tilde{\mathbf{r}}_w^T\tilde{J}\mathbf{p} + \frac{1}{2}\tilde{\mathbf{r}}_w^T\tilde{\mathbf{r}}_w + \tau\psi(\mathbf{p}) \tag{5.31}$$

where $\tilde{J}^T\tilde{J}$ corresponds to the matrix H, and $\tilde{\mathbf{r}}_\xi^T\tilde{J}$ to relation (5.26). Therefore, the trust region least squares step is given by

$$\begin{aligned} \mathbf{p}_{LS} &= -\left(\tilde{J}^T\tilde{J} + \tau D^2\psi\right)^{-1}\left[\tilde{J}^T\tilde{\mathbf{r}}_\xi + \tau\nabla\psi\right] = \\ &= \left(J(\gamma_0)^T J(\gamma_0) + \lambda I + \tau D^2\psi(\gamma_0)\right)^{-1}\left[J(\gamma_0)^T\mathbf{r}_\xi(\gamma_0) + \tau\nabla\psi(\gamma_0)\right] \end{aligned} \tag{5.32}$$

The addition of the term λI makes the denominator of (5.32) to be positive definite, and accordingly its eigenvalues to be positive for all $\lambda > 0$. This effectively grants uniqueness of a minimiser search direction $\mathbf{p}_{LS}$ even when J is rank deficient. By plugging this search direction into Newton's general step scheme (5.12), the *Levenberg-Marquardt* [291;292] method is obtained

$$\gamma_{t+1} = \gamma_t - \left(J(\gamma_t)^T J(\gamma_t) + \lambda_t I_{n\times n} + \tau D^2\psi(\gamma_t)\right)^{-1}\left[J(\gamma_t)^T\mathbf{r}_\xi(\gamma_t) + \tau\nabla\psi(\gamma_t)\right] \tag{5.33}$$

Basically, Levenberg-Marquardt is a hybrid method which combines the robustness of steepest descent together with Gauss-Newton's fast convergence. λ_t can be interpreted as a steering factor between the two: when $\lambda_t \to 0$ the method reduces back to the Gauss-Newton step, whereas choosing $\lambda_t \to \infty$ approaches the steepest descent direction. It is clear, that selection of a suitable value for λ_t is essential in order to achieve rapidly a robust solution. A variety of techniques address this issue. The general idea is to start with a large value for the first iterations, so the method manifests the robustness of steepest descent, so that the initial guess can be chosen with less caution. Further on, at each iteration, if the value of the minimised functional decreased sufficiently [12] λ_t is divided, which effectively speed up the convergence, otherwise, λ_t value is increased to expand the search area (trusted region).

Levenberg-Marquardt is not optimal, and yet considered very popular, mainly since it works exceptionally well in practice. In a similar manner as for the all other Newton-type methods, the down side of this approach is the requirement for formation and inversion of the Hessian matrix. The cost of the update becomes

[12] Commonly the Armijo term (described in length in 5.3.2.2), or equivalent, serves as a measure for sufficient decrease of the minimised function

prohibitive whenever the model size increases to a few thousand parameters and beyond, thus its use is limited to moderately sized models.

An underdetermined form of Levenberg-Marquardt method can be used in order to handle the scalability problem better. Based on the matrix inversion lemma [282]

$$A = BCD + E \Rightarrow A^{-1} = E^{-1} + E^{-1}B\left(C^{-1} + DE^{-1}B\right)^{-1} DE^{-1} \tag{5.34}$$

where C, E are positive definite. Relation (5.33) without a regularisation term can be reformulated as follows

$$\gamma_{t+1} = \gamma_t + \alpha_t J(\gamma_t)^T \left(J(\gamma_t)J(\gamma_t)^T + \lambda_t I_{m\times m}\right)^{-1} \mathbf{r}_\xi(\gamma_t) \tag{5.35}$$

This approach requires $m \times m$ matrix inversion rather than the conventional $k \times k$ inversion. Since dense matrix inversion through *Gauss elimination* is a computationally expensive operation of the order of $O\left(k^3\right)$, for large-scale problems where $k \gg m$, this variant is considerably more efficient than its conventional counterpart. On the other hand, for ill-posed problems the lack of the spatial regularisation term embedded within the update step, requires the employment of some additional spatial filtering procedure.

5.3.1.6 Quasi-Newton (Variable–Metric)

One way to circumvent the computationally demanding necessity for explicit formation and inversion of the Hessian matrix is to approximate the Hessian inverse directly. This idea is the underlying principle of the *Quasi-Newton* methods. Two popular variants of this approach are the *Davidson-Fletcher-Powell* (DFP) procedure and the *Broyden-Fletcher-Goldfarb-Shanno* (BFGS) variant [293]. These schemes mainly differ by the way they treat roundoff error and convergence tolerances.

As before, the function $\mathbf{f}(\gamma)$ is assumed to be approximated locally to a quadratic form

$$\mathbf{f}(\gamma) \approx \frac{1}{2}\gamma^T H\gamma - \mathbf{b}^T\gamma + \mathbf{c}. \tag{5.36}$$

Newton's method general search direction was brought by (5.11) as

$$\mathbf{p} = -H^{-1}\nabla\mathbf{f}(\gamma_t). \tag{5.37}$$

The motivation in this case is to iteratively construct a good approximation for the inverse Hessian matrix H^{-1}. Such approximation can be constructed from a sequence of matrices $\tilde{H}_t$ with the property

$$\lim_{t\to\infty} \tilde{H}_t = H^{-1} \tag{5.38}$$

which hopefully for some finite $t \geq t_0$ holds

$$\tilde{H}_t = H^{-1}. \tag{5.39}$$

This algorithm is termed 'Quasi'-Newton since instead of the actual Hessian matrix of $\mathbf{f}$, a current approximation of it is used. Counter-intuitively, this method often yield search directions which are even better than those obtained using the true Hessian. This rather paradoxal result can be explained by considering the descent directions of $\mathbf{f}$ at γ_t. These are the directions $\mathbf{p}$ along which $\mathbf{f}$ decreases

$$\nabla\mathbf{f}(\gamma_t)\mathbf{p} < 0. \tag{5.40}$$

Newton search directions (5.37) are in descent direction when H is positive definite

$$\nabla\mathbf{f}(\gamma_t)\mathbf{p} = \nabla\mathbf{f}(\gamma_t)(\gamma-\gamma_t) = -(\gamma-\gamma_t)H(\gamma-\gamma_t). \tag{5.41}$$

For realistic problems, there are no guarantees that the Hessian is positive definite away from a minimum. In these cases, the actual Newton step with the precise Hessian can inevitably lead to parameter values for which the objective function is increasing in value. Hence, the general idea of the quasi-Newton methods is to start with a positive definite, symmetric approximation to H (usually simply taken as a unit matrix), and then build up approximations $\tilde{H}_t$'s for its inverse, which maintain the Hessian positive definite and symmetric. Far from the minimum, this property guarantees progression in a downhill direction. Closer to the minimum, the update formula approaches the true Hessian, which manifests the prompt convergence of Newton-type methods.

By subtraction of two consequent search directions: $\gamma-\gamma_{t+1} = -H^{-1}\nabla\mathbf{f}(\gamma_{t+1})$ from $\gamma-\gamma_t = -H^{-1}\nabla\mathbf{f}(\gamma_t)$ one has

$$\gamma_{t+1}-\gamma_t = H^{-1}\left(\nabla\mathbf{f}(\gamma_{t+1})-\nabla\mathbf{f}(\gamma_t)\right) \tag{5.42}$$

The new approximation $\tilde{H}_{t+1}$ is required to satisfies this relation as if it was actually H^{-1}

$$\gamma_{t+1}-\gamma_t = \tilde{H}_{t+1}\left(\nabla\mathbf{f}(\gamma_{t+1})-\nabla\mathbf{f}(\gamma_t)\right) \tag{5.43}$$

In order to generate the approximated Hessian inverse, the BFGS recursion formula, whose derivation goes beyond the scope of this work, is considered

$$\tilde{H}_{t+1} = \tilde{H}_t + \frac{(\gamma_{t+1}-\gamma_i)\otimes(\gamma_{t+1}-\gamma_t)}{(\gamma_{t+1}-\gamma_t)\left(\nabla\mathbf{f}(\gamma_{t+1})-\nabla\mathbf{f}(\gamma_t)\right)} - \frac{\left[\tilde{H}_t\left(\nabla\mathbf{f}(\gamma_{t+1})-\nabla\mathbf{f}(\gamma_t)\right)\right]\otimes\left[\tilde{H}_t\left(\nabla\mathbf{f}(\gamma_{t+1})-\nabla\mathbf{f}(\gamma_t)\right)\right]}{\left(\nabla\mathbf{f}(\gamma_{t+1})-\nabla\mathbf{f}(\gamma_t)\right)\tilde{H}_t\left(\nabla\mathbf{f}(\gamma_{t+1})-\nabla\mathbf{f}(\gamma_t)\right)} + \ldots$$
$$\ldots + \left[\left(\nabla\mathbf{f}(\gamma_{t+1})-\nabla\mathbf{f}(\gamma_t)\right)\tilde{H}_t\left(\nabla\mathbf{f}(\gamma_{t+1})-\nabla\mathbf{f}(\gamma_t)\right)\right]u\otimes u$$

where

$$u \equiv \frac{(\gamma_{t+1} - \gamma_t)}{(\gamma_{t+1} - \gamma_t)(\nabla \mathbf{f}(\gamma_{t+1}) - \nabla \mathbf{f}(\gamma_t))} - \frac{\tilde{H}_t(\nabla \mathbf{f}(\gamma_{t+1}) - \nabla \mathbf{f}(\gamma_t))}{(\nabla \mathbf{f}(\gamma_{t+1}) - \nabla \mathbf{f}(\gamma_t))\tilde{H}_t(\nabla \mathbf{f}(\gamma_{t+1}) - \nabla \mathbf{f}(\gamma_t))}$$

and $\otimes$ denotes the outer product of two vectors, a matrix

$$[u \otimes v]_{ij} = u_i v_j \tag{5.44}$$

The general framework of the BFGS variant of this method is described by the following algorithm

$t \leftarrow 0$
$\gamma_0 \leftarrow$ initial guess for γ
while (halting condition not fulfilled) begin quasi-Newton iterations
  $\mathbf{g}_t \leftarrow \nabla \mathbf{f}(\gamma_t)$ compute gradient
  $H_t^{-1}(\gamma_t) \leftarrow$ SPD approximation for the Hessian's inverse
  $\mathbf{p}_t \leftarrow -H_t^{-1}(\gamma_t)\mathbf{g}_t$ compute quasi-Newton step
  $\alpha_t \leftarrow \arg\min_{\alpha_t > 0} \mathbf{f}(\gamma_t + \alpha_t p_t)$ line search
  $\gamma_{t+1} \leftarrow \gamma_t + \alpha_t \mathbf{p}_t$ update approximate solution
  $t \leftarrow t + 1$
end

Algorithm 5-1. Quasi-Newton algorithm formulated for EIT inverse problem

Under mild assumptions, this variant provides a super-linear local convergence rate. The major disadvantage of this method, in its original form, is related to the way accumulated information is stored and updated. Fortunately, a memory-limited version (L-BFGS) of this variant, which only requires the storage of limited number of solution and gradient step vectors is available [294].

5.3.1.7 Krylov subspace inversion

Another effective way to avoid formation of the Hessian and its inverse, which is particularly memory efficient, is the non-linear variant of the Conjugated Gradients (NLCG) algorithm. Since each of the search directions $\mathbf{p}_t$ is conjugated (A-orthogonal) to all its precedents $\{\mathbf{p}_0, \mathbf{p}_1, ..., \mathbf{p}_{t-1}\}$, and yet requires only the previous search direction $\mathbf{p}_{t-1}$ and a gradient to be constructed, Conjugate Gradients requires intermediate storage of the order of k. For that reason this method is especially attractive for large-scale problems. Unlike Newton-type methods which require both 1st and 2nd order derivatives, non-linear Conjugated Gradients employs only the first derivative information.

The non-linear variant of conjugated gradient differs from the linear variant by three features [248]: 1) Residual - $\mathbf{r}$ can no longer be calculated recursively. 2) Step size α - can not be determined exactly anymore. 3) Direction parameter β - there are several options for choosing the direction parameter β. The first matter can be handled by derivation of the residual from the gradient of non-linear functional. As for the step size, incorporation of an inexact line search is required (as described later in 5.3.2). Among the different ways of determining β, the most common variants are called *Fletcher-Reeves* and *Polak-Ribière*. For the Fletcher-Reeves [295] variant the residuals are replaced by the gradients

$$\beta_{t+1}^{FR} = \frac{\nabla \mathbf{f}(\gamma_{t+1})^T \nabla \mathbf{f}(\gamma_{t+1})}{\nabla \mathbf{f}(\gamma_t)^T \nabla \mathbf{f}(\gamma_t)}. \tag{5.45}$$

Polak and Ribière suggested later two minor but significant changes. The first of which was

$$\tilde{\beta}_{t+1}^{PR} = \frac{\nabla \mathbf{f}(\gamma_{t+1})^T (\nabla \mathbf{f}(\gamma_{t+1}) - \nabla \mathbf{f}(\gamma_t))}{\nabla \mathbf{f}(\gamma_t)^T \nabla \mathbf{f}(\gamma_t)} \tag{5.46}$$

which for the exact quadratic form functional, is equivalent to the Fletcher-Reeves (5.45) variant. For all other cases, whenever the angle between the new gradient $\nabla \mathbf{f}(\gamma_{t+1})$ and the old one $\nabla \mathbf{f}(\gamma_t)$ is smaller than 90°, the new Polak-Ribière search direction will be closer to the steepest descent direction than the Fletcher-Reeves one, and whenever the angle is greater than 90°, the new Polak-Ribière search direction will be closer to the previous search direction than to the Fletcher-Reeves search direction.

The second adjustment ensures generation of descent search directions. For $\beta_{t+1}^{PR} < 0$, the new search direction could be non-descent; hence, restarting the procedure anew would be the strategy in such cases

$$\beta_{t+1}^{PR} = \max\left\{\tilde{\beta}_{t+1}^{PR}, 0\right\} \tag{5.47}$$

There are many other variants for choosing β, however, numerical trials have shown [247;296] that Polak-Ribière is the most robust and efficient variant. The obtained algorithm is given below

$$\textbf{while } \left\|\nabla \mathbf{f}(\gamma_{t+1})\right\| \geq \varepsilon$$

$$\begin{cases} \beta_{t+1}^{PR} = \max\left\{ \dfrac{\nabla \mathbf{f}(\gamma_{t+1})^T \left(\nabla \mathbf{f}(\gamma_{t+1}) - \nabla \mathbf{f}(\gamma_t)\right)}{\nabla \mathbf{f}(\gamma_t)^T \nabla \mathbf{f}(\gamma_t)}, 0 \right\} \\ \mathbf{p}_{t+1} = -\nabla \mathbf{f}(\gamma_{t+1}) + \beta_{t+1}^{PR} \mathbf{p}_t \\ \alpha_{t+1} \leftarrow \textit{line search} \\ \gamma_{t+1} = \gamma_t + \alpha_{t+1} \mathbf{p}_{t+1} \end{cases}$$

Algorithm 5-2. Non-linear Conjugated Gradients algorithm formulated for the EIT inverse problem

This method was considered up to recently to be the most effective approach for large-scale problems [221;223;249;297]. While the computational effort required for generation of a new search direction is merely vector multiplication, a comparison of its convergence rate per iteration with typical Newton-type methods (whenever that was possible), showed that this method manifests excessively slow convergence [220;249;298;299]. The memory requirement for NLCG can be reduced even further, by employing a Jacobian-free Adjoint Fields Method (AFM). This formulation requires the solutions for a single forward problem and a single adjoint forward problem at a time. Instead of solving for all the current patterns altogether, the Adjoint Fields method allows non-linear inverse computation for one or more current patterns at a time. This approach has been implemented successfully for Optical Tomography [267;275] and later for EIT [249;300].

5.3.1.8 Direct non-linear inversion

Another way to address the great computational demand associated with non-linear image reconstruction is through direct, rather than iterative, non-linear inversion. Muller et al [286] developed a revolutionary direct inversion method based on an inverse-scattering transform. This method, namely the d-bar method, consist of two steps: the first step takes Dirichlet to Neumann map Λ_γ to an intermediate scattering transform complex-valued function $\Lambda \rightarrow t$. This function is then transformed into an admittivity map $\Lambda \rightarrow t \rightarrow \gamma$. Preliminary chest phantom reconstructions have been presented by Isaacson et al [18;301] and proved to have superior results over those acquired by the Newton One Step Error Reconstruction (NOSER) algorithm [302]. However, for the time being, this method is limited to two dimensional problems; and therefore, is unfortunately not suitable for 3D human head reconstruction.

5.3.1.9 Geometric Multi-Grid and Regular Grid transformation

One of the most efficient ways to treat large-scale problems is by a multi-scale framework. The general idea is to solve the inverse problem using a coarser representation of the model, and later to interpolate this solution onto a finer representation. This can be performed in a simple form, using a dual-grid representation, or in a more sophisticated multi-grid framework, which is recursive and involves utilisation of smoothing procedures throughout the process. Unfortunately, as efficient and promising this method may appear at first glance [247;254], its applicability for medical applications is limited. The effectiveness of these methods relies on the ability to produce a hierarchy of coarser model discretisations which still encloses the imperative geometrical features of the model. Such discretisation either employs similar element type as of the original model, or an alternative basis, such as a *regular grid* which avoid any meshing procedure [303]. Medical applications often deal with complex geometric structures, involving thin tissue layers of large impedance contrast (such as the CSF in the head). For these cases generation of hierarchy of discretisations is difficult at best, if possible at all. Figure 5-1 demonstrates the degradation in reconstructed images resulted from reconstruction over a regular-grid for shelled concentric sphere model.

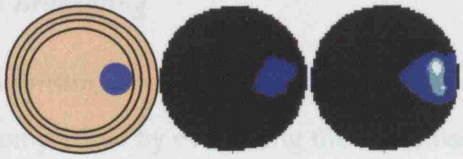

Figure 5-1. Left: Four concentric sphere model with a perturbation at 3 o'clock in the innermost sphere; Middle: Difference image acquired by linear reconstruction (Generalised Tikhonov) over a tetrahedral concentric four-shelled model; Right: difference image acquired by linear reconstruction (Generalised Tikhonov) over regular-grid representation. The recovered perturbation in this image was mis-located outwards

5.3.2 Globalisation

Frequently, the derived search direction approximation is valid only in the close vicinity of the current solution, and advancing by a full step in the proposed direction might even result in solution divergence. Two strategies can be used to restore local convergence: line search and trust region. The first is performed once a search direction is determined and then an inexact one dimensional line search is applied to find a step

size α_t. The second approach defines a trust region, which shifts the original Hessian matrix by $\lambda_t I$. The trust region control parameter is adjusted at each iteration to meet with a sufficient convergence criterion as described in 5.3.1.5.

A general update step in a new search direction $\mathbf{p}_t$, and a step size α_t is

$$\gamma_{t+1} = \gamma_t + \alpha_t \mathbf{p}_t \tag{5.48}$$

where γ_t is the solution at the t^{th} iteration, and α_t is a positive scalar. There are various ways to perform a one dimensional line search, where usually the trade-off of these methods is between convergence ratio, and confidence of finding the minimum. These methods vary by the way they bracket the minimum, and split the sections of interest. One approach is by facilitation of the Newton-Raphson method to generate an approximate parabola from which a minimum in 1D can easily be deduced. However, such an approach requires second derivative calculation which can be computationally prohibitive for large-scale problems. An alternative approach is the *Secant* method, which only employs two first derivatives of the objective function at adjacent locations along the search direction. As gradients calculation may still be computationally intensive, other methods, such as the *Brent* method, require only evaluation of the objective function along the search direction. Such approaches are advantageous for large-scale problems [293].

5.3.2.1 Bracketing

While seeking for a minimum, one must first assure that it lies within the search interval. This can be accomplished by evaluating the minimised function at a sequence of points, starting at a distance of δ, then increasing the step size at every stage, either by a fixed factor, or by parabolic extrapolation along the search direction [293]. When the value of the function increases between two successive iterations, the minimum is successfully bracketed.

5.3.2.2 Inexact Armijo backtrack

A compromise between accuracy and computational time can be achieved by performing an inexact line search which encloses conditions to ensure fast and safe convergence. The first reasonable condition would be to demand

$$\mathbf{f}(\gamma_t + \alpha_t \mathbf{p}_t) < \mathbf{f}(\gamma_t) \tag{5.49}$$

The first derivative of the minimised function in the new search direction $\phi(\alpha_t)=\mathbf{f}(\gamma_t+\alpha_t\mathbf{p}_t)$ with respect to the step size α_t is given by the following expression

$$\frac{d\phi(\alpha_t)}{d\alpha_t}=\nabla\mathbf{f}(\gamma_t+\alpha_t\mathbf{p}_t)^T\mathbf{p}_t. \tag{5.50}$$

One choice for α_t which will ensure this condition would be

$$\mathbf{f}(\gamma_t+\alpha_t\mathbf{p}_t)\approx\mathbf{f}(\gamma_t)+\alpha_t\nabla\mathbf{f}(\gamma_t)^T\mathbf{p}_t\le\mathbf{f}(\gamma_t)+c_1\alpha_t\nabla\mathbf{f}(\gamma_t)^T\mathbf{p}_t \tag{5.51}$$

where $0<c_1<1$. Since $\mathbf{p}_t$ is a descent direction it is known that $\nabla\mathbf{f}(\gamma_t)^T\mathbf{p}_t<0$ holds. The condition (5.51) is called *Armijo condition*. Nevertheless, this condition is satisfied for any small values of α_t, which may lead to slow convergence. For that purpose, it is advisable to add another condition which forces the derivative value at $\gamma_t+\alpha_t\mathbf{p}_t$ to be greater than the gradient at $\alpha_t=0$

$$\nabla\mathbf{f}(\gamma_t+\alpha_t\mathbf{p}_t)^T\mathbf{p}_t\ge c_2\nabla\mathbf{f}(\gamma_t)^T\mathbf{p}_t \tag{5.52}$$

where $c_2\in[c_1,1]$. This condition (5.52), known as the curvature condition, together with Armijo condition forms *Wolfe conditions*. Sometimes, a stricter rule is employed to ensure that the slope will not be too positive, on the one hand, and not too far from the stationary point of $\phi(\alpha_k)$ on the other hand

$$\left|\nabla\mathbf{f}(\gamma_t+\alpha_t\mathbf{p}_t)^T\mathbf{p}_t\right|\le c_2\left|\nabla\mathbf{f}(\gamma_t)^T\mathbf{p}_t\right| \tag{5.53}$$

Armijo condition together with (5.53) are known as the *strong Wolfe conditions*.

5.3.2.3 Golden-Section

Golden Section of the bracketed minimum interval is among the most robust ways for backtracking. Let us denote the bracketed minimum by the triplet points $(a<b<c)$. First, either the interval $[a,b]$ or the interval $[b,c]$ is divided by the golden ratio $\phi=(\sqrt{5}-1)/2\approx 0.61803$ at the point x. Considering for an instance the case where $\mathbf{f}(\gamma(b))<\mathbf{f}(\gamma(x))$, the new bracketing triplet will be $(a<b<x)$. A new interior point is placed within the new interval. This procedure is continued until the interval of uncertainty is reduced to a desired tolerance width. The convergence of this method is linear. Figure 5-2 demonstrates Golden Section bracketing method [293].

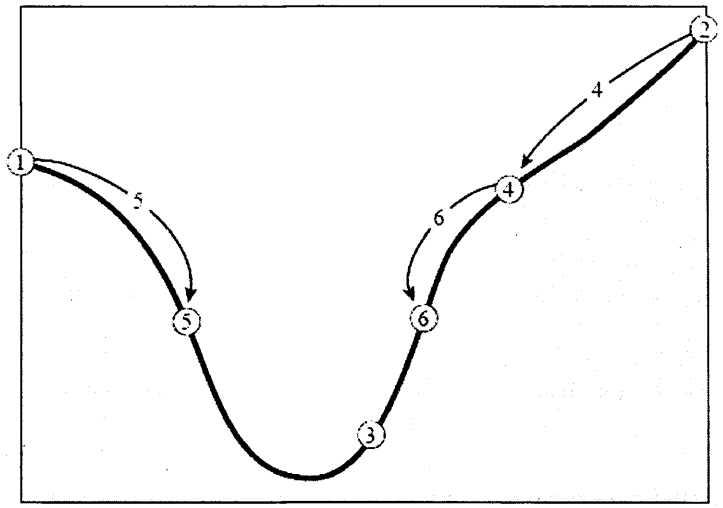

Figure 5-2. Successive bracketing of a minimum [293]. The minimum is originally bracketed by points 1, 3, 2. Then the function is evaluated at 4, which replaces 2; then at 5, which replaces 1; then at 6, which replaces 4. The rule at each stage is to keep the centre point lower than the two outer points. After the steps shown, the minimum is bracketed by points 5, 3, 6

5.3.2.4 Brent line search

Methods like Golden Section are highly robust, but are designed to handle the worst possible case of function minimisation, in the sense of existence of arbitrary large high derivative components. In practice, a parabolic interpolation for 3 points can approach the minimum much more effectively. Since robustness cannot be compromised, a good strategy would be to rely on a steady, but slow method, like Golden Section search when the function is not cooperative, but, on the other hand, to switch over to inverse parabolic interpolation whenever the function allows. Brent method [304] incorporates these two ideas by keeping track of 6 function points.

do

$x_m = mean(a,b)$

$u_{parabolic\ fit} \leftarrow parabolic\ fit(x,v,w)$ parabolic interpolation attempted, through x, v and w

if

- $a \le u_{parabolic\ fit} \le b$ parabolic fit falls within the bounding interval (a,b)
- **and**
- $\left|x - u_{parabolic\ fit}\right| \le \frac{1}{2}\left|x_{previous} - x\right|$ step from the best current value x is less than half of the step before last (avoids in non-convergent limit cycle)

then

$x = u_{parabolic\ fit}$ parabolic fit is acceptable

else

$x \leftarrow golden\ section(a,b,x,x_m)$ perform Golden Section step

housekeeping update tracking points for the next step

until $|a-b| \ge 2|x-x_m|\,tol$

Algorithm 5-3. Brent line search algorithm

In the worst case, the method will perform useless parabolic steps, but then the method will alternate between parabolic steps and golden section, whereas the convergence advances due to the latter. Figure 5-3 illustrates the convergence of the Brent method towards the minimum [293].

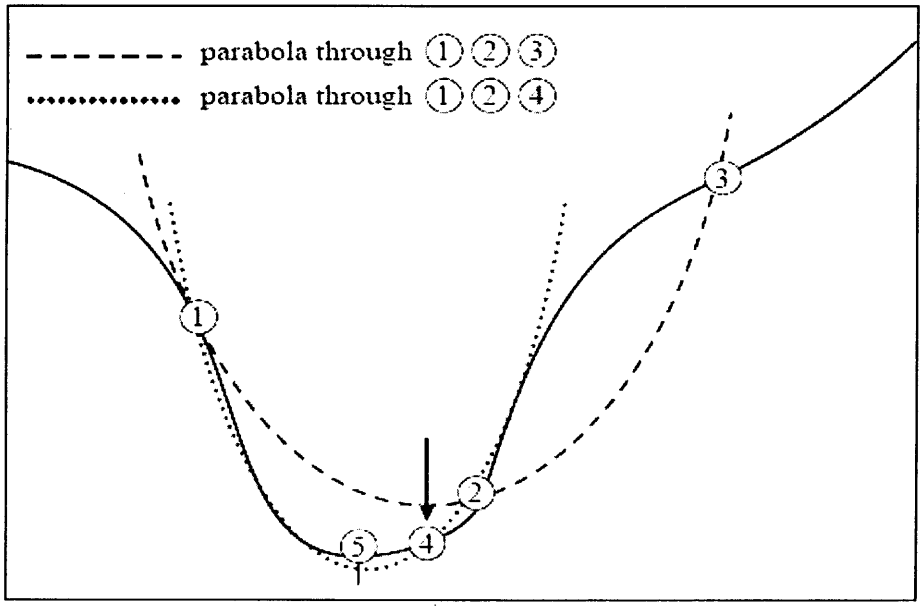

Figure 5-3. Convergence to a minimum by inverse parabolic interpolation [293]. A parabola (dashed line) is drawn through the three original points 1, 2, 3 on the given function (solid line). The function is evaluated at the parabola's minimum, 4, which replaces point 3. A new parabola (dotted line) is drawn through points 1, 4, 2. The minimum of this parabola is at 5, which is close to the minimum of the function

5.3.3 Regularisation

5.3.3.1 Motivation

Due to the ill-posed nature of the EIT problem, mere least square minimisation of the weighted residual error term $\mathbf{r}_{\xi}(\gamma)$ is doomed to failure [305]. As the measured data V_{Γ} is contaminated with noise, such minimisation would attempt to recover a admittivity distribution which fits the noise as well. Since the problem is unstable, even small deviations in the data space can translate into enormous changes in the solution space. Under these conditions, there is more than one solution that can fit the data up to the noise level, and therefore the solution is no longer unique. A straightforward way to restore uniqueness and stabilise the solution is by regularisation.

There are several known regularisation methods, such as Standard and Generalised Tikhonov. In these methods, the original problem is modified in a manner that provides a stable solution. More sophisticated regularisation approaches impose prior information regarding the solution. The prior term is represented by a function $\psi(\gamma,\eta)$ which penalises the minimised function, along with a hyper-parameter τ which regulates the amount of prior imposed over the objective function given in expression (5.1)

$$\mathbf{f}(\gamma,\eta)=\left\|\xi\left(V_{\Gamma}-F_{\Gamma}(\gamma)\right)\right\|^{2}+\tau\psi(\gamma,\eta) \tag{5.54}$$

A choice of a suitable prior may be a difficult task. A good prior should characterise some defining features of the solution on the one hand, but on the other hand, must be adequately general to avoid from biasing the solution towards subjective assumptions (and sometimes wishes) of the researcher. One of the most common choices for a prior is to penalise oscillatory behaviour of the solution, using some approximation of a partial differential operator R [35]

$$\psi(\gamma,\eta)=\left\|R\left(\gamma-\gamma_{g}\right)\right\|_{2}^{2} \tag{5.55}$$

While this method is highly effective for approximately homogeneous parameter distribution, for applications which intrinsically involve sharp transients in different regions, such a prior is not consistent with the actual situation. In such cases, more advanced approaches, such as relaxing the smoothness constraints in the direction normal to a discontinuity [306], or total variation are advisable [307]. In statistical inversion a-priori information is expressed in the form of probability distribution.

Solutions obtained in statistical inversion are actually probability distributions [36;283;284]. However, point estimates, such as *Maximum a Posteriori* (MAP) estimate, are usually considered. With certain assumptions, the MAP estimate can be written in the form of the Generalised Tikhonov regularised solution, although the interpretation is different. The computational complexity of calculating the posterior distribution for arbitrary distribution is enormous.

There is a trade-off between incorporation of accurate a-priori information and the computational requirements for reconstruction. As this study concentrates on scalability, more sophisticated regularisation frameworks were beyond the scope of this work, although this important topic should rigorously addressed in further studies.

5.3.3.2 Regularisation parameter estimation

The success of currently available regularisation techniques relies on proper choice of the regularisation parameter. Although many methods have been proposed, very few of them are used in engineering practice. This is due to the fact that theoretically justified methods often require unrealistic assumptions, while empirical methods can not guarantee good regularisation parameter for any set of data. Among the methods that have found their way into engineering practice, the most common are the *Discrepancy Principle* (DP) [308], *Generalised Cross Validation* (GCV) [309] and the *L-curve method* [310;311].

The Discrepancy Principle is based on the assumption that the expected value of the measurement noise δ is known. In this case the regularisation hyper-parameter is chosen to abide

$$\|J\gamma - V_\Gamma\| = \varsigma\delta \tag{5.56}$$

where $\varsigma > 1$ is some predefined real number. The sensitivity of this approach to erroneous noise level estimation limits its application to cases in which the noise level can be estimated with high fidelity. Alternatively, Generalised Cross-Validation does not depend on a-priori knowledge regarding the noise variance. The key principle of GCV is preventing the computed model from being sensitive to elimination of one data point. This means that the solution should predict a measurement fairly well even if that datum is not used when calculating the model. The Cross Validation (CV) function

is defined as the sum of square differences between the predicted right hand side without the i[th] measurement and the actual i[th] measurement

$$CV(\tau)=\sum_{i=1}^{m}\left(\widehat{F_{\Gamma i}}(\tau)-V_{\Gamma i}\right)^2 \tag{5.57}$$

where $\widehat{F_{\Gamma i}}(\tau)$ is the forward model predication derived by excluding the i[th] channel of the minimised function, and $V_{\Gamma i}$ is the i[th] measurement channel. The minimum of the CV function with respect to τ, corresponds to the regularisation parameter for which the predicted data would change the least subject to exclusion of one measurement point. The Cross Validation function was replaced by the Generalised CV in order to keep its minimum under orthogonal transformation

$$GCV(\tau)=\frac{\left\|I-C(\tau)\right\|^2}{tr\left(I-C(\tau)\right)^2} \tag{5.58}$$

where

$$C(\tau)=J\left(J^TJ+\tau R^TR\right)^{-1}J^T \tag{5.59}$$

Despite the firm theoretical foundation and the notable numerical experiments [312], GCV occasionally fails in the presence of correlated noise [309]. In addition, frequently the GCV functional has a very flat minimum (Figure 5-4, left), which makes it difficult to determine a regularisation hyper-parameter reliably [313].

The more recent method of L-curve is noise-estimate-free as well. The general idea is to display the trade-off between the two quantities of the objective function: the prior term versus the corresponding residual error norm for each of a set of regularisation parameter values (Figure 5-4, right). Intuitively, the best regularisation parameter should lie on the corner of the L-curve, since for values higher than this, the residual increases without reducing the norm of the solution much, while for values smaller than this, the norm of the solution increases rapidly without much decrease in residual. In practice, only a few points on the L-curve are computed and the corner is located by estimating the point of maximum curvature [20]. Despite its broad use, the *L-curve* method is non-convergent [314].

Other popular methods are Vogel's Unbiased Predictive Risk Estimator (UPRE) [315], and methods based on information criteria [316]. In the latter, statistical measures, such as the Kullback-Leibler distance between a true probability distribution and an arbitrary probability distribution, are employed in order to quantify the loss of

information which is attributed when an approximate model is used instead of the unknown truth.

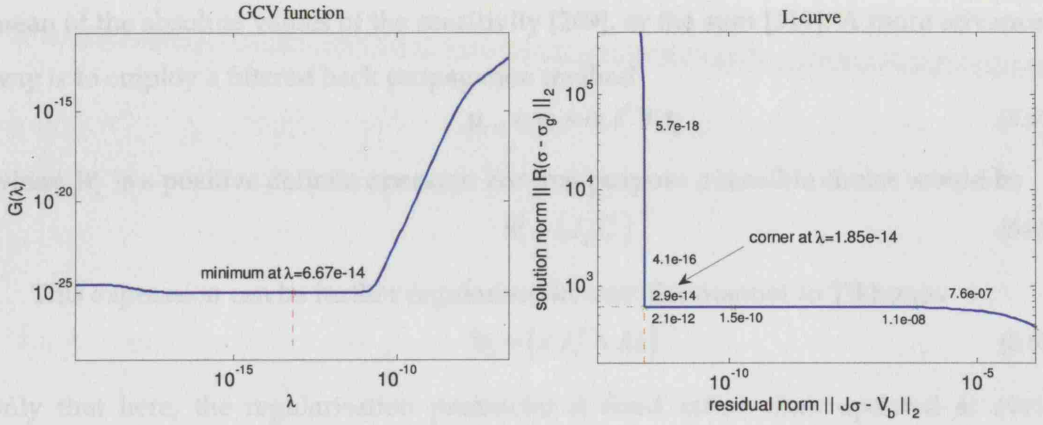

Figure 5-4. Regularisation hyper-parameter selection methods applied over a large-scale head-model. Left: Generalised Cross Validation; Right: L-curve criteria

Over the years, several studies compared the effectiveness of these methods for EIT and related problems [313;314;317;317]. As the performance of these methods is highly problem dependent, most studies were either inconclusive or favoured GCV or L-curve marginally.

5.3.4 Rescaling and conditioning

Optimisation over the parameters in their standard form, occasionally results in poor contrast images and slow convergence. In order to maximise the propagation of information through the reconstruction process, an alternative parameter representation and preconditioning is advisable.

5.3.4.1 Preconditioning

EIT problems and, in particular, head EIT are characterised by a wide sensitivity range. In the vicinity of the electrodes, there are high sensitivity values, whereas, in interior and in poorly sampled regions, the sensitivity is low. As a result, the Jacobian is ill-conditioned. It would be desirable to apply a transformation that clusters the eigenvalues of Jacobian or the regularised Hessian, and therefore allows a faster and more stable inversion procedure.

A simple way to precondition the Jacobian is by a diagonal matrix $C \in \mathbb{R}^{k \times k}$

$$\hat{J} \leftarrow JC \tag{5.60}$$

where typically the entries of C are the inverse of the root mean square (rms) of the sensitivity matrix for each element (i.e. a Jacobian column) [318]. Other choices are the mean of the absolute values of the sensitivity [269], or the sum [319]. A more advanced way is to employ a filtered back propagation method

$$\mathbf{p}_{t+1} = \mathbf{p}_t + \alpha_t J^T W_t \mathbf{r}_\xi \tag{5.61}$$

where W_t is a positive definite operator. For that purpose a sensible choice would be

$$W_t = \left(J_t J_t^T\right)^{-1} \tag{5.62}$$

This expression can be further regularised in a similar manner to Tikhonov

$$W_t = \left(J_t J_t^T + \lambda I\right)^{-1}. \tag{5.63}$$

only that here, the regularisation parameter is fixed rather than updated at every iteration. However, this variant still requires a moderate matrix inversion. A method to resolve this difficulty is by taking W_t to be [320]

$$W_{t_{i,j}} = \begin{cases} \left(J_{ii} J_{ii}^T\right)^{-1} & i = j \\ 0 & i \neq j \end{cases} \tag{5.64}$$

A modified filtered back-propagation version, which combines both the efficiency of the above method, together with the regularisation of the filtered back propagation method has been suggested [225;249;274]

$$W_t = \left(\sum_{j=i}^{k} J_{j,i}^2 + \sqrt{\lambda_t} \right)_i^{-1} \tag{5.65}$$

where the search direction expressed as

$$\mathbf{p}_{t+1} = -\left(W_t \nabla \mathbf{f}(\gamma_t) + \lambda I \gamma_t\right) + \beta_t \mathbf{p}_t \tag{5.66}$$

where β_t equal one for Newton-type methods, or as defined in (5.47) for NLCG.

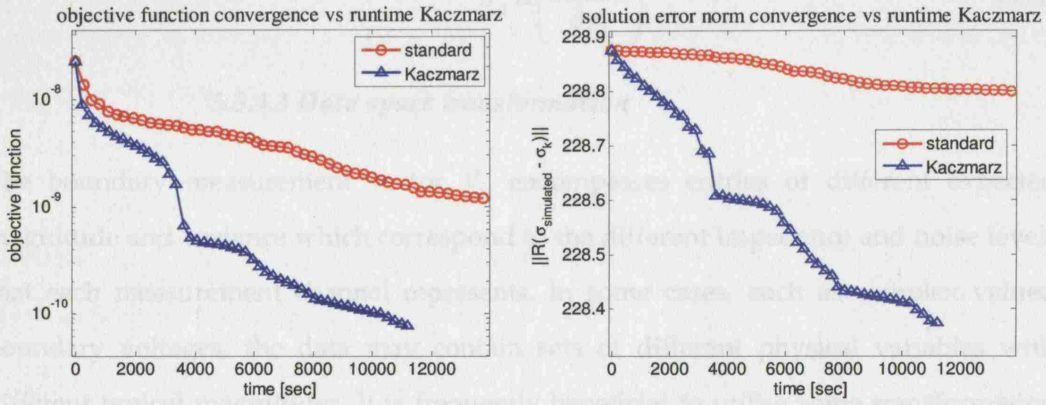

Figure 5-5. Objective function (Left) and solution error norm (Right) convergence over time in standard form and with modified back-propagation filter

5.3.4.2 *Parameter space transformation*

In some formulations, the recovered parameter may include parameters which represent different physical entities, and therefore correspond to different typical scales. An example would be recovery of the real and the imaginary components of the admittivity, or recovery of conductivity and contact impedance. In other cases, the recovered parameter may have a very wide dynamic range. The scaling variability may discriminate certain parameter types or range throughout the optimisation process. This problem can be addressed by parameterisation. A suitable parameterisation, should render the recovered parameter to be dimensionless and strive to set a representation for which the transformed parameter lies in an Equal Variance Domain [321]. A general parameterisation would take the form

$$\tilde{\gamma} \leftarrow s(\gamma). \tag{5.67}$$

The original problem is transformed into

$$\tilde{\gamma}(V_\Gamma) = \arg\min_{\tilde{\gamma}} \left\| \xi\left(\tilde{F}_\Gamma(\tilde{\gamma}) - V_\Gamma\right) \right\|^2 + \tau\psi(\tilde{\gamma}) \tag{5.68}$$

where $\tilde{F}_\Gamma(\tilde{\gamma}) = F_\Gamma\left(s^{-1}(\tilde{\gamma})\right)$ is the transformed forward model. The gradient takes the form

$$\nabla\tilde{\mathbf{f}} = \tilde{J}^T \xi\left(\tilde{F}_\Gamma(\tilde{\gamma}) - V_\Gamma\right) + \tau\nabla\psi(\tilde{\gamma}) \tag{5.69}$$

and the Jacobian gets the following form

$$\tilde{J}_{ij} = \frac{\partial V_{\Gamma i}}{\partial \tilde{\gamma}_j} = \frac{\partial V_{\Gamma i}}{\partial s(\gamma)_j} = \frac{\partial V_{\Gamma i}}{\partial \gamma_j} \frac{\partial \gamma_j}{\partial s(\gamma_j)} = J_{ij} S \tag{5.70}$$

where

$$S_{jj} \equiv \left(\frac{\partial s(\gamma_j)}{\partial \gamma_j} \right)^{-1}. \tag{5.71}$$

5.3.4.3 *Data space transformation*

The boundary measurement vector V_Γ encompasses entries of different expected magnitude and variance which correspond to the different impedance and noise levels that each measurement channel represents. In some cases, such as complex valued boundary voltages, the data may contain sets of different physical variables with different typical magnitudes. It is frequently beneficial to utilise some transformation or parameterisation that will scale the data to meet the terms of an equal variance domain. Typical transformation would make the data dimensionless, and scale it to

comply with the level of confidence given to each of the measurement channels. Such a transformation is a generalisation of the scaling parameter ξ, given in the objective function (5.1). A general transformation over the data space would be

$$\widehat{V_\Gamma} \leftarrow h(V_\Gamma). \tag{5.72}$$

The original problem would then transformed into the following minimisation problem

$$\gamma\left(\widehat{V_\Gamma}\right) = \arg\min_{\gamma} \left\| \widehat{F_\Gamma}(\gamma) - \widehat{V_\Gamma} \right\|^2 + \tau\psi(\gamma). \tag{5.73}$$

In practice, data space transformation can frequently be represented by a linear transformation

$$\widehat{V_\Gamma} \leftarrow TV_\Gamma \qquad T \in \mathbb{R}^{m\times m} \tag{5.74}$$

This transformation linearly rescales the forward solution

$$\widehat{F_\Gamma}(\gamma) = TF_\Gamma(\gamma). \tag{5.75}$$

T typically takes the form of diagonal matrix multiplication, where the diagonal entries include a rescaling factor for each measurement channel. Common choices are the inverse of the predicted model data at the initial parameter distribution, inverse of the RMS of each row of the sensitivity matrix [27;110;269], or a measure of confidence given to each of the channels based on the data variance. For such cases the rescaled Jacobian takes the following form

$$\hat{J} = TJ. \tag{5.76}$$

5.4 Newton - Krylov Inversion for Large-Scale EIT Problems

5.4.1 Motivation and rationale

Convergence of iterative inversion methods which employ 2nd order derivatives is frequently significantly faster than methods employing only 1st order derivative information. Nevertheless, both the explicit formulation and the direct inversion of the approximate Hessian are computationally intractable for large-scale problems. As the Newton search direction employs only an approximation of the true Hessian and since linearisation of the original non-linear problem is valid only locally anyway, an accurate calculation of the Hessian inverse is redundant. As the Hessian formation by itself is computationally excessive, the challenge is to produce such an approximation, with no explicit formation of the Hessian or its inverse. The proposed way to meet

these requirements, in this work, is by derivation of an approximation for the Newton update using an iterative inner loop which solves the normal systems brought in (5.24) or in (5.33). At the first stage, the normal equation are rewritten as follows

$$H_t^{\lambda}\Delta\gamma_{NKt+1} = \alpha_t g_t \tag{5.77}$$

where for Gauss-Newton $H_t^{\lambda} = H_t^0$, and for Levenberg-Marquardt $\alpha_t = 1$. In this formulation the update step $\Delta\gamma_{NKt+1}$ can be calculated up to a predefined tolerance using an iterative solver. The defining feature of Krylov-subspace solvers is that the coefficient system, which is taken to be the approximate Hessian H_t^{λ} in this formulation, is accessed only for matrix-vector product operations. Thus, the explicit formulation of the Hessian can be replaced by an implicit one by substitution of all the occurrences of the operation $H_t\gamma$ with the following operation

$$H_{NKt}\gamma = J_t^T(J_t\gamma) + \tau_t\nabla^2\psi(\gamma)\gamma + \lambda_t\gamma \tag{5.78}$$

The brackets surrounding the product $J_t\gamma$ result in a vector, which is then multiplied again by J_t^T, so that the immense term of $J_t^T J_t$ is never formed explicitly. The product $H_t\gamma$ for explicit Hessian formulation requires k^3 floating point operations, whereas the implicit formulation requires $k^2m + km^2$ (assuming that the computational cost of the product $\psi(\gamma_t)\gamma$ is negligible, due to the sparsity of $\psi(\gamma_t)$). Therefore, the implicit formulation is more efficient whenever $m < \left(\sqrt{5}-1\right)/2k$. For a typical large-scale problem $m \ll k$, and therefore this formulation is favoured.

In this study, General Minimal Residual (GMRes) [250] Krylov solver was used to solve the set of linear normal equations (5.77). As described in Chapter 4, this Krylov subspace method, is based on a modified variant of the Gram-Schmidt orthogonalisation process (Arnoldi method), and therefore, only requires storage of a moderate number of internal search directions.

The application of Newton-Krylov inversion was recently suggested for Diffusion Optical Tomography [322], but its application for EIT was first presented by the author [220;299].

5.4.2 Preconditioning

The convergence and stability of Krylov-subspace solvers depends strongly on the spectrum of the system. The main difficulties in preconditioning the approximate Hessian system are twofold: it is a dense matrix, and in effect this matrix is never formed explicitly. Numerous methods, such as Newton-Krylov-Schur (NKS) domain

decomposition or Newton-Krylov Multi-Grid (NKMG) approaches can be employed for that purpose [323]. Since in this case the physical factors which affect the conditioning of the system are known, it is reasonable to compensate for their effect, rather than employ some general-purpose preconditioning scheme, which will 'blindly' attempt to construct a suitable preconditioner. The main cause of ill-conditioning is related to the wide sensitivity range, which is particularly profound for shelled geometries and non-equally sampled domains. Since the Hessian entails both J and J^T terms, both its rows and its columns require rescaling. For that purpose, the following diagonal preconditioner is proposed

$$C_{ii} = \frac{1}{\sqrt{\sum_j J_{ji} + \tau\left(R^T R\right)_{ii} + \lambda}}. \tag{5.79}$$

For all Newton methods (including the Newton-Krylov), this transformation can be applied from the left, as a standard preconditioner, but also on the right side of the Hessian. The preconditioned system gets the form

$$\underbrace{CH_t^{\lambda} C}_{\tilde{H}_t^{\lambda}} \Delta\tilde{\gamma}_{t+1} = \alpha_t \underbrace{Cg_t}_{\tilde{g}_t} \tag{5.80}$$

where the desired update $\Delta\gamma_{t+1}$ can be recovered from the following

$$\Delta\tilde{\gamma}_{t+1} := C^{-1}\Delta\gamma_{t+1}. \tag{5.81}$$

This transformation spherifies the solution space, and therefore stabilises and accelerates the inversion process.

5.4.3 Choice of GMRes relative residual tolerance

One of the outstanding implementation questions related to the Newton-Krylov inversion is to decide to what tolerance a new search direction needs to be solved? It is not cost-effective to perform Krylov inversion up to the numerical round-off accuracy. Experience shows that almost similar convergence to that of an explicit inversion can be achieved with moderately low residual error requirement. This can be inferred from a comparison of the convergence of the explicit inversion versus the convergence of the implicit inversion performed with several different tolerances. Convergence over time of Damped Gauss-Newton algorithm applied over a small head model problem with explicit inversion as well as for a range of different GMRes relative residual tolerances is presented in Figure 5-6 on the left. The runtime requirement for GMRes inversion depends on the conditioning of the approximate Hessian system, which can be

addressed separately in terms of cost efficiency once a specific preconditioning scheme has been determined. An insight into the residual error convergence versus iteration count (Figure 5-6 right) shows that a moderate relative residual tolerance of 10^{-3} or 10^{-4} provided convergence which was almost similar to that achieved by the explicit Hessian inverse. In this study relative residual of 10^{-3} was considered.

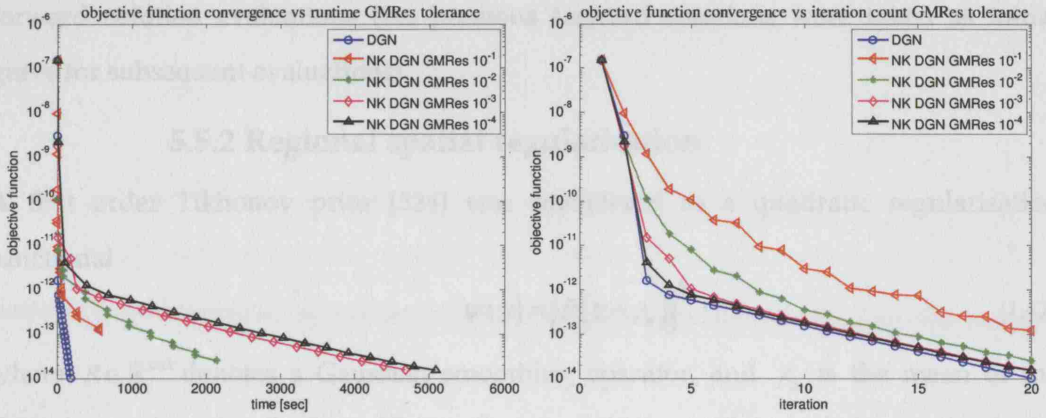

Figure 5-6. Objective function convergence vs. runtime (left) and iteration (right) for a small head model using standard and Damped Gauss-Newton-Krylov with different drop tolerances for GMRes solver

5.5 Comparison of Non-linear Inversion Methods

In order to assess and quantify the benefits of the proposed Newton-Krylov inversion approach for large-scale problems, its performance was compared with that of conventional non-linear inverse solvers over small and large-scale problems.

5.5.1 Inverse solver configurations

The following non-linear inverse solvers were implemented and used for comparison:

1. Damped Newton Gauss (DGN)
2. Damped Gauss-Newton-Krylov (NK-DGN)
3. Levenberg-Marquardt (LM)
4. Newton-Krylov Levenberg-Marquardt (NK-LM)
5. Variable-Metric Method (VMM) (Quasi-Newton)
6. Non-linear Conjugated Gradients (NLCG)

Gradient-based inversion methods employed a Kaczmarz back-propagation scheme for enhanced convergence, whereas 2nd order derivative methods were

preconditioned by the proposed diagonal preconditioner brought in 5.4.2. A Brent line search was used for all methods except for Levenberg-Marquardt variants, which employed a trust region strategy. The inverse solvers employed the monopolar source framework for forward modelling and inverse-based multi-level forward solver preconditioning. In addition, a feed-forward strategy was employed for prompt forward solution evaluations (i.e. previous forward solutions were taken as initial guess for subsequent evaluations).

5.5.2 Regional spatial regularisation

A first order Tikhonov prior [324] was considered as a quadratic regularisation functional

$$\psi(\gamma) = \left\| R(\gamma - \gamma_g) \right\|^2 \tag{1.82}$$

where $R \in \mathbb{R}^{k \times k}$ denotes a Gaussian smoothing operator, and γ_g is the mean of the Gaussian prior distribution. This prior penalises oscillatory behaviour of the conductivity with respect to neighbouring elements. The derivatives of this prior are

$$\begin{aligned} \nabla \psi(\gamma_t) &= R^T R(\gamma_t - \gamma_g) \\ \nabla^2 \psi(\gamma_t) &= R^T R \end{aligned} \tag{5.83}$$

The layered structure of the human head was treated here by construction of regional smoothing prior. The prior application was restricted to affect within each of the layers only, therefore, smoothing was not applied over sharp transition area between layers (Figure 5-7).

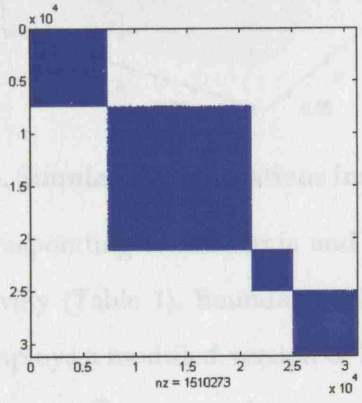

Figure 5-7. Regional regularisation smoothing prior sparsity pattern. This pattern demonstrate that there is no intersection at the interface points between the different tissues types (These are represented here as separate squares)

For this specific problem type, GCV provided a shallow minimum, therefore, L-curve was chosen to determine the regularisation hyper-parameter values in this study. In order to avoid an overdose of structure imposition into the model at early stages of the reconstruction process, a cooling-schedule-type approach was employed [317]. This procedure was performed by setting τ_t to be the maximum between the one calculated for the current iteration and the previous one τ_{t-1} multiplied by a small factor $c \leq 0.5$.

5.5.3 Simulated data generation

Two head models of 4K and 31K elements were assigned with conductivity values of the head tissues for the frequency of 10Hz derived from the review in Chapter 2. The dimensions of the large model (31K elements) were taken to be such that would allow complete calculation of the inverse problem within the physical RAM limitations of the processing workstation. 31 electrodes were placed over the head according to the extended 10-20 EEG scheme. The protocol contained 258 injection-measurement combinations. Two spherical perturbations with radius of 1.7cm were placed in the left temporal and occipital lobe regions of the modelled brain (Figure 5-8).

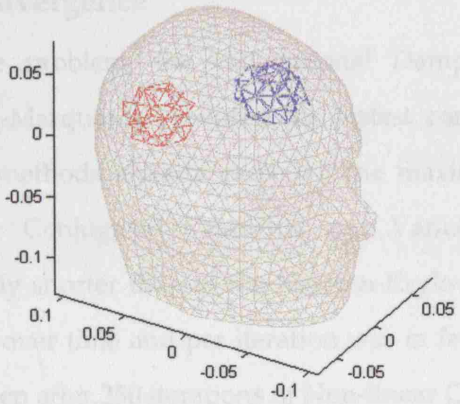

Figure 5-8. Simulated perturbations inside the brain

Conductivity values corresponding to ischaemia and haemorrhage were assigned to the perturbation respectively (Table 1). Boundary voltages were generated using UCL Super-Solver, which employs a modified version of EIDORS 3D and the ILUPack package [225;234;261]. Zero mean Gaussian noise was simulated with amplitude of 0.01% of the maximal boundary voltages. Due to the large dynamic range of the expected boundary voltages this choice is rather harsh. For noise level which was 10 times larger, very weak convergence was achieved with all inversion methods.

Table 5-1. Assigned conductivity values

Tissue	Conductivity [S/m]
Scalp	0.25
Skull	0.02
CSF	1.79
Brain	0.15
Haemorrhage	0.56
Ischaemia	0.1

5.5.4 Evaluation

The solvers were compared with respect to the following criteria: 1) Convergence - objective function convergence over time and iterations. 2) Robustness - the actual regularised solution error convergence $\|R(\gamma_{simulated} - \gamma_k)\|$. 3) Memory requirements - peak memory consumption. 4) Image quality - maximal intensity and localisation error. All evaluations were performed on a single thread over a dual Xeon 2.8GHz workstation with 2GB RAM, Debian OS and Matlab 7.1 [244].

5.6 Numerical Results

5.6.1 Convergence

For the small scale problem, the conventional Damped Gauss-Newton and conventional Levenberg-Marquardt provided the fastest convergence. However, for the large model, these methods already exceeded the maximum memory limit. For both scales, Non-linear Conjugated Gradients and Variable Metric runtime per iteration was significantly shorter than of the Newton-Krylov methods. Nevertheless, the overall convergence over time and per iteration was in favour of the latter (Figure 5-9 and Figure 5-10). Even after 250 iterations of Non-linear Conjugated Gradients and Variable Metric, they only managed minimise the objective function to a value that was 20 and 200 times larger than the one achieved from 20 iterations of Damped Gauss-Newton-Krylov.

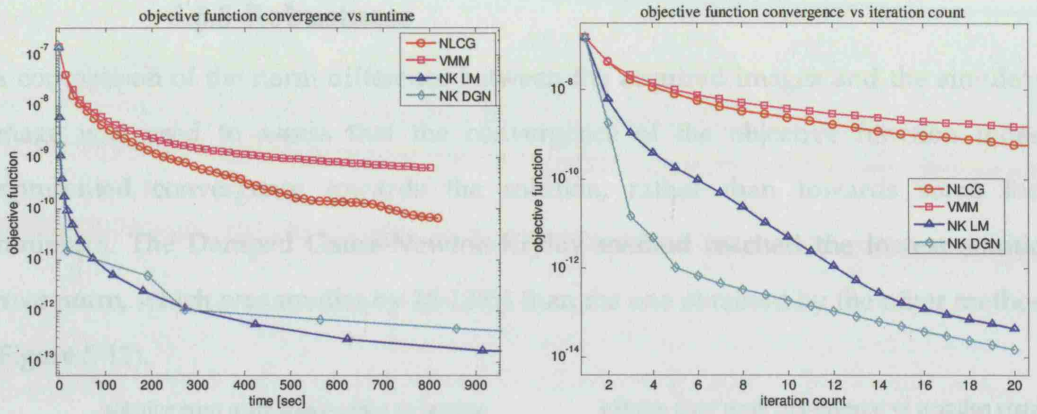

Figure 5-9. Left: objective function convergence vs. iteration count for the small model; Right: objective function convergence vs. runtime for the small model

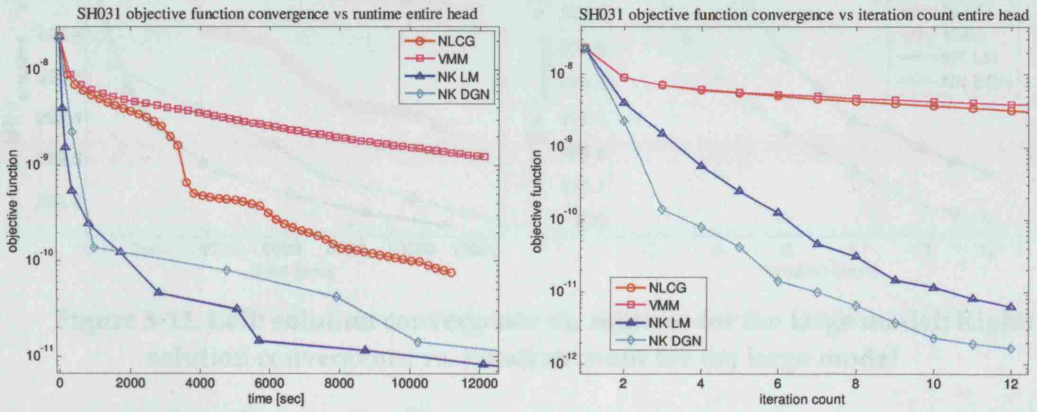

Figure 5-10. Left: objective function convergence vs. runtime for the large model; Right: objective function convergence vs. iteration count for the large model

5.6.2 Memory requirements

Conventional Newton-type methods were manageable only for the smaller model. Among the remaining methods, Non-linear Conjugated Gradients was the most memory efficient. Memory consumption of the Newton-Krylov method was up to 15% more expensive (Table 5-2).

Table 5-2. Peak memory consumption percentage of physical memory

Model	NLCG		VMM		NK LM		NK DGN	
	[%]	Relative [%]	[%]	Relative [%]	[%]	Relative [%]	[%]	Relative [%]
Small	25.6	100	25.8	100. 8	26.4	103.1	26.4	103.1
Large	58.0	100	61.8	104.8	63.4	109.3	63.4	109.3

5.6.3 Robustness

A comparison of the norm difference between the acquired images and the simulated image was used to assess that the convergence of the objective function indeed represented convergence towards the solution, rather than towards some local minimum. The Damped Gauss-Newton-Krylov method reached the lowest solution error norm, which was smaller by 28-138% than the one obtained by the other methods (Figure 5-11).

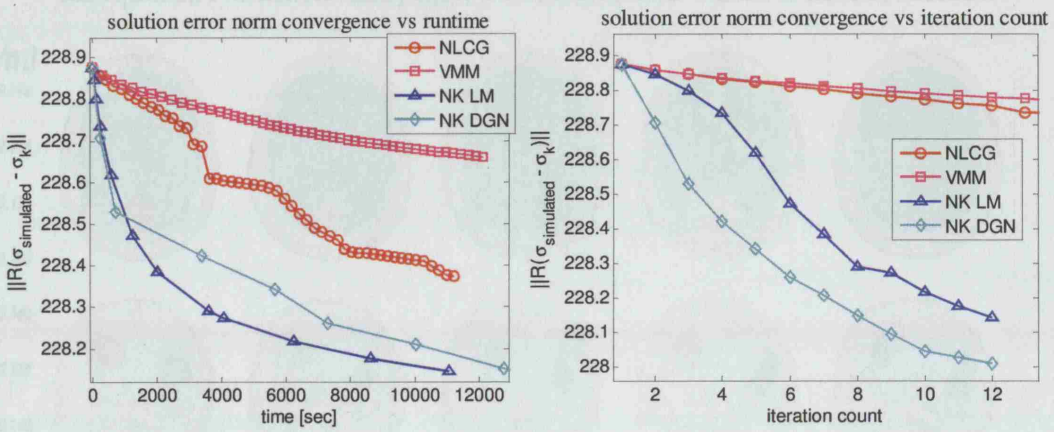

Figure 5-11. Left: solution convergence vs. runtime for the large model; Right: solution convergence vs. iteration count for the large model

5.6.4 Image Quality

Newton-Krylov methods provided the sharpest recovered images; with perturbation peak values larger by up to 166% and 141% than those achieved by Variable Metric for the small and the large model respectively (Figure 5-12 and Figure 5-13). Images acquired with Variable Metric and Non-linear Conjugated Gradients provided a larger localisation error with respect to the Newton-Krylov method. This effect was more profound for the large and more complex model, for which the recovered perturbations were considerably shifted towards the boundary (Figure 5-13).

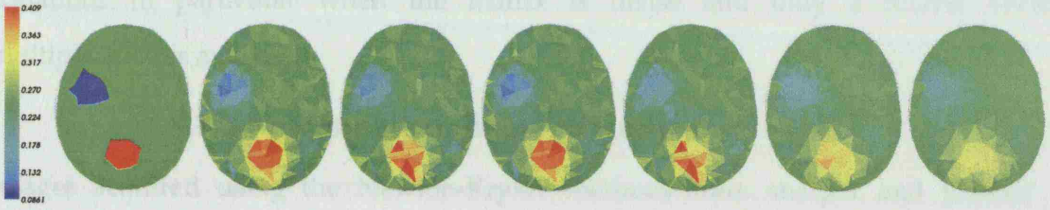

Figure 5-12. Top projection of images reconstructed for the small model. Left to right: simulated image; recovered images for Damped Gauss-Newton, Damped Gauss-Newton-Krylov, Levenberg Marquardt, Newton-Krylov Levenberg Marquardt, Nonlinear Conjugated Gradients and Variable Metric method

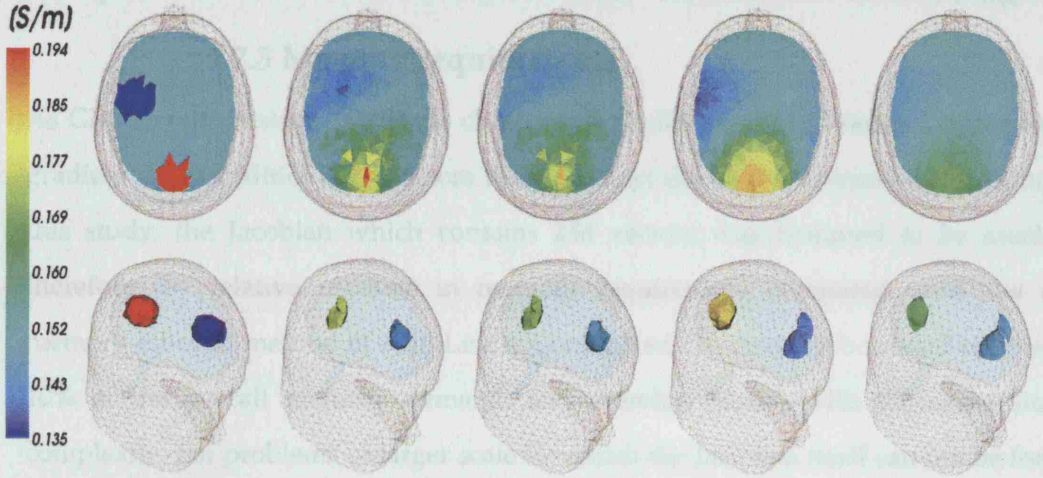

Figure 5-13. Images reconstructed for the large model. Left to right: simulated image; recovered images for Damped Gauss-Newton-Krylov, Newton-Krylov Levenberg Marquardt, Nonlinear Conjugated Gradients and Variable Metric method

5.7 Discussion

5.7.1 Convergence

Newton-Krylov methods showed an obvious advantage over their conventional counterparts in sense of convergence speed. Runtime per iteration of the Newton-Krylov Levenberg-Marquardt method grew gradually, as the trust region became smaller, and correspondingly the system became more ill-conditioned. This suggests that further acceleration of Newton-Krylov methods can be achieved by improved preconditioning of the normal equations. This can be performed through Newton-Krylov-Schur (NKS) domain decomposition or Multi-Grid (NKMG) [323], or alternatively with more advanced methods such as the fast multipole method [325] or by hierarchical matrices [326;327]. These methods are frequently used in integral

equations in particular when the matrix is dense and only a matrix vector multiplication is available.

5.7.2 Robustness and image quality

Images acquired using the Newton-Krylov methods were sharper and yielded a smaller error norm with respect to the true solution compared to those of their conventional counterparts. Yet, the images were still blurred, which suggests that employment of better priors for regularisation, and determination of a more appropriate excitation-measurement protocol may still yield more accurate images.

5.7.3 Memory requirements

As GMRes with restarts of 20 was chosen as a Krylov inversion method, apart from a gradient up to additional 20 vectors were retained during the inversion procedure. In this study, the Jacobian which contains 258 vectors was assumed to be available; therefore the relative increase in memory requirement compared with the most memory-efficient method of Non-Linear Conjugated Gradients is bounded to be about 10% of the overall memory demand, and therefore scales with the same storage complexity. For problems of larger scale for which the Jacobian itself can not be formed explicitly, Jacobian-free variants of all the proposed large-scale methods can be developed [275;323;328].

5.7.4 Technical remark

The draws from Matlab's random noise generator which were employed for noise simulation in this study were only pseudo-random, i.e. no initialisation of the seed was performed. These values represent typical error levels and comply with the intended noise distribution; however, care should be taken in future studies to assure initialisation of the random noise generator [37].

5.8 Conclusions

The novel Newton-Krylov inversion method demonstrated superior computational and image quality results over the conventional large-scale methods which were in common use so far. With suitable preconditioning of the normal equations, this approach offers rapid calculation of inverse problems with moderate computational resources. As this inversion procedure is rather general it can be easily transferable to

many related large-scale inverse problems, such as multi-frequency and anisotropic image reconstruction.

6 ACUTE CEREBRAL STROKE TYPE CLASSIFICATION - A FEASIBILITY STUDY

6.1 Introduction

To date, stroke is the leading cause of morbidity and the third leading cause of death in the western world. Acute cerebral stroke is characterised by a sudden loss of circulation to an area of the brain, resulting in a corresponding loss of neurological function. Stroke is a non-specific term which encompasses a heterogeneous group of pathophysiologic causes, including ischaemia (due to thrombosis or embolism), and haemorrhage.

Tissue plasminogen activator (t-PA) is a medication that can break up blood clots and restore blood flow when administered within 3 hours of an ischaemic event. However, its use in patients with haemorrhagic stroke is contra-indicated, as it can lead to extension of the haemorrhage; this can cause deterioration of their cerebral pathology and may be fatal. Currently, CT and MRI serve as tools for differentiating between these conditions. Due their poor availability, only about 2.5-5% of the ischaemic stroke patients in UK are classified in time and treated [329].

EIT has the potential to provide an accessible low cost imaging method that could be deployed in emergency situations such as in ambulances or casualty departments. Acute cerebral stroke results in distinctive local impedance changes over time and frequency. So far, all clinical Electrical Impedance Tomography (EIT) applications have been of differences over time in order to reduce modelling and instrumentation errors [40;42;330;331]. Unfortunately, time-difference imaging is not practical, because it is not possible to obtain a reference measurement prior to onset of the acute stroke. The lack of time-referenced data may be compensated by employment of additional information obtained from multi-frequency electric potential measurements. Multi-Frequency EIT (MFEIT) might therefore be an inexpensive portable method which could be used in emergency situations where CT or MRI are impractical.

Unfortunately, the requirement for a single absolute or multifrequency image places stringent requirements for accuracy on the measurements. There are no clinical multifrequency studies in which images are accurate and independently validated, although reasonably accurate results have been reported in a breast cancer study conducted by the Dartmouth group in USA and in a lung respiration study in Sheffield, UK [9;332]. Two preliminary studies of MFEIT in stroke or similar tissue

were unsuccessful [25;333]. The purpose of this study was to determine the expected changes in acute stroke and assess the feasibility of this application in relation to the performance of existing instrumentation and the effect of confounding errors, using a Finite Element Model of the human adult head.

This study has been presented at the VI International Conference on Biomedical Applications of Electrical Impedance Tomography, in London, 2005 [164] and at the 3rd European Medical and Biological Engineering Conference, in Prague, 2005 [163].

6.2 Background

6.2.1 Cerebral stroke

Acute cerebral stroke occurs due to a sudden interruption in blood flow to part of the brain. As a result, oxygen and nutrients supply as well as waste product removal is disrupted, which consequent in loss of neurological function. Depending on the region of the brain affected, a stroke may cause paralysis, speech impairment, a loss of memory and reasoning ability, coma, or death.

Ischaemic stroke is due to interruption of the blood supply to a region of the brain and occurs in about 80% of all strokes. It may be due to cerebral thrombosis or embolism. Cerebral thrombosis occurs when a blood clot, or thrombus, forms within the brain itself, while cerebral embolism occurs when a blood clot originating elsewhere in the circulatory system breaks free and lodges in an artery supplying blood to the brain.

Haemorrhagic stroke can occur due to intracerebral haemorrhage or subarachnoid haemorrhage. Intracerebral haemorrhage affects vessels within the brain itself, while subarachnoid haemorrhage affects arteries at the brain's surface, just below the protective arachnoid membrane.

6.2.1.1 Acute stroke affected regions

In the modelling below, the volume and site of the ischaemic region is clearly important. This section therefore reviews the clinical data relating to this. It has been demonstrated that the volume of stroke seen on CT imaging is correlated with severity of symptoms, clinical outcome and time to presentation [334-336]. In one study, CT scans obtained at stroke onset, at 7 to 10 days and at 3 months of 65 patients were analysed for the presence, site, size and volume measurement of ischaemic stroke [334].

At the time of admission the mean lesion volume was 33 cm^3, it increased to 51 cm^3 at 7 to 10 days, and after 3 months from stroke onset was 49 cm^3. With lesion size expressed as percentage of brain volume, the largest infarction was 47%, but the mean infarction size was only 5% of brain volume. The infarctions were shown by CT at 7-10 days to involve the middle cerebral artery distribution in 82% of positive scans (Figure 6-1).

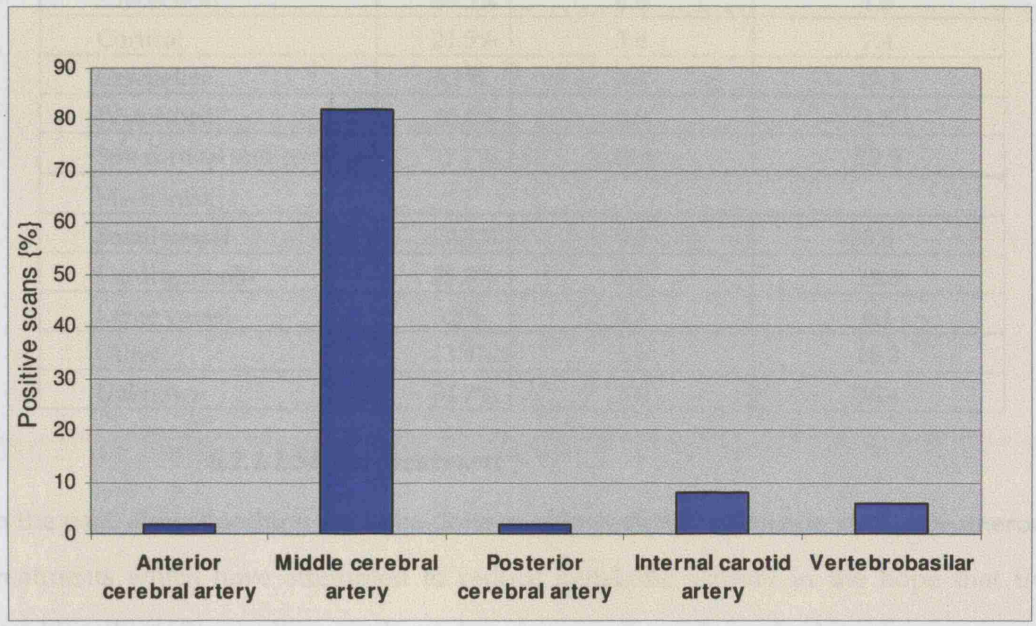

Figure 6-1. Arterial distribution of ischaemic stroke

The National Institute of Neurological Disorders and Stroke (NINDS) [337] have reported a median volume of ischaemic stroke within 24 hours of onset to be 10.6 cm^3, with a mean volume of 48 cm^3.

Kissela et al [338] have determined the volume and location of infarcts in 79 African-Americans based on CT and MRI evaluations for comparison with available literature regarding the volume of ischaemic infarcts in the Caucasian population [337]. The median and mean volumes by location of infarct, seen on imaging are summarised in Table 6-2. Table 6-1 provides an overall summary of infraction size from different authors.

Table 6-1. Summary of volume of stroke lesions

Study	n	Median volume [cm^3]	Mean volume [cm^3]
Cincinnati 1989	65	Not available	33
NINDS trial 2000	87	10.6	48.8
Cincinnati 2001	79	2.5	20.1

Table 6-2. Infarct volumes by anatomical location and mechanism of stroke (reproduced from Kissela et al [338])

	n (%)	Median volume [cm³]	Mean volume [cm³]
Location of infarct			
Brainstem	2.5%	0.1	0.1
Subcortical	40.5%	0.6	1.5
Cortical	21.5%	3.8	7.4
Cerebellar	5.1%	3.9	17.1
Watershed	10.1%	4.0	4.5
Sub cortical and cortical	17.7%	38.4	79.9
Mechanism			
Small vessel	27.8%	0.5	0.6
Cardioembolic	25.3%	5.1	25.8
Large vessel	3.8%	8.8	6.1
Other	11.4%	1.9	16.3
Unknown	31.7%	3.6	36.4

6.2.1.2 Stroke treatment

In the past, almost nothing could be done to help patients with acute stroke. Numerous treatments which have attempted to reduce metabolic activity in the hope that this would reduce tissue damage, have been assessed, such as barbiturate coma and neuroprotective agents such as MK801, but, unfortunately, none have been shown to be effective [339]. In the past 25 years significant advances have been made in stroke prevention, supportive care, and rehabilitation. Still, little treatment existed for ischaemic stroke until 1995, when the National Institute of Neurologic Disorders and Stroke recombinant tissue-type plasminogen activator (rt-PA) stroke study group first reported that the early administration of rt-PA benefited some carefully selected patients with acute ischaemic stroke. Encouraged by this breakthrough study and the subsequent approval of t-PA (clot busting medication) for use in acute ischaemic stroke by the US FDA, medical professionals now consider acute ischaemic stroke to be a medical emergency which, when detected and treated early, can have few, if any, permanent consequences [340]. The effectiveness of the treatment is unfortunately limited because administration of t-PA is needed within 3-6 hours of the onset of the ischaemic event; after this, the brain injury becomes irreversible. Since this therapy carries a 6% risk of causing brain haemorrhage, it cannot be given without definite

diagnosis [167]. Sadly, less than 5% of the ischaemic patients in UK are classified in time and treated, and even fewer worldwide [329]. This is mainly due to the poor availability of suitable diagnosis tools, such as non-contrast head CT or MRI, within the available short time-window.

EIT is portable and inexpensive. In principle, it could provide urgent neuroimaging in such an acute situation - a scan could be collected in a few minutes with the use of a headnet, and it could be rapidly reported over the internet by a radiologist.

6.2.2 Admittivity changes during acute stroke

This subject has been reviewed in detail in Chapter 3. In summary, in ischaemic brain tissue, impedivity changes between 50-100% occurred in the frequency band below 100Hz, while at higher frequencies, smaller impedivity changes of about 15-20% are expected. These changes can be attributed predominately to cell-swelling which reduces the extracellular space. This provokes the greatest effect at low frequencies, because ionic current does not cross into the intracellular space and so low frequency resistance is more sensitive to the properties of the extracellular environment. Admittivity changes during haemorrhagic stroke have not been directly measured, but may be estimated. Most feasibility studies in the field have simply considered complete displacement of brain tissue by blood [341;342]. This situation can occur in severe cases; nevertheless, it seems more reasonable to assume that mainly a replacement of the extracellular fluid with blood occurs, or alternatively, that a more complex description, in which an internal region of extracellular fluid saturated with blood is surrounded by a thin layer of ischaemic tissue (Figure 6-2 and Figure 6-3).

6.2.3 Previous studies on EIT of stroke

In a four vessel model of total cerebral ischaemia in the rat, Holder demonstrated that the resulting intracranial impedance changes could be recorded on the scalp [22;181]. His measurements were taken at a single frequency and therefore represented changes over time only. Bonmassar et al presented some preliminary results of clinical trials performed in chronic stroke patients. Recording was in the Electrical Impedance Spectroscopy mode, in which measurements were of raw impedance data from a small set of channels; no images were produced. However, these results seemed to include instrumentation errors, as calibration data indicated changes over frequency for

resistive test objects such as saline, and the measured changes in humans appeared to be in the opposite direction to those expected from the pathophysiology [333]. In another study conducted in UCL group, measurements from human subjects with arteriovenous malformations or chronic stroke, which resembled changes in haemorrhagic or ischaemic stroke, no reproducible changes were observed, although the study was limited due to hardware restrictions, to the range of 16kHz – 64 kHz [25].

Several publications have raised the feasibility of stroke type classification using EIT and related methods. Clay et al [318] addressed the application of EIT for acute stroke as an example to demonstrate the importance of column normalisation preconditioning in the image reconstruction process. The head was modelled as a 2D circle with conductivity values of a single frequency, Images were reconstructed over the modelled mesh using noiseless data and reference data of the normal state was assumed to be available. Merwa et al have recently investigated the feasibility of stroke differentiation using Magnetic Induction Tomography (MIT) [341]. A single frequency of 100kHz was considered, although it was suggested that multi-frequency measurement would yield significant improvement. They concluded that a central perturbation with contrast larger than 100% and diameter of 40mm (33.5cm^2) could be detected. This suggests that only a large haemorrhage is likely to be detected. This is probably because MIT is usually employed at higher frequencies of MHz, in order to improve the signal to noise ratio. At such frequencies, only displacement of brain by blood is likely to provide suitable tissue contrast. Gao et al performed a similar feasibility study for the use of Magnetic Resonance EIT (MREIT) [342]. The study employed a four sphere model for the head, and considered a single frequency. Both ischaemic and haemorrhagic anomalies of 50 cm^3 were simulated. The influence of addition of Gaussian white noise over time-referenced reconstruct images was examined, and the authors concluded that MREIT, which provide superior spatial resolution over conventional EIT, was capable of performing such differentiation. The results indicated that identification of haemorrhagic stroke can be achieved with higher correlation with target images than ischaemia (0.92 versus 0.67). Although this application appears to be technically possible, it would require the use of an MRI

scanner and so obviate the proposed practical advantages of EIT; imaging of stroke is already possible with proton and diffusion weighted MRI.

6.2.4 Measurement limitations in Multi-Frequency EIT

The aim of bioimpedance measurements is to measure changes in electric properties of the tissues under investigation with respect to frequency. Effectively, the measured system is also sensitive to additional confounding factors which are not desirable, such as variability over frequency and load dependency of the acquisition system or changes in contact impedance across frequency [331]. Normally, difference-imaging is employed in order to cancel out most systematic errors. This approach is effective if it can be assumed that nothing but the object of interest changes from one instance to another and that systematic errors are stationary. Unfortunately, since time-referenced data prior to stroke onset is not available, time-difference imaging is not applicable. Due to the frequency dependence of tissues in the entire domain, and the variability of the confounding factors mentioned above throughout frequency, frequency-difference imaging is not sensible either.

For relatively simple domains, which are approximately homogeneous, it is possible to find a narrow frequency band in which the background tissue is almost stationary, while a noticeable dispersion is expected for some tissue of interest. However, when more than two tissue types are involved, it is essential to perform measurements over a wide bandwidth of about 5-6 orders of magnitudes, so that integration of spectroscopic data would provide sufficient evidence for differentiation between the tissues [41;343-345]. In addition, complex structures are also likely to have heterogeneous impedance properties which correspond to a wider load range. It is likely to be difficult to maintain instrumentation linearity over a wide range of loads. In a recent study in the field, targeted specifically for the stroke application, flatness of 0.2% was achieved over the expected loads in the human head (1-70Ω) from 20Hz - 500 kHz [24;228].

6.2.5 Previous Multi-Frequency EIT studies

Ideally, EIT should be performed with absolute imaging; however, in practice this has not yet been achieved in human subjects. Instead, there has been considerable interest in the use of multifrequency data, because this offers superior tissue characterisation,

and also the ability to produce pseudo-absolute images. The latter attempts to harness spectral information in order to compensate for instrumentation errors. Nevertheless, there are, to the author's knowledge, only two clinical studies which have employed this approach. Brown et al were able to produce simple parameters of neonatal lung tissue with no anatomical images [332]. A group at Dartmouth University in the USA has produced preliminary images of breast cancer but these were not sufficiently robust to be considered suitable for clinical use without further development [9]. In another study a direct parametric estimation of Cole parameters, rather than the conventional recovery of the admittivity values, has been proposed. Yet, so far only differential mode images of the human thorax were presented with this technique [213;346].

6.3 Purpose

The underlying purpose of this study was to determine if multi-frequency electric impedance data recorded with existing instrumentation could be expected to distinguish between ischaemic stroke and intracranial haemorrhage. The specific questions addressed were:

1. How large are the expected boundary voltages changes measured with scalp electrodes?
2. Which frequency would give the best discrimination?
3. How large are such changes in relation to the variability from confounding factors such as head shape, contact impedance, variation in head tissue properties, and electrode locations?
4. Would real or quadrature measurement give better discrimination?
5. Could there be any advantage in placing electrodes over regions such as the eyes in which a low resistance path to the cranial cavity might be expected?

6.4 Design

Admittivity values from the literature reviews in Chapters 2 and 3 were incorporated into clinically realistic volumes in an anatomically accurate finite element model, in order to provide a simulation of acute cerebral ischaemia or haemorrhage. The simulated pathologies were designed to be of three levels of influence over the boundary voltages, due to the partial volume effect and proximity of the pathology to

the electrodes. In order to assess the likelihood of distinguishing the resulting changes over frequency in realistic conditions, variations due to electrode position, normal variation in tissue dielectric properties, electrode contact impedance uncertainty and extracerebral shell thicknesses deviations were modelled too. The possibility of using additional current injection sites which bypass the shunting effect of the skull and CSF was also examined in this study. Using the solver developed in Chapter 4, the resulting boundary voltage changes were computed. Due to the large number of measurement combinations, the maximal absolute changes were considered. In addition, analysis of the distribution of all other measurement channels was assessed using the median and 90th percentile indicators of that value.

6.5 Methods

6.5.1 Admittivity values employed

Admittivity values in the frequency range of 10Hz and 2.5MHz obtained using a cubic interpolation between the admittivity data points were taken from the literature review given in Chapters 2 and 3. Whenever the frequency range was only partially covered, data were extrapolated from different studies. Data obtained at temperatures closest to that of the body were used when available and if not a linear correction was applied. The model used in this study was isotropic and homogeneous; therefore, average representative admittivity values for anisotropic tissues such as scalp, skull and white matter were adopted (Figure 6-2 and Figure 6-3)

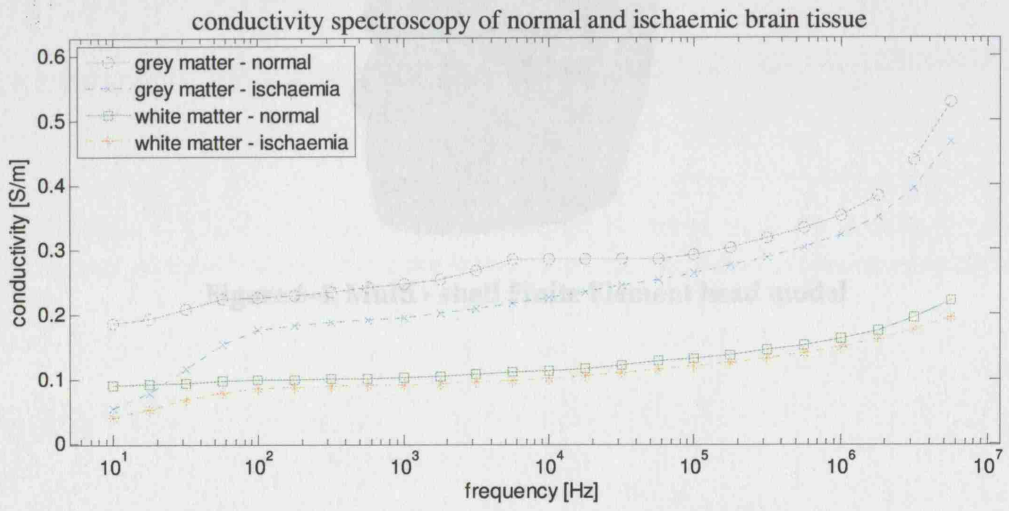

Figure 6-2. Conductivity spectroscopy of brain tissues

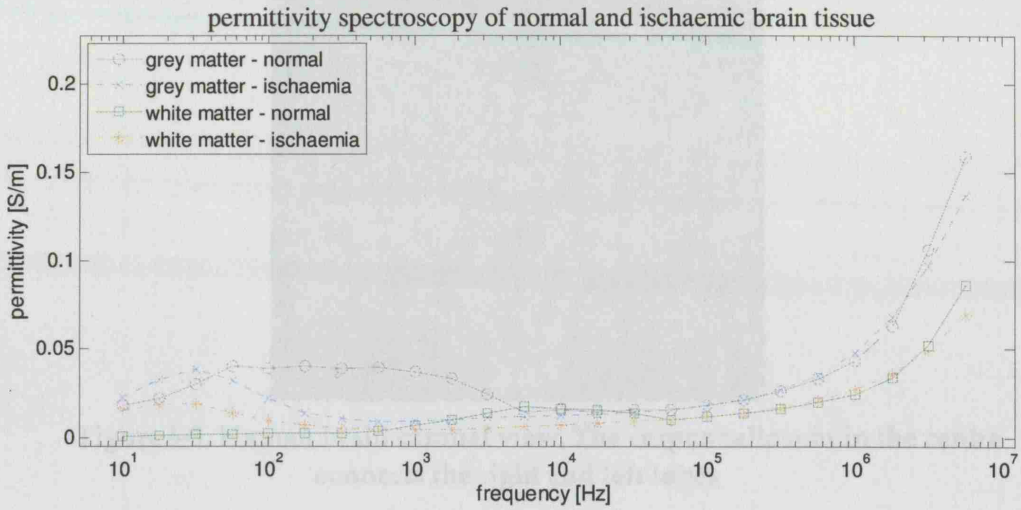

Figure 6-3. Permittivity spectroscopy of brain tissues

6.5.2 Finite Element Model

A multi layer realistic Finite Element head model of 53,336 elements [33], which comprised ventricles, white matter, grey matter, CSF, skull, scalp, eyes, optic canal, olfactory tracts and auditory meatus was generated (Figure 6-4). The brain was modelled as two separate lateral lobes connected only at the corpus callosum (Figure 6-5). These compartments were assigned with multi-frequency admittivity properties from 10Hz to 2.5MHz (Figure 6-2 and Figure 6-3).

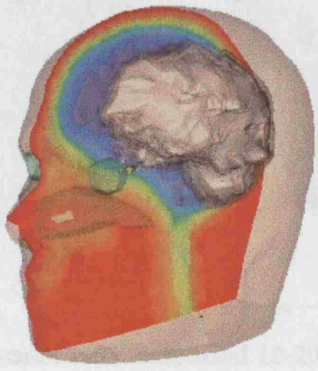

Figure 6-4. Multi - shell Finite Element head model

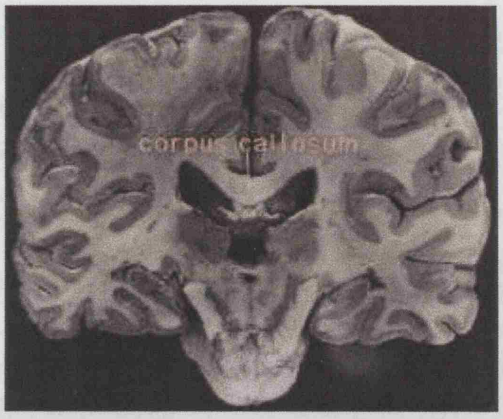

Figure 6-5. Human brain coronal view. The corpus callosum in the centre connects the right and left lobes

The model included 37 scalp electrodes (Figure 6-6), each with desired radius of 10mm. These electrodes were placed using an extended 10-20 position scheme, with the addition of 2 electrodes over the eyelids, two electrodes inside the ear canals and two electrodes in the olfactory caves (Figure 6-7).

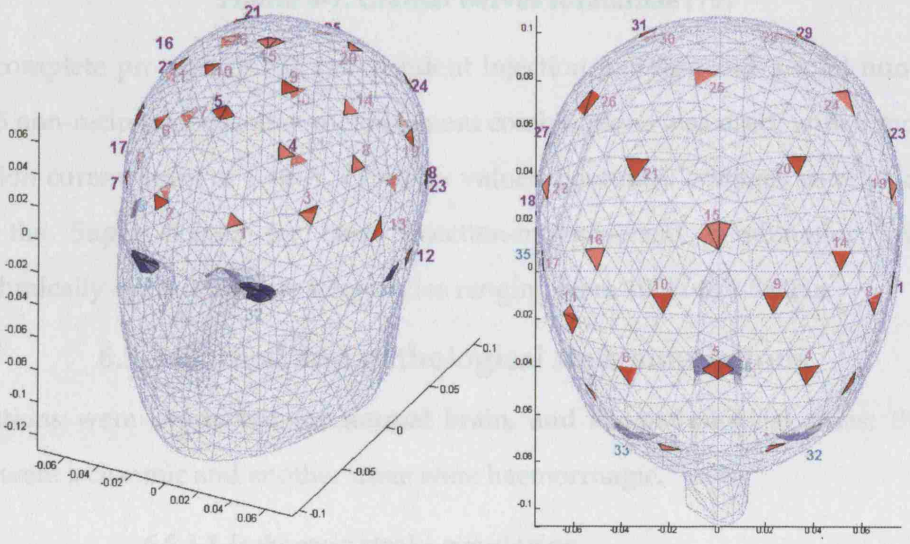

Figure 6-6. Multi shell model with extended 10-20 electrodes (red with purple numerals) and extra electrodes over the eyelids, ear canal and olfactory cave (blue with cyan numerals)

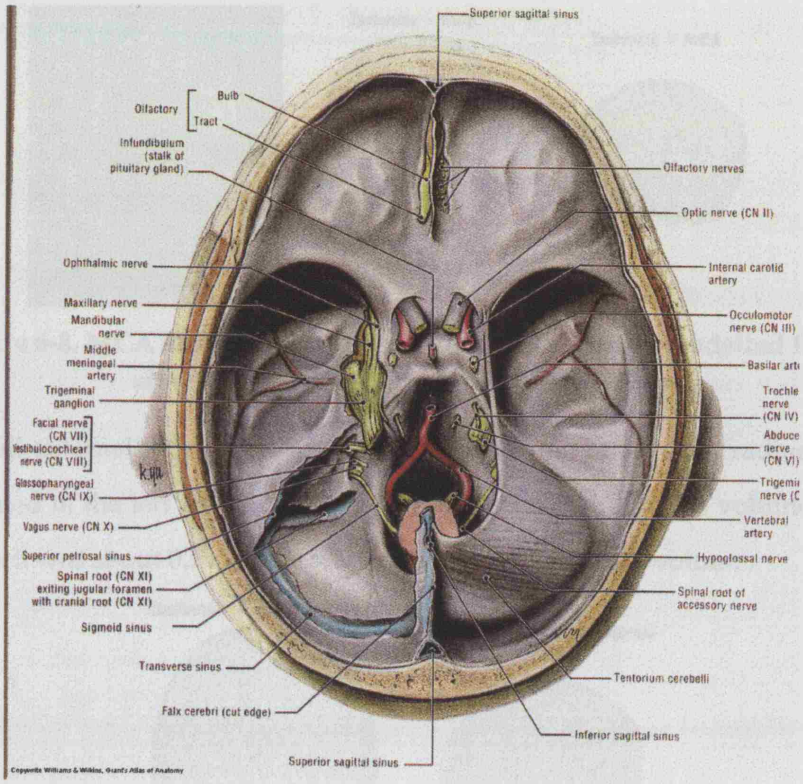

Figure 6-7. Cranial nerves foraminae [79]

A complete protocol of 528 independent injection patterns and a total number of 198,135 non-reciprocal injection-measurement combinations was used, with a modelled excitation current level of 100μA. Complex valued boundary voltages were calculated using the Super Solver for each injection-measurement combination over 12 logarithmically-spaced discrete frequencies ranging from 10Hz to 2.5MHz.

6.5.3 Normal and pathological state simulations

Simulations were conducted for normal brain, and six pathological cases: three of which were ischaemic and another three were haemorrhagic.

6.5.3.1 Ischaemic stroke simulation

Middle Cerebral Artery (MCA) infarction and two small ischaemic infarctions were simulated, represented in the following manner:

1. MCA - represented as a large ischaemic region (embodies grey and white matter) located at the right temporal lobe. The lesion comprised a volume of 44.4 cm^3, which was about 4.5% of the total grey and white matter volume in the model (977 cm^3).

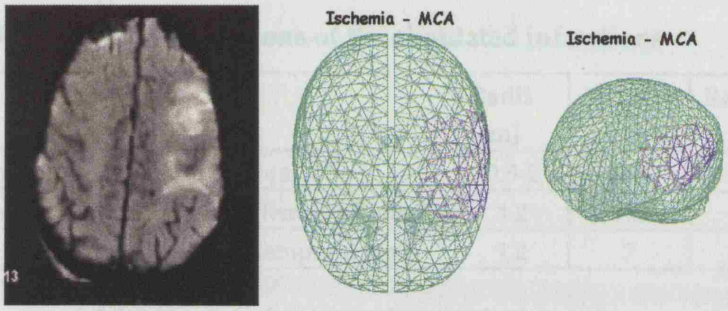

Figure 6-8. MCA ischaemia. Left: diffusion MRI; Centre: modelled from top view; Right: modelled from isometric view

2. Small external infarction – a sphere of ischaemic brain with radius of 12mm, located in the left temporal lobe. This infraction comprised a volume of 7.2cm^3, which was about 0.7% of the total grey and white matter volume.

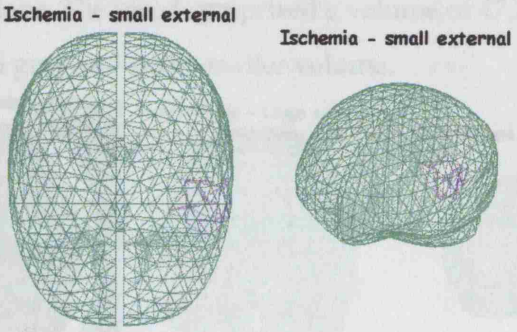

Figure 6-9. Modelled small external ischaemia. Left: top view; Right: isometric view

3. Small internal infarction – a sphere of ischaemic brain with radius of 12mm, located in the inner left temporal lobe. It had volume of 7cm^3, which was about 0.7% of the total grey and white matter volume of the brain.

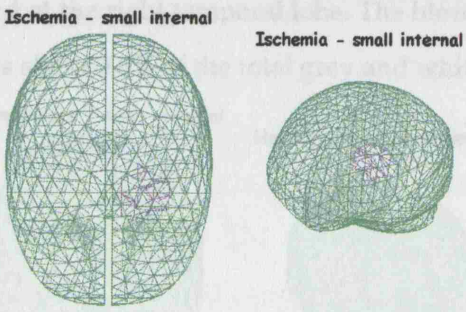

Figure 6-10. Modelled small internal ischaemia. Left: top view; Right: isometric view

Table 6-3. Volumes and locations of the simulated infarctions

Infarction	Location	Radii [cm]	Volume [cm³]	Relative volume
Large external (MCA)	Left temporal lobe	0.5-2	44.4	4.5%
Small external	Outer left temporal lobe	1.2	7.2	0.7%
Small internal	Inner left temporal lobe	1.2	7	0.7%

6.5.3.2 Haemorrhagic stroke simulation

Boundary voltage across frequency in haemorrhagic stroke pathologies were modelled in the following manner:

4. Intraparenchymal haemorrhage - represented by a large external haemorrhage, as a sphere of radius of 24mm of brain saturated with 75% blood, located at the right temporal lobe. The bleed comprised a volume of 47.7cm³, which was about 4.9% of the total grey and white matter volume.

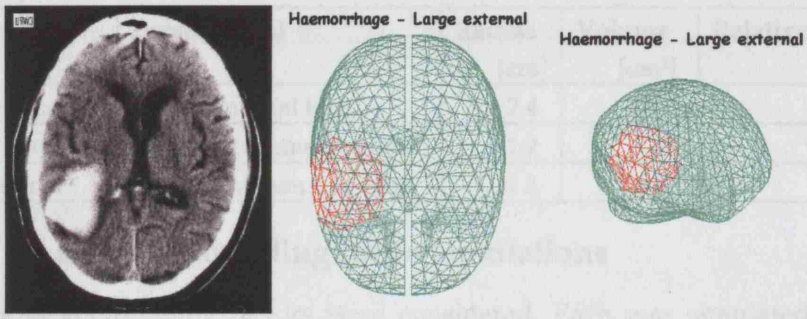

Figure 6-11. Large external haemorrhagic stroke. Left: CT of intraparechymal haemorrhage; Centre and Right: realistic head model simulation from top and isometric view

5. Small external haemorrhage - a 12mm radius sphere of brain saturated with 75% blood, located at the right temporal lobe. The bleed comprised a volume of 7.7cm³, which was about 0.8% of the total grey and white matter volume.

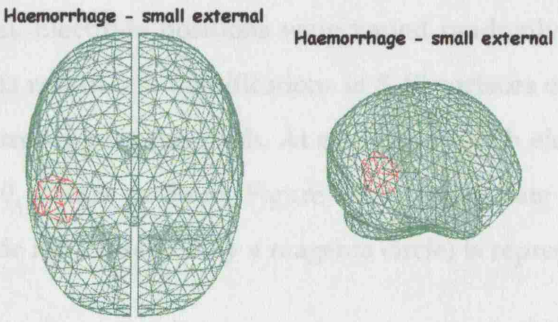

Figure 6-12. Modelled small external haemorrhage. Left: top view; Right: isometric view

6. Small internal haemorrhage - a 12mm radius sphere of brain saturated with 75% blood, located at the inner right temporal lobe. It comprised a volume of 6.8cm^3, which was about 0.7% of the total grey and white matter volume of the brain.

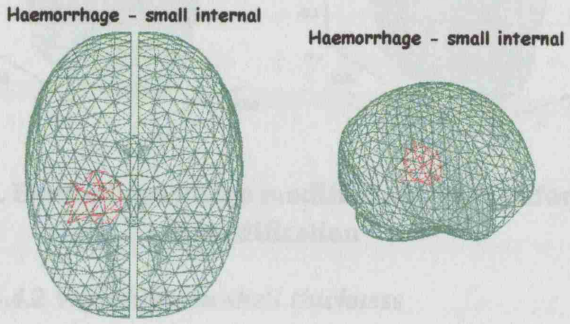

Figure 6-13. Modelled small internal haemorrhage. Left: top view; Right: isometric view

Table 6-4. Volumes and locations of the simulated bleeds

Haemorrhage	Location [cm]	Radius [cm]	Volume [cm^3]	Relative volume
Large external	Right temporal lobe	2.4	47.7	4.9%
Small external	Outer right temporal lobe	1.2	7.7	0.8%
Small internal	Inner right temporal lobe	1.2	6.8	0.7%

6.5.4 Confounding factor simulations

Four types of confounding factors were considered. Each was simulated with four increasing levels of severity.

6.5.4.1 Electrode mis-locations

Each electrode was represented in the model as a union of finite element surfaces. Electrode locations were projected over the exterior mesh surface and expanded to comply with a desired surface area. Thus, electrodes positions were modified on a discrete surfaces level. Electrode positions were varied randomly with four levels by 0.5mm to 2.5mm. This resulted in modifications of 5-18 surfaces out of the 37 surfaces representing the electrodes over the mesh. At every stage each electrode position was either translated by 0, 2.5mm or 5mm. Figure 6-14 demonstrate electrodes positions modification; electrode no. 2 (marked by a magenta circle) is represented by a different surface.

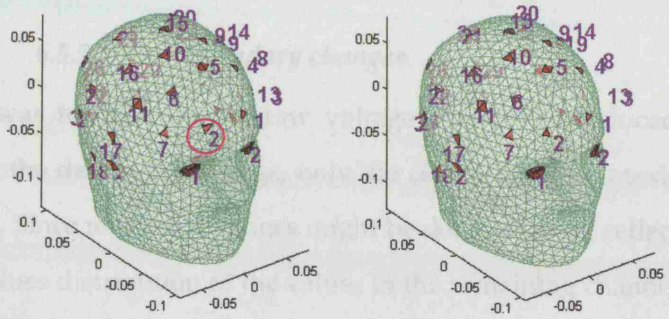

Figure 6-14. Electrode positions modification. Left: before; Right: after modification

6.5.4.2 Variations in shell thickness

A 3D linear scaling has been performed independently for each of the outer shells: scalp, skull, CSF, grey and white matter (Figure 6-15). Four increasing levels of deviation from the original values were modelled, with scaling factors ranging from 0.96 to 1.07, which resulted in mean vertices translation deviation of 0.2% to 2.5%. These changes correspond to the standard deviation in normal adult skull circumference (2cm).

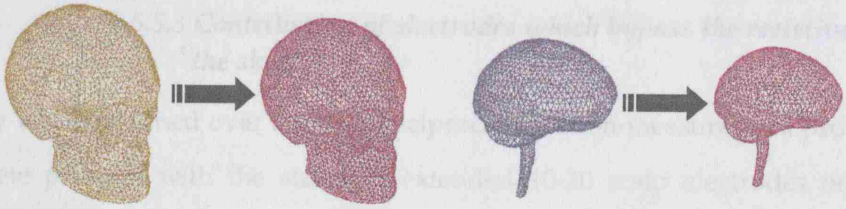

Figure 6-15. Biases in shell thickness

6.5.4.3 Reference admittivity variations

The prior conductivity and permittivity values of each of the compartments were varied by four increasing levels of bias up to a single standard deviation [48] of the Cole parameters representing the different tissues. These values were chosen to represent expected variability between normal subjects. This resulted in changes in conductivity of 2.6% to 9.1% and change of 0.9% to 7.2% in permittivity.

6.5.4.4 Reference contact impedance variation

Electrode contact impedances were modified with four levels of deviation from the original value of 1KΩ, with standard deviation ranging from 0.5KΩ up to 2KΩ.

6.5.5 Evaluation

6.5.5.1 Raw boundary changes

The first step was to quantify the raw voltage changes introduced by each of the pathologies. As the data set was large, only the channels of the maximal change were considered first. Since maximal changes might be deceptive and reflect erroneously the majority, the values distribution of the values in the remaining channels was obeserved as well.

6.5.5.2 Errors and confounding factor simulations

At this stage, the effect of the confounding factors was quantified. Since channels with low standing voltages may have been more sensitive to the confounding factors (in percentage), values below the median were ruled out. This was on the basis that careful injection - measurement protocol design would exclude them. The mean variation and the standard deviation were calculated for each bias type, in order to account for the contribution of the confounding factors within each frequency and between frequencies.

6.5.5.3 Contribution of electrodes which bypass the resistive effect of the skull

The study was performed over two non-reciprocal injection-measurement protocols: 1) A complete protocol with the standard extended 10-20 scalp electrodes only. 2) A complete protocol which involved at least a single pericranial nerve electrode. This way the contribution of the additional electrodes which bypass the shunting effect of the skull and CSF could be quantified.

6.5.5.4 Real vs. complex boundary voltages

The simulations accounted for both the real and the imaginary components of the admittivity; hence, at the first instance the real part of the boundary measurements is considered, later the evaluation process is repeated for the complex. The additive information content related to the imaginary component of the data was quantified in this way.

6.6 Results

6.6.1 Boundary voltages with standard electrode positioning

6.6.1.1 Raw boundary changes - real component

Considering the simulations results of brain in normal state as a reference, the maximal boundary voltage change appeared for all pathologies in the lowest modelled frequency of 10Hz (Figure 6-16). In terms of absolute voltages, within each frequency, the peak changes ranged between +0.2 to +1.9% ($8.6\ 10^{-6}$ V to $8.4\ 10^{-5}$ V) for ischaemia, whereas for haemorrhage they ranged from -0.8 to -7.1% ($-4.3 \cdot 10^{-5}$ V to $-3.8 \cdot 10^{-4}$ V). At 2.5MHz, the changes reduced to +0.07 to +0.3% and -0.7 to -5.5% for ischaemia and haemorrhage respectively (Figure 6-17 and Figure 6-18). Maximal changes over frequency were about 0.2 to 1.7% for ischaemia and 0.3 to 2.4% for haemorrhage. (Figure 6-17 and Figure 6-18).

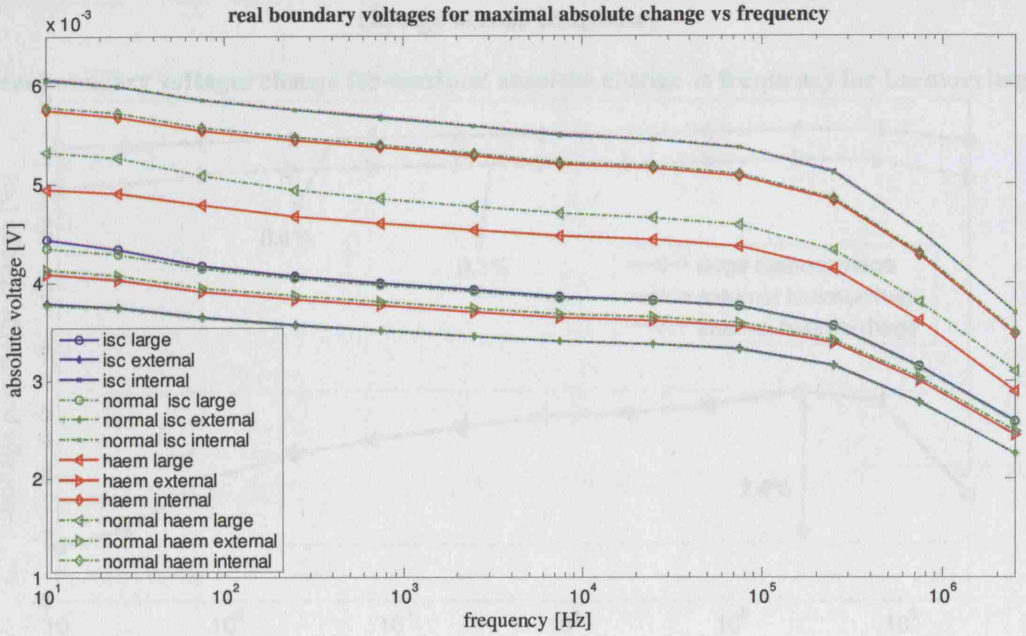

Figure 6-16. Absolute voltages of the real component with the maximal change vs. frequency. The blue lines stands for the three ischaemic pathologies, red for haemorrhagic pathologies, and green lines stands for their respective normal states

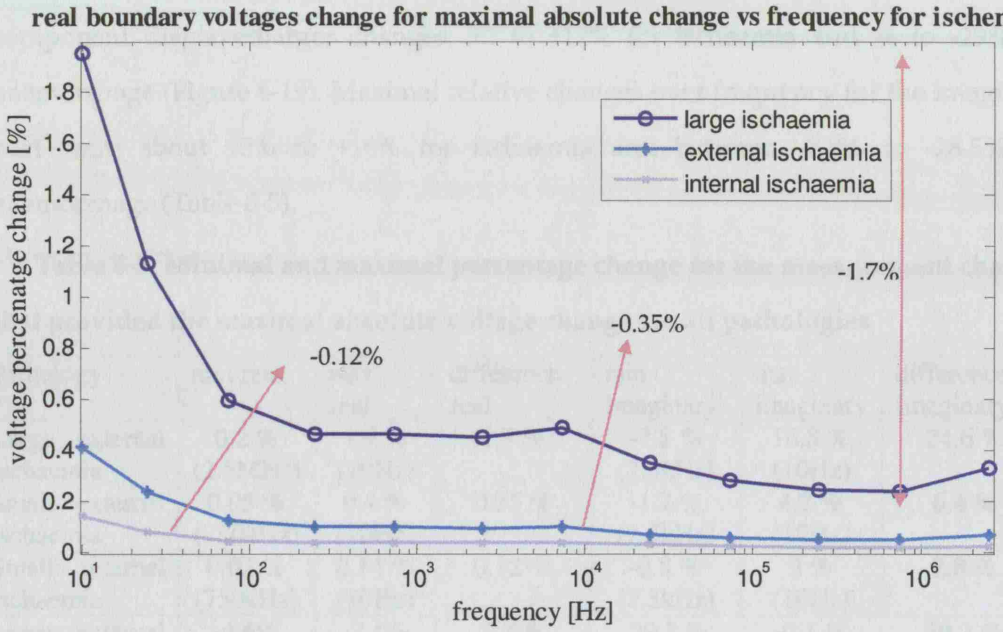

Figure 6-17. Percentage change for absolute maximal changes of all ischaemic lesions across frequency. The values near the pink arrows stand for the maximal change across frequency

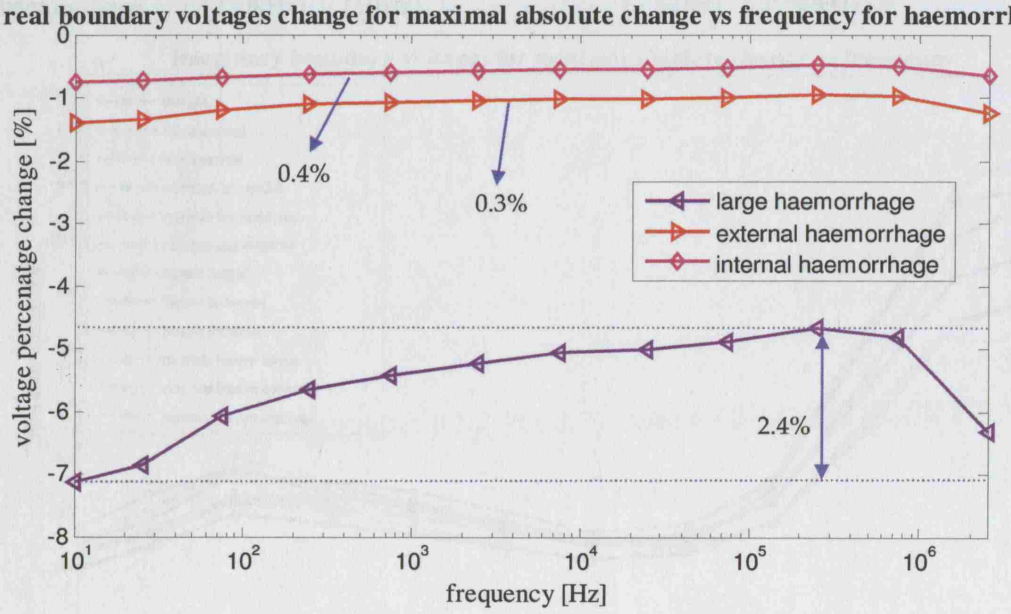

Figure 6-18. Percentage change for absolute maximal changes of all haemorrhagic lesions across frequency. The values near the blue arrows stand for the maximal change across frequency

6.6.1.2 Raw boundary changes - imaginary component

The standing voltages for the imaginary component were smaller by about an order of magnitude compared with the real cases. However, in terms of percentage change, this

component displayedlarger changes: +2 to +17% for ischaemia and -4 to -29% for haemorrhage (Figure 6-19). Maximal relative changes over frequency for the imaginary part were about +3% to +16% for ischaemia and between -3.5% to -28.5% for haemorrhage (Table 6-5).

Table 6-5. Minimal and maximal percentage change for the measurement channel that provided the maximal absolute voltage change for all pathologies

Pathology	min real	max real	difference real	min imaginary	max imaginary	difference imaginary
Large external ischaemia	0.2 % (2.5MHz)	1.9 % (10Hz)	1.7 %	-7.8 % (7.5kHz)	16.8 % (10Hz)	24.6 %
Small external ischaemia	0.05 % (750kHz)	0.4 % (10Hz)	0.35 %	-1.7 % (7.5kHz)	4.7 % (10Hz)	6.4 %
Small internal ischaemia	0.02 % (750kHz)	0.14 % (10Hz)	0.12 %	-0.8 % (7.5kHz)	2 % (10Hz)	2.8 %
Large external haemorrhage	-4.6% (250kHz)	-7.1% (10Hz)	2.4%	-29.3 % (25Hz)	-0.1 % (750kHz)	29.2 %
Small external haemorrhage	-1 % (250kHz)	-1.4% (10Hz)	0.4%	-4.7% (75Hz)	-0.1 % (750kHz)	4.6 %
Small internal haemorrhage	-0.5% (250kHz)	-0.8% (10Hz)	0.3%	-3.6 % (7.5kHz)	-0.1 % (750kHz)	3.5 %

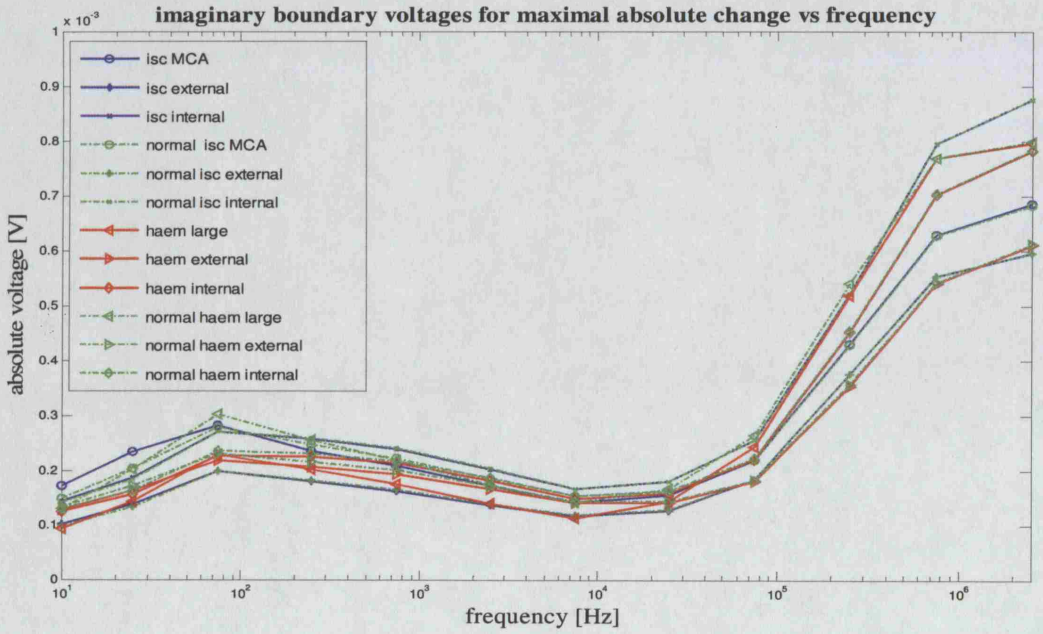

Figure 6-19. Absolute voltages of the imaginary component with the maximal change vs. frequency

6.6.1.3 Measurement distribution

About 2 - 4.3% of the total number of channels, displayed a change which exceeded half of the maximal change of the real component (Table 6-6). Figure 6-20 and Figure

6-21 provide another insight into the distribution of injecting and sensing electrodes with respect to the pathology size and location.

Table 6-6. Minimal and maximal number of channels above half maximum change value

	Minimal number of channels above half max	Maximal number of channels above half max
Large external ischaemia	5616 (at 10Hz)	6434 (at 2.5KHz)
Small external ischaemia	4976 (at 10Hz)	6324 (at 7.5KHz)
Small internal ischaemia	3798 (at 10Hz)	4540 (at 2.5MHz)
Large external haemorrhage	6948 (at 2.5MHz)	8050 (at 2.5KHz)
Small external haemorrhage	5756 (at 2.5MHz)	6810 (at 250KHz)
Small internal haemorrhage	4128 (at 75Hz)	4502 (at 2.5MHz)

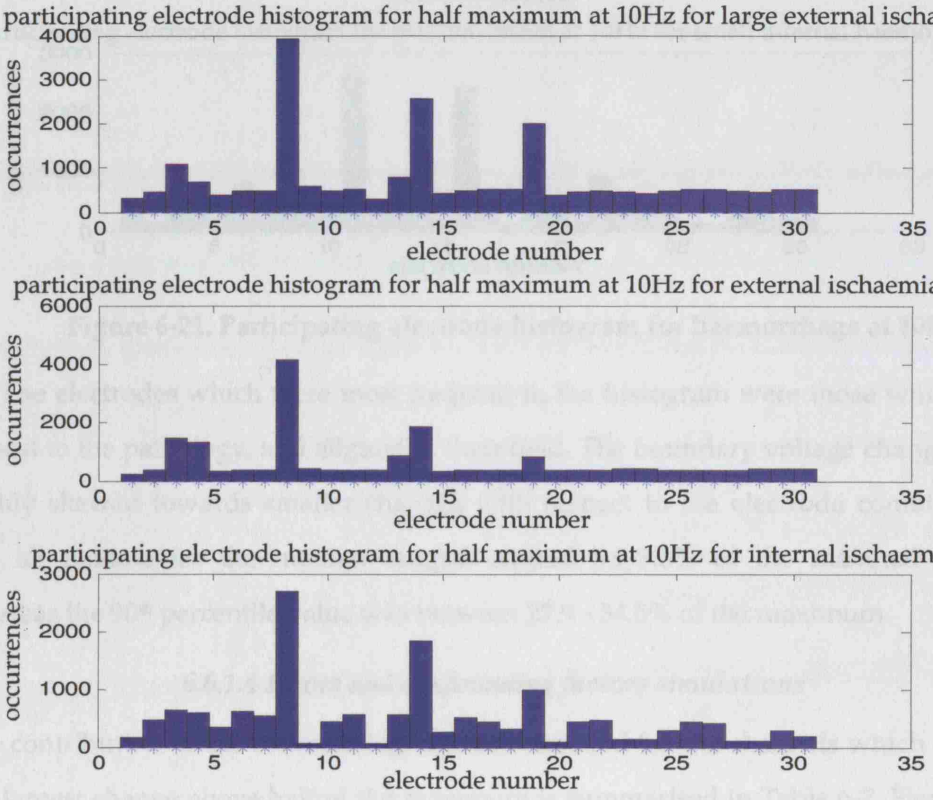

Figure 6-20. Participating electrode histogram for ischaemia at 10Hz

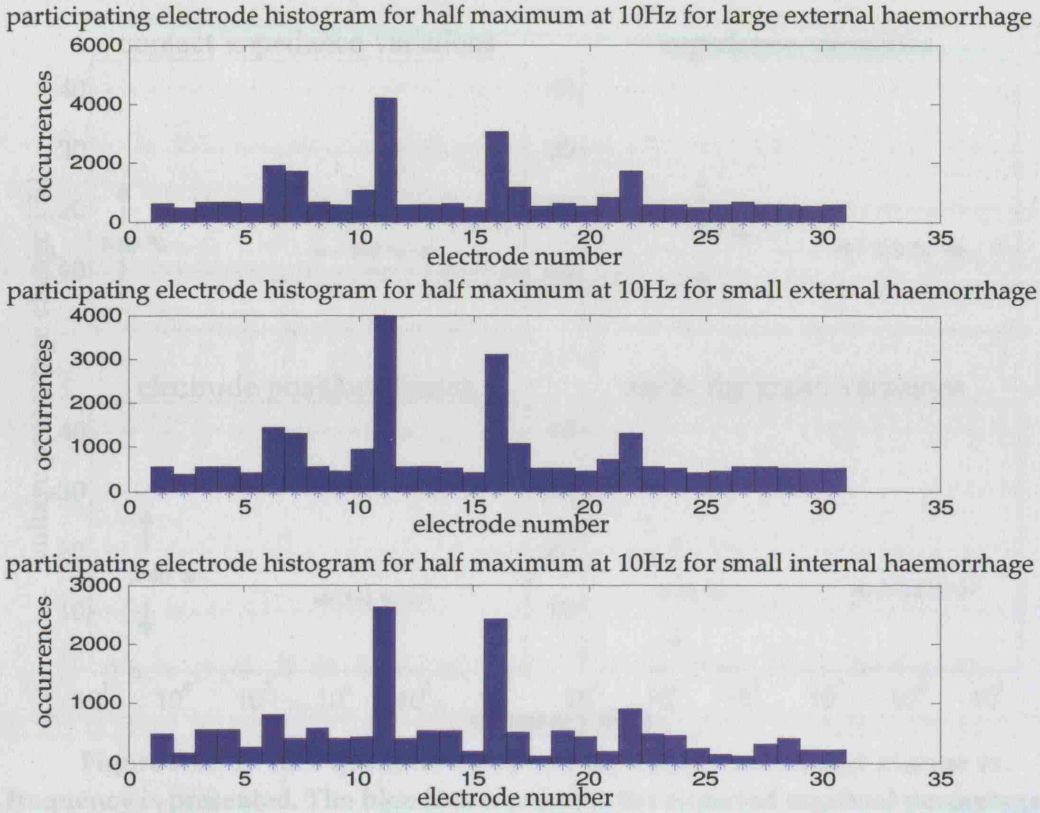

Figure 6-21. Participating electrode histogram for haemorrhage at 10Hz

The electrodes which were most frequent in the histogram were those which were closest to the pathology, and aligned in their field. The boundary voltage changes were highly skewed towards smaller changes with respect to the electrode combinations. For all pathologies the median ranged around 5.9-9.3% of the maximal change, whereas the 90th percentile value was between 27.9 - 34.5% of the maximum.

6.6.1.4 Errors and confounding factors simulations

The contribution of the confounding factors estimated for the channels which showed the largest change above half of the maximum is summarised in Table 6-7. Figure 6-22 demonstrates the effect of the different confounding factors with comparison to the maximal change expected for the large ischaemic condition.

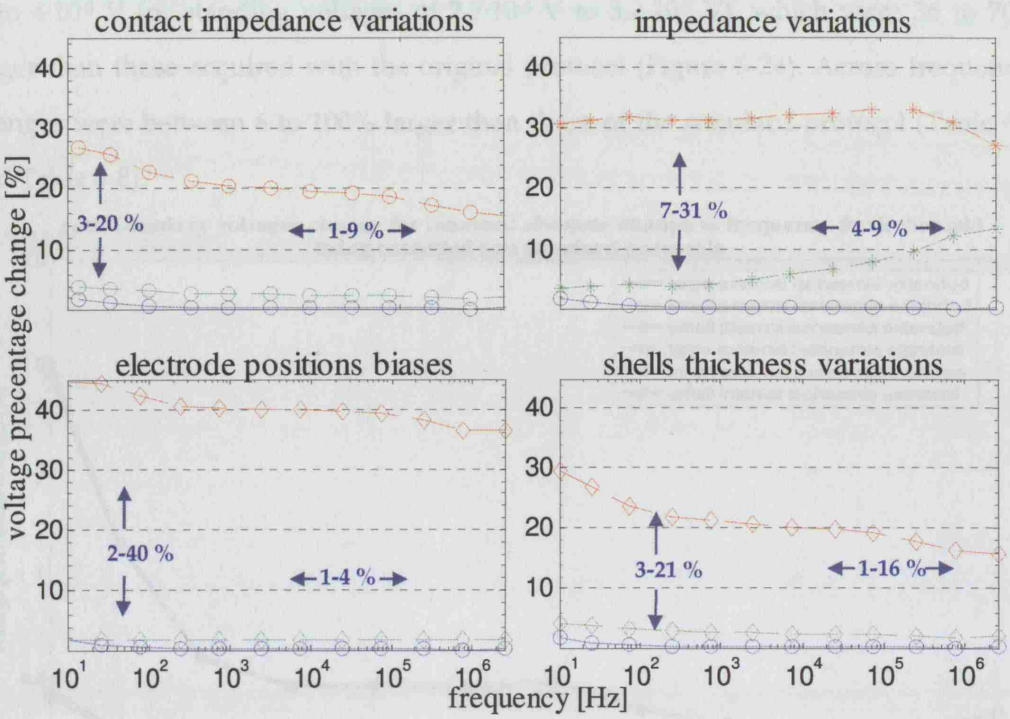

Figure 6-22. In each quadrate a graph of the voltage percentage change vs. frequency is presented. The blue line represents the expected maximal percentage change in boundary voltages for a large ischaemic lesion (as in Figure 6-17); the red and green lines stand for the expected changes due to the modelled confounding factors

Table 6-7. Changes from normal brain conditions introduced by the confounding factors

	Electrodes positions		Admittivity variability		Shells thickness		Contact admittivity	
	mean %	std %	mean %	std %	mean %	std %	mean %	std %
Real	6.3-38.6	1.6-4.2	0.8-43.7	0.05-3.2	1.2-23.5	0.6-4.2	0.8-22.2	0.6-4.4
Imaginary	1.4-41.2	0.5-14.5	11.6-19.8	13.6-24.5	6.5-80.9	2.6-53.8	4.6-76.2	1.5-42.5

6.6.2 Contribution of recording with pericranial electrodes

6.6.2.1 Real component

For an extended protocol including at least one of the additional electrodes, the peak changes for all lesions appeared at 10Hz. For ischaemia the maximal absolute changes were between +0.2 to +2% ($8 \cdot 10^{-6}$ V to 10^{-4} V for standing voltages between $3.5 \cdot 10^{-3}$ V to $4.3 \cdot 10^{-3}$ V). This was 3 to 43% larger than those acquired with the original protocol (Figure 6-23). For the haemorrhagic lesions, maximal changes were -1.2 to -12.1% ($3 \cdot 10^{-4}$

V to $4 \cdot 10^{-5}$ V for standing voltages of $2.7 \cdot 10^{-3}$ V to $3.2 \cdot 10^{-3}$ V), which were 36 to 70% larger than those acquired with the original protocol (Figure 6-24). Across frequency, changes were between 6 to 100% larger than those of the standard protocol (Table 6-5 and Table 6-8).

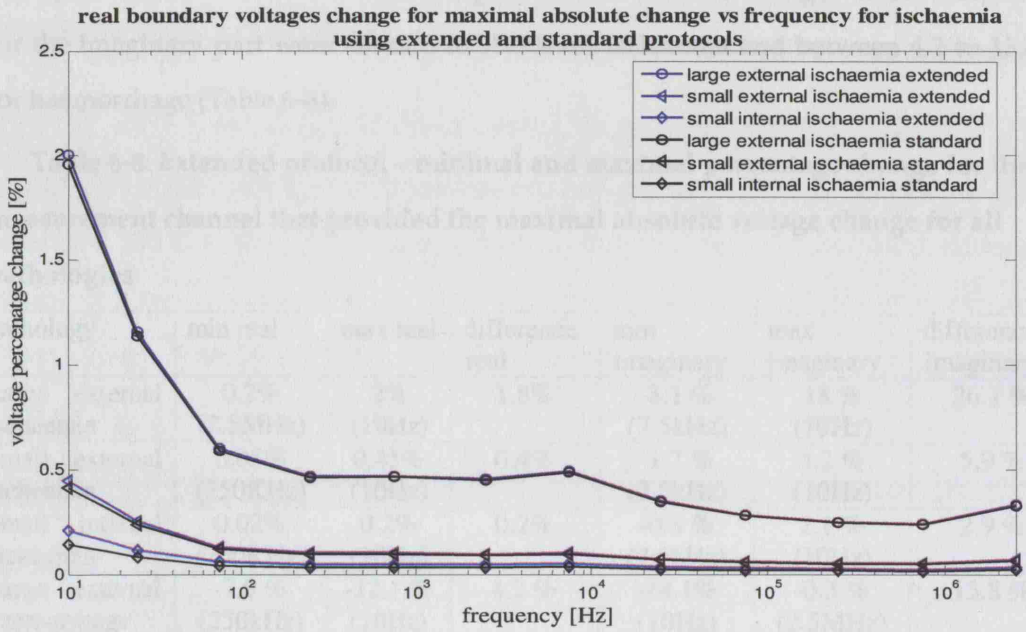

Figure 6-23. Extended protocol - real part of boundary voltages percentage change for ischaemia vs. frequency. Blue line stands for the extended protocol (extra electrodes) and black for the standard protocol

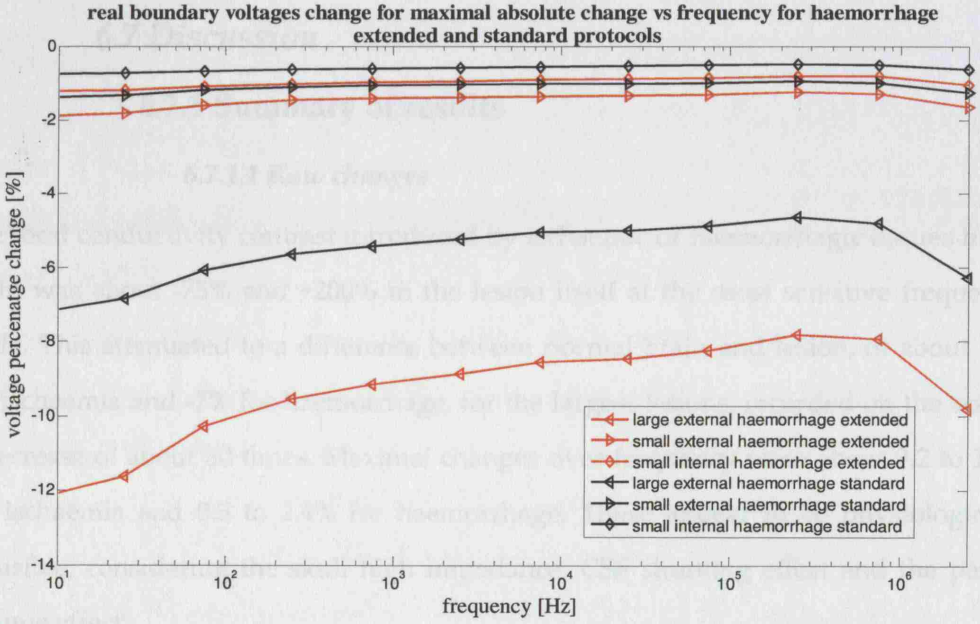

Figure 6-24. Extended protocol - real part of boundary voltages percentage change for haemorrhage vs. frequency. Red line stands for the extended protocol (extra electrodes) and black for the standard protocol

6.6.2.2 Imaginary component

Similarly, the standing voltages for the imaginary component using this protocol were smaller by about an order of magnitude compared to the real cases. In terms of absolute percentage change, for ischaemia a change of +2.1 to +18% was acquired and a change of -4.3 to -14.1% for haemorrhage. Maximal relative changes across frequency for the imaginary part were about 3 to 15.5% for ischaemia and between 4.2 to 13.8% for haemorrhage (Table 6-8).

Table 6-8. Extended protocol – minimal and maximal percentage change for the measurement channel that provided the maximal absolute voltage change for all pathologies

Pathology	min real	max real	difference real	min imaginary	max imaginary	difference imaginary
Large external ischaemia	0.2% (2.5MHz)	2% (10Hz)	1.8%	-8.1 % (7.5kHz)	18 % (10Hz)	26.1 %
Small external ischaemia	0.05% (750KHz)	0.45% (10Hz)	0.4%	-1.7 % (7.5kHz)	4.2 % (10Hz)	5.9 %
Small internal ischaemia	0.02% (750KHz)	0.2% (10Hz)	0.2%	-0.8 % (7.5kHz)	2.1 % (10Hz)	2.9 %
Large external haemorrhage	-7.9 % (250kHz)	-12.1 % (10Hz)	4.2 %	-14.1% (10Hz)	-0.3 % (2.5MHz)	13.8 %
Small external haemorrhage	-1.3 % (250kHz)	-1.9 % (10Hz)	0.6 %	-6.4 % (25Hz)	-0.1 % (750kHz)	6.3 %
Small internal haemorrhage	-0.8 % (250kHz)	-1.2 % (10Hz)	0.4 %	-4.3 % (7.5kHz)	-0.1 % (750kHz)	4.2 %

6.7 Discussion

6.7.1 Summary of results

6.7.1.1 Raw changes

The local conductivity contrast introduced by ischaemic or haemorrhagic tissues in the brain was about -75% and +200% in the lesion itself at the most sensitive frequency, 10Hz. This attenuated to a difference between normal brain and lesion, of about +2% for ischaemia and -7% for haemorrhage, for the largest lesions, recorded on the scalp - a decrease of about 30 times. Maximal changes over frequency were about 0.2 to 1.7% for ischaemia and 0.3 to 2.4% for haemorrhage. These appear to be physiologically plausible, considering the skull high impedance, CSF shunting effect and the partial volume effect.

For ischaemia which occurs at the left temporal lobe region and inward, the closest electrodes (i.e. electrodes no. 3, 8, 14 and 19 in Figure 6-6) were the most sensitive to the pathology; deeper (lower sections of Figure 6-20) changes were sensed less locally and with weaker intensity. A similar behaviour was apparent for haemorrhages in a symmetrical manner, as they were simulated at the right temporal lobe (lower sections of Figure 6-21).

6.7.1.2 Low resistance path to the cranial cavity channels

Maximal changes using cranial foraminae as a low resistance path to the cranial cavity were 3 to 43% and 36 to 70% larger than those acquired with the standard electrodes positioning for ischaemia and haemorrhage respectively. Across frequency, changes were between 6 to 100% larger than those of the standard protocol. A comparison between all pathologies showed that the improvement in the magnitude of the signal peak were more profound for the smaller and internal lesions.

6.7.1.3 Confounding factors

The introduced variation caused apparent scalp voltage changes which were of up to 40% with respect to the standing voltages of the most sensitive channels in 10Hz. Changes across frequency were up to 16%. These changes were approximately up to 20 times larger in absolute value and larger by up to an order of magnitude across frequency compared with those expected due to the large ischaemic lesion alone.

6.7.2 Technical issues

The aim of this study was to provide qualitative estimates as for the feasibility of stroke differentiation. Therefore, several compromises and approximations were necessarily made in this modelling.

Quasi-static approximation - The forward model used in this study employed a quasi-static approximation of Maxwell equations to represent the governing equations. Therefore, measurable discrepancies between its predictions and the true boundary voltages may be expected to arise; for bioimpedance measurements, these probably are significant above 1MHz [219]. To the author's knowledge, no studies were performed to quantify the differential errors for 3D models, rather than the absolute errors, arising from this modelling approximation. In recent study in 2D, maximal absolute changes

of 1% were quantified between the two approximations at 10MHz [347]. The differences between the standing voltages in various channels with the two approximations were systematic and followed a consistent trend. This may suggest that the expected impact of the quasi-static approximation would alter the absolute values by less than 1%, and differentially by a small, but yet uncertain, amount. For future studies, it would be desirable to quantify the boundary voltages changes in higher frequencies using a three dimensional full-Maxwell equation forward modeller.

Isotropy - Tissues were modelled as isotropic despite the fact that the scalp, skull and white matter are anisotropic. The impact of anisotropic modelling of white matter is probably negligible, as this tissue is internal and anisotropy can be approximated to be equally oriented. Conversely, anisotropy of the scalp tissue may be expected to have a greater influence on injected current paths. Its anisotropy ratio is about 3, but the ultimate influence of this is unknown. More accurate modelling to account for anisotropy is desirable; in fact, this work is being undertaken by Abascal J.F. in the UCL group at the time of writing, but unfortunately was not available in time for this work. In a recent EEG source modelling study, in which anisotropy of the skull and white matter was accounted for, discrepancies of about 5% in EEG potentials were observed between an isotropic model and anisotropic ratio of 3 [56].

Admittivity values - Another modelling issue is the fidelity of the admittivity values employed in this study. As argued in Chapter 3, much of the available knowledge regarding admittivity of tissues in the head and impedance behaviour during stroke is incomplete and had to be estimated. When reasonable uncertainties in the reference admittivity were modelled, this altered the standing voltage by up to an order of magnitude more than changes due to intracranial pathology. The changes in boundary voltages due to pathology using a different reference admittivity value were different by up to 25% from those obtained for the selected reference. More reliable data regarding human normal and pathological admittivity is desirable. One possible way, which could avoid further animal studies, would be to derive impedance changes from Diffusion Weighted MRI (DWI) images in ischaemia. DWI reflects water mobility (mainly in the extra-cellular fluid space) and therefore, the DWI signal changes during cell swelling. There is probably an almost linear relationship between the DWI tensor

and the anisotropic admittivity [55]. However, large admittivity changes of 20% and above occur in the region of stroke and translate into relatively small boundary changes due to the non-linearity of the problem; it therefore seems likely that the uncertainties in estimates of the pathological regions will have had relatively little effect on the overall conclusions.

Geometry - The scalp was modelled as a continuous muscle surrounding the entire head, although, in practice it covers only partial segments of the scalp. In addition, the skull was modelled as a single homogeneous layer, rather than by three layers of cancellous bone separated by a vascular space, as suggested in Chapter 2. Due to current limitations, modelling of these structures, as well as fine structure as the CSF is difficult and problematic. Such fine structures are difficult to segment; since MRI provides poor contrast for bone tissue, and since generation of high quality meshes would require a tremendous number of elements in order to represent such thin layers. This would result in a sharp increase in computational demand, for processing the forward model. The quantitative effect of this approximation is unclear. However, there was a good approximation between modelling values and those recorded *In-vivo* for the case of standing voltages [231], so this is unlikely to have been a major source of error. Future developments in segmentation and meshing techniques should allow modelling of the head with higher resolution, and this should allow quantification of these effects.

Limitations in modelling of confounding factors - Modelling of confounding factors was subject to incomplete published data regarding the variability of these factors, as well as practical lab experience. As the general purpose of the study was to quantify how these factors compete with the true physiological related signal changes, it is plausible to accept the impact of these factors as representing the right order of magnitude rather than accurately quantifying their effect. It is a subject for further studies to provide more accurate and quantitative results related to these factors.

6.7.3 Are the expected boundary voltages changes large enough to be reliably imaged with MFEIT?

In an ideal world, when geometry is known accurately and in the absence of any of other confounding factors, an acquisition system is required to be accurate and robust

to measure signals smaller than 0.1% with (linear) SNR of 10 within and across frequency in order to capture the raw changes associated with all modelled pathologies. These requirements can be considered as optimistic bounds, as these relate to the largest changes, and as the channel measuring the maximal change is unknown, a reasonable hardware requirement might be required to be accurate by even another order of magnitude. These harsh requirements set severe constraints on the accuracy of instrumentation, and goes beyond the ability of any available system hitherto. Available instrumentation, such as the UCH Mk2.5, are capable of measuring all differential changes within each frequency, but can only reliably treat changes across frequency larger than 0.2% [24]. On the face of it, therefore, this suggests that current instrumentation is not sufficiently accurate.

MFEIT reconstruction can benefit from both spatial and spectral averaging and this may be expected to improve the overall acquired SNR. According to Table 6-6, about 2 - 4.3% of the overall channels provided measurement changes larger than half of the maximal signal. Thus, it is plausible, that for carefully selected channels, this figure can approach 10% of the number of channels. Considering about 1000 channels, and about 10 measured frequencies, with random normal noise distribution, an overall SNR improvement by a factor of 30 can be expected. Of course, this figure depends upon the noise characteristics and its statistical distribution. However, with these assumptions, MFEIT image reconstruction might be successful for this demanding application.

6.7.4 Which frequency provides the best discrimination?

Differences across frequency were clearly greatest around the 10Hz region, and were about 80% of the absolute changes. The most profound boundary voltage gradient trend for ischaemia appeared at the very low frequency band of 10Hz - 100Hz, which agrees with the α dispersion centre frequency of grey matter [119], whilst for haemorrhage additional notable trend could be found at the frequency range above 750 KHz. This result conforms with the β-dispersion of the blood [48;133]. The current instrumentation available in the UCL group only extends up to about 1MHz [24]. As such, the practical consequence of this work is that recording should be made down to 10Hz in order to focus on the α-dispersion of ischaemic tissue. However, for the design of future systems, an extension up to several MHz is desirable as this would permit the

additional discrimination which is associated with the β-dispersion of blood in haemorrhage.

6.7.5 How large are the changes in relation to the variability from confounding factors?

Modelling of likely confounding factors was alarming. These factors gave rise to biases in the boundary voltages which were up to an order of magnitude larger than the expected changes due to the largest pathological changes within each frequency and across frequency. Since these biases appear to have an unpredictable frequency signature, their elimination cannot be performed through frequency difference imaging. These results were consistent with previous reports from Kolehmainen et al who studied the effect of modelling errors in boundary shape, electrodes location and size, and contact impedance variations [40]. For random distribution of 10% in contact impedance, absolute image reconstruction with trigonometric current pattern was completely corrupted. Similar results were obtained for a shifting of quarter of the electrodes by 10% of their mutual distance, and by skewing the circular model used by 1%.

However, it may be possible to reduce the size of such errors with careful experimental procedures. Taking possible errors in turn:

1) Exact electrode positions acquisition - This could be obtained manually in a few minutes by the use of a digitising wand or photogrammetry method [348]. In UCL group, a method has been developed in which electrode positions were obtained with photogrammetric triangulation of positions from a series of images around the subject obtained with a handheld digital camera; it was possible to obtain a precision of about one millimetre [349].

2) Patient specific finite element meshes - A method for production of patient specific finite element models has been recently development in UCL group [350]. More accurate patient specific models could allow incorporation of precise positions of electrodes obtained with such methods. Unfortunately, this could not help directly for imaging stroke, as the whole advantage of EIT is that it could replace CT or MRI - such images would therefore not be available in an acute casualty situation. However, surface information obtained with a digitising wand or external light based

photogrammetric method might still be used to improve the accuracy of the geometric model employed in image reconstruction. This could be by mesh warping of a prototype head model to conform with measured registration points [226;351], by selection of one of a bank of anatomical images obtained with patient specific meshes as above, or by embedding shape reconstruction within the reconstruction process as suggested for Optical Tomography [352].

3) Contact impedance - Variability in contact impedance could also be recovered as part of the inverse problem procedure [353-355]. Alternatively, an estimate by means of two terminals measurements can be considered, possibly as part of a modified inverse problem formulation.

4) Admittivity reference values - Initial values could in principle be inferred from MREIT or Diffusion Weighted MRI or as an average from absolute EIT imaging [88] although the accuracy of these approaches remains to be established.

Assuming all confounding factors could be treated, additional study is required to validate that these were diminished to a sufficient level, such that the changes related to pathology were not obscured.

6.7.6 Would real or quadrature measurements give better discrimination?

It was shown that the imaginary component of EIT measurements can be derived with higher accuracy by using Kramers-Kronig relations rather than by direct acquisition of this component. Therefore, this component does not yield additional independent information, and should be considered for acquisition only in case its SNR is equivalent to that of the real part.

In this study, the absolute voltage changes and differences across frequency of the imaginary component were greater than those of the real component by several times, whilst the standing voltages of the imaginary component were smaller by about an order of magnitude. Considering the fact that absolute measurement of this component, using most recent acquisition systems, is far less accurate than measurement of the real part, such measurements are unlikely to confer an advantage.

6.7.7 What is the expected advantage in using pericranial electrodes?

In principle, it might have been expected that the use of additional electrodes placed near cranial foraminae might have short-circuited the large resistivity of the skull and the CSF shunting effect and conferred a significant advantage. However, in the event, there was only an improvement within and across frequency which was up to a factor of 1.7 and 1.75. These findings appear reasonable, since, in the absence of shunting, current is delivered from a smaller injection site; thus, boundary voltages change noticeably only if the lesion is located immediately adjacent to high current density pathways. The distribution of the sensitive electrodes for the extended protocol was broader than before, which suggests that this paradigm delivers more current through the internal regions of interest, and therefore enables more electrodes, rather than just the neighbouring electrodes, to sense the lesion. This important feature could allow expansion of the application for smaller and deeper lesions, which are difficult to sense by the conventional procedure.

7 SUMMARY AND FUTURE WORK

7.1 Summary

The thesis covered three infrastructural topics: 1) Accurate representation of the human head through a comprehensive study of the inner structures of the head and the dielectric properties related to its constituting tissues for normal and pathophysiological states. 2) Development of methods for modelling large-scale EIT problems. 3) Development of methods for solving large-scale non-linear inverse problems. Additionally, in a feasibility study, which utilised these tools, the possibility of acute cerebral stroke type differentiation by MFEIT was examined.

The first study set to map the spectral behaviour of the tissues constituting in the human head. Reported impedance measurements which were reviewed differed in frequency range, measurement method, temperature, species, tissue condition and preparation procedures. Studies related to pathophysiological conditions differed also in the severity and method of invoking the pathology. Since the subject is interdisciplinary, part of the measurements were performed by researchers that either had insufficient physiological knowledge regarding the measured phenomena, or were not equipped with sufficient knowledge regarding acquisition and instrumentation considerations. Consequently, the overall reports that were considered valid, provided only an incomplete representation of the true impedance characteristics of the human head tissues. The study discusses ways to adjust the available data to provide a physiologically reasonable compromise that suit the desired setup and conditions.

An insight into impedance changes related to pathophysiological processes revealed that previous modelling work in the field treated these processes with rather simplistic naive reasoning, and therefore, a deeper understanding of the complex influence of these processes is necessary for reliable modelling. The author acknowledges the intrinsic difficulties associated with acquisition of *In-vivo* bioimpedance measurements, but yet believes that for the evolution of medicine, it would be valuable to obtain intra-operative measurements of the human head tissues over a wide frequency range. Such measurements could be acquired as part of epileptic surgery, which requires invasive interference in the head anyway.

The study observed the human head tissues from an EIT modelling perspective, and highlighted the need for structural modelling of the human head with a higher precision. In particular, the anisotropic properties of the scalp and white matter tissues should be taken into account, as well as the inclusion of additional structures and layers, such as modelling the skull by three layers and modelling of the eyes and intracranial nerves.

To the author's knowledge, this has been the first such comprehensive review, in particular in the way in which the data was extrapolated so as to provide a continuous basis for modelling studies. Of course, the underlying data set was incomplete, but hopefully this will provide, for the first time, a sound basis for any further modelling studies in this area and provoke further experimental work in order to fill in the gaps in the data. This could also provide guidance for hardware specifications and acquisition requirements for the field of EIT and for related fields as MIT, MREIT and inverse source EEG.

The second aim of the thesis was to develop infrastructural tools, which could allow prompt calculation of detailed and accurate forward models. The study identifies the main computational bottleneck in forward modelling to be the multiple solutions of the system matrix, which are derived from FEM discretisation. This bottleneck was addressed from two different angles: minimisation of the number of linear systems that are required to be solved and stored, and reduction of the computational effort required for preconditioning and solving these systems. The first bottleneck was approached by the proposed monopolar current sources formulation, whilst the second one was treated through employment of an inverse-based multi-level preconditioning scheme. The superior computational efficiency of the proposed inverse-based multi-level preconditioning approach was demonstrated through a comparative study with conventional preconditioning methods over problems of growing scale. This approach is generic and applicable for other soft-field imaging modalities. Its use has already been implemented for Optical Tomography by the author [234]. Further computational improvement can be achieved in the future by development of a hybrid BEM-FEM forward solver. This promising approach could offer accurate modelling of thin and

homogeneous layers, such as the CSF or the skull layers using BEM, while regions with complex admittivity distribution would be represented by FEM [241;242]. The coupling of these two methods yields hybrid dense and sparse system matrices, which would require development of custom made preconditioning and solution procedures. 3D forward modellers developed for EIT were based on the quasi-static approximation for Maxwell equations. As proposed in the feasibility study in Chapter 6, useful information resides in frequencies above 1MHz. For this frequency range, the accuracy of such forward modellers is questionable. Development of a 3D full-Maxwell equation based forward modeller, is therefore, essential.

As the complexity of EIT forward models increases, the need for efficient methods for their solution will become increasingly important. Following the innovations proposed in this work, the computational limitation in processing accurate forward models is resolved, and therefore allows addressing other limiting factors more effectively. The ideas presented here are generic, and therefore can be applied more widely for other related fields such as MIT and EEG source modelling.

The third objective of this work, as presented in Chapter 5, was development of generic non-linear inversion method suitable for large-scale inverse problems, such as those involving complex-shaped domains. In this study, most of the established inversion methods were examined with respect to their potential to handle large-scale problems. The shortcomings of those methods raised the need for a robust inversion method, which is computationally efficient. A novel Newton-Krylov inversion approach was proposed and demonstrated superior convergence using moderate memory resources. This approach combined the memory efficiency of the Krylov-subspace methods together with the prompt convergence property of Newton-type methods. The study focused on comparing the computational efficiency of the different inversion methods, rather than performing a quantitative comparison of image quality and optimal priors for the minimised problem. Further computational improvement can be achieved by improved implicit preconditioning of the normal equations system. This can be accomplished in several ways, such as by domain decomposition or hierarchical matrices [323;326;327]. To the author's knowledge, this was the first time

that this novel approach has been applied to EIT and it now permits of large-scale inverse which were hitherto intractable. The generality of the proposed Newton-Krylov inversion allows its implementation within many similar and more complex inverse problems.

Acute stroke differentiation is probably one of the most challenging problems for EIT. The difficulties associated with this application can be attributed to three main reasons: the lack of reference data, the geometric complexity associated with the human head structures, and the large and complex impedance contrast associated with the pathology. In the last study, knowledge and tools, which were developed in this work, were used to address the feasibility of this application. The primary goals of the study were to provide a qualitative estimate for the expected boundary voltage changes due to acute cerebral stroke across a wide frequency range, as well as to estimate the influence of likely confounding factors related to acquisition uncertainty and intrinsic physiological variability. The results gave a rough guideline for the highly demanding hardware specification, which are required to permit reliable acquisition of the pathology-related changes. The study triggered hardware redesign work within the UCL group, which was performed in order to meet these specifications [24;227;228]. The impact of the confounding factors, which were considered in this study, appeared to obscure the changes associated with the pathology, unless these can be diminished significantly. In light of the effect of these factors, classification by means of absolute imaging or bioimpedance measurements seems highly unlikely. It may well be that EIT is not suitable for this application; albeit, in this study the expected measurable signals were quantified for the first time in a realistic way, and so, gave this idea a fair try. The work presented here emphasised the importance of accurate modelling as an integral part in development of new imaging application. Following this work, several multi-frequency EIT modelling studies were conducted in the UCL group [28;231;356;357]. These studies employed the physiological knowledge and computational tools developed here to asses the feasibility of other head EIT applications.

7.2 Future Work

It is acknowledged that multi-frequency data provide crucial spectral information, which can help to assess and discriminate between tissues in different functional states [358]. Image reconstruction of the data from each frequency separately followed by some post-fitting over frequency is possible, but such an approach would permit the recovered parameters to vary independently over frequency throughout the reconstruction process. In the author's view, higher fidelity reconstruction can be achieved by introducing a frequency-dependent parameterisation of the original recovered parameters. In this way, a physiological frequency-dependent behaviour could be imposed on the problem [346]. Such a constraint would make the problem more well-determined, stable and robust. This approach is destined to increase the problem size considerably, and, until now, has been applied only for small-scale 2D EIT problems. A 3D large-scale framework solution for this problem can be approached with implicit derivation of the Hessian in a Newton-Krylov framework as proposed in Chapter 5. The large-scale forward modelling tools developed in Chapter 4 would be crucial for such an application, through the repeated use of the forward model in the globalisation process as well as in the sensitivity matrix derivation. Knowledge regarding the spectroscopic behaviour of body tissue and the pathology-related expected changes will serve as vital guideline in choosing appropriate parametric representation for the problem. Such a framework could hopefully exploit better the information content which resides in the problem and allow effective fusion of this knowledge. The deliverable of this approach would be useful for a large range of applications apart from stroke type discrimination.

The entire solution procedure can be more effective and stable by reformulation of the problem using an 'All at once' or Lagrange Newton Krylov Schur (LNKS) constrained optimisation formulation [359;360]. With this formulation, additional parameters such as the fields and a set of Lagrange multipliers are employed. This leads to a much larger problem than the traditional unconstrained formulation. Nevertheless, the constrained problem can be solved faster than the unconstrained one, as the forward problem does not have to be solved exactly until the very end of the optimisation process. In addition, the fields are permitted to vary from their

constrained values in the initial stages, which offers flexibility so that a stationary point of the objective function can be found more quickly.

7.3 A Glance to the Future

EIT has been considered as a medical imaging method for over two decades now, and yet its use as a routine clinical diagnosis tool has not been established. It always seemed as if (a) resolution is just around the corner, but the further we went the further the horizon has receded. Several questions inevitably arise: was that due to the smooth frequency behaviour of the different tissues and their relatively large spectroscopic similarity? Maybe the problem is too ill-posed to be solved reliably? Does the difficulty arise from the broad multi-disciplinary spectrum of the problem? Are technical or technological difficulties are to be blamed? And probably above all, with the advances of more established imaging methods, and their commercialisation, will EIT ever have a clinical role?

In the author's belief the main reason is that EIT had not got a fair try yet. It is highly difficult to get all the necessary ingredients for imaging in place (that is a good clinical case, suitable hardware, well designed acquisition routine, accurate forward modelling and effective and robust inverse solvers). Similar imaging methods to EIT utilised for geophysics applications are already well established. An in depth study of this related field may assist identifying the weakest links in the medical applications of EIT and possibly pave the way for new approaches, which will tackle the EIT problem in a more effective way. The author's future plan is to elaborate his knowledge in these related problems through his post-doctoral experience in the hope of resolving this challenging problem.

8 APPENDICES

Appendix A - Tabulated Dielectric Properties of the Head Tissues

Table A- 1. Dielectric properties of muscle tissue

Authors	Orientation	ρ [Ωcm]	ε_r	Temp [°C]	Frequency [Hz]	Method	Samples
Burger Van-Millan 1947		230		37	DC	4 terminal	Human scalp *In-vivo*
Schwan 1957		758 - 962	$5.5 \cdot 10^4$ - 10^7	BT	10 - 10^4	2 terminal	Canine skeletal muscle In-situ
Burger Van-Dongen 1961	Axial	238		20	20 - $5 \cdot 10^3$	4 terminal	Bovine
	Transversal	666			100 - 10^3		
Schwan 1963		250 - 980	$2 \cdot 10^3$ - 10^5	20	10^3 - 10^6	2 terminal - electrodes covered with platinum black to reduce electrodes polarisation	Rabbit *in-vitro* Canine in-situ
			$5 \cdot 10^4$ - $8 \cdot 10^5$	37	100 - 10^4		
Stoy et al 1982		145 - 288 ±2%-5%	200 - $1.6 \cdot 10^4$ ± 25%-100%	25	10^5 - 10^8	2 terminal - electrodes covered with platinum black to reduce electrodes polarisation	Rat *In-vitro* 1 h after excision
		126 - 229 ±2%-5%	251 - $2 \cdot 10^4$ ± 25%-100%	37	10^5 - 10^8		
Epstein et al 1983	Axial	125 - 182	800 - $1.2 \cdot 10^6$	36-38	100 - 10^6	2 terminal	Canine
	Transversal	172 - $1.3 \cdot 10^3$	$3.5 \cdot 10^3$ - $3.7 \cdot 10^5$				

Table A- 2. Dielectric properties of muscle tissue (continued)

Authors	Orientation	ρ [Ωcm]	ε_r	Temp [°C]	Frequency [Hz]	Method	Samples
Gielen et al 1984	Axial	91 - 351	$2.1 \cdot 10^4$ - $1.6 \cdot 10^7$	37 ±1	10 - 10^5	2 terminal	Rat
	Transversal	167 - 541	$4.2 \cdot 10^4$ - $6.4 \cdot 10^6$				*In-vivo*
Bodakian et al 1994	Axial	385 - $2.2 \cdot 10^3$	$9.3 \cdot 10^3$ - $5.8 \cdot 10^7$	20	10 - 10^5	2 terminal	Bovine
	Transversal	714 - $2.9 \cdot 10^3$	$1.7 \cdot 10^4$ - $3.5 \cdot 10^7$				
Gabriel et al 1996	Axial	148 – 412	131 - $8.3 \cdot 10^7$	37	10 - $2 \cdot 10^{10}$	2 terminal	Ovine
	Transversal	149 – 448	146 - $4.1 \cdot 10^7$				
Hart et al 1999	Axial	292 - $1.3 \cdot 10^3$		20	10^3 - 10^6	2 terminal	Bullfrog
	Transversal	334 - $1.5 \cdot 10^3$					*In-vivo*

Table A- 3. Impedance values of the skull

Authors	ρ_{skull} [Ωcm]	Temp [°C]	Frequency [Hz]	Method	Samples
Law 1993	7560 ± 4130 Range 1360 (at back of the head) - 21400 (in the temporal region)	-	100	4-terminal Electrodes and bone samples soaked 24 hours before testing	Dry skull, soaked in 0.9% saline for 24 hours 20 different sites from all over skull
Oostendorp et al 2000	7600 ± 400 (490±90 brain and scalp)	37	200ms +/-1μA pulses 100-10^4	4 terminal + FEM + inverse problem	Live human
	6700 ± 1300			4 terminal directly on tissue	Human cadaver *In-vitro*

Table A- 4. Impedance values of the skull (continued)

Authors	ρ_{skull} [Ωcm]	Temp [°C]	Frequency [Hz]	Method	Samples
Akhtari et al 2002 Akhtari et al 2003	10500 (4.6% decrease over frequency) phase angles: +2.1° - 8.3° (across samples and frequencies) maximal phase changes: 8.3° at 10Hz ($\varepsilon_r = 2 \cdot 10^6$) and -6.2° at 90Hz ($\varepsilon_r = 2 \cdot 10^5$) relaxation time upper limits: ~10^{-3} and ~10^{-4} seconds	-	10 - 90	4 terminal	Live human skull Different layers of skull and in different samples Skull flaps excised during surgery (15-65min delay) First 2/4 samples included sutures
Goncalves et al 2003a	20355 ± 7100 (305 ± 70 brain and scalp)	37	60	4 terminal + spherical shells analytical solution for the inverse problem	Live human skull *In-vivo*
Goncalves et al 2003a	16200 ± 6000 (234±40 brain and scalp)		2 (stimulus)	Combined analysis of EEG/MEG inverse problem	
Goncalves et al 2003b	12230 ± 2200 (301 ± 39 brain and scalp)		60	4 terminal + BEM + inverse problem	
Hoekema et al 2003	1250 - 3125	37	10	Extended 4 terminal Finite difference model to account for the geometry and current paths	Live temporal skull, temporarily excised temporal bone
	4670 ± 280				Post mortem

Table A- 5. Dielectric properties of the bone

Authors	Orientation	ρ [Ωcm]	ε_r	Temp [°C]	Frequency [Hz]	Method	Samples
Kosterich et al 1983	Radial	4504 - 8130	37 - $8.5 \cdot 10^3$	37	10 - 10^8	2 terminal, coaxial platinum sample cell	Cortical rat femur Samples were immersed in saline or Hank's solution
Reddy et al 1984	Axial	9100 - 16600	89 - $1.6 \cdot 10^3$	21	10^3 - 10^6	2 terminal, differential method	Cortical bovine femur defrosted Samples were immersed in Ringer's solution
	Radial	26700 - 53900	25.7 - 631				
	Circumferential	21600 - 36100	31.6 - 794				
Smith et al 1985	Radial	6407 - 14986	36 - $2.2 \cdot 10^3$	37	10^3 - $1.3 \cdot 10^7$	2 terminal	Cortical rat femur
		471 - 476	58 - $4.6 \cdot 10^3$	25	10^3 - 10^9		Bone marrow from bovine calf femur and tibia, contains a mixture of yellow and red marrow
De Mercato & Garcia-Sanchez 1988	Diaphysis	4000 - 5000	87 - $5.8 \cdot 10^3$	37	10^3 - 10^6	2 terminal differential method Silver electrodes (not chloride)	Cancellous bovine femur proximal epiphysis and diaphysis trabecular samples Samples saturated in physiological solution with no immersion
	Proximal epiphysis	1460 - 3410	95 - $4.2 \cdot 10^4$				
	Distal epiphysis	1770 - 2020	10^5 - $2.8 \cdot 10^4$				
Saha & Williams 1989	Axial	417 - 599	39 - $7 \cdot 10^3$	27	120 - 10^7	2 terminal Silver - silver chloride electrodes	Cancellous human distal tibia - sujects suffered from peripheral vascular disease Samples were defrosted and soaked in Ringer's solution
	Anterior-posterior	484 - 507	83 - 603				
	Lateral-medial	452 - 484	72 - 579				

Table A- 6. Dielectric properties of the bone (continued)

Authors	Orientation	ρ [Ωcm]	ε_r	Tem p [°C]	Frequency [Hz]	Method	Samples
De Mercato & Garcia-Sanchez 1992	Axial	11180 - 11250	43 - $5.8 \cdot 10^3$	23	10^3 - 10^6	2 terminal calibrated to compensate for interconnection parasites Silver - silver chloride electrodes	Cortical bovine femur Samples were immersed in physiological solution
	Radial	22222 - 24064	37.1 - $3.6 \cdot 10^3$				
	Circumferential	16187 - 16453	40 - $4.4 \cdot 10^3$				
Saha et al 1992	Axial	1334 - 1670	51 - $6.4 \cdot 10^4$	27	120 - 10^7	2 terminal Silver - silver chloride electrodes	Cortical human sample from distal tibia which was vasculary compromised Samples were defrosted and soaked in Ringer's solution
	Radial	14903 - 19011	41 – 308		10^4 - 10^6		
	Circumferential	12600 - 16500	Negligible		10^4 - 10^6		
Gabriel et al 1994		864 - 1143	119 - 50^7	37	10^6 - $2 \cdot 10^{10}$	2 terminal	Cancellous ovine skull
Gabriel et al 1996b		1695 - 2647	114 – 335	23	10^6 - $2 \cdot 10^{10}$	2 terminal	Cancellous human
		2502 - 3280	54 – 209	37	10^6 - $2 \cdot 10^{10}$		Cortical ovine
		14843 - 72529	27- $8.5 \cdot 10^5$	37	10 - $2 \cdot 10^{10}$		Bone marrow from bovine
Sierpowska et al 2003		2496 - 2947	44 - $4.6 \cdot 10^5$	-	50 - $5 \cdot 10^6$	2 terminal	Cancellous bovine femur Samples were defrosted and soaked in phosphate buffered saline
Sierpowska et al 2005		1027 - 1927	30 - $1.2 \cdot 10^7$	22	50 - $5 \cdot 10^6$	2 terminal	Cancellous human cadaver tibia and femur Samples were defrosted and soaked in phosphate buffered saline

Table A- 7. Dielectric properties of CSF

Authors	ρ [Ωcm]	Temp [°C]	Frequency [Hz]	Method	Samples
Radvan-Ziemnowicz et al 1964	64.0 - 65.2	24.5	10^3 - $3{\cdot}10^4$	Not given	Human
Baumann et al 1997	68.6 - 68.9 $\varepsilon_r = 0$	25	10 - 10^4	4 terminal	Human defrosted CSF
	55.5 - 55.9 $\varepsilon_r = 0$	37			
Latikka et al 2001	80.0	37	$5{\cdot}10^4$	2 terminal	Human during surgery

Table A- 8. Dielectric properties of grey matter

Authors	ρ cortex [Ωcm]	ε_r	Temp [°C]	Frequency [Hz]	Method	Samples
Freygang & Landau 1955	222 ± 37		37	up to $3.3{\cdot}10^3$	4 terminal 0.3-0.7ms pulse	Cat *In-vivo*
Ranck 1963	230 ± 37 - 321 ± 45 256 - 356 with 10% correction for blood conductivity	$3{\cdot}10^4$ - $7.8{\cdot}10^6$	BT	5 - $5{\cdot}10^4$	4 terminal point electrodes on cortex	Rabbit *In-vivo*
Van Harreveld et al 1963	208 ± 6 220 with 10% correction for blood conductivity		38	10^3	3 terminal	Rabbit cortex slab samples grey and white matter *In-vivo*

Table A- 9. Dielectric properties of grey matter (continued)

Authors	ρ cortex [Ωcm]	ε_r	Temp [°C]	Frequency [Hz]	Method	Samples
Ranck 1964	230 - 330 242 - 363 with 10% correction for blood conductivity		BT	$5 - 5 \cdot 10^4$	4 terminal Point electrodes on cortex	Rabbit *In-vivo*
Ranck 1966	250		BT	$1.5 - 3 \cdot 10^3$	4 terminal Point electrodes on cortex	Rat dorsal part of the hippocampal formation *In-vivo*
Li et al 1968	556 ± 45		36	0.1 – 1	4 terminal Pulses amplitude 4-40μA, duration 0.6-10ms	Cat *In-vivo*
Robillard & Poussart 1977	300 - 500		BT	Averaged over $20 - 2 \cdot 10^3$	4 terminal	Feline *In-vivo*
Stoy et al 1982	332 - 588 ± 2%-5%	$557 - 3.8 \cdot 10^3$	37	$10^5 - 10^8$	2 terminal	Canine *In-vitro*
Suroweic et al 1986	394 - 588	$420 - 2.8 \cdot 10^3$	24	$10^5 - 10^8$	4 electrode coaxial cell	Bovine *In-vitro*
Gabriel et al 1996	407 - 2918	$384 - 5.3 \cdot 10^7$	37	$10 - 2 \cdot 10^{10}$	2 terminal	Ovine
	411 - 1028	$572 - 1.9 \cdot 10^3$		$3 \cdot 10^5 - 2 \cdot 10^{10}$		Human cadaver 24 - 48 h after death
Latikka et al 2001	351		BT	$5 \cdot 10^4$	Monopolar needle electrode	Human *In-vivo*

Table A- 10. Dielectric properties of white matter

Authors	ρ [Ωcm]	ε_r	Temp [°C]	Frequency [Hz]	Method	Samples
Freygang & Landau 1955	333±56 (1.5 times that of grey matter)		37	up to $3.3 \cdot 10^3$	4 terminal 0.3-0.7ms pulse	Cat *In-vivo*
Van Harreveld et al 1963	957±42 (4.6 times that of grey matter) 1012 with 10% correction for blood conductivity		38	10^3	3 terminal	Rabbit cortex slab samples grey and white matter *In-vivo*
Nicholson 1965	Longitudinal 78 - 89	$2.1 \cdot 10^5$ - $7.9 \cdot 10^7$	BT	20 - $2 \cdot 10^4$	4 terminal point electrode and remote electrode + 2 measurement electrodes	Cat *In-vivo*
	Transverse 750 - 850 790 - 890 with correction for blood conductivity	$2.1 \cdot 10^5$ - $8.3 \cdot 10^6$				
Ranck 1965	Longitudinal 169 - 215	0 - $1.3 \cdot 10^4$	BT	5 - $5 \cdot 10^4$	4 terminal point electrodes on cortex + 2 measurement electrodes	Cat spinal cord *In-vivo*
	Transverse 524 - 674 Ratio 5.7 to 8.8	0 - 3278				
Geddes & Baker 1967	682 Transverse/longitudinal ratio 5.7 - 9.4		BT	Averaged over 5 - $5 \cdot 10^3$	2 to 4 terminals	Rabbit & cat *In-vivo*
Li, Bak & Parker 1968	580 ± 53		36	0.1-1	4 terminal Pulses amplitude 4-40μA, duration 0.6-10ms	Cat *In-vivo*
Robillard & Poussart 1977	Larger than 600		BT	Averaged over 20 - $2 \cdot 10^3$	4 terminal	Cat *In-vivo*
Stoy et al 1982	357 - 666	209-3400	22	10^5 - 10^8	2 terminal	Dog *In-vitro*
	476 - 833	163-1960	37			

Table A- 11. Dielectric properties of white matter (continued)

Authors	ρ [Ωcm]	ε_r	Temp [°C]	Frequency [Hz]	Method	Samples
Suroweic et al 1986	500 - 809	180 - 1400	24 - 25	10^5 - 10^8	4 electrode coaxial cell	Bovine *In-vitro*
Gabriel et al 1996b	695 - 4043	244 - $3.3 \cdot 10^7$	37	10 - $2 \cdot 10^{10}$	2 terminal	Ovine *In-vitro*
	427 - 723	270 - 1310		10 - $2 \cdot 10^{10}$		Human *In-vitro*
Latikka et al 2001	391		BT	$5 \cdot 10^4$	Monopolar needle electrode	Human *In-vivo*

Table A- 12. Dielectric properties of blood

Authors	ρ [Ωcm]	ε_r	Frequency [Hz]	Temp [°C]	Haematocrit [%]	Method	Samples
Schwan 1941	166.7		10^2	18		2 terminal	Ovine blood
Burger and Van Milaan 1943	230		DC	18		4 terminal Platinum electrodes	Human blood 0.01% - 0.001% heparin
	160			Calculated as 37			
	100			18	0		Human blood with no erythrocytes 0.01% - 0.001% heparin
Rosenthal & Tobias 1948	137.8 - 180		10^3	37	34.4 - 56.4	2 terminal	Human blood

Table A- 13. Dielectric properties of blood (continued)

Authors	ρ [Ωcm]	ε_r	Frequency [Hz]	Temp [°C]	Haematocrit [%]	Method	Samples
Hirsch et al 1950	75.2 - 352.1		1,075 - $1.95 \cdot 10^4$	30	20 - 70	2 terminal Electrodes were made of coiled platinum wire coated by platinum black Horizontal cell	Human blood with heparin
Schwan 1956, 1963	114 - 147	407 - 2900	10^3 - 10^7	BT		2 terminal	Rabbit blood
Burger and Van Dongen 1961	195		20 - $5 \cdot 10^3$	20		4 terminal Horizontal cell	Human blood with heparin
	155			40			
Pfutzner 1984	125		$5 \cdot 10^3$	21	20 - 90	2 terminal Raster electrodes	Sheep blood
	181						Cow blood
	500						Normal human blood
Zhao et al 1993	123 - 148		10^4 - $1.2 \cdot 10^6$	37		4 terminal	Flowing human blood
Gabriel et al 1996	72 - 80	662 - 3662	10^6 - $2 \cdot 10^{10}$	37±0.1		2 terminal	Ovine blood
Casas et al 1999			100 - 10^6	BT		4 terminal Platinum black electrode array	Porcine blood *In-vivo*
Jaspard et al 2003	143 - 768	50 - 2500	10^6 - 10^9	37	41	2 terminal Open ended coaxial probe	Bovine blood
	143 - 719	50 - 2500					Ovine blood

Table A- 14. Dielectric properties of the eye

Authors	ρ [Ωcm]		ε_r		Temp [°C]	Frequency [Hz]		Method	Samples	
Watanabe et al 1993					25	10^3-10^6		2 terminal	White rabbit cornea In-situ	
Gandhi 1995	0.11					60			Whole eye	
Jurgens et al 1996	63.5				RT	10^3-10^7		4 terminal Four-wire coaxial probe	Porcine aqueous humour	24 h after excision *In-vitro*
	64.5								Porcine vitreous humour	
	43.5								Porcine cornea	
Gabriel et al 1996	130 - 188	121 - 243	669 - 4743	506 - $2{\cdot}10^7$	37	10^6-$2{\cdot}10^{10}$	10-$2{\cdot}10^{10}$	2 terminal	Ovine cornea	Ovine cornea extrapolated
	229 - 309	207 - 321	442 - 1913	354 - $2{\cdot}10^7$					Ovine cortex lens	Ovine cortex lens extrapolated
	469 - 531	477 - 500	157 - 609	116 – 3634					Ovine nucleus lens	Ovine nucleus lens extrapolated
	132 - 161	131 - 199	486 - 3115	413 - $2.6{\cdot}10^8$					Ovine sclera	Ovine sclera extrapolated
	164 - 231		845 - 2610						Ovine retina	
	143 - 166		435 - 2170						Ovine iris	
	139 - 163		465 - 2300						Ovine choroid	
	62 - 66								Ovine aqueous humour	
		67		71 - 99					Ovine vitreous humour extrapolated	

Table A- 15. Dielectric properties of the eye (continued)

Authors	ρ [Ωcm]	ε_r	Temp [°C]	Frequency [Hz]	Method	Samples	
Lindenblatt et al 2001	200	$5.4 \cdot 10^5$ - $2.4 \cdot 10^8$	32	$5\text{-}2 \cdot 10^3$	4 terminal Silver disk injecting electrodes Silver ring measurement electrodes 5 μA current	Bovine cornea	4 h after excision
	62 - 66	$7.1 \cdot 10^5$ - $8.3 \cdot 10^8$				Bovine aqueous humour	
	302 - 309	$1.1 \cdot 10^5$ - $7.1 \cdot 10^7$				Bovine lens	
	64 - 74	$1.1 \cdot 10^6$ - $1.1 \cdot 10^9$				Bovine vitreous humour	
	166 – 178	$2.3 \cdot 10^5$ - $2.5 \cdot 10^8$				Minced bovine sclera	

Appendix B - Tabulated Pathophysiology Behaviour of the Head Tissues

Table A- 16. Summary of bioimpedance changes during ischaemia

Author	Impedance change	Temp [°C]	Frequency [Hz]	Method	Samples	
Van Harreveld et al 1956	Resistance increase of 100%, 200% and 500% after 5min, 25min, and 4 hours, then on a slow reduction of 50% on the following 20 hours. Reactance increased by 300% during first 5min, 500% by the first 25min, and then remained elevated	BT down to 25C	10^3	2 terminal Electrodes placed over the dorso-lateral aspect of a hemisphere	Rabbit brain undergoing a circulatory arrest I*In-vivo* and in-situ	
Holder 1992	Cortical resistance increase of 50 - 200% scalp measurement increase of 5 - 20%	BT	$5.1 \cdot 10^4$	4 terminal (Sheffield system) Cortical electrodes placed over the fronto-occipital plane	Rat brain *In-vivo*	
Holder 1992	Cortical resistance increase of 15 - 60% scalp measurement increase of 1.5 - 12%	37-39	$5 \cdot 10^4$	4 terminal (single channel system)	Rat brain *In-vivo*	
Gabriel 1996		37	$10\text{-}2 \cdot 10^{10}$	2 terminal Corrections for electrode polarisation at low frequencies, and inductance errors over the high frequencies	Ovine grey and white matter *In-vitro*	24-48 h post-mortem

Table A- 17. Summary of bioimpedance changes during ischaemia (continued)

Author	Impedance change	Temp [°C]	Frequency [Hz]	Method	Samples
Wu et al 2003	75% increase for frequencies lower than 10 Hz, 15% increase between 1kHz to 1MHz	BT	0.1- 10^6	4 terminal	Rabbit brain *In-vivo*
Lingwood et al 2003	8.5% increase for mild ischaemia which returned to baseline after resuscitation. 23.5% cerebral impedance increase during severe hypoxia	BT	4-10^6	4 terminal 2 electrodes above the eyes, and two at the occipital region	Live neonatal porcine brain *In-vivo*
Seoane et al 2004	71% increase for severe hypoxia at 50kHz and reduced to 18% 2 hours later	BT	$2{\cdot}10^4$-$7.5{\cdot}10^5$	4 terminal Electrodes positioned over the dura located at P3 P4 C3 and C4	Live neonatal porcine brain *In-vivo*
Seoane et al 2005	Up to 25%-121% increase at 50kHz, smaller changes at 200kHz		$5{\cdot}10^4$,$2{\cdot}10^5$		
	Maximal resistance increase of 34% at 20kHz, maximal reactance change of 58.5% around 300kHz		$2{\cdot}10^4$-$7.5{\cdot}10^5$		
Seoane et al 2005	35% increase at 30kHz and 30% increase at 200kHz		$3{\cdot}10^4$,$2{\cdot}10^5$	4 terminal Intracranial electrodes	Live fetal sheep brain *In-vivo*

Table A- 18. Impedance changes during epilepsy

Author	Impedance change	Temp [°C]	Frequency[Hz]	Method	Samples
Shalit 1965	Impedance increase of more than 100%	BT	10^4	2 terminal W.B.	Feline cortex
Elazar 1996	Resistance increase of up to 10-12% Capacitance decrease	BT	10^3	Coaxial W.B.	Feline cortex

Table A- 19. Impedance changes during epilepsy (continued)

Author	Impedance change	Temp [°C]	Frequency [Hz]	Method	Samples
Rao 2000	Resistance increase of 9.5±1.4% during local seizure Resistance increase of 14.3± 0.5% during general seizure	BT	47.10^3	4 cortical (HP)	Rabbits
Fox 2004	Resistivity: increase 22±3%		DC	3 terminal	Rat hippocampus

Table A- 20. Dielectric properties of tumour tissue

Author	Impedance change	Temp [°C]	Frequency [Hz]	Method	Sample
Surowiec et al 1988	Conductivity of tumour tissue was between 20 - 25 times larger than of normal tissue, where larger differences appeared near the high frequency end Relative permittivity of the tumour tissue was up to 15 times larger than of the normal tissue	37	$2{\cdot}10^4$-10^8	2 terminal (HP 3577) Platinum black coated electrodes Calibrated by substitution of saline solution	breast carcinoma - central part, surrounding tissue and peripheral tissue 28 samples 4 h after excision
Morimoto et al 1993	R_e and R_i were significantly higher in breast cancers than in benign tumours and normal breast tissues C_m was significantly lower in breast cancers than in other tissues R_e and R_i were significantly higher, and C_m was significantly lower, in normal lung tissues than in pulmonary masses R_e and R_i were significantly higher, and C_m was significantly lower, in malignant tumours than in organised pneumonias	37	$0{\text-}2{\cdot}10^5$	3 terminal	31 breast cancers, 13 fibroadenomas, and 10 fibrocystic diseases 44 lung cancers, 5 metastatic pulmonary tumours, 4 pulmonary tuberculoses, and 4 organised pneumonias *In-vivo*

Table A- 21. Dielectric properties of tumour tissue (continued)

Author	Impedance change	Temp [°C]	Frequency [Hz]	Method	Sample
Osypka et al 1995	Tumour tissue had centre frequency of 250kHz Tumour tissue had centre frequency of 500kHz	35, 42.5	10-1-10^7	4 terminal (Solartron 1260 impedance analyser or HP 4194A) Stainless needle electrodes	Rat hind feet sarcoma In-situ
Blad and Baldetorp 1996	Normal tissue showed higher resistivity at low frequencies Centre frequency of normal tissue @ 20kHz, and tumour tissue @ 100kHz	37, 45, 24, 21 37	$1.5 \cdot 10^3$ - $7 \cdot 10^5$	4 terminal Stainless steel needle electrodes Calibration on water with different salt concentrations	Mouse thigh muscle in normal and with squamous cell carcinoma *Ex-vivo* 5 minutes after excision
Jossinet 1998	The resistivity of the normal connective and adipose tissues were significantly larger than any other groups Significant differences in conductivity at frequencies <32kHz in carcinoma vs. fibroadenoma and carcinoma vs. normal mammary gland Phase angle of the group of carcinomas has differed from all the other groups @ 125kHz to 1MHz Normal mammary gland group differed from all other groups by the phase angle at frequencies <16kHz	20	488-10^6	4 terminal Stainless steel needle electrodes	Normal human breast mammary gland, connective and adipose tissue Pathological human breast tissues: mastopathy, fibroadenoma, carcinoma *In-vitro* 10 min of excision
Haemmerich et al 2003	Conductivity of tumour tissue was higher than normal tissue by a factor of 2.1 at 10Hz and 1.1 @1MHz	37	10-10^6	4 terminal (HP54600B and HP33120A function generator) Silver -silver chloride electrodes Calibration with saline solution	Rat liver normal and tumour (K12/TRb colon) tissue *In-vivo*

Appendix C - Linear Inversion Methods

Backprojection

In the reconstruction of CT images, a sensor detects the attenuation of an X-ray beam, which has travelled along a known path and attributes an equal value of attenuation to each of the pixels it has passed through. When multiple beams have been passed through the object at all angles, the pixel values are combined. A pixel in a region of high attenuation will have affected all the beams passing through it and will have cumulated high pixel values relative to those surrounding it. The same principal had been applied for EIT reconstruction in the early days of EIT. However, this approach mistreated the fact that current paths are much less well-defined than X-rays.

Inspired by that idea, Barber [361;362] presented the *Sheffield Algorithm* which was compatible with data collected from the Sheffield Mark 1 system. The x-y plane was transformed into a *u-v* plane, where u stands for iso-potentials and v for iso-currents and a weighting function $W = 2v - 1$ was applied to each iso-current pixel. Filtration was also required to deblur the image, and been applied empirically to produce uniform resolution. Later, Bayford [363] had suggested a constrained optimisation framework, in which the variance of pixel values is minimised given that their backprojection-weighted sum is equal the sum of all the boundary potentials.

Perturbation methods

For *perturbation methods*, a perturbation matrix is generated instead of a sensitivity matrix, the elements of which are the inverse of the ratio of calculated change in measured voltage $\delta V_{\Gamma i}$ to the conductivity perturbation $\delta\gamma_j$ that causes it. It is also possible to generate a *direct inverse sensitivity matrix*, for which its elements approximately equal to $\frac{\partial\gamma_j}{\partial V_{\Gamma i}}$,thus, can be multiplied by the vector of voltage changes in order to give an approximate solution for $\Delta\gamma$ [364].

Singular Value Decomposition

Framework

Singular Value Decomposition (SVD) is the discrete analogue of *Singular Value Expansion* (SVE), which allow orthogonal diagonalisation of non-square Hermitian matrices [365].

For a matrix $A \in \mathbb{C}^{m\times k}$, the term A^*A is non-negative definite Hermitian, hence, has a complete set of orthonormal eigenvectors $\{v_1, v_2 ... v_k\}$ with real eigenvalues $\lambda_1 \geq \lambda_2 \geq ... \geq 0$. In that case the matrix $\Upsilon = [v_1|v_2|...|v_k]$ is unitary. By denoting the singular values as $\varsigma_i := \sqrt{\lambda_i}$ and defining $u_i = \varsigma_i^{-1} A v_i \in \mathbb{C}^m, \varsigma_i \neq 0$, the following relations are obtained

$$A^*Av_i = \lambda_i v_i = \varsigma_i^2 v_i \tag{5.84}$$

$$A^*u_i = \varsigma_i^{-1} A^*Av_i = \varsigma_i^{-1}\lambda_i v_i = \varsigma_i v_i \tag{5.85}$$

$$AA^*u_i = AA^*\varsigma_i^{-1}Av_i = A\varsigma_i^{-1}A^*Av_i = \varsigma_i^2 u_i \tag{5.86}$$

From (5.86) it is evident that u_i's form eigenvectors of the Hermitian matrix AA^*, as such they are orthonormal as well

$$\begin{aligned} v_i^* v_j &= \delta_{ij} \quad i,j = 1..k \\ u_i^* u_j &= \delta_{ij} \quad i,j = 1..m \end{aligned} \tag{5.87}$$

The singular values of A satisfy

$$\varsigma_1 \geq \varsigma_2 \geq ... \varsigma_{\min(m,k)} \geq 0 \tag{5.88}$$

In an equivalent way to Υ, $U = [u_1|u_2|...|u_m]$ is defined, and S is denoted as a diagonal matrix of the singular values padded with zeros, so that it forms $m \times k$ matrix, and therefore, obtain the following

$$U^*A\Upsilon = S \tag{5.89}$$

$$A = US\Upsilon^* \tag{5.90}$$

Once the SVD has been performed, Moore-Penrose generalised inversion can be applied [282]. The inverse of an orthogonal vector is its transpose and that of a diagonal matrix is simply a diagonal matrix whose diagonal elements are $1/\varsigma_{ii}$ so that

$$A^{-1} = \Upsilon S^{-1} U^* \tag{5.91}$$

In the case m<k, as is what usually occur in the problem of EIT, where few voltage measurements are required to provide a solution for many admittivity values, that matrix is *underdetermined*. Hence, AA^* which is a square matrix is inverted rather than A. If each of these are decomposed according to (5.90) then

$$AA^* = US\Upsilon^*\Upsilon SU^* = US^2U^*. \tag{5.92}$$

By pre-multiplying the inverse of AA^* by A^* a pseudo-inverse of A is acquired

$$A^\Diamond = A^*\left(AA^*\right)^{-1} = \Upsilon SU^* US^{-2}U^* = \Upsilon S^{-1}U^*. \tag{5.93}$$

This formula is valid regardless of the rank of A, and provides the minimum least squares solution for the non-regularised inverse problem

$$\gamma_{LS} = \gamma_{ref} + \Upsilon S^{-1}U^*\left(F_\Gamma(\gamma_{ref}) - V_\Gamma\right) = \gamma_{ref} + \sum_{\varsigma_i \neq 0} \frac{1}{\varsigma_i}\left(U^*_{(i,:)}\left(F_\Gamma(\gamma_{ref}) - V_\Gamma\right)\right)\Upsilon_{(:,i)} \tag{5.94}$$

where colon denotes all the entries in a row or a column.

Analysis and regularisation

SVD provide a useful numerical analysis tool for discrete ill-posed problems. The eigenvectors represent domains within the object of increasing spatial frequency and with increasing weight towards the centre [366]. The decay rate of the singular values provides an insight into the instability of the inverse problem. Due to the ill-conditioning of the EIT problem, the singular values decay rapidly and reach values below bit-precision. In effect, the rank of the matrix is normally less than its size, as the measurements are degraded by the contamination of noise and are not entirely independent either. Figure 8-1 illustrates the decay of the singular values for a four shell head model on a logarithmic scale.

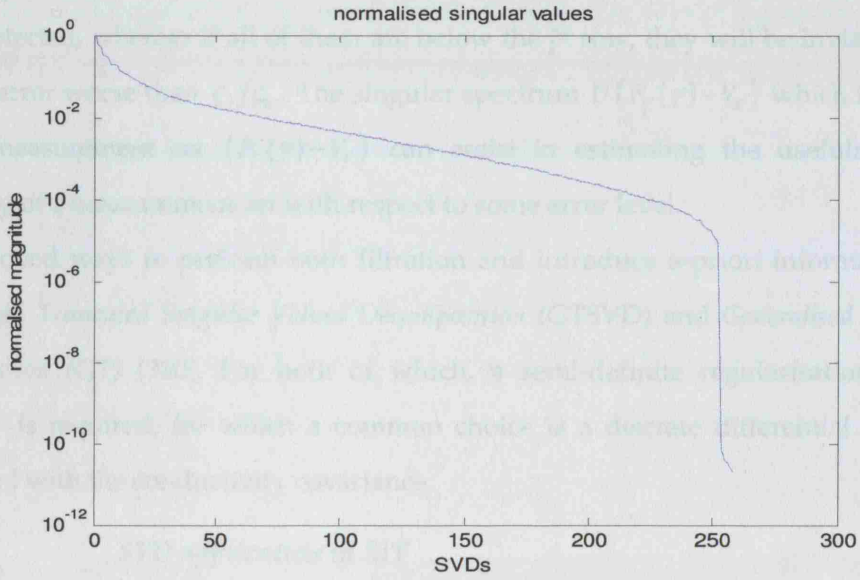

Figure 8-1 Log of normalised Singular Values of four-shell head model with 258 measurement combinations

It is clear from (5.94) that any errors in the measurement $\left(F_\Gamma\left(\gamma_{ref}\right)-V_\Gamma\right)$ shall be magnified in the image component $\left(U^*_{(i,:)}\left(F_\Gamma\left(\gamma_{ref}\right)-V_\Gamma\right)\right)$ by the inverse of the ith singular value $1/\varsigma_i$. For this reason, it is clear that retaining the smaller singular values is not only meaningless, but also quite destructive. Reasonably, for relative measurement error of ε, it can only be expected to recover reliably the image components $v_i^*\gamma$ for which $\frac{\varsigma_i}{\varsigma_1}>\varepsilon$ holds. It is essential, therefore, to regularise by

truncation [13] of the diagonal of S^{-1}, so that its diagonal elements ς_{ii}^{-1} will be zero beyond a defined threshold value, thus (5.94) becomes

$$\gamma_{TSVD} = \gamma_{ref} + \sum_{i=1}^{m} f_i \frac{\left(U_{(i,:)}^{*}\left(F_b\left(\gamma_{ref}\right) - V_b\right)\right)\Upsilon_{(:,i)}}{\varsigma_i} \tag{5.95}$$

where

$$f_{i_{TSVD}} = \begin{cases} 1 & \frac{\varsigma_i}{\varsigma_1} \geq \varepsilon \\ 0 & \frac{\varsigma_i}{\varsigma_1} < \varepsilon \end{cases} \tag{5.96}$$

are the filter factors for the truncation. This approach is known as *Truncated SVD* (TSVD). The singular values themselves provide only partial information about the problem; additional information resides in the singular spectrum $\Upsilon\gamma$. In cases where most of the large components are near the top values of this vector, the change can easily detected, whereas if all of them are below the j[th] row, they will be invisible with relative error worse than ς_j/ς_0. The singular spectrum $U\left(F_\Gamma(\gamma) - V_\Gamma\right)$ which is related to the measurement set $\left(F_\Gamma(\gamma) - V_\Gamma\right)$ can assist in estimating the usefulness and reliability of a measurement set with respect to some error level.

Improved ways to perform both filtration and introduce a-priori information are *Generalised Truncated Singular Values Decomposition* (GTSVD) and *Generalised Tikhonov regularisation* (GT) [310]. For both of which, a semi-definite regularisation matrix $W \in \mathbb{R}^{p \times k}$ is required, for which a common choice is a discrete differential operator associated with the conductivity covariance.

SVD application in EIT

Eyüboğlu [367] used SVD of the sensitivity matrix for reconstruction of 2D tank data. He had described an empirical process for choosing a pseudo-inverse truncation level; and reported that without truncation, it was impossible to identify the objects. Kleinermann [368] used a truncated SVD algorithm with 2D and 3D sensitivity matrices in order to reconstruct images of objects inside a cylindrical tank. Truncated SVD has also been used to invert recalculated Jacobian based on iteratively updated conductivity distributions in order to approach the true distribution [318].

[13] or preferably by decay, as perfomed by Tikhonov regularisation, which is described later

Up until recently, UCL group has employed the linear, non-iterative, truncated SVD algorithm for all 3D EIT images it has presented of tanks and human evoked responses [27;39;109;369]. In these studies they managed to localise, to a limited degree, sponge [14] resistance changes within a saline tank and some focal impedance changes within the brain, although at locations other than those suggested by physiology, and bounded to the limitation of a linear approximation.

Tikhonov

Tikhonov [324] and Phillips have developed independently a regularisation technique for discrete linear least square systems. Similarly to TSVD and TGSVD, *Standard Tikhonov* (ST) and *Generalised Tikhonov* (GT) incorporate filtration to diminish the impact of the Jacobian's smallest singular values. However, instead of truncation of the singular values, their impact is damped gradually according to the regularisation term τ. For GT this term penalises solutions with non-smooth behaviour

$$\gamma_{GT} = \arg\min_{\gamma} \left\| J(\gamma_{ref})\gamma_{ref} - V_{\Gamma} \right\|_{Q}^{2} + \tau \left\| \gamma_{ref} - \gamma \right\|_{P}^{2} \tag{5.97}$$

where Q is a diagonal weighting matrix which accounts for variable reliability assigned to each measurement channel, and $P \in \mathbb{R}^{k \times k}$ is positive definite matrix which usually imposes spatial prior over neighbouring elements. In case where $Q = I$ and $P = \tau I$, which is a reduction of GT to ST, only extreme admittivity values are penalised. In this case the filter factors are

$$f_{i_{ST}} = \frac{\varsigma_i^2}{\varsigma_i^2 + \tau^2} \tag{5.98}$$

Iterative Methods

Most of the calculation time is consumed over precise calculation of the regularised inverse, while in effect this is a redundant refinement, which is pointless beyond the noise level. This can be avoided by iteratively calculating the regularised inverse up to the measurement precision. This approach has been suggested by methods like Landweber scheme and regularised hybrid. At each step t the conductivity distribution is updated

$$\gamma_{t+1} = \gamma_t - \upsilon J^* (J\gamma_t - V_{\Gamma}) \tag{5.99}$$

[14] The use of sponges enables introducing low-contrast controlled perturbations (as oppose to the common high contrast perturbations achieved by the use of Perspex for example)

where $J\gamma_t - V_\Gamma$ corresponds to the difference between the modelled voltages at the t^{th} iteration and the actual boundary measurements, υ is a proportion which weights the error image $J^*(J\gamma_t - V_\Gamma)$.

Single Step Reconstruction Methods

These techniques have been developed and are employed by the Rensselaer group [302;370]. The Newton One-Step Error Reconstruction (NOSER) technique first finds the value of the homogeneous conductivity that minimises the error between modelled and measured boundary voltages on a homogeneous and isotropic 2D object of arbitrary shape. The code takes only one step of the Newton iterative method described in section 5.3.1.3. FNOSER is the computationally streamlined version of NOSER and ToDLeR is its extension for the 3D case.

9 REFERENCES

[1] P. W. Nicholson, "Specific impedance of cerebral white matter," *Exp. Neurol.*, vol. 13, pp. 386-401, 1965.

[2] J. B. Ranck, Jr. and S. L. BeMent, "The specific impedance of the dorsal columns of cat: an inisotropic medium," *Exp. Neurol.*, vol. 11, pp. 451-463, Apr.1965.

[3] P. L. Nunez, "A study of origins of the time dependencies of scalp EEG: I theoretical basis," *IEEE Trans. Biomed. Eng*, vol. 28, no. 3, pp. 271-280, Mar.1981.

[4] P. L. Nunez, "A study of origins of the time dependencies of scalp EEG: II experimental support of theory," *IEEE Trans. Biomed. Eng*, vol. 28, no. 3, pp. 281-288, Mar.1981.

[5] L. A. Geddes and L. E. Baker, "The specific resistance of biological material--a compendium of data for the biomedical engineer and physiologist," *Med. Biol. Eng.*, vol. 5, no. 3, pp. 271-293, May1967.

[6] R. P. Henderson and J. G. Webster, "An impedance camera for spatially specific measurements of the thorax," *IEEE Trans. Biomed. Eng*, vol. 25, no. 3, pp. 250-254, May1978.

[7] A. P. Calder'on, "On an inverse boundary value problem," *Seminar on Numerical Analysisand its applications to Continuum Physics, Soc. Brasileira de Mat`ematica, Rio deJaneiro*, vol. p. 65-73. 1980.

[8] B. H. Brown, D. C. Barber, and A. D. Seagar, "Applied potential tomography: possible clinical applications," *Clin. Phys. Physiol Meas*, vol. 6, no. 2, pp. 109-121, May1985.

[9] N. K. Soni, A. Hartov, C. Kogel, S. P. Poplack, and K. D. Paulsen, "Multi-frequency electrical impedance tomography of the breast: new clinical results," *Physiol. Meas.*, vol. 25, no. 1, pp. 301-314, Feb.2004.

[10] J. L. Mueller, D. Isaacson, and J. C. Newell, "A reconstruction algorithm for electrical impedance tomography data collected on rectangular electrode arrays," *IEEE Trans. Biomed. Eng*, vol. 46, no. 11, pp. 1379-1386, Nov.1999.

[11] J. L. Mueller, D. Isaacson, and J. C. Newell, "Reconstruction of conductivity changes due to ventilation and perfusion from EIT data collected on a rectangular electrode array," *Physiol. Meas.*, vol. 22, no. 1, pp. 97-106, Feb.2001.

[12] M. D. Cheney, D. Isaacson, and J. C. Newell, "Electrical Impedance Tomography," *SIAM Review*, vol. 41, no. 1, pp. 85-101, Jan.1999.

[13] J. C. Newell, P. M. Edic, X. Ren, J. L. Larson-Wiseman, and M. D. Danyleiko, "Assessment of acute pulmonary edema in dogs by electrical impedance imaging," *IEEE Trans. Biomed. Eng*, vol. 43, no. 2, pp. 133-138, Feb.1996.

[14] B. M. Eyuboglu, B. H. Brown, and D. C. Barber, "Problems of cardiac output determination from electrical impedance tomography scans," *Clin. Phys. Physiol Meas*, vol. 9 Suppl A, pp. 71-77, 1988.

[15] I. Frerichs, J. Hinz, P. Herrmann, G. Weisser, G. Hahn, M. Quintel, and G. Hellige, "Regional lung perfusion as determined by electrical impedance tomography in comparison with electron beam CT imaging," *IEEE Trans. Med. Imaging*, vol. 21, no. 6, pp. 646-652, June2002.

[16] I. Frerichs, "Electrical impedance tomography (EIT) in applications related to lung and ventilation: a review of experimental and clinical activities," *Physiol Meas*, vol. 21, no. 2, pp. R1-21, May2000.

[17] B. H. Brown, D. C. Barber, A. H. Morice, and A. D. Leathard, "Cardiac and respiratory related electrical impedance changes in the human thorax," *IEEE Trans. Biomed. Eng*, vol. 41, no. 8, pp. 729-734, Aug.1994.

[18] D. Isaacson, J. L. Mueller, J. C. Newell, and S. Siltanen, "Imaging cardiac activity by the D-bar method for electrical impedance tomography," *Physiol Meas*, vol. 27, no. 5, p. S43-S50, May2006.

[19] C. T. Soulsby, M. Khela, E. Yazaki, D. F. Evans, E. Hennessy, and J. Powell-Tuck, "Measurements of gastric emptying during continuous nasogastric infusion of liquid feed: Electric impedance tomography versus gamma scintigraphy," *Clin. Nutr.*, May2006.

[20] R. H. Smallwood, Y. F. Mangnall, and A. D. Leathard, "Transport of gastric contents," *Physiol Meas*, vol. 15 Suppl 2a, p. A175-A188, May1994.

[21] A. P. Gibson, R. H. Bayford, and D. S. Holder, "Two-dimensional finite element modelling of the neonatal head," *Physiol. Meas.*, vol. 21, no. 1, pp. 45-52, Feb.2000.

[22] D. S. Holder, "Electrical impedance tomography with cortical or scalp electrodes during global cerebral ischaemia in the anaesthetised rat," *Clin. Phys. Physiol. Meas.*, vol. 13, no. 1, pp. 87-98, Feb.1992.

[23] F. J. McArdle, B. H. Brown, R. G. Pearse, and D. C. Barber, "The effect of the skull of low-birthweight neonates on applied potential tomography imaging of centralised resistivity changes,", 1988;9 Suppl A:55-60 ed 1988.

[24] A. McEwan, A. Romsauerova, R. Yerworth, L. Horesh, R. Bayford, and D. Holder, "Design and calibration of a compact multi-frequency EIT system for acute stroke imaging," *Physiol Meas*, vol. 27, no. 5, p. S199-S210, May2006.

[25] A. Romsauerova, A. McEwan, L. Horesh, R. Yerworth, R. H. Bayford, and D. S. Holder, "Multi-frequency electrical impedance tomography (EIT) of the adult human head: initial findings in brain tumours, arteriovenous malformations and chronic stroke, development of an analysis method and calibration," *Physiol Meas*, vol. 27, no. 5, p. S147-S161, May2006.

[26] A. T. Tidswell, "Functional Electrical Impedance Tomography of adult and neonatal brain function." 2004.

[27] A. P. Bagshaw, A. D. Liston, R. H. Bayford, A. Tizzard, A. P. Gibson, A. T. Tidswell, M. K. Sparkes, H. Dehghani, C. D. Binnie, and D. S. Holder, "Electrical impedance tomography of human brain function using reconstruction algorithms based on the finite element method," *NeuroImage*, vol. 20, no. 2, pp. 752-764, Oct.2003.

[28] L. Fabrizi, M. Sparkes, L. Horesh, J. F. Perez-Juste Abascal, A. McEwan, R. H. Bayford, R. Elwes, C. D. Binnie, and D. S. Holder, "Factors limiting the application of electrical impedance tomography for identification of regional conductivity changes using scalp electrodes during epileptic seizures in humans," *Physiol Meas*, vol. 27, no. 5, p. S163-S174, May2006.

[29] *Process Tomography, principles, techniques and applications.* Oxford: Butterworth-Heinemann Ltd, 1995.

[30] K. Bryan, J. Haugh, and D. McCune, "Fast imaging of partially conductive linear cracks using impedance data<footnote pos="info_bottom" id="*">This work was partially supported by an NSF-REU grant, DMS-0352940.</footnote>," *Inverse problems*, vol. 22, no. 4, pp. 1337-1358, 2006.

[31] P. G. Kaup, F. Santosa, and M. Vogelius, "Method for imaging corrosion damage in thin plates from electrostatic data," *Inverse problems*, vol. 12, no. 3, pp. 279-293, 1996.

[32] A. D. Liston, "Models and image reconstruction in Electrical Impedance Tomography of human brain function." PhD Middlesex University, 2003.

[33] A. Tizzard, L. Horesh, R. J. Yerworth, D. S. Holder, and R. H. Bayford, "Generating accurate finite element meshes for the forward model of the human head in EIT," *Physiol Meas*, vol. 26, no. 2, p. S251-S261, Apr.2005.

[34] P. J. Vauhkonen, M. Vauhkonen, T. Savolainen, and J. P. Kaipio, "Three-dimensional electrical impedance tomography based on the complete electrode model," *IEEE Trans. Biomed. Eng*, vol. 46, no. 9, pp. 1150-1160, Sept.1999.

[35] M. Vauhkonen, "Electrical impedance tomography and prior information." PhD 1997.

[36] J. P. Kaipio, V. Kolehmainen, M. Vauhkonen, and E. Somersalo, "Inverse problems with structural prior information," *Inverse problems*, vol. 15 (1999), no. Printed in the UK PII: S0266-5611(99)99228-6, pp. 713-729, Nov.1998.

[37] W. R. B. Lionheart, "EIT reconstruction algorithms: pitfalls, challenges and recent developments," *Physiological Measurement*, vol. 25, no. 1, pp. 125-142, 2004.

[38] D. C. Barber, "A review of image reconstruction techniques for electrical impedance tomography," *Med. Phys.*, vol. 16, no. 2, pp. 162-169, Mar.1989.

[39] A. D. Liston, R. H. Bayford, A. T. Tidswell, and D. S. Holder, "A multi-shell algorithm to reconstruct EIT images of brain function," *Physiol. Meas.*, vol. 23, no. 1, pp. 105-119, Feb.2002.

[40] V. Kolehmainen, M. Vauhkonen, P. A. Karjalainen, and J. P. Kaipio, "Assessment of errors in static electrical impedance tomography with adjacent and trigonometric current patterns," *Physiol. Meas.*, vol. 18, no. 4, pp. 289-303, Nov.1997.

[41] P. J. Riu, J. Rosell, A. Lozano, and R. Pallas-Areny, "Multi-frequency static imaging in electrical impedance tomography: Part 1. Instrumentation requirements," *Med. Biol. Eng Comput.*, vol. 33, no. 6, pp. 784-792, Nov.1995.

[42] P. J. Vauhkonen, M. Vauhkonen, and J. P. Kaipio, "Errors due to the truncation of the computational domain in static three-dimensional electrical impedance tomography," *Physiol. Meas.*, vol. 21, no. 1, pp. 125-135, Feb.2000.

[43] L. Enfield , "Electrical Impedance Tomography of brain function." 2006.

[44] H. P. Schwan, "Electrical characteristics of tissues: a survey," *Biophysik*, vol. 1, pp. 198-208, 1963.

[45] M. A. Stuchly and S. S. Stuchly, "Dielectric-Properties of Biological Substances - Tabulated," *Journal of Microwave Power and Electromagnetic Energy*, vol. 15, no. 1, pp. 19-26, 1980.

[46] K. R. Foster and H. P. Schwan, "Dielectric properties of tissues and biological materials: a critical review," *Crit Rev. Biomed. Eng*, vol. 17, no. 1, pp. 25-104, 1989.

[47] C. Gabriel, S. Gabriel, and E. Corthout, "The dielectric properties of biological tissues: I. Literature survey," *Phys. Med. Biol.*, vol. 41, no. 11, pp. 2231-2249, Nov.1996.

[48] S. Gabriel, R. W. Lau, and C. Gabriel, "The dielectric properties of biological tissues: III. Parametric models for the dielectric spectrum of tissues," *Phys. Med. Biol.*, vol. 41, no. 11, pp. 2271-2293, Nov.1996.

[49] S. Gabriel, R. W. Lau, and C. Gabriel, "The dielectric properties of biological tissues: II. Measurements in the frequency range 10 Hz to 20 GHz," *Phys. Med. Biol.*, vol. 41, no. 11, pp. 2251-2269, Nov.1996.

[50] H. P. Schwan, "Electrical properties of tissue and cell suspension," *Advances in Biological and Medical Physics*, vol. 5, pp. 147-209, 1957.

[51] H. P. Schwan, "Electrical Properties of Blood and its Constituents: Alternating Current Spectroscopy," *Blut*, vol. 46, pp. 185-197, 1983.

[52] W. D. Hurt, "Multiterm Debye dispersion relations for permittivity of muscle," *IEEE Trans. Biomed. Eng*, vol. 32, no. 1, pp. 60-64, Jan.1985.

[53] R. d. L. Kronig and H. A. Kramers, " and," *Atti Congr. Intern. Fisici*, vol. 2, p. 545, 1927.

[54] J. Richards, "Innovations in impedance testing," *Medical Device & Diagnostic Industry*, 1996.

[55] D. S. Tuch, V. J. Wedeen, A. M. Dale, J. S. George, and J. W. Belliveau, "Conductivity tensor mapping of the human brain using diffusion tensor MRI," *Proc. Natl. Acad. Sci. U. S. A*, vol. 98, no. 20, pp. 11697-11701, Sept.2001.

[56] C. H. Wolters, A. Anwander, X. Tricoche, D. M. Weinstein, M. A. Koch, and R. S. MacLeod, "Influence of Tissue Conductivity Anisotropy on EEG/MEG Field and Return Current Computation in a realistic Head Model: A Simulation and Visualization Study using High-Resolution Finite Element Modeling," 2005.

[57] W. R. B. Lionheart, "Conformal uniqueness results in anisotropic electrical impedance imaging," *Inverse problems*, vol. 13, no. 1, pp. 125-134, 1997.

[58] C. Gabriel, "Dielectric properties of biological tissue: Variation with age," *Bioelectromagnetics*, vol. Suppl 7, p. S12-S18, 2005.

[59] S. N. Austad, J. Crocker, W. Gaynor, M. Hansen, P. McNamara, J. Quinn, and V. Schmall, "The amazing aging of the brain," 2006.

[60] A. Surowiec, S. S. Stuchly, M. Keaney, and A. Swarup, "In vivo and in vitro dielectric properties of feline tissues at low radiofrequencies," *Phys. Med. Biol.*, no. 8, pp. 901-909, 1986.

[61] J. Rosell, J. Colominas, P. Riu, R. Pallas-Areny, and J. G. Webster, "Skin impedance from 1 Hz to 1 MHz," *IEEE Trans. Biomed. Eng*, vol. 35, no. 8, pp. 649-651, Aug.1988.

[62] K. G. Boone and D. S. Holder, "A model of the effect of variations in contact and skin impedance on electrical impedane tomography measurement artefacts," *Innov. Tech. Biol. Med.*, vol. 16, no. suppl. 2, pp. 61-70, 1995.

[63] K. G. Boone and D. S. Holder, "Effect of skin impedance on image quality and variability in electrical impedance tomography: a model study," *Med. Biol. Eng Comput.*, vol. 34, no. 5, pp. 351-354, Sept.1996.

[64] T. Yamamoto and Y. Yamamoto, "Electrical properties of the epidermal stratum corneum," *Med. Biol. Eng.*, vol. 14, no. 2, pp. 151-158, Mar.1976.

[65] T. Yamamoto and Y. Yamamoto, "Dielectric constant and resistivity of epidermal stratum corneum," *Med. Biol. Eng.*, vol. 14, no. 5, pp. 494-500, Sept.1976.

[66] R. Pethig, "Dielectric properties of body tissues," *Clin. Phys. Physiol. Meas.*, no. 4A, pp. 5-12, 1987.

[67] C. Gabriel, "Comments on 'dielectric properties of the skin'," *Phys. Med. Biol.*, vol. 42, no. 8, pp. 1671-1673, Aug.1997.

[68] C. Gabriel, "Compilation of the dielectric properties of body tissues at RF and microwave frequencies," BollinReport DC 20332-00001g AFB,Bolling AFB Report DC 20332-00001, 1995.

[69] V. Raicu, N. Kitagawa, and A. Irimajiri, "A quantitative approach to the dielectric properties of the skin," *Phys. Med. Biol.*, vol. 45, no. 2, p. L1-L4, Feb.2000.

[70] H. C. Burger and J. B. Van Milaan, "Measurements of the specific resistnace of the human body to direct current," *Act Med Scand*, vol. 114, pp. 584-607, 1943.

[71] H. P. Schwan, "Electrical properties measured with alternating currents; body tissues," in *Handbook of biological data*. W. S. Spencer, Ed. Philadelpia: W B Sounders Co, 1956.

[72] H. C. Burger and R. Van Dongen, "Specific Electrical Resistance of Body Tissue," *Phys. Med. Biol.*, vol. 5, pp. 431-447, 1960.

[73] R. D. Stoy, K. R. Foster, and H. P. Schwan, "Dielectric properties of mammalian tissues from 0.1 to 100 MHz: a summary of recent data," *Phys. Med. Biol.*, vol. 27, no. 4, pp. 501-513, Apr.1982.

[74] B. R. Epstein and K. R. Foster, "Anisotropy in the dielectric properties of skeletal muscle," *Med. Biol. Eng Comput.*, vol. 21, no. 1, pp. 51-55, Jan.1983.

[75] F. L. Gielen, J. W. Wallinga-de, and K. L. Boon, "Electrical conductivity of skeletal muscle tissue: experimental results from different muscles in vivo," *Med. Biol. Eng Comput.*, vol. 22, no. 6, pp. 569-577, Nov.1984.

[76] B. Bodakian and F. X. Hart, "The dielectric properties of meat," *IEEE Transaction on Dielectrics and Electrical Insulation*, vol. 1, no. 2, pp. 181-187, Apr.1994.

[77] F. X. Hart, N. J. Berner, and R. L. McMillen, "Modelling the anisotropic electrical properties of skeletal muscle," *Phys. Med. Biol.*, vol. 44, no. 2, pp. 413-421, Feb.1999.

[78] S. Rush, "Methods of measuring the resistivities of anisotropic conducting media in situ," *Journal of Research of the National Bureau of Standards - C. Engineering and Instrumentation*, vol. 66C, no. 3 Apr.1962.

[79] *Grant's Atlas of Anatomy* Lippincott Williams & Wilkins, 2004, p. -848.

[80] S. Rush and D. A. Driscoll, "Current distribution in the brain from surface electrodes," *Anesth. Analg.*, vol. 47, no. 6, pp. 717-723, Nov.1968.

[81] S. Rush and D. A. Driscoll, "EEG electrode sensitivity--an application of reciprocity," *IEEE Trans. Biomed. Eng*, vol. 16, no. 1, pp. 15-22, Jan.1969.

[82] S. K. Law, "Thickness and resistivity variations over the upper surface of the human skull," *Brain Topogr.*, vol. 6, no. 2, pp. 99-109, 1993.

[83] T. F. Oostendorp, J. Delbeke, and D. F. Stegeman, "The conductivity of the human skull: results of in vivo and in vitro measurements," *IEEE Trans. Biomed. Eng*, vol. 47, no. 11, pp. 1487-1492, Nov.2000.

[84] M. Akhtari, H. C. Bryant, A. N. Mamelak, E. R. Flynn, L. Heller, J. J. Shih, M. Mandelkern, A. Matlachov, D. M. Ranken, E. D. Best, M. A. DiMauro, R. R. Lee, and W. W. Sutherling, "Conductivities of three-layer live human skull," *Brain Topogr.*, vol. 14, no. 3, pp. 151-167, 2002.

[85] M. Akhtari, H. C. Bryant, D. Emin, W. Merrifield, A. N. Mamelak, E. R. Flynn, J. J. Shih, M. Mandelkern, A. Matlachov, D. M. Ranken, E. D. Best, M. A. DiMauro, R. R. Lee, and W. W. Sutherling, "A model for frequency dependence of conductivities of the live human skull," *Brain Topogr.*, vol. 16, no. 1, pp. 39-55, 2003.

[86] S. Goncalves, J. C. de Munck, R. M. Heethaar, F. H. Lopes da Silva, and B. W. van Dijk, "The application of electrical impedance tomography to reduce systematic errors in the EEG inverse problem--a simulation study," *Physiol. Meas.*, vol. 21, no. 3, pp. 379-393, Aug.2000.

[87] S. I. Goncalves, J. C. de Munck, J. P. Verbunt, R. M. Heethaar, and F. H. da Silva, "In vivo measurement of the brain and skull resistivities using an EIT-based method and the combined analysis of SEF/SEP data," *IEEE Trans. Biomed. Eng*, vol. 50, no. 9, pp. 1124-1128, Sept.2003.

[88] S. I. Goncalves, J. C. de Munck, J. P. Verbunt, F. Bijma, R. M. Heethaar, and d. S. Lopes, "In vivo measurement of the brain and skull resistivities using an EIT-based method and realistic models for the head," *IEEE Trans. Biomed. Eng*, vol. 50, no. 6, pp. 754-767, June2003.

[89] R. Hoekema, G. J. Huiskamp, G. H. Wieneke, F. S. Leijten, C. W. van Veelen, P. C. van Rijen, J. Ansems, and A. C. van Huffelen, "Measurement of the conductivity of skull, temporarily removed during epilepsy surgery," *Brain Topogr.*, vol. 16, no. 1, pp. 29-38, 2003.

[90] "Anatomy of a Long Bone," 2006.

[91] D. A. Chakkalakal, M. W. Johnson, R. A. Harper, and J. L. Katz, "Dielectric properties of fluid-saturated bone," *IEEE Trans. Biomed. Eng*, vol. 27, no. 2, pp. 95-100, Feb.1980.

[92] D. A. Chakkalakal and M. W. Johnson, "Electrical properties of compact bone," *Clin. Orthop. Relat Res.*, no. 161, pp. 133-145, Nov.1981.

[93] G. B. Reinish and A. S. Nowick, "A model for dielectric behaviour of wet bone," in *Electrical properties of bone and cartliage*, New York Grune & Stratton ed. C. T. e. a. Brighton, Ed. 1979, pp. 13-29.

[94] J. D. Kosterich, K. R. Foster, and S. R. Pollack, "Dielectric permittivity and electrical conductivity of fluid saturated bone," *IEEE Trans. Biomed. Eng*, vol. 30, no. 2, pp. 81-86, Feb.1983.

[95] G. N. Reddy and S. Saha, "Electrical and dielectric properties of wet bone as a function of frequency," *IEEE Trans. Biomed. Eng*, vol. 31, no. 3, pp. 296-303, Mar.1984.

[96] S. R. Smith and K. R. Foster, "Dielectric properties of low-water-content tissues," *Phys. Med. Biol.*, vol. 30, no. 9, pp. 965-973, Sept.1985.

[97] De Mercato G. and F. J. Garcia-Sanchez, "Dielectric properties of fluid-saturated bone: a comparison between diaphysis and epiphysis," *Med. Biol. Eng Comput.*, vol. 26, no. 3, pp. 313-316, May1988.

[98] S. Saha and P. A. Williams, "Electric and dielectric properties of wet human cancellous bone as a function of frequency," *Ann. Biomed. Eng*, vol. 17, no. 2, pp. 143-158, 1989.

[99] S. Saha and P. A. Williams, "Electric and dielectric properties of wet human cortical bone as a function of frequency," *IEEE Trans. Biomed. Eng*, vol. 39, no. 12, pp. 1298-1304, Dec.1992.

[100] G. De Mercato and F. J. G. Sanchez, "Correlation Between Low-Frequency Electric-Conductivity and Permittivity in the Diaphysis of Bovine Femoral Bone," *IEEE Trans. Biomed. Eng*, vol. 39, no. 5, pp. 523-526, May1992.

[101] J. Sierpowska, J. Toyras, M. A. Hakulinen, S. Saarakkala, J. S. Jurvelin, and R. Lappalainen, "Electrical and dielectric properties of bovine trabecular bone--relationships with mechanical properties and mineral density," *Phys. Med. Biol.*, vol. 48, no. 6, pp. 775-786, Mar.2003.

[102] J. Sierpowska, M. A. Hakulinen, J. Toyras, J. S. Day, H. Weinans, J. S. Jurvelin, and R. Lappalainen, "Prediction of mechanical properties of human trabecular bone by electrical measurements," *Physiol. Meas.*, vol. 26, no. 2, p. S119-S131, Apr.2005.

[103] S. A. Radvan-Ziemnowicz, J. C. McWilliams, and W. E. Kucharski, "Conductivity versus frequency in human and feline cerebrospinal fluid,", 6 ed *17th Ann. Conf. Eng. Med., Biol.*: 1964, p. 108.

[104] S. B. Baumann, D. R. Wozny, S. K. Kelly, and F. M. Meno, "The electrical conductivity of human cerebrospinal fluid at body temperature," *IEEE Trans. Biomed. Eng*, vol. 44, no. 3, pp. 220-223, Mar.1997.

[105] J. Latikka, T. Kuurne, and H. Eskola, "Conductivity of living intracranial tissues," *Phys. Med. Biol.*, vol. 46, no. 6, pp. 1611-1616, June2001.

[106] "Heart and Stroke Foundation," 2006.

[107] "BIOON - Grey and white matter," 2006.

[108] J. O. Ollikainen, M. Vauhkonen, P. A. Karjalainen, and J. P. Kaipio, "Effects of local skull inhomogeneities on EEG source estimation," *Med. Eng Phys.*, vol. 21, no. 3, pp. 143-154, Apr.1999.

[109] A. T. Tidswell, A. P. Gibson, R. H. Bayford, and D. S. Holder, "Validation of a 3D reconstruction algorithm for EIT of human brain function in a realistic head-shaped tank," *Physiol. Meas.*, vol. 22, no. 1, pp. 177-185, Feb.2001.

[110] A. D. Liston, R. H. Bayford, and D. S. Holder, "The effect of layers in imaging brain function using electrical impedance tomograghy," *Physiol. Meas.*, vol. 25, no. 1, pp. 143-158, Feb.2004.

[111] "ASA - Advanced Source Analysis," ANT Software BV, 2004.

[112] T. C. Ferree, K. J. Eriksen, and D. M. Tucker, "Regional head tissue conductivity estimation for improved EEG analysis," *IEEE Trans. Biomed. Eng*, vol. 47, no. 12, pp. 1584-1592, Dec.2000.

[113] A. Romsauerova, R. J. Yerworth, A. McEwan, L. Horesh, J. F. P. J. Abascal, and D. S. Holder, "Calibration and preliminary human measurements for multifrequency EIT of the human head," *VI International Conference on Biomedical Applications of Electrical Impedance Tomography, London, UK*: 2005.

[114] U. Baysal and J. Haueisen, "Use of a priori information in estimating tissue resistivities--application to human data in vivo," *Physiol. Meas.*, vol. 25, no. 3, pp. 737-748, June2004.

[115] D. Guti'errez, A. Nehorai, and C. H. Muravchik, "Estimating Brain Conductivities and Dipole Source Signals with EEG Arrays," *IEEE Trans. Biomed. Eng*, Nov.2002.

[116] E. Luders, H. Steinmetz, and L. Jancke, "Brain size and grey matter volume in the healthy human brain," *Neuroreport*, vol. 13, no. 17, pp. 2371-2374, Dec.2002.

[117] C. L. Li, A. F. Bak, and L. O. Parker, "Specific resistivity of the cerebral cortex and white matter," *Exp. Neurol.*, vol. 20, no. 4, pp. 544-557, Apr.1968.

[118] W. H. Freygang and W. M. Landau, "Some relations between resistivity and electrical activity in the cerebral cortex of the cat," *Journal of Cellular Comparative Physiology*, vol. 45, pp. 377-392, 1955.

[119] J. B. Ranck, Jr., "Specific impedance of rabbit cerebral cortex," *Exp. Neurol.*, vol. 7, pp. 144-152, Feb.1963.

[120] J. B. Ranck, Jr., "Analysis of specific impedance of rabbit cerebral cortex," *Exp. Neurol.*, vol. 7, pp. 153-174, Feb.1963.

[121] J. B. Ranck, Jr., "Electrical impedance in the subicular area of rats during paradoxical sleep," *Exp. Neurol.*, vol. 16, no. 4, pp. 416-437, Dec.1966.

[122] A. Van Harreveld, T. Murphy, and K. W. Nobel, "Specific Impedance of rabbit's cortical tissue," *American Journal of Physiology*, vol. 2, pp. 203-205, 1963.

[123] G. W. Crile, H. R. Hosmer, and A. F. Rowland, "The electrical conductivity of animal tissues under normal and pathological conditions," *American Journal of Physiology*, vol. 60, pp. 59-106, 1922.

[124] P. N. Robillard and Y. Poussart, "Specific-impedance measurements of brain tissues," *Med. Biol. Eng Comput.*, vol. 15, no. 4, pp. 438-445, July1977.

[125] A. Surowiec, S. Stuchly, and A. Swarup, "Postmortem changes of the dielectric properties of bovine brain tissues at low radiofrequencies," *Bioelectromagnetics*, vol. 7, no. 31, p. 43, 1986.

[126] "VetMed - Grey and white matter of the spinal cord," 2006.

[127] N. A. Coulter, Jr. and J. R. Pappenheimer, "Development of turbulence in flowing blood," *Am. J. Physiol*, vol. 159, no. 2, pp. 401-408, Nov.1949.

[128] F. G. Hirsch, E. C. Texter, Jr., L. A. Wood, W. C. Ballard, Jr., F. E. Horna, and I. S. WRIGHT, "The electrical conductivity of blood. I: Relationship to erythrocyte concentration," *Blood*, vol. 5, no. 11, pp. 1017-1035, Nov.1950.

[129] R. Hober, "Messungen der innem Leitfahigkeit von Zellen III," *Arch. Ges. Physiol.*, vol. 150, pp. 15-145, 1913.

[130] R. Hober, "Ein zweites Verfahren die Leitfahigkeit im Innem von Zellen zu messen," *Arch. Ges. Physiol.*, vol. 148, pp. 189-221, 1912.

[131] R. Hober, "Eine methode, die elektrische Leitfahigkeit im Innem von Zellen zu Messen," *Sen Axh. Ges. Physiol.*, vol. **133** , pp. 59-237, 1910.

[132] R. L. Rosenthal and C. W. Tobias, "Measurement of the Electrical resistance of human blood;use in coagulation studies and cell volume determinations," *Journal of Laboratory and Clinical Medicine*, vol. 33, pp. 1110-1121, 1948.

[133] H. Pfutzner, "Dielectric analysis of blood by means of a raster-electrode technique," *Med. Biol. Eng Comput.*, vol. 22, no. 2, pp. 142-146, Mar.1984.

[134] T. X. Zhao, "Electrical impedance and haematocrit of human blood with various anticoagulants," *Physiol. Meas.*, vol. 14, no. 3, pp. 299-307, Aug.1993.

[135] T. X. Zhao, B. Jacobson, and T. Ribbe, "Triple-frequency method for measuring blood impedance," *Physiol. Meas.*, vol. 14, no. 2, pp. 145-156, May1993.

[136] O. Casas, R. Bragos, P. J. Riu, J. Rosell, M. Tresanchez, M. Warren, A. Rodriguez-Sinovas, A. Carreno, and J. Cinca, "In vivo and in situ ischemic tissue characterization using electrical impedance spectroscopy," *Ann N. Y. Acad. Sci.*, vol. 873, pp. 51-58, Apr.1999.

[137] F. Jaspard, M. Nadi, and A. Rouane, "Dielectric properties of blood: an investigation of haematocrit dependence," *Physiol. Meas.*, no. 1, pp. 137-147, 2003.

[138] "Discovery fund for the eye research - Anatomy of the eye," 2006.

[139] M. Watanabe, Y. Mokudai, H. Ueno, M. Ando, and A. Irimajiri, "Dielectric measurements on the rabbit cornea using a surface electrode," *Nippon Ganka Gakkai Zasshi*, vol. 97, no. 5, pp. 569-574, May1993.

[140] O. P. Gandhi, "Some Numerical-Methods for Dosimetry - Extremely Low-Frequencies to Microwave-Frequencies," *Radio Science*, vol. 30, no. 1, pp. 161-177, Jan.1995.

[141] I. Jurgens, J. Rosell, and P. J. Riu, "Electrical impedance tomography of the eye: in vitro measurements of the cornea and the lens," *Physiol. Meas.*, vol. 17 Suppl 4A, p. A187-A195, Nov.1996.

[142] K. S. Kohli, D. V. Rai, V. K. Jindal, and N. Goyal, "Impedance of goat eye lens at different DC voltages," *Med. Biol. Eng Comput.*, vol. 36, no. 5, pp. 604-607, Sept.1998.

[143] G. Lindenblatt and J. Silny, "A model of the electrical volume conductor in the region of the eye in the ELF range," *Phys. Med. Biol.*, vol. 46, no. 11, pp. 3051-3059, Nov.2001.

[144] O. G. Martinsen and S. Grimnes, "Facts and myths about electrical measurement of stratum corneum hydration state," *Dermatology*, vol. 202, no. 2, pp. 87-89, 2001.

[145] J. H. Calderwood, "Electrode-skin impedance from a dielectric viewpoint," *Physiol. Meas.*, vol. 17 Suppl 4A, p. A131-A139, Nov.1996.

[146] R. W. de Boer and A. van Oosterom, "Electrical properties of platinum electrodes: impedance measurements and time-domain analysis," *Med. Biol. Eng Comput.*, vol. 16, no. 1, pp. 1-10, Jan.1978.

[147] P. Hua, E. J. Woo, J. G. Webster, and W. J. Tompkins, "Finite element modeling of electrode-skin contact impedance in electrical impedance tomography," *IEEE Trans. Biomed. Eng*, vol. 40, no. 4, pp. 335-343, Apr.1993.

[148] E. J. Woo, P. Hua, J. G. Webster, W. J. Tompkins, and R. Pallas-Areny, "Skin impedance measurements using simple and compound electrodes," *Med. Biol. Eng Comput.*, vol. 30, no. 1, pp. 97-102, Jan.1992.

[149] Z. Szczepanik and Z. Rucki, "Frequency analysis of electrical impedance tomography system," *IEEE Trans. Instrumentation and Measurement*, vol. 49, no. 4, pp. 844-851, Aug.2000.

[150] Y. Jiang, J. Zhao, P. Augat, X. Ouyang, Y. Lu, S. Majumdar, and H. K. Genant, "Trabecular bone mineral and calculated structure of human bone specimens scanned by peripheral quantitative computed tomography: relation to biomechanical properties," *J. Bone Miner. Res.*, vol. 13, no. 11, pp. 1783-1790, Nov.1998.

[151] M. Akhtari, H. C. Bryant, A. N. Mamelak, L. Heller, J. J. Shih, M. Mandelkern, A. Matlachov, D. M. Ranken, E. D. Best, and W. W. Sutherling, "Conductivities of three-layer human skull," *Brain Topogr.*, vol. 13, no. 1, pp. 29-42, 2000.

[152] T. Siegal, U. Sandbank, A. Gabizon, T. Siegal, R. Mizrachi, E. Ben-David, and R. Catane, "Alteration of blood-brain-CSF barrier in experimental meningeal carcinomatosis. A morphologic and adriamycin-penetration study," *J. Neurooncol.*, vol. 4, no. 3, pp. 233-242, 1987.

[153] K. R. Foster, J. L. Schepps, R. D. Stoy, and H. P. Schwan, "Dielectric properties of brain tissue between 0.01 and 10 GHz," *Phys. Med. Biol.*, vol. 24, no. 6, pp. 1177-1187, Nov.1979.

[154] N. R. Nightingale, V. D. Goodridge, R. J. Sheppard, and J. L. Christie, "The dielectric properties of the cerebellum, cerebrum and brain stem of mouse brain at radiowave and microwave frequencies," *Phys. Med. Biol.*, vol. 28, no. 8, pp. 897-903, Aug.1983.

[155] J. B. J. Ranck, "Specific impedance of cerebral cortex during spreading depression, analysis of neuronal neuroglial, interstitial contributions," *Exp. Neurol.*, vol. 9, no. 1, p. 1-&, 1964.

[156] A. Anwander, C. H. Wolters, M. Dumpelmann, and T. Knosche, "Influence of realistic skull and white matter anisotropy on the inverse problem in EEG/MEG-source localization," BioMag - 13th international Conference on Biomagnetism, Jena, Germany: 2002.

[157] J. Haueisen, D. S. Tuch, C. Ramon, P. H. Schimpf, V. J. Wedeen, J. S. George, and J. W. Belliveau, "The influence of brain tissue anisotropy on human EEG and MEG," *NeuroImage*, vol. 15, no. 1, pp. 159-166, Jan.2002.

[158] The Discovery Fund for Eye Research, "Anatomy of the Eye," http://www.discoveryfund.org/anatomyoftheeye.html: 2006.

[159] G. Lindenblatt and J. Silny, "Electrical phosphenes: on the influence of conductivity inhomogeneities and small-scale structures of the orbita on the current density threshold of excitation," *Med. Biol. Eng Comput.*, vol. 40, no. 3, pp. 354-359, May2002.

[160] D. Attwell, "Interaction of low frequency electric fields with the nervous system: the retina as a model system," *Radiat. Prot. Dosimetry.*, vol. 106, no. 4, pp. 341-348, 2003.

[161] C. F. Dalziel, "Electric Shock Hazard," *IEEE Spectrum*, vol. 9, no. 2, p. 41-&, 1972.

[162] O. Gilad, L. Horesh, and D. Holder, "Design of electrodes and current limits for low frequency Electrical Impedance Tomography of the brain," 2006.

[163] L. Horesh, O. Gilad, A. Romsauerova, A. McEwan, S. R. Arridge, and D. S. Holder, "Stroke type differentiation by Multi-Frequency Electrical Impedance Tomography (MFEIT) - A feasibility study,", 11 ed *3rd European Medical and Biological Engineering Conference, Prague, Czech Republic*: 2005.

[164] L. Horesh, O. Gilad, A. Romsauerova, and D. S. Holder, "Stroke type detection by Multi-Frequency Electrical Impedance Tomography (MFEIT) - A feasibility study," *VI International Conference on Biomedical Applications of Electrical Impedance Tomography, London, UK*: 2005.

[165] J. Bamford, P. Sandercock, M. Dennis, J. Burn, and C. Warlow, "Classification and natural history of clinically identifiable subtypes of cerebral infarction," *Lancet*, vol. 337, no. 8756, pp. 1521-1526, June1991.

[166] J. Bogousslavsky, M. G. Van, and F. Regli, "The Lausanne Stroke Registry: analysis of 1,000 consecutive patients with first stroke," *Stroke*, vol. 19, no. 9, pp. 1083-1092, Sept.1988.

[167] G. W. Albers, J. D. Easton, R. L. Sacco, and P. Teal, "Antithrombotic and thrombolytic therapy for ischemic stroke," *Chest*, vol. 114, no. 5 Suppl, pp. 683S-698S, Nov.1998.

[168] "National Society for Epilepsy," 2006.

[169] G. G. Somjen, *Ions in the Brain: Normal Function, Seizures, and Stroke.* New York: Oxford University Press, 2004, p. -470.

[170] J. Engel, Jr., "Update on surgical treatment of the epilepsies. Summary of the Second International Palm Desert Conference on the Surgical Treatment of the Epilepsies (1992)," *Neurology*, vol. 43, no. 8, pp. 1612-1617, Aug.1993.

[171] J. Engel, Jr., "Update on surgical treatment of the epilepsies. Summary of the Second International Palm Desert Conference on the Surgical Treatment of the Epilepsies (1992)," *Neurology*, vol. 43, no. 8, pp. 1612-1617, Aug.1993.

[172] K. Boone, A. M. Lewis, and D. S. Holder, "Imaging of cortical spreading depression by EIT: implications for localization of epileptic foci," *Physiol Meas*, vol. 15 Suppl 2a, p. A189-A198, May1994.

[173] A. Rao, "Impedance Tomography of brain activity: studies into its accuracy and physiological mechanisms." University College London, 2000.

[174] D. du Plessis, "Primary Brain Tumours," *Neuropathology*, vol. 4, no. 6, pp. 17-19, 2005.

[175] "Utha University Medical Library," 2006.

[176] C. D. Cone, Jr. and C. M. Cone, "Induction of mitosis in mature neurons in central nervous system by sustained depolarization," *Science*, vol. 192, no. 4235, pp. 155-158, Apr.1976.

[177] P. C. Burger and B. W. Scheithauer, *Tumors of the central nervous system*, Atlas of Tumor Pathology 3rd series ed. Washington DC: Armed Forces Institute of Pathology, 1994, pp. 317-320.

[178] L. Vargova, A. Homola, J. Zamecnik, M. Tichy, V. Benes, and E. Sykova, "Diffusion parameters of the extracellular space in human gliomas," *Glia*, vol. 42, no. 1, pp. 77-88, Apr.2003.

[179] A. Van Harreveld and S. Ochs, "Cerebral Impedance Changes After Circulatory Arrest," *Am. J. Physiol*, vol. 187, no. 1, pp. 180-192, Sept.1956.

[180] A. Surowiec, S. S. Stuchly, and A. Swarup, "Radiofrequency dielectric properties of animal tissues as a function of time following death," *Phys. Med. Biol.*, vol. 30, no. 10, pp. 1131-1141, Oct.1985.

[181] D. S. Holder, "Detection of cerebral ischaemia in the anaesthetised rat by impedance measurement with scalp electrodes: implications for non-invasive imaging of stroke by electrical impedance tomography," *Clin. Phys. Physiol. Meas.*, vol. 13, no. 1, pp. 63-75, Feb.1992.

[182] B. E. Lingwood, K. R. Dunster, G. N. Healy, L. C. Ward, and P. B. Colditz, "Cerebral impedance and neurological outcome following a mild or severe hypoxic/ischemic episode in neonatal piglets," *Brain Res.*, vol. 969, no. 1-2, pp. 160-167, Apr.2003.

[183] B. H. Cornish, B. J. Thomas, and L. C. Ward, "Improved prediction of extracellular and total body water using impedance loci generated by multiple frequency bioelectrical impedance analysis," *Phys. Med. Biol.*, vol. 38, no. 3, pp. 337-346, Mar.1993.

[184] X. Wu, X. Dong, M. Qin, F. Fu, Y. Wang, F. You, H. Xiang, R. Liu, and X. Shi, "In vivo measurement of rabbits brain impedance frequency response and the elementary imaging of EIT," *Chinese Journal of Biomedical Engineering*, vol. 20, no. 1, pp. 49-51, Mar.2003.

[185] X. Wu, X. Dong, M. Qin, F. Fu, Y. Wang, F. You, H. Xiang, R. Liu, and X. Shi, "The in vitro measurements of rabbit brain complex impedance frequency response and the equivalent circuit model," *Chinese Journal of Biomedical Engineering*, vol. 22, no. 3 June2003.

[186] F. Seoane, K. Lindecrantz, T. Olsson, I. Kjellmer, A. Flisberg, and R. Bågenholm, "Brain electrical impedance at various frequencies: the effect of hypoxia," 26th annual international conference of the IEEE Engineering in Medicine and Biology Society. San Francisco, California: 2004.

[187] F. Seoane, K. Lindecrantz, T. Olsson, I. Kjellmer, and C. Mallard, "Evolution of cerebral bioelectrical resistance at various frequencies during hypoxia in fetal sheep," annual conference of Engineering and Physical Sciences in Medicine, EPSM2004. Geelong, Australia. November 2004 : 2004.

[188] F. Seoane, K. Lindecrantz, T. Olsson, I. Kjellmer, A. Flisberg, and R. Bågenholm, "Spectroscopy Study of the Dynamics of the Transencephalic Electrical Impedance in the Perinatal Brain during Hypoxia ," *Phys. Med. Biol.*, Apr.2005.

[189] "Subarachnoid haemorrhage and intracerebral haemorrhage," 2006.

[190] C. R. Falyar, "Using transcranial Doppler sonography to augment the neurological examination after aneurysmal subarachnoid hemorrhage," *J. Neurosci. Nurs.*, vol. 31, no. 5, pp. 285-293, Oct.1999.

[191] M. Chow, A. S. Dumont, and N. F. Kassell, "Endothelin receptor antagonists and cerebral vasospasm: an update," *Neurosurgery*, vol. 51, no. 6, pp. 1333-1341, Dec.2002.

[192] P. Warnell, "Advanced concepts in the management of cerebral vasospasm associated with aneurysmal subarachnoid hemorrhage," *Axone.*, vol. 17, no. 4, pp. 86-92, June1996.

[193] T. E. Bell and G. L. Kongable, "Innovations in aneurysmal subarachnoid hemorrhage: intracisternal t-PA for the prevention of vasospasm," *J. Neurosci. Nurs.*, vol. 28, no. 2, pp. 107-113, Apr.1996.

[194] M. Adamczyk, E. M. Brate, E. G. Chiappetta, S. Ginsburg, E. Hoffman, C. Klein, M. M. Perkowitz, S. D. Rege, P. P. Chou, and A. G. Costantino, "Development of a quantitative vancomycin immunoassay for the Abbott AxSYM analyzer," *Ther. Drug Monit.*, vol. 20, no. 2, pp. 191-201, Apr.1998.

[195] R. L. Macdonald, "Pathophysiology and molecular genetics of vasospasm," *Acta Neurochir. Suppl*, vol. 77, pp. 7-11, 2001.

[196] H. A. Van and J. P. Schade, "Changes in the electrical conductivity of cerebral cortex during seizure activity," *Exp. Neurol.*, vol. 5, pp. 383-400, May1962.

[197] W. R. Adey, R. T. Kado, and J. Didio, "Impedance measurements in brain tissue of animals using microvolt singals," *Exp. Neurol.*, vol. 5, pp. 47-66, Jan.1962.

[198] R. Porter, W. R. Adey, and R. T. Kado, "Measurement of electrical impedance in the human brain: some preliminary observations," *Neurology*, vol. 14, pp. 1002-1012, Nov.1964.

[199] M. N. Shalit, "The effect of Metrazol on the hemodynamics and impedance of the cat's brain cortex," *J. Neuropathol. Exp. Neurol.*, vol. 24, pp. 75-84, Jan.1965.

[200] Z. Elazar, R. T. Kado, and W. R. Adey, "Impedance changes during epileptic seizures," *Epilepsia*, vol. 7, no. 4, pp. 291-307, Dec.1966.

[201] J. E. Fox, M. Bikson, and J. G. Jefferys, "Tissue resistance changes and the profile of synchronized neuronal activity during ictal events in the low-calcium model of epilepsy," *J. Neurophysiol.*, vol. 92, no. 1, pp. 181-188, July2004.

[202] A. J. Surowiec, S. S. Stuchly, J. B. Barr, and A. Swarup, "Dielectric properties of breast carcinoma and the surrounding tissues," *IEEE Trans. Biomed. Eng*, vol. 35, no. 4, pp. 257-263, Apr.1988.

[203] T. Morimoto, S. Kimura, Y. Konishi, K. Komaki, T. Uyama, Y. Monden, Y. Kinouchi, and T. Iritani, "A study of the electrical bio-impedance of tumors," *J. Invest Surg.*, vol. 6, no. 1, pp. 25-32, Jan.1993.

[204] M. Osypka and E. Gersing, "Tissue impedance spectra and the appropriate frequencies for EIT," *Physiol Meas*, vol. 16, no. 3 Suppl A, p. A49-A55, Aug.1995.

[205] B. Blad and B. Baldetorp, "Impedance spectra of tumour tissue in comparison with normal tissue; a possible clinical application for electrical impedance tomography," *Physiol Meas*, vol. 17 Suppl 4A, p. A105-A115, Nov.1996.

[206] J. Jossinet, "The impedivity of freshly excised human breast tissue," *Physiol Meas*, vol. 19, no. 1, pp. 61-75, Feb.1998.

[207] D. Haemmerich, S. T. Staelin, J. Z. Tsai, S. Tungjitkusolmun, D. M. Mahvi, and J. G. Webster, "In vivo electrical conductivity of hepatic tumours," *Physiol Meas*, vol. 24, no. 2, pp. 251-260, May2003.

[208] R. S. Yoon, A. Czaya, H. C. Kwan, and M. L. Joy, "Changes in the complex permittivity during spreading depression in rat cortex," *IEEE Trans. Biomed. Eng*, vol. 46, no. 11, pp. 1330-1338, Nov.1999.

[209] J. Zamecnik, L. Vargova, A. Homola, R. Kodet, and E. Sykova, "Extracellular matrix glykoproteins and diffusion barriers in human astrocytic tumours,", 30 ed Neuropathology and Applied Neurobiology: 2003, pp. 338-350.

[210] K. S. Cheng, D. Isaacson, J. C. Newell, and D. G. Gisser, "Electrode models for electric-current Computed-Tomography," *IEEE Trans. Biomed. Eng*, vol. 36, no. 9, pp. 918-924, Sept.1989.

[211] E. Somersalo, M. D. Cheney, and D. Isaacson, "Existence and uniqueness for electrode models for electric-current Computed-Tomography," *SIAM J. Appl. Math*, vol. 52, no. 4, pp. 1023-1040, Aug.1992.

[212] F. Kleinermann and N. J. Avis, "Analytical solution to the three dimensional forward problem for a circular cylinder," *Inverse problems*, vol. 16, pp. 461-468, 2000.

[213] M. Mayer, P. Brunner, R. Merwa, F. M. Smolle-Juttner, A. Maier, and H. Scharfetter, "Direct reconstruction of tissue parameters from differential multifrequency EIT in vivo," *Physiol Meas*, vol. 27, no. 5, pp. S93-101, May2006.

[214] A. Corlu, T. Durduran, R. Choe, M. Schweiger, E. M. Hillman, S. R. Arridge, and A. G. Yodh, "Uniqueness and wavelength optimization in continuous-wave multispectral diffuse optical tomography," *Opt. Lett.*, vol. 28, no. 23, pp. 2339-2341, Dec.2003.

[215] J. Fritschy, L. Horesh, D. S. Holder, and R. H. Bayford, "Using the GRID to improve the computation speed of electrical impedance tomography (EIT) reconstruction algorithms," *Physiol. Meas.*, vol. 26, no. 2, p. S209-S215, 2005.

[216] J. Fritschy, L. Horesh, D. S. Holder, and R. H. Bayford, "Applications of GRID in clinical neurophysiology and Electrical Impedance Tomography of brain function," *Stud. Health Technol. Inform.*, vol. 112, pp. 138-145, 2005.

[217] C. R. Johnson and D. M. Weinstein, "Biomedical computing and visualization,", 48 ed. V. Estivill-Castro and G. Dobbie, Eds. Twenty-Ninth Australasian Computer Science Conference (ACSC2006), Hobart, Australia. Conferences in Research and Practice in Information Technology (CRPIT): 2006, pp. 3-10.

[218] A. H. Barnett, A. G. Culver, A. Soresend, A. Dale, and D. A. Boas, "Robust Inference of Baseline Optical Properties of the Human Head with 3D Segmentation from Magnetic Resonance Imaging," *Appl. Optics*, vol. 42, pp. 3095-3108, 2003.

[219] N. K. Soni, K. D. Paulsen, H. Dehghani, and A. Hartov, "Image reconstruction in Electrical Impedance Tomography using the full set of Maxwell's equations," *VI International Conference on Biomedical Applications of Electrical Impedance Tomography, London, UK, June 2005*: 2005.

[220] L. Horesh, M. Schweiger, S. R. Arridge, and D. S. Holder, "Large Scale Non-Linear 3D Reconstruction Algorithms for Electrical Impedance Tomography of the Human Brain," *Applied Inverse Problems Conference, Royal Agricultural College, Conference Centre, UK* : 2005.

[221] M. Molinari, S. J. Cox, BH Blott, and GJ Daniell, "Efficient non-linear 3D Electrical Tomography reconstruction 2," in *ISBN 0 85316 2247*, 2nd World Congress on Industrial Process Tomography ed Hannover,Germany: 2001.

[222] M. Molinari, H. Fangohr, J. Generowicz, and S. J. Cox, "Efficient non-linear 3D Electrical Tomography reconstruction 1," in *ISBN 0 85316 2247*, 2nd World Congress on Industrial Process Tomography ed Hannover,Germany: 2001.

[223] L. Horesh, R. H. Bayford, R. J. Yerworth, A. Tizzard, G. M. Ahadzi, and D. S. Holder, "Beyond the linear domain - The way forward in MFEIT image reconstruction of the human head,", *proceedings of the ICEBI'04 - XII International Conference on Electrical Bio-Impedance joint with EIT - V Electrical Impedance Tomography, ISBN 83-917681-6-3* ed 2004, pp. 683-686.

[224] M. Bollhöfer and Y. Saad, "Multilevel preconditioners constructed from inverse-based ILUs," *SIAM J. Sci. Comput.*, vol. 27, no. 5, pp. 1627-1650, 2006.

[225] N. Polydorides and W. R. Lionheart, "A Matlab toolkit for three-dimensional electrical impedance tomography: a contribution to the Electrical Impedance and Diffuse Optical Reconstruction Software project," *Meas. Sci. Technol.*, vol. 13, no. 12, pp. 1871-83, 2002.

[226] A. Tizzard, R. H. Bayford, L. Horesh, R. J. Yerworth, and D. S. Holder, "Effects of warping Finite Element meshes for the forward model of the head in EIT," *proceedings of the ICEBI'04 - XII International Conference on Electrical Bio-Impedance joint with EIT - V Electrical Impedance Tomography, ISBN 83-917681-6-3*: 2004.

[227] A. McEwan, R. J. Yerworth, L. Horesh, and D. S. Holder, "Specification and calibration of a Multi-frequency MEIT system for stroke," *3rd European Medical and Biological Engineering Conference, Prague, Czech Republic*: 2005.

[228] A. McEwan, R. J. Yerworth, L. Horesh, A. Romsauerova, R. H. Bayford, and D. S. Holder, "Specification and calibration of a Multifrequency EIT of the head," *VI International Conference on Biomedical Applications of Electrical Impedance Tomography, London, UK*: 2005.

[229] O. Gilad, G. M. Ahadzi, R. H. Bayford, and D. S. Holder, "Near DC conductivity change measurement of fast neuronal activity during human VEP," in *XII International Conference on Electrical Bio-Impedance* 2004, pp. 279-282.

[230] O. Gilad, L. Horesh, G. M. Ahadzi, R. H. Bayford, and D. S. Holder, "Could synchronized neuronal activity be imaged using low frequency electrical impedance tomography (LFEIT)?," *VI International Conference on Biomedical Applications of Electrical Impedance Tomography, London, UK*: 2005.

[231] O. Gilad, L. Horesh, and D. S. Holder, "Non-invasive imaging of synchronized neuronal activity using low frequency electrical impedance tomography (LFEIT) - simulation study," in *IFMBE, 2005. ISSN 1727-1983,* 11 ed. Jiri Hozman and P. Kneppo, Eds. *3rd European Medical and Biological Engineering Conference, Prague, Czech Republic, November 2005*: 2005.

[232] J. Fritschy, L. Horesh, R. H. Bayford, and D. S. Holder, "Applications of GRID in clinical neurophysiology and Electrical Impedance Tomography of brain function," *3rd Healthcare conference, Oxford*: 2005.

[233] L. Fabrizi, M. K. Sparkes, J. F. P. J. Abascal, L. Horesh, and D. S. Holder, "EIT during epileptic seizures: not an easy task," *VI International Conference on Biomedical Applications of Electrical Impedance Tomography, London, UK*: 2005.

[234] L. Horesh, M. Schweiger, M. Bollhöfer, A. Douiri, D. S. Holder, and S. R. Arridge, "Multilevel preconditioning for 3D large-scale soft field medical applications modelling," *Journal of Information and Systems Sciences,* vol. Volume 2, Number 4, no. Special Issue on *Computational Aspect of Soft Field Tomography,* pp. 532-556, 2006.

[235] L. Horesh, M. Schweiger, S. R. Arridge, and D. S. Holder, "Novel large-scale 3D Electrical Impedance Tomography modelling of the human head,", World Congress on Medical Physics and Biomedical Engineering in Seoul ed 2006.

[236] F. Kleinermann, N. J. Avis, and F. A. Alharghan, "Mathematical and experimental investigation of the quasi-static conditions for multi-frequency Electrical Impedance Tomography,", Proceedings of 2nd World Congress on Industrial Process Tomography ed Hannover: 2001, p. 795.

[237] F. Kleinermann, "Three Dimensional Image Reconstruction Algorithm for Electrical Impedance Tomography (EIT)." 2001.

[238] N. Hyv¨onen, "Complete electrode model of electrical impedance tomography: Approximation properties and characterization of inclusions," *SIAM J. Appl. Math,* vol. 64, no. 3, pp. 902-931, 2004.

[239] H. Jain, D. Isaacson, P. M. Edic, and J. C. Newell, "Electrical impedance tomography of complex conductivity distributions with noncircular boundary," *IEEE Trans. Biomed. Eng*, vol. 44, no. 11, pp. 1051-1060, Nov.1997.

[240] J. C. de Munck, "A linear discretization of the volume conductor boundary integral equation using analytically integrated elements," *IEEE Trans. Biomed. Eng*, vol. 39, no. 9, pp. 986-990, Sept.1992.

[241] J. Sikora, S. R. Arridge, R. H. Bayford, and L. Horesh, "The application of hybrid BEM/FEM methods to solve electrical impedance tomography's forward problem for the human head,", *XII ICEBI & V EIT Conference.*, Gdansk. ed 2004.

[242] J. Sikora, A. Zacharopoulos, A. Douiri, M. Schweiger, L. Horesh, S. R. Arridge, and J. Ropoll, "Diffuse photon propagation in multi layered geometries," *Phys. Med. Biol.*, Aug.2005.

[243] J. Jin, *The Finite Element Method in electromagnetics*. New York: 1993, p. 464.

[244] Mathworks LTD, "Matlab the language of numerical computing," Mathworks, 2006.

[245] J. R. Shewchuk, "What is a good linear element? Interpolation, conditioning, and quality measures,", 11th international Meshing Roundtable ed Sandia National Laboratories: Ithaca, New York, 2002, pp. 115-126.

[246] R. Barrett, M. Berry, T. F. Chan, J. Demmek, J. M. Donato, J. Dongarra, V. Eijkhout, P. Roldan, C. Rommie, and H. Van der Vorst, *Templates for the Solution of Linear Systems: Building Blocks for Iterative Methods* SIAM, 1994.

[247] J. Nocedal and S. J. Wright, "Numerical optimization," *Springer series in operations research*, vol. Springer-Verlag, New-York 1999.

[248] J. R. Shewchuk, "An Introduction to the Conjugate Gradient method without the agonizing pain,"2003.

[249] P. J. Vauhkonen, "Image reconstruction in three-dimensional Electrical Impedance Tomography." 2004.

[250] Y. Saad and M. H. Schultz, "GMRes: A generalized minimal residual algorithm for solving nonsymmetric linear systems," *SIAM J. Sci. Statist. Comput.*, vol. 7, pp. 856-869, 1986.

[251] R. W. Freund and N. M. Nachtigal, "QMR Quasi Minimal Residual method for non-Hermitian linear systems," *Numer. Math*, vol. 60, pp. 315-339, 1991.

[252] R. W. Freund and N. M. Nachtigal, "A new Krylov-subspace method for symmetric indefinite linear systems,", 94-07 ed 1994.

[253] Y. Yao, Y. Wang, Y. Pei, W. Zhu, J. Hu, and R. L. Barbour, "Frequency domain optical tomography in human tissue,", 2570 ed. R. Barbour, M. Carvlin, and M. Fiddy, Eds. *Experimental and Numerical Methods for Solving Ill-Posed Inverse Problems: Medical and Nonmedical Applications*: 1995, pp. 254-266.

[254] L. Borcea, "A nonlinear multigrid for imaging electrical conductivity and permittivity at low frequency," *Inverse problems*, vol. 17, no. 2, pp. 329-359, 2001.

[255] A. Brandt, S. McCormick, and J. W. Ruge, "Algebraic multigrid (AMG) for automatic multigrid solution with application to geodetic computations,"POB - 1852, 1982.

[256] M. Soleimani, C. E. Powell, and N. Polydorides, "Improving the forward solver for the complete electrode model in EIT using algebraic multigrid," *IEEE Trans. Med. Imaging*, vol. 24, no. 5, pp. 577-583, May2005.

[257] Comsol Labs, "COMSOL Multiphysics (FEMLab),", Multiphysics ed 2005.

[258] W. L. Briggs, V. E. Henson, and S. F. McCormick, *A multigrid tutorial*, 2nd ed SIAM, 2002.

[259] M. Bollhöfer, "A robust ILU based on monitoring the growth of the inverse factors," *Linear Algebra Appl.*, vol. 338, no. 1-3, pp. 201-218, 2001.

[260] M. Bollhöfer and Saad.Y., "On the relations between ILU s and factored approximate inverses," *SIAM J. Matrix Anal. Appl.*, vol. 24, no. 1, pp. 219-237, 2002.

[261] M. Bollhöfer, Y. Saad, and O. Schenk, "ILUPACK - preconditioning software package,", Available online at http://www.math.tu-berlin.de/ilupack/, Release V2.1, January ed 2006.

[262] O. Schenk, K. Gärtner, and W. Fichtner, "Efficient sparse LU factorization with left-right looking strategy on shared memory multiprocessors," *BIT*, vol. 40, no. 1, pp. 158-176, 2000.

[263] O. Schenk and K. Gärtner, "Solving unsymmetric sparse systems of linear equations with PARDISO," *Journal of Future Generation Computer Systems*, vol. 20(3), no. 475, p. 487, 2004.

[264] O. Schenk and K. Gärtner, "On fast factorization pivoting methods for sparse symmetric indefinite systems," Department of Computer Science, University of Basel,CS-2004-004, 2004.

[265] Y. Saad, "A flexible inner-outer preconditioned GMRes algorithm," *SIAM J. Sci. Stat. Comput.*, vol. 14, pp. 461-469, 1993.

[266] D. B. Geselowitz, "An Application of Lead Theory to Impedance Plethysmography," *IEEE Trans. Biomed. Eng*, vol. 18, no. 1, pp. 38-41, 1971.

[267] S. R. Arridge, "Optical tomography in medical imaging," *Inverse problems*, vol. 15, no. 2, p. R41-R93, 1999.

[268] S. R. Arridge, J. P. Kaipio, V. Kolehmainen, M. Schweiger, E. Somersalo, T. Tarvainen, and M. Vauhkonen, "Approximation errors and model reduction with an application in optical diffusion tomography," *Inverse problems*, vol. 22, no. 1, pp. 175-195, 2006.

[269] A. P. Gibson, "Electrical Impedance Tomography of Human Brain Function." 2000.

[270] "Curry," Neuroscan, Neurosoft, Inc., 2004.

[271] "UGS I-DEAS," 2004.

[272] M. Schweiger and S. R. Arridge, "TOAST - Time-resolved Optical Absorption and Scattering Tomography,", Available online at http://www.medphys.ucl.ac.uk/~martins/toast/index.html ed 2006.

[273] R. J. Yerworth, L. Horesh, R. H. Bayford, A. Tizzard, and D. S. Holder, "Robustness of linear and non-linear reconstructions algorithms for brain EITS - Non-linear - is it worth the effort?," *proceedings of the ICEBI'04 - XII International Conference on Electrical Bio-Impedance joint with EIT - V Electrical Impedance Tomography, ISBN 83-917681-6-3*: 2004.

[274] S. R. Arridge and M. Schweiger, "A gradient based optimization scheme for optical tomography," *Optics Express*, vol. 2, no. 6, p. 213, Mar.1998.

[275] O. Dorn, H. Bertete-Aguirre, J. G. Berryman, and G. C. Papanicolaou, "A nonlinear inversion method for 3D electromagnetic imaging using adjoint fields," *Inverse problems*, vol. 15, pp. 1523-1558, 1999.

[276] L. Horesh, A. Romsauerova, O. Gilad, A. McEwan, S. R. Arridge, and D. S. Holder, "Review of the dielectric properties of the human head for Multi-Frequency Electrical Impedance Tomography (MFEIT)," 2006.

[277] Y. Saad, "Iterative methods for sparse linear systems - Preconditioning techniques,", 2nd ed SIAM, 2003.

[278] S. Röllin and O. Schenck, "Maximum-weighted matching strategies and the application to symmetric indefinite systems,", Lecture Notes in Computer Science LNCS 3732 ed 2005, pp. 808-817.

[279] J. Hadamard, "Boundary value problems for partial differential equations and their physical interpretation," *Bull. Univ. Princeton*, vol. **13**, no. 49 1902.

[280] J. Hadamard, "Lectures on Cauchy's problem in linear Partial Differential Equations," 1923.

[281] Bertero B. and Boccacci P., *Inverse problems in imaging* Institute of Physics publishing Bristol and Philadelphia, 1998.

[282] G. H. Golub and C. F. van Loan, *Matrix computation*, third edition ed. Baltimore: John Hopkins university press, 1996.

[283] J. P. Kaipio, M. Vauhkonen, E. Somersalo, and V. Kolehmainen, "Statistical inversion and Monte Carlo sampling methods in electrical impedance tomography," *Inverse problems*, vol. **16**, pp. 1487-1522, June2000.

[284] J. P. Kaipio, S. Aku, E. Somersalo, and Heikki Haario, "Statistical inversion approach for optimizing current patterns in EIT," 3rd World Congress on Industrial Process Tomography, Banff, Canada, September 2-5, 2003: 2003.

[285] M. Vauhkonen, D. Vadasz, P. A. Karjalainen, E. Somersalo, and J. P. Kaipio, "Tikhonov regularization and prior information in electrical impedance tomography," *IEEE Trans. Med. Imaging*, vol. 17, no. 2, pp. 285-293, Apr.1998.

[286] J. L. Mueller, S. Siltanen, and D. Isaacson, "A direct reconstruction algorithm for electrical impedance tomography," *IEEE Trans. Med. Imaging*, vol. 21, no. 6, pp. 555-559, June2002.

[287] B. H. Blott, S. J. Cox, G. J. Daniell, M. J. Caton, and D. A. Nicole, "High fidelity imaging and high performance computing in nonlinear EIT," *Physiol. Meas.*, vol. 21, no. 1, pp. 7-13, Feb.2000.

[288] S. R. Arridge and J. C. Hebden, "Optical imaging in medicine: II. Modelling and reconstruction," *Phys. Med. Biol.*, vol. 42, no. 5, pp. 841-853, May1997.

[289] W. R. Breckon and M. K. Pidcock, "Ill-posedness and non-Linearity in Electrical-Impedance Tomography," *Information Processing in Medical Imaging*, vol. Ed de Graaf and Viergever, pp. 235-244, 1988.

[290] A. Ranganathan, "The Levenberg-Marquardt Algorithm,"June2004.

[291] K. Levenberg, "A method for the solution of certain problems in least squares," *Quart. Appl. Math.*, vol. 2, pp. 164-168, 1944.

[292] D. Marquardt, "An algorithm for least-squares estimation of nonlinear parameters," *SIAM J. Appl. Math*, vol. 11, pp. 431-441, 1963.

[293] W. H. Press, S. A. Teukolsky, W. T. Vetterling, and B. P. Flannery, *Numerical recipes in C - The art of scientific computing*, Second Edition ed. *Cambridge New York Port Chester Melbourne Sydney*: Press Syndicate of the University of Cambridge, 2002.

[294] J. Nocedal, "Updating quasi-Newton matrices with limited storage," *Mathematics of Computation*, vol. 95, pp. 339-353, 1980.

[295] R. Fletcher and M. C. Reeves, "Function minimization by Conjugate Gradients," *Computer Journal*, pp. 149-154, 1964.

[296] D. A. H. Jacobs, *The state of the art in numerical analysis* (London: Academic Press), 1977.

[297] N. Polydorides, W. R. Lionheart, and H. McCann, "Krylov subspace iterative techniques: on the detection of brain activity with electrical impedance tomography," *IEEE Trans. Med. Imaging*, vol. 21, no. 6, pp. 596-603, June2002.

[298] M. Molinari, S. J. Cox, B. H. Blott, and G. J. Daniell, "Comparison of algorithms for non-linear inverse 3D electrical tomography reconstruction," *Physiol. Meas.*, vol. 23, no. 1, pp. 95-104, Feb.2002.

[299] L. Horesh, M. Schweiger, S. R. Arridge, and D. S. Holder, "Novel large-scale non-linear 3D reconstruction algorithms for Electrical Impedance Tomography of the human head,", World Congress on Medical Physics and Biomedical Engineering in Seoul ed 2006.

[300] N. Polydorides, "Image reconstruction algorithms for soft-field tomography." 2002.

[301] D. Isaacson, J. L. Mueller, J. C. Newell, and S. Siltanen, "Reconstructions of chest phantoms by the D-bar method for electrical impedance tomography," *IEEE Trans. Med. Imaging*, vol. 23, no. 7, pp. 821-828, July2004.

[302] M. D. Cheney, D. Isaacson, J. C. Newell, S. Simske, and J. Golbe, "NOSER: An algorithm for solving the inverse conductivity problem," *Int. J. ImagingSystems & Technology*, vol. 2, pp. 66-75, 1990.

[303] M. Schweiger and S. R. Arridge, "Optical tomographic reconstruction in a complex head model using a priori region boundary information," *Phys. Med. Biol.*, vol. 44, no. 11, pp. 2703-2721, Nov.1999.

[304] R. P. Brent, "Algorithms for minimization without derivatives," Englewood Cliffs, NJ: Prentice-Hall, 1973.

[305] M. Vauhkonen, J. P. Kaipio, E. Somersalo, and P. A. Karjalainen, "Electrical impedance tomography with basis constraints," *Inverse problems*, vol. 13, no. 2, pp. 523-530, 1997.

[306] A. Borsic, W. R. Lionheart, and C. N. McLeod, "Generation of anisotropic-smoothness regularization filters for EIT," *IEEE Trans. Med. Imaging*, vol. 21, no. 6, pp. 579-587, June2002.

[307] A. Borsic, "Regularisation methods for imaging from electrical measurements." School of Engineering Oxford Brookes University, 2002.

[308] V. A. Morozov, "On the solution of functional equations by the method of regularization," *SovietMath. Dokl.*, vol. 7, pp. 414-417, 1966.

[309] G. Wahba, "Spline models for observational data,", SIAM. CBMS-NSF Regional Conference Series in Applied Mathematics ed 1990.

[310] P. C. Hansen, "Regularization tools - A Matlab package for analysis and solution of discrete ill-posed problems," 1992.

[311] C. L. Lawson and R. J. Hanson, *Solving Least Squares Problems*, EnglewoodCliffs ed. NJ: 1974.

[312] E. Haber and D. W. Oldenburg, "A GCV based method for nonlinear ill-posed problems,"1998.

[313] E. M. Kilmer and D. P. O'leary, "Choosing regularization parameters in iterative methods for ill-posed problems," *SIAM J. Matrix Anal. Appl.*, vol. Vol. 22, no. 4, pp. 1204-1221, 2001.

[314] C. R. Vogel, "Non-convergence of the L-curve regularization parameter selection method," *Inverse problems*, no. 4, pp. 535-547, 1996.

[315] C. R. Vogel, *Computational Methods for Inverse Problems* SIAM, Philadelphia, 2002.

[316] A. M. Urmanov, A. V. Gribok, H. Bozdogan, J. W. Hines, and R. E. Uhrig, "Information complexity-based regularization parameter selection for solution of ill conditioned inverse problems," *Inverse problems*, no. 2, p. L1-L9, 2002.

[317] C. G. Farquharson and D. W. Oldenburg, "A comparison of automatic techniques for estimating the regularization parameter in nonlinear inverse problems," *Geophysical Journal International*, vol. 156, pp. 411-425, 2004.

[318] M. T. Clay and T. C. Ferree, "Weighted regularization in electrical impedance tomography with applications to acute cerebral stroke," *IEEE Trans. Med. Imaging*, vol. 21, no. 6, pp. 629-637, June2002.

[319] C. J. Kotre, "EIT image reconstruction using sensitivity weighted filtered backprojection," *Physiol. Meas.*, vol. 15 Suppl 2a, p. A125-A136, May1994.

[320] S. Kaczmarz, "Approximate solution of systems of linear equations," *Bull. Acad. Polon. Sci. Lett.*, vol. A 35, no. English transl.: Internat. J. Control 57(1993), 1269-1271, pp. 355-357, 1937.

[321] N. A. Thacker and P. A. Bromiley, "The Equal Variance Domain: Issues surrounding the use of probability densities in algorithm design,", Tina Memo No. 2004-005 ed BMVA and Royal Statistical Society: Imaging Science and Biomedical Engineering Division,
Medical School, University of Manchester,
Stopford Building, Oxford Road,
Manchester, M13 9PT., 2004.

[322] M. Schweiger, S. R. Arridge, and I. Nissila, "Gauss-Newton method for image reconstruction in diffuse optical tomography," *Phys. Med. Biol.*, vol. 50, no. 10, pp. 2365-2386, May2005.

[323] D. A. Knoll and D. E. Keyes, "Jacobian-free Newton–Krylov methods:a survey of approaches and applications," *Computational Physics*, pp. 357-397, 2004.

[324] Tikhonov A.N., "Solution of incorrectly formulated problems and the regularization method," *Soviet Math. Dokl.*, vol. 4, pp. 1035-1038, 1963.

[325] E. Darve and P. Have, "A fast multipole method for Maxwell equations stable at all frequencies," *Philos. Transact. A Math. Phys. Eng Sci.*, vol. 362, no. 1816, pp. 603-628, Mar.2004.

[326] S. Börm and L. Grasedyck, "Hlib,", http://www.hlib.org/ ed 2006.

[327] M. Bebendorf, "AHMED,", http://www.math.uni-leipzig.de/~bebendorf/AHMED.html ed 2006.

[328] E. Haber, "Quasi-Newton methods for large-scale electromagnetic inverse problems," *Inverse problems*, vol. 21, no. 1, pp. 305-323, 2005.

[329] M. Power, "An update on thrombolysis for acute ischaemic stroke," *ACNR*, vol. 4, no. 3 Aug.2004.

[330] A. Lozano, J. Rosell, and R. Pallas-Areny, "Errors in prolonged electrical impedance measurements due to electrode repositioning and postural changes," *Physiol. Meas.*, vol. 16, no. 2, pp. 121-130, May1995.

[331] J. Schlappa, E. Annese, and H. Griffiths, "Systematic errors in multi-frequency EIT," *Physiol. Meas.*, vol. 21, no. 1, pp. 111-118, Feb.2000.

[332] B. H. Brown, D. C. Barber, W. Wang, L. Lu, A. D. Leathard, R. H. Smallwood, A. R. Hampshire, R. Mackay, and K. Hatzigalanis, "Multi-frequency imaging and modelling of respiratory related electrical impedance changes," *Physiol. Meas.*, vol. 15 Suppl 2a, pp. A1-12, May1994.

[333] G. Bonmassar, S. Iwaki, L. Angelone, J. W. Belliveau, J. D. Schaecter, and M. H. Lev, "A novel and portable device for real-time, noninvasive stroke assesment," 2005.

[334] T. Brott, J. R. Marler, C. P. Olinger, H. P. Adams, Jr., T. Tomsick, W. G. Barsan, J. Biller, R. Eberle, V. Hertzberg, and M. Walker, "Measurements of acute cerebral infarction: lesion size by computed tomography," *Stroke*, vol. 20, no. 7, pp. 871-875, July1989.

[320] S. Kaczmarz, "Approximate solution of systems of linear equations," *Bull. Acad. Polon. Sci. Lett.*, vol. A 35, no. English transl.: Internat. J. Control 57(1993), 1269-1271, pp. 355-357, 1937.

[321] N. A. Thacker and P. A. Bromiley, "The Equal Variance Domain: Issues surrounding the use of probability densities in algorithm design,", Tina Memo No. 2004-005 ed BMVA and Royal Statistical Society: Imaging Science and Biomedical Engineering Division,
Medical School, University of Manchester,
Stopford Building, Oxford Road,
Manchester, M13 9PT., 2004.

[322] M. Schweiger, S. R. Arridge, and I. Nissila, "Gauss-Newton method for image reconstruction in diffuse optical tomography," *Phys. Med. Biol.*, vol. 50, no. 10, pp. 2365-2386, May2005.

[323] D. A. Knoll and D. E. Keyes, "Jacobian-free Newton–Krylov methods:a survey of approaches and applications," *Computational Physics*, pp. 357-397, 2004.

[324] Tikhonov A.N., "Solution of incorrectly formulated problems and the regularization method," *Soviet Math. Dokl.*, vol. 4, pp. 1035-1038, 1963.

[325] E. Darve and P. Have, "A fast multipole method for Maxwell equations stable at all frequencies," *Philos. Transact. A Math. Phys. Eng Sci.*, vol. 362, no. 1816, pp. 603-628, Mar.2004.

[326] S. Börm and L. Grasedyck, "Hlib,", http://www.hlib.org/ ed 2006.

[327] M. Bebendorf, "AHMED,", http://www.math.uni-leipzig.de/~bebendorf/AHMED.html ed 2006.

[328] E. Haber, "Quasi-Newton methods for large-scale electromagnetic inverse problems," *Inverse problems*, vol. 21, no. 1, pp. 305-323, 2005.

[329] M. Power, "An update on thrombolysis for acute ischaemic stroke," *ACNR*, vol. 4, no. 3 Aug.2004.

[330] A. Lozano, J. Rosell, and R. Pallas-Areny, "Errors in prolonged electrical impedance measurements due to electrode repositioning and postural changes," *Physiol. Meas.*, vol. 16, no. 2, pp. 121-130, May1995.

[331] J. Schlappa, E. Annese, and H. Griffiths, "Systematic errors in multi-frequency EIT," *Physiol. Meas.*, vol. 21, no. 1, pp. 111-118, Feb.2000.

[332] B. H. Brown, D. C. Barber, W. Wang, L. Lu, A. D. Leathard, R. H. Smallwood, A. R. Hampshire, R. Mackay, and K. Hatzigalanis, "Multi-frequency imaging and modelling of respiratory related electrical impedance changes," *Physiol. Meas.*, vol. 15 Suppl 2a, pp. A1-12, May1994.

[333] G. Bonmassar, S. Iwaki, L. Angelone, J. W. Belliveau, J. D. Schaecter, and M. H. Lev, "A novel and portable device for real-time, noninvasive stroke assesment," 2005.

[334] T. Brott, J. R. Marler, C. P. Olinger, H. P. Adams, Jr., T. Tomsick, W. G. Barsan, J. Biller, R. Eberle, V. Hertzberg, and M. Walker, "Measurements of acute cerebral infarction: lesion size by computed tomography," *Stroke*, vol. 20, no. 7, pp. 871-875, July1989.

[335] P. D. Lyden, R. Zweifler, Z. Mahdavi, and L. Lonzo, "A rapid, reliable, and valid method for measuring infarct and brain compartment volumes from computed tomographic scans," *Stroke*, vol. 25, no. 12, pp. 2421-2428, Dec.1994.

[336] J. L. Saver, K. C. Johnston, D. Homer, R. Wityk, W. Koroshetz, L. L. Truskowski, and E. C. Haley, "Infarct Volume as a Surrogate or Auxiliary Outcome Measure in Ischemic Stroke Clinical Trials," *Stroke*, vol. 30, no. 2, pp. 293-298, Feb.1999.

[337] NINDS, "Effect of intravenous recombinant tissue Plasminogen Activator on ischemic stroke lesion size measured by Computed Tomography," *Stroke*, vol. 31, no. 12, pp. 2912-2919, Dec.2000.

[338] B. Kissela, J. Broderick, D. Woo, R. Kothari, R. Miller, J. Khoury, T. Brott, A. Pancioli, E. Jauch, J. Gebel, R. Shukla, K. Alwell, T. Tomsick, and E. Kenton, "The greater Cincinnati/Northern Kentucky stroke study: Volume of first-ever ischemic stroke among blacks in a population-based study editorial comment," *Stroke*, vol. 32, no. 6, pp. 1285-1290, June2001.

[339] S. Schwab, M. Spranger, S. Schwarz, and W. Hacke, "Barbiturate coma in severe hemispheric stroke: Useful or obsolete?," *Neurology*, vol. 48, no. 6, pp. 1608-1613, June1997.

[340] J. L. Arnold, "Stroke, Ischemic,"Mar.2005.

[341] R. Merwa, K. Hollaus, O. Biro, and H. Scharfetter, "Detection of brain oedema using magnetic induction tomography: a feasibility study of the likely sensitivity and detectability," *Physiol. Meas.*, no. 1, pp. 347-354, 2004.

[342] N. Gao, S. A. Zhu, and B. He, "Use of 3-D magnetic resonance electrical impedance tomography in detecting human cerebral stroke: a simulation study," *J. Zhejiang. Univ Sci. B*, vol. 6, no. 5, pp. 438-445, May2005.

[343] P. J. Riu, J. Rosell, A. Lozano, and R. Pallas-Areny, "A broadband system for multifrequency static imaging in electrical impedance tomography," *Clin. Phys. Physiol. Meas.*, vol. 13 Suppl A, pp. 61-65, 1992.

[344] D. Jennings and I. D. Schneider, "Front-end architecture for a multi-frequency electrical impedance tomography system," *Med. Biol. Eng Comput.*, vol. 39, no. 3, pp. 368-374, May2001.

[345] A. J. Wilson, P. Milnes, A. R. Waterworth, R. H. Smallwood, and B. H. Brown, "Mk3.5: a modular, multi-frequency successor to the Mk3a EIS/EIT system," *Physiol. Meas.*, vol. 22, no. 1, pp. 49-54, Feb.2001.

[346] M. Mayer, P. Brunner, R. Merwa, and H. Scharfetter, "Direct reconstruction of tissue parameters from differential multifrequency EIT in vivo," *VI International Conference on Biomedical Applications of Electrical Impedance Tomography, London, UK*: 2005.

[347] N. K. Soni, K. D. Paulsen, H. Dehghani, and A. Hartov, "Finite element implementation of Maxwell's equations for image reconstruction in electrical impedance tomography," *IEEE Trans. Med. Imaging*, vol. 25, no. 1, pp. 55-61, Jan.2006.

[348] G. S. Russell, E. K. Jeffrey, P. Poolman, P. Luu, and D. M. Tucker, "Geodesic photogrammetry for localizing sensor positions in dense-array EEG," *Clin. Neurophysiol.*, vol. 116, no. 5, pp. 1130-1140, May2005.

[349] A. Romsauerova, A. McEwan, L. Horesh, O. Tong, W. Eung, and D. S. Holder, "A Comparison of Multi-Frequency EIT systems intended for imaging acute stroke,", World Congress on Medical Physics and Biomedical Engineering in Seoul ed 2006.

[350] R. Shindmes and D. S. Holder, "Development of patient specific finite element meshes for Electrical Impedance Tomography," UCL Medical Physics 1st year PhD presentation session: 2006.

[351] A. P. Gibson, J. Riley, M. Schweiger, J. C. Hebden, S. R. Arridge, and D. T. Delpy, "A method for generating patient-specific finite element meshes for head modelling," *Phys. Med. Biol.*, vol. 48, no. 4, pp. 481-495, Feb.2003.

[352] V. Kolehmainen, S. R. Arridge, M. Vauhkonen, and J. P. Kaipio, "Simultaneous reconstruction of internal tissue region boundaries and coefficients in optical diffusion tomography," *Phys. Med. Biol.*, vol. 45, no. 11, pp. 3267-3283, Nov.2000.

[353] L. M. Heikkinen, T. Vilhunen, R. M. West, and M. Vauhkonen, "Simultaneous reconstruction of electrode contact impedances and internal electrical properties: II. Laboratory experiments," *Measurement Science & Technology*, vol. 13, no. 12, pp. 1855-1861, Dec.2002.

[354] L. M. Heikkinen, T. Vilhunen, R. M. West, and A. Vauhkoneny, "Simultaneous reconstruction of electrode contact impedances and internal electrical properties. Part II:Application,"2005.

[355] T. Vilhunen, J. P. Kaipio, P. J. Vauhkonen, T. Savolainen, and M. Vauhkonen, "Simultaneous reconstruction of electrode contact impedances and internal electrical properties: I. Theory," *Measurement Science & Technology*, vol. 13, no. 12, pp. 1848-1854, Dec.2002.

[356] L. Fabrizi, L. Horesh, A. McEwan, and D. S. Holder, "A feasibility study for imaging of epileptic seizures by EIT using a realistic FEM of the head,", World Congress on Medical Physics and Biomedical Engineering in Seoul ed 2006.

[357] O. Gilad, Horesh.L., and D. S. Holder, "Could Synchronized Neuronal Activity be Imaged Using Magnetic Detection Electrical Impedance Tomography (MD-EIT)?,", World Congress on Medical Physics and Biomedical Engineering in Seoul ed 2006.

[358] D. A. Boas, A. M. Dale, and M. A. Franceschini, "Diffuse optical imaging of brain activation: approaches to optimizing image sensitivity, resolution, and accuracy," *NeuroImage*, vol. 23 Suppl 1, p. S275-S288, 2004.

[359] G. Biros and O. Ghattas, "Parallel Lagrange-Newton-Krylov-Schur algorithms for constrained optimization part I: The Krylov-Schur solver," 2005.

[360] E. Haber, U. M. Ascher, and D. W. Oldenburg, "Inversion of 3D electromagnetic data in frequency and time domain using an inexact all-at-once approach," *Geophysics*, vol. 69, no. 5, pp. 1216-1228, Sept.2004.

[361] D. C. Barber and B. H. Brown, "Recent developments in applied potential tomography," *Information Processing in Medical Imaging. S. L. Bacharach. Dordrecht, Martinus Nijhoff:* pp. 106-121, 1986.

[362] D. C. Barber and A. D. Seagar, "Fast reconstruction of resistance images," *Clin. Phys. Physiol. Meas.*, vol. 8, no. A, pp. 47-54, 1987.

[363] R. H. Bayford, Y. Hanquan, K. G. Boone, and D. S. Holder, "Experimental validation of a novel reconstruction algorithm for electrical impedance tomography based on backprojection of Lagrange multipliers," *Physiol. Meas.*, vol. 16, no. 3 Suppl A, p. A237-A247, Aug.1995.

[364] J. P. Morucci, P. M. Marsili, M. Granie, Y. Shi, M. Lei, and W. W. Dai, "A direct sensitivity matrix approach for fast reconstruction in electrical impedance tomography," *Physiol. Meas.*, vol. 15, p. A107-A114, May1994.

[365] P. C. Hansen, *Rank-Deficient and Discrete Ill-Posed Problems: Numerical Aspects of Linear Inversion*, 2 ed SIAM, 1997, p. -247.

[366] W. R. Breckon, "Singular value decomposition and least squares solutions." Oxford Polytechnic, 1990.

[367] B. M. Eyuboglu, "An interleaved drive electrical impedance tomography image reconstruction algorithm," *Physiol. Meas.*, vol. 17 Suppl 4A, p. A59-A71, Nov.1996.

[368] F. Kleinermann, N. J. Avis, S. K. Judah, and D. C. Barber, "Three-dimensional image reconstruction for electrical impedance tomography," *Physiol. Meas.*, vol. *17*, p. *A77-A83*, 1996.

[369] A. T. Tidswell, A. P. Bagshaw, D. S. Holder, R. J. Yerworth, L. Eadie, S. Murray, L. Morgan, and R. H. Bayford, "A comparison of headnet electrode arrays for electrical impedance tomography of the human head," *Physiol. Meas.*, vol. 24, no. 2, pp. 527-544, May2003.

[370] A. Le Hyaric and M. K. Pidcock, "An image reconstruction algorithm for three-dimensional electrical impedance tomography," *IEEE Trans. Biomed. Eng*, vol. 48, no. 2, pp. 230-235, Feb.2001.